UNIVERSITÀ DEGLI STUDI DI PAVIA
DOTTORATO DI RICERCA IN FISICA – XXXII CICLO

Nonclassical states of light: fundamental physics and CMOS devices

Francesco Garrisi

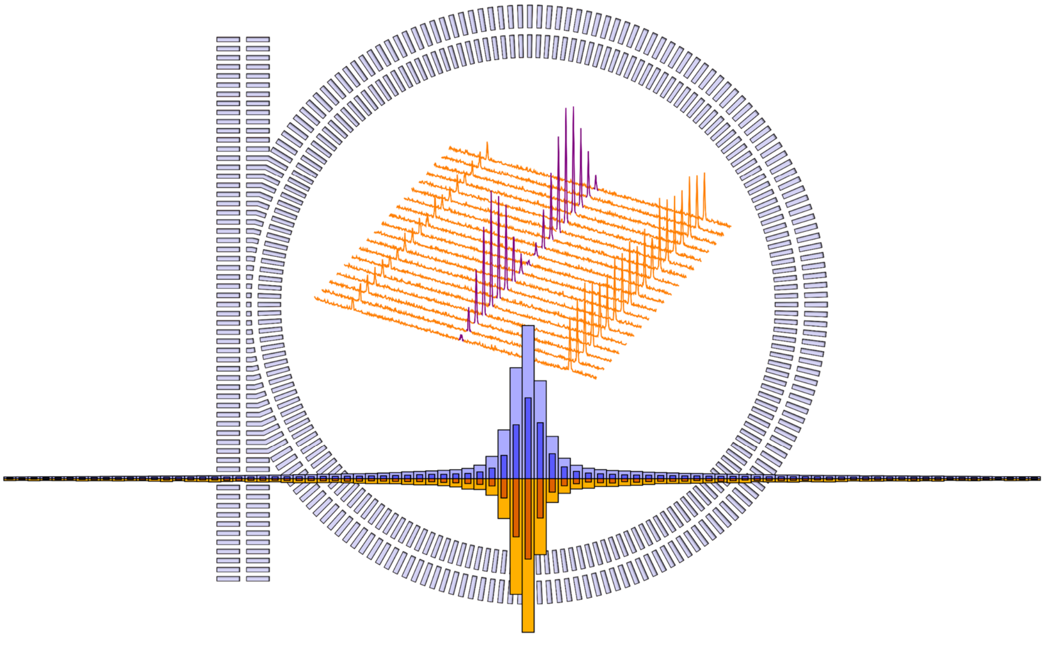

Tesi per il conseguimento del titolo

Università degli Studi di Pavia
Dipartimento di Fisica

DOTTORATO DI RICERCA IN FISICA – XXXII CICLO

Nonclassical states of light: fundamental physics and CMOS devices

Francesco Garrisi

Submitted to the Graduate School of Physics in partial
fulfillment of the requirements for the degree of
DOTTORE DI RICERCA IN FISICA
DOCTOR OF PHILOSOPHY IN PHYSICS
at the
University of Pavia

Supervisors: Prof. Daniele Bajoni, Prof. Matteo Galli

Cover: Artistic representations. Foreground: comparison of various histograms produced by classical and quantum light (Chapter 5). Background: scheme of a microring resonator based on suspended waveguides (Chapter 4). Center: coincidence histograms produced by entangled states of light (Chapter 3).

Nonclassical states of light: fundamental physics and CMOS devices
Francesco Garrisi
PhD thesis - University of Pavia
Pavia, Italy, September 2019

To my family and friends.

Acknowledgements

The realization of this work would not have been possible without the help of many people.

First of all, I wish to thank my supervisors, Matteo and Daniele. You put so much effort in making me a better researcher, and I should listen more to what you tell me. Three years of life are a long time span, and I am very happy to have made the descision to spend them in Pavia with you.

I wish also to thank Marco Liscidini for his precious suggestions and discussions, both on physics and on life. I know I can always count on your steady support.

Working surrounded by friends makes it a much richer experience, for which I am so grateful to Marco, Federico, Andrea, Alberto, Micol, Savda. As we all know, at times a PhD can be challenging both on a professional and personal level, but all this is so easily forgotten around you. Naturally, many thanks go to all the other collegues I met during these years in Pavia, especially to Daniele, Nicola, Matteo, Marco, Tommaso.

I spent several months of the past three years in Southampton. Alberto, the continuous support and teaching you provide is invaluable, and I am greatful to have had the opportunity to spend some time in your group. Life in England has been more joyful thanks to my friends and collegues there, especially Ioannis, Robert, who spent so much time in the clean room for me (thank you!), and also Silvia, Nick, Chris, Giacomo, Julian, Stella, Helgi, Lucy and all others. It is a truly special experience to sit at tables where almost no two people have the same nationality.

Special thanks go to the reviewers of this thesis, Prof. Marcello Ferrera and Prof. Marcelo França Santos, who thoroughly read the thesis and whose suggestions helped improving the manuscript.

Last but not least, the support one receives from his family and friends is invaluable. Even if indirect, your contribution has been far more important than it might seem.

You are all in my heart.

Contents

List of Figures

Apart from Fig. 2.19, all the figures have been realized by the Author.

List of Tables

Introduction

The discovery of the quantum nature of light, through the explanations of black body radiation and the photoelectric effect [1] by Planck and Einstein, have brought enormous progress in the understanding of the quantum mechanical properties of the universe, and it helped to shape the theory of Quantum Mechanics itself.

The theoretical description of light in the framework of the Second Quantization [2] and advances in the generation, manipulation and measurement of quantum light has improved to the point that more and more technological application are emerging that exploit the quantum properties of electromagnetic radiation, promising better performances compared to applications where classical light is employed.

Two of the most successful areas in this regard are Quantum Metrology [3] and Quantum Communication [4]. The former is the study of measurements with the eyes of Quantum Mechanics; exploiting the quantum properties of the system under observation and of the probe (which can be electromagnetic radiation) can produce more information per measurement than possible with classical resources. The latter is the study of the transmission of quantum information, codified with the qubit; photons are particularly well suited in this respect, not only because they travel at the speed of light, but most importantly because their weak interaction with the environment and among themselves preserves the delicate quantum information that they carry along the propagation.

Recently, quantum photonic devices are moving towards the integrated platform. If this approach will prove successful, the advantage compared to bulk platforms would reside in the larger production volumes and lower costs that an industrial platform grants, and to the possibility of integrating photonic and electronic circuits on the same device.

Challenges remain to be solved, however, before large scale quantum photonic applications become viable. For instance, current fabrication technologies do not allow the realization of effectively indistinguishable single-photon sources, a key requirement for obtaining quantum interference phenomena, without which the advantage compared to classical platforms is lost. Another challenge, specifically related to sources of photon pairs based on microring resonators, is the extraction of the pairs from the strong pump beam used to generate them. Much of the work described in this thesis has been dedicated to integrated quantum photonic applications, operating in the near infrared telecom frequency range, where some of these problems have been addressed.

Nonetheless, bulk optical experiments remain fundamental tools for the study of the properties of light itself because of the ease of manipulation of light at more macroscopic scales. Fundamental experimental demonstrations have been performed with quantum states of light, such as the violation of local realism [5] and teleportation [6]. The last part of the thesis indeed regards a fundamental physics experiment where a bulk optical source of photon pairs has been employed.

Outline

Chapter 1 gives an overview on the basic theoretical concepts of Quantum Information Theory and illustrates the state of the art of quantum technologies related to the experimental work described in later chapters. In particular, common bulk and integrated photonic platforms used for quantum applications are described, with a focus on the generation of quantum states of light.

Chapter 2 illustrates in more detail the theoretical concepts at the basis of the experiments described in the following chapters.

Chapter 3 describes how a source of photon pairs is realized by closing on itself a Silicon microresonator inside an optical fiber loop cavity containing an amplifier. As detailed in the Chapter, this so-called *self-pumping* configuration, removes the need for an external tunable laser pump, and it was the first time that entangled pairs of photons were produced from a self-pumped microresonator. The Chapter describes the setup and the characterization measurements of the microresonator, of the cavity and of the nonlinear optical processes occurring inside the resonator.

Chapter 4 describes two works performed by the Author in collaboration with Alberto Politi and his group at the University of Southampton, and it is based on two different periodic dielectric structures. In order to simplify the fabrication process of Silicon Carbide photonic structures, subwavelength periodic geometries have been exploited to design and realize a complete photonic platform. The first part of the Chapter describes the design process of the platform and illustrates the results of the characterization of the first fabricated devices.

The second part of the Chapter illustrates a novel design of a waveguide Bragg filter which is to be used to suppress the strong pump field below the level of generated photon pairs in microring resonators. The design process for a Silicon Nitride filter is illustrated, and then a comparison between the theoretical predictions and the experimental characterization of the first test sample is performed.

Chapter 5 describes a bulk optical experiment that was used to test a fundamental property of Quantum Mechanics, the collapse of the wavefunction.

Finally, the conclusions are given in Chapter 6.

Contributions

The contribution of the Author to the works described in this thesis is as follows.

In Chapter 2, the Author employed the formalism of time and frequency-dependent ladder operator to theoretically describe the Franson experiment.

Regarding the work on microresonators described in Chapter 3, the Author designed and built the self-pumped cavity, he realized the experimental setup apart from the Franson interferometer, he performed all the measurements shown on this thesis and performed modeling and data analysis.

For both the Silicon Nitride and Silicon Carbide projects, described in Chapter 4, the Author performed the theoretical analysis and numerical simulation of the structures, he produced the samples' design and he performed characterization measurements and data analysis.

Regarding the work on the photon wavefunction's collapse, described in Chapter 5, the Author built the parametric source of photon pairs, he realized the setup of the experiment, and he performed data acquisition and analysis with contributions by A. Zambianchi and M. Previde Massara.

Chapter 1

Context: light in quantum technologies

This chapter illustrates the background on which the work of the Author is building upon. In this chapter we first give, in Section 1.1, a brief description of qubits, quantum operations and entanglement. Then, in Section 1.2 we describe various ways in which qubits can be encoded on photonic states. Section 1.3 describes the technological applications of photons in quantum technologies: we first give brief overviews of the fields of Quantum Communication, Quantum Computation and Metrology, followed by an introduction on common integrated platform for photonics and on integrated devices that are commonly used, such as the waveguide, the microring resonator, couplers and photonic crystals; the theoretical description of some of these components is found in Chapter 2. Finally, Section 1.4 gives a more detailed overview on integrated applications of quantum photonics focusing on the generation of quantum states of light.

1.1 The Qubit

While the fundamental unit of classical information is the bit, the fundamental unit of quantum information is the *qubit* [7]. At variance with its classical counterpart, that can only assume values 0 or 1, the qubit is described by the wavefunction of a two-level quantum system that can be represented by the following expression

$$|\psi\rangle = \alpha\,|0\rangle + \beta\,|1\rangle \tag{1.1.1}$$

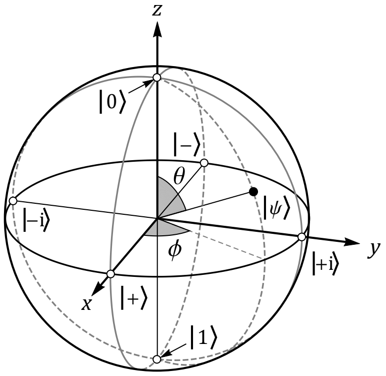

Figure 1.1: Any one-qubit state can be represented in polar coordinates on the surface of the Bloch sphere.

where α and β are complex numbers such that $|\alpha|^2 + |\beta|^2 = 1$ (normalization) and where $|0\rangle$ and $|1\rangle$ are two orthonormal quantum states, in Dirac notation, that, in the context of quantum information theory, are usually called the *computational basis*. The qubit therefore can assume any of an infinite continuum of states, determined by the complex coefficients α and β and it can be equivalently represented by the complex vector

$$|\psi\rangle = \begin{pmatrix} \alpha \\ \beta \end{pmatrix} = \alpha \begin{pmatrix} 1 \\ 0 \end{pmatrix} + \beta \begin{pmatrix} 0 \\ 1 \end{pmatrix} \tag{1.1.2}$$

Mathematically, all the possible qubits $|\psi\rangle$ live in a Hilbert space $\mathcal{H}$ spanned by the computational basis, and restricted by the normalization requirement. A visual representation of the qubit is the *Bloch sphere* (Figure 1.1): without loss of generality, we can assume that α is real, since any global phase is irrelevant in Quantum Mechanics, and we can rewrite the qubit state as

$$|\psi\rangle = \cos(\theta/2)\,|0\rangle + e^{i\phi}\sin(\theta/2)\,|1\rangle \tag{1.1.3}$$

where θ and ϕ are angles varying between 0 and π and 0 and 2π, respectively. If θ and ϕ are taken as polar coordinates, the qubit can be represented as in Figure 1.1. The basis states $|0\rangle$ and $|1\rangle$ are the poles of the Bloch sphere, and the state (1.1.3) lives on the surface of such sphere.

1.1.1 Multipartite states and entanglement

States of multiple qubits can also be defined. By extending the definition (1.1.1), a two-qubit state will be represented by a superposition between extended basis states that are given by the tensor product of the basis states of the individual qubits:

$$\begin{aligned}|\psi\rangle = \begin{pmatrix}\alpha\\ \beta\\ \gamma\\ \delta\end{pmatrix} &= \alpha\,|0,0\rangle_{A,B} + \beta\,|0,1\rangle_{A,B} + \gamma\,|1,0\rangle_{A,B} + \delta\,|1,1\rangle_{A,B} = \\ &= \alpha\begin{pmatrix}1\\0\\0\\0\end{pmatrix} + \beta\begin{pmatrix}0\\1\\0\\0\end{pmatrix} + \gamma\begin{pmatrix}0\\0\\1\\0\end{pmatrix} + \delta\begin{pmatrix}0\\0\\0\\1\end{pmatrix}\end{aligned} \tag{1.1.4}$$

where $|\alpha|^2 + |\beta|^2 + |\gamma|^2 + |\delta|^2 = 1$ is the normalization requirement. If $\mathcal{H}_A$ and $\mathcal{H}_B$ are the Hilbert spaces of qubits 1 and 2, the global state will live in a higher-dimensional Hilbert state

$$|\psi\rangle \in \mathcal{H}_A \otimes \mathcal{H}_B \tag{1.1.5}$$

and indexes A and B in equation (1.1.4) indicate in which Hilbert state the qubit lives. In this case it is not straightforward to give a clear visual representation analogous to the Bloch sphere.

Take the following state:

$$\begin{aligned}|\psi\rangle &= \frac{1}{\sqrt{2}}(|0\rangle_A + |1\rangle_A)\frac{1}{\sqrt{2}}(|0\rangle_B + |1\rangle_B) = \\ &= \frac{1}{2}(|0,0\rangle_{A,B} + |0,1\rangle_{A,B} + |1,0\rangle_{A,B} + |1,1\rangle_{A,B})\end{aligned} \tag{1.1.6}$$

This state is called *factorized* or *separable* because it is given by the tensor product of independent states, which live in different Hilbert spaces. Measuring the state of the first qubit does not reveal information on the other qubit.

Take, instead, the following state:

$$|\psi\rangle = \frac{1}{\sqrt{2}}(|0,0\rangle_{A,B} + |1,1\rangle_{A,B}) \tag{1.1.7}$$

This state cannot be obtained as a tensor product of states living in independent Hilbert spaces. Upon measurement, if the first qubit is found having eigenvalue 0 (1), the global wavefunction of the qubit will reduce to $|0,0\rangle_{A,B}$ ($|1,1\rangle_{A,B}$), meaning that a subsequent measurement of the second qubit on the same basis will produce the same outcome 0 (1). This state is called *entangled*, since measurements on different particles are correlated, implying that the global state cannot be described in terms of the states of individual particles alone.

1.1.2 Purity of the quantum state

By using the formalism of the density operator, which will not be illustrated in a detail manner here, it is possible to distinguish between *pure* states and *mixed* states (or *mixtures*).

A state is called pure when we have perfect knowledge of it. In terms of the density operator, it can be represented with

$$\hat{\rho} = |\psi\rangle\langle\psi| \qquad \text{(pure state)} \tag{1.1.8}$$

where $|\psi\rangle$ is any normalized quantum state.

A mixture, instead, is a state of which we have imperfect knowledge, in the sense that we may know only that a state is found with probability p_n on one of a series of states $|\psi_n\rangle$. We describe this state with the following expression

$$\hat{\rho} = \sum_n p_n \, |\psi_n\rangle\langle\psi_n| \quad \text{(mixed state)} \tag{1.1.9}$$

and a mixed state cannot be put in the form (1.1.8). In general, there exist intermediate states between the ideal pure state and the mixture, as measured by the *purity.* The purity P of a state is determined by the trace of the squared density operator

$$P = \mathrm{Tr}\{\hat{\rho}^2\} = \sum_n \langle\psi_n| \, \hat{\rho}^2 \, |\psi_n\rangle \tag{1.1.10}$$

where the $|\psi_n\rangle$ states are any orthonormal basis of the complete Hilbert space, and where P varies between 1 and $1/d$ for a perfectly pure state and for a perfect mixture, respectively, where d is the dimension of the Hilbert space.

The marginal state of qubit A, which represents the knowledge that we have on it when we ignore all information on qubit B, is defined in terms of partial traces of the global density operator:

$$\hat{\rho}_A = \mathrm{Tr}_B\{\hat{\rho}\} = \sum_n {}_B\langle\psi_n|\hat{\rho}\,|\psi_n\rangle_B \tag{1.1.11}$$

Even if the global state is pure, the marginal state may be a mixture, as seen in the examples below.

Examples

The density matrix associated to the entangled state of eq. (1.1.7) is

$$\hat{\rho} = \frac{1}{2}(|0,0\rangle\langle 0,0| + |0,0\rangle\langle 1,1| + |1,1\rangle\langle 0,0| + |0,0\rangle\langle 0,0|) \tag{1.1.12}$$

where we dropped the indexes for simplicity of notation. This is not a mixed state because of the presence of the non-diagonal elements $|0,0\rangle\langle 1,1|$ and $|1,1\rangle\langle 0,0|$, and in fact the purity P of this state is 1. If we take the partial trace of this expression, we get the marginal density operator associated to the first particle:

$$\hat{\rho}_A = \mathrm{Tr}_B(\hat{\rho}) = \sum_{n=0,1} {}_B\langle n|\hat{\rho}\,|n\rangle_B = \frac{1}{2}(|0\rangle\langle 0| + |1\rangle\langle 1|) \tag{1.1.13}$$

which is a *mixture*, so that we either find the qubit in the eigenstate 0 or 1 with 50% probability. This state is qualitatively different from the superposition of a qubit (1.1.1), because the two parts of the partial density operator cannot interfere with each other, at variance with two parts of the pure state (1.1.1). In practice, as information was shared between the two qubits, ignoring qubit B results in imperfect knowledge on the qubit A.

The partial trace of the density operator associated to the separable state (1.1.6) corresponds, instead, to a pure state:

$$\hat{\rho}_A = \frac{1}{2}(|0\rangle\langle 0| + |0\rangle\langle 1| + |1\rangle\langle 0| + |1\rangle\langle 1|) = \frac{1}{2}(|0\rangle + |1\rangle)(\langle 0| + \langle 1|) \tag{1.1.14}$$

underlining the fact that the two qubits are independent and that information is not shared between the two qubits.

These concepts are particularly important for the realization of heralded sources of single photons; as it will be illustrated in detail in Section 2.5, the complete separability of the generated photon pair state is fundamental.

1.1.3 Quantum logic gates

As classical computations on bits are performed by logic gates, the *quantum logic gates* are their counterparts that act on qubits [8]. We define as *single-qubit quantum gate* any unitary operation that performs a rotation of the qubit on the Bloch sphere. Two examples of single-qubit gates are the Hadamard gate H, that rotates a basis state to the equator of the Bloch sphere, and the phase gate P, that applies a phase to the second component of the qubit (and that corresponds to a rotation around the poles' axis):

$$H = \frac{1}{\sqrt{2}} \begin{pmatrix} 1 & 1 \\ 1 & -1 \end{pmatrix}, \qquad P = \begin{pmatrix} 1 & 0 \\ 0 & e^{i\phi} \end{pmatrix} \tag{1.1.15}$$

We can also define quantum gates that operate on multiple qubits (and we will have *two-qubit gates*, *three-qubit gates*, and so on). These gates are necessary to make qubits interact with one another. For instance, the most known two-qubit gate is the Controlled-NOT (CNOT) gate, the quantum counterpart of the XOR gate: it operates by performing a state-flip on the second qubit, called *target* (t), conditioned on the state of the first qubit, called *control* (c), and by using the formalism of eq. (1.1.4) it can be described by the following matrix

$$\mathrm{CNOT} = \begin{pmatrix} 1 & 0 & 0 & 0 \\ 0 & 1 & 0 & 0 \\ 0 & 0 & 0 & 1 \\ 0 & 0 & 1 & 0 \end{pmatrix} \tag{1.1.16}$$

The CNOT gate is particularly significant as it is an *entangling gate*, because it can produce entanglement between qubits starting from single-qubit superpositions: if the control qubit is in a superposition state, the resulting state will be entangled.

$$\mathrm{CNOT} \frac{1}{\sqrt{2}} \left(|0\rangle_c + |1\rangle_c \right) |0\rangle_t = \frac{1}{\sqrt{2}} \left(|0,0\rangle_{c,t} + |1,1\rangle_{c,t} \right) \tag{1.1.17}$$

A set of *universal quantum gates* is the one that can bring any n-qubit state to any other n-qubit state [9], and it always involves at least a two-qubit gate.

1.1.4 Quantum algorithms

A quantum algorithm is a procedures that applies a sequence of quantum gates to a prepared input state, and that terminates with the readout of the qubits. The quantum algorithms are aimed at solving computational problems, analogously to classical algorithms, but they exploit quantum superposition and entanglement between qubits to perform the computation. The importance of quantum algorithms resides in the fact that some problems can be solved by such algorithms with an advantage, sometimes exponential, with respect to any known classical algorithm. In the early 1990s the first quantum algorithms that possess such advantage were found, which immediately sparked great interest in the quantum computation field. The most famous algorithms are the Deutsch-Jozsa's [10], the Shor's [11] and the Grover's algorithms [12].

The Deutsch-Jozsa's algorithm, discovered in 1992, can determine whether a function is balanced or constant. More precisely, the function produces either output 0 or 1 out of a string of N input bits and we are promised that either all the outputs are equal (constant function) or that they are equally divided into 0s and 1s (balanced function). The function is actually a quantum computer, in the sense that the input and output are strings of qubits and that a superposition in the input state will produce a superposition in the output state. It is a deterministic algorithm, in the sense that it always gives the correct answer at the first execution. Although it is of little use, the Deutsch-Jozsa algorithm has an exponential advantage compared to any other classical algorithm that solves the same problem, because it can exploit quantum superposition to probe all the outcomes at once.

The Deutsch-Jozsa's algorithm inspired the Shor's algorithm, discovered in 1994, which is capable of factorizing numbers with an almost exponential advantage compared to the fastest classical algorithm known [13].

Given a black box function, the Grover's algorithm (1996) can find the one input that produces a given output of the function among all the possible N inputs, quering it only $O(\sqrt{N})$ times on average; any classical algorithm will employ $N/2$ queries on average, since the only viable strategy is to randomly try all the inputs. Hence, the Grover algorithm has a quadratic advantage compared to classical strategies.

1.2 Photonic Qubits

In principle, qubits can be encoded on any two-level quantum system. When the quantization of the electromagnetic fields is performed, it is found that the fields oscillate as quantum harmonic oscillators, whose quantum is called *photon.* While the mathematical description of the quantization of light can be found in Section 2.2, here we illustrate the most common ways in which a qubit can be encoded into photons.

1.2.1 Polarization encoding

Polarization encoding employs two orthogonal polarization states of a photon as the computational basis: common choices are linear horizontal/vertical polarization states ($|H\rangle$, $|V\rangle$) or right/left circular states ($|+\rangle$, $|-\rangle$). The qubit may be defined in the former case as

$$|\psi\rangle = \alpha\,|H\rangle + \beta\,|V\rangle \tag{1.2.1}$$

and in the latter case as

$$|\psi\rangle = \alpha\,|+\rangle + \beta\,|-\rangle \tag{1.2.2}$$

One can be obtained from the other, since $|\pm\rangle = (|H\rangle \pm |V\rangle)/\sqrt{2}$.

Polarization encoding has significant advantages compared to other platforms. For instance, manipulation of qubits is very easy since any one-qubit operation can be realized easily using half- and quarter-waveplates, and it can be performed with high precision and little effort; polarization is also rather insensitive to the coherence properties of the underlying field. Moreover, polarizing beam splitters allow an easy conversion between polarization and path encoding.

Polarization encoding is rarely used in other contexts, however. For instance, normal optical fibers tend to randomly rotate polarization states due to slight birefringence asymmetries, either intrinsically present in the fiber core or caused by the interaction with the environment, forcing the adoption of feedback systems [14]. Unless frequency-distinguishable photons are allowed [15], using polarization encoding in integrated circuits is unhandy because the waveguides' TE and TM modes generally have to be degenerate [16]; this requirement complicates the fabrication process of integrated devices because a very precise control of the waveguide's cross-section is necessary.

Bulk sources of polarization entangled states that exploit Type-II Spontaneous Parametric Down-Conversion in nonlinear crystals [17] are often used to perform proof of principle experiments, as in ref. [18] where entanglement between up to 12 photons has been observed.

1.2.2 Path encoding

Path encoding is another common choice for photons and other systems, where the qubit is defined as a quantum superposition of a single photon propagating along one ($|1\rangle$) or another path ($|2\rangle$):

$$|\psi\rangle = \alpha\,|0\rangle + \beta\,|1\rangle \tag{1.2.3}$$

Path encoding is commonly used in bulk experiments, where it is easily converted to polarization encoding, as mentioned, and in integrated circuits, where the qubit travels in pairs or arrays of waveguides [19, 20], in which case the qubit has higher dimensionality.

One-qubit gates are easily realized. For instance, phase shifters can be used to apply a phase on the path of a basis state, for example using electro-optic or thermo-optic modulators in integrated devices, or delay lines in bulk experiments. The Hadamard gate can be implemented with beam splitters (or directional couplers in integrated devices), which can make two basis states interact to produce quantum interference effects. A combination of phase shifters and beam splitters can realize interferometers, with which reconfigurable circuits can be realized [21].

1.2.3 Time-bin encoding

The basis states of time-bin encoding are represented by photons travelling in different time slots that are separated by more than the coherence time of the photons themselves [22]. In particular, the qubit is encoded in the relative amplitudes and phase of the split wavefunction. So, for instance, if $|E\rangle$ and $|L\rangle$ represent the photon respectively travelling in an Early and Late time-bin, the qubit state may be represented with

$$|\psi\rangle = a\,|E\rangle + e^{i\phi}b\,|L\rangle \tag{1.2.4}$$

where $|a|^2 + |b|^2 = 1$. Preparation of this state is realized by splitting a pulse of light with an interferometer whose unbalance equals the time delay between the bins and is larger than the coherence length of the pulses; the split pulses are then sent to a nonlinear crystal to produce pairs of photons by either Parametric Down-Conversion or Four-Wave Mixing. If the pulses are not too strong, a pair of photons will be generated either by the first or by the second pulse (but not both), thus producing the superposition state (1.2.4), provided that the information on which of the two pulses generated the photons is erased.

Time-bin encoding is better suited than polarization encoding for optical fiber applications, since it suffers much more lightly from decoherence effects [23, 24]. The two states of the time-bin qubit can be made to interfere in an interferometer whose unbalance is equal to the time delay between the bins; the interferometer has to keep a high phase stability and it usually requires stabilization techniques to successfully operate. A drawback of time-bin encoding is that fast (and lossy) optical switches are required to realize the a general one-qubit gate: in fact, passive optical elements cannot transform deterministically one time bin into the other or apply a phase shift to only one of the two bins.

1.2.4 Other encodings

There exist a wide range of possible encodings, each exploiting various degrees of freedom of electromagnetic radiation.

Frequency-bin encoding

Frequency-bin encoding uses the frequency of the photon to encode quantum information. It is a common choice when photons are produced by Spontaneous Four-Wave Mixing inside microring resonators [25], since the resonances of the ring represent a natural set of basis states.

The main drawback of frequency-bin encoding is the difficulty to perform operations involving multiple frequencies, making qubits interact with each other, because either high-frequency modulation or nonlinear optical operations have to be performed to do so [26].

Photon-number encoding

Photon-number encoding uses Fock states [2] as the computational basis. It is common to use only the vacuum state ($|0\rangle$) and the single excitation state ($|1\rangle$), so that the qubit may be encoded as $|\psi\rangle = \alpha|0\rangle + \beta|1\rangle$. A higher number of Fock states can be included in the computational basis, but photon-number-resolving detectors have to be employed for measurements, in this case.

Multiple encodings

Applications in which multiple encodings are used at the same time are common because they allow access to a Hilbert space with higher dimensionality without increasing the number of quantum resources. For instance, hyperentanglement is obtained when two particles are entangled on more than one degree of freedom [27]. A notable example is ref. [28] where 18 qubits have been encoded onto six photons by exploiting at the same time the frequency, polarization and orbital angular momentum degrees of freedom.

1.3 Photonic quantum technologies

The role of photons in quantum technologies is growing. In this section we make a brief overview of technological areas in which quantum states of light play an important role: quantum computation, quantum communication and quantum metrology. Since much of the work described in this thesis is based on integrated optical structures, we will also give an overview of integrated photonic technologies, and of some important components that can be used to generate and manipulate quantum states of light.

A more detailed overview on the state of the art of integrated sources of light is found in Section 1.4, while the theoretical description of these components is found in Chapter 2.

1.3.1 Quantum computation

As mentioned, a key requirement to perform quantum computation is the availability of a complete set of quantum gates. While photonic one-qubit gates are straightforward to obtain, since they usually involve simple phase shifts, two-qubit gates are much more difficult to achieve. The CNOT gate, for instance, has to coherently perform a flip operation on the target qubit conditioned on the state of the control qubit, which means that the behaviour of an optical CNOT has to be nonlinear at the single photon level. The interaction between light and matter is extremely weak, making the achievement of single-photon nonlinearities extremely challenging. The extremely weak nonlinearity of optical phenomena is the main drawback of the use of photons for quantum computation, with alternative approaches appearing more promising at the moment.

Although single-photon nonlinearities are being pursued [29, 30], other approaches exist to obtain the required nonlinearity. One is the so-called KLM scheme, from the authors Knill, Laflamme and Milburn of ref. [31]. Based on previous works on teleportation [32, 33], the required nonlinearities are introduced by the measurement process, by means of the collapse of the wavefunction. The main disadvantage of the original KLM scheme is the intrinsic probabilistic nature of the ports, that is responsible for an exponential scaling of the resources with the number of qubits required. First bulk demonstrations of optical quantum gates [34–37] were followed by the first example of a quantum integrated gate [38], and by reconfigurable circuits [21, 39, 40].

Important improvements on the scheme tackled the issue of non-deterministic operations. In 2001 Raussendorf and Briegel [41] proposed a novel scheme for quantum computation, called *one-way quantum computation*. The scheme relies on *cluster states* [42], highly entangled states of a large number of particles. Such states are difficult to prepare, but once they are available, quantum operations can be performed deterministically with simple one-qubit operations, measurements, and classical feed-forward. While the Raussendorf-Briegel scheme is in general valid for any kind of quantum system, such as interacting spin particles, Nielsen [43] extended it to photonic quantum computation, where the single-qubit operations are performed with linear optical components. Similar extensions have been performed for superconducting qubits [44] and quantum dots [45]. Although original proposals of computation with cluster states was limited to discrete variables, the scheme was extended to continuous variables, as well, in 2006 [46].

A review on optical quantum computers can be found in ref. [47].

Other platforms are being investigated for the realization of the quantum computer [48].

Qubits can be encoded in atomic energy levels. For atoms in vacuum, these levels have very long coherence times, in the order of seconds, and, since atoms are equal to each other, distinct qubits will naturally be equal to each other, as well. Atomic ions can be fixed in place through the use of electric fields, in conjunction with laser cooling [49–51], while neutral atoms are fixed in place through the use of optical lattices. Single-qubit and entangling gates are performed by contact interactions between atoms, or by supplying electric and magnetic fields at the ions [52, 53] or atoms [54–56]. The main challenges for this approach are the difficult scalability of the system regarding the measurement, initialization and interaction between large numbers of atoms.

Some of the issues affecting vacuum trapped atoms can be addressed by “trapping” the atoms in solid hosts, where the qubit can be encoded in electronic levels or electronic/nuclear spins [57]. This is the case for qubits based on quantum dots, either self-assembled [58–60] or electrostatically defined [61, 62], and color centers and point-defects such as donor atoms [63, 64] and vacancy-based defects in Silicon [65–67] and Diamond [68, 69]. Such systems can be considered artificial atoms because electrons are three-dimensionally confined, giving rise to discrete energy levels, analogously to the electronic states of atoms [70]. Generally, the shallow confining potential requires the system to be cooled at liquid-helium cryogenic temperatures, or lower, in order to avoid the thermal escape of the electrons. Another disadvantage is the low coherence time due to nuclear spin interactions [71].

Another important platform for quantum computation is based on superconducting circuits [72]. Although cryogenic temperatures are necessary, they are realized out of standard electronic components, and they benefit from decades-long experience in microelectronics manufacture. Manipulation and readout of superconducting qubits can be performed with microwave fields [73, 74], that can be routed to different qubits with transmission lines, and the interaction between different qubits can be controlled electronically [75]. The main limitation of superconducting qubits is their short coherence times, in the order of few hundred microseconds [76]. One and two-qubit gates have been demonstrated [77] and chips with up to 53 physical qubits have been recently realized [78].

1.3.2 Quantum communication

Photons are naturally well suited to achieve the task of transferring a quantum state between distant physical systems: as already mentioned, photons are very well isolated from decoherence effects, and of course they travel at the speed of light.

In a scenario known as the Quantum Internet [79], the transfer of qubits encoded in photons [4, 79, 80] could be used to coherently connect different quantum computers in order to merge their computational capability, exploiting, for instance, already deployed fiber-based telecommunication networks. The coupling between a qubit (an atom) and a travelling photon can be enhanced in an optical cavity to completely transfer the qubit to the photon and vice versa [81, 82].

Even if the losses in modern telecommunication fibers are very low, in the order of 0.1 dB/km at 1550 nm, quantum communication protocols have to face great loss of information when the transfer is attempted in link exceeding few tens of kilometers. This corresponds to an exponential loss of the fidelity of the transfer as the length of the link is increased. While losses can be overcome with amplification and regeneration in classical networks, quantum states cannot be copied, as the No-Cloning Theorem demonstrates [83, 84]. Thus, strategies to improve the transmission rely on different approaches, such as quantum distillation [85–87] and quantum repeaters [88–91], which achieved a polynomial scaling of the fidelity. In all of these schemes, entangled pairs of photons play a crucial role.

In the past few years, remarkable demonstrations of long-range quantum communication have been performed with the use of a satellite in low Earth orbit [92–95], establishing records in the distance achieved by quantum communication protocols of up to 7600 km.

Quantum computers, and Shor's factoring algorithm in particular [11], threaten to break current cryptographic protocols such as the most commonly used RSA scheme [13]. These protocols allow to publicly share cryptographic keys relying on mathematical problems that are difficult to solve for current classical computers, such as the factorization of big prime numbers. In principle, however, enough time and computational power, or the use of quantum computers, can break such encryption.

In 1984 Bennet and Bassard proposed a cryptographic protocol (BB84 [96]) for public key distribution based on quantum states of light (single photons) and the no-cloning theorem [83, 84]. The security of the key exchange is granted not by hard mathematical operations, but by the physical laws described by Quantum Mechanics itself. As such, this kind of key exchange is also called Quantum Key Distribution (QKD) and, provided that the practical implementation of the protocol fulfills appropriate assumptions, it is impossible to break [97], even with infinite computational power.

While the BB84 protocol relies on single photons, in 1991, another QKD protocol (E91 [98]), was proposed that relied on the exchange of entangled pairs of photons between Alice and Bob and on the violation of the Bell inequality [99]. Shortly after that, the first experimental proof of principle realization of QKD implemented BB84 [100].

QKD protocols do not necessarily have to use single photons or entangled photon states, but Weak Coherent Pulses (WCP) [101] can be used, as well. WCP can be produced by strongly attenuating laser pulses until the average number of photons is roughly 0.1; in this case photon-splitting attacks are possible, but countermeasures involve the use of so-called decoy states [102, 103], that ensure the security of the protocol. The advantage of this approach resides in the easier implementation and higher rates that a source of laser pulses allows compared to a source of single photons.

While original QKD proposals based on polarization encoding are appropriate for free-space links, their implementation on optical fiber networks is more involved [104]; typical implementations [97] exploit phase encoding, time-bin/time-energy entangled photons and frequency bins.

Regarding technological applications, quantum cryptography is arguably the most successful field based on quantum states of light. Different commercial QKD systems are already available on the market, and many field studies have been performed [103, 105–109], including impressive satellite applications [93, 95].

1.3.3 Quantum metrology

The third field where quantum states of light play an important role is the one of Quantum Metrology [3], which studies how the precision and resolution of measurements can be improved with the use of the quantum properties of the probe and measured object.

The statistical error of classical measurements can be reduced by repeating the experiment N times and by averaging the outcomes; by the Central Limit Theorem, the precision of the measurement scales as $1/\sqrt{N}$. This is known as the Standard Quantum Limit, which represents the maximum precision that an experiment can achive using only classical resources. If the quantum nature of the probe and of the measured system is exploited, the Standard Quantum Limit can be beaten with a quadratic advantage, potentially achieving the Heisenberg limit, with precision scaling as $1/N$.

Many experiments exploit light to perform measurements. In such cases the use of entangled photons or otherwise quantum states of light can beat classical boundaries. For instance, the use of NOON states [110] (states in the form $|\psi\rangle = (|N,0\rangle + |0,N\rangle)/\sqrt{2}$) in interferometers allows to achieve higher phase sensitivities: while a coherent state going through a phase shifter acquires a ϕ phase shift irrespective of the average number of photons it possesses, an N-photon Fock state acquires an $N\phi$ shift, thus NOON states in an interferometer produce interference fringes N times more frequent. However, these states are degraded very rapidly by losses and are increasingly difficult to produce as N is scaled up. Other states that provide increased phases sensitivity are squeezed states of light [111], which are being used, for example, to improve the sensitivity of gravitational-wave interferometers [112].

Quantum imaging [113] and quantum lithography [114] are other applications where quantum optical states are used to beat the standard Rayleigh diffraction limit.

1.3.4 Integrated photonic platforms

The field of quantum optics benefits greatly from the possibility of realizing devices in an integrated platform. The high confinement between the guiding and cladding materials allows to realize optical waveguides whose cross-section is in the order of few hundred nanometers squared. The consequent reduction of the footprint of each device allows the realization of hundreds or thousands of devices on the same wafer, reducing the cost of integrated photonic devices and making the approach more scalable in terms of production volumes than bulk optics. These are all appealing features for large scale industrial production, and they benefit both classical and quantum applications.

Common platforms for quantum photonics [115] currently under development are Silicon, transparent glasses like Silicon Nitride [116] and Hydex [117], Diamond [118, 119], Silicon Carbide [120], Lithium Niobate [121, 122], and III-V semiconductors like AlAs, GaAs, InP and InGaAs.

Among these platforms, Silicon photonics is the one that benefits most from the decades-long experience in the fabrication of Silicon electronic devices. In particular, a thin film of Silicon, usually 220 or 300 nm thick, is grown on top of a 2 μm layer of Silicon Oxide in what is known as a Silicon on Insulator (SOI) wafer. These wafers, normally used to realize Complementary Metal-Oxide Semiconductor (CMOS) electronics, are readily available for the realization of optical devices, exhibiting extremely low impurity levels, large dimensions and very high overall quality. Both optical and electronic lithography together with chemical etching processes can be used to remove part of the Silicon layer to realize waveguides, usually in a CMOS compatible manner. Electronic components can then be realized in the remaining part of the layer or directly on top of the waveguides, allowing the realization of hybrid structures [123]

In recent years, various commercial fabrication facilities around the world began to offer to researchers the possibility of realizing devices using Photonic Integrated Chip (PIC) fabrication technology [124]. In an approach called Multi Project Wafer (MPW), many users share the high costs of the fabrication runs, which are high due to the cost of the masks used in optical lithography and that are rarely affordable by small research groups [125]. Examples of facilities offering these services are CEA-LETI, IHP and IMEC, all under the Europractice consortium, the A*STAR Institute of Microelectronics based in Singapore and AIM Photonics in the United States.

Nonetheless, as it will be detailed in the next section, while Silicon has other important advantages, such as high optical third-order nonlinearities, in other respects it is not an ideal platform: being centrosymmetric, second-order nonlinearities are suppressed and high power operations are limited by nonlinear losses due to its limited bandgap.

For these reasons, other platforms are rapidly gaining ground, most notably Silicon Nitride and Hydex [117]; their larger bandgap implies lower linear and nonlinear losses [126], allowing higher power applications, which also compensate for their lower optical nonlinearities.

Besides, the benefit of former experience in fabrication technology is not limited to Silicon. In fact, due to its high thermal conductivity, Silicon Carbide is used as a platform for high power electronics [127], as well.

1.3.5 Common integrated optical components

The **waveguide** is the fundamental component of a photonic platform [16]; it is composed of a straight region of high-index dielectric region surrounded by low-index cladding material [16]. The waveguide exploits Total Internal Reflection (TIR) to laterally confine light; the degree of confinement depends on the contrast between the core and cladding refractive indexes. Generally, in the case of scalable quantum photonic applications, the highest possible contrast is desirable because it maximizes the lateral confinement, thus reducing the total footprint of devices; moreover, at given optical powers travelling

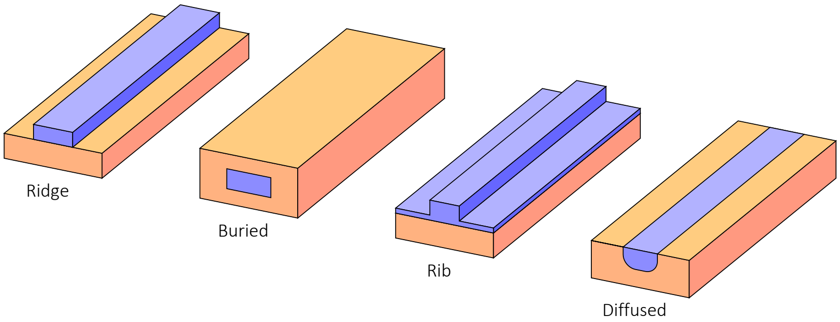

Figure 1.2: Scheme of common types of waveguides.

in a waveguide, higher confinements correspond to higher optical intensities, thus increasing the efficiency of optical nonlinear properties, which are at the core of sources of photons based on Parametric Down-Conversion and Four-Wave Mixing.

Depending on its lateral dimensions, the waveguide may support one or more optical modes; the waveguide is called *single-moded* in the former case or *multi-moded* in the latter. The modes may be also classified according to polarization: when the electric field is mostly polarized in the vertical direction the mode is called *quasi-TM* (or simply *TM*), while it is called *quasi-TE* (or simply *TE*) when it is mostly polarized in the horizontal direction.

Various kinds of waveguides exist, and the most common are shown in Figure 1.2. Buried and ridge waveguides have typically a rectangular or trapezoidal cross-section; while the former is completely surrounded by the cladding, the latter may be left exposed to air or to a lower-index cladding. Rib waveguides are the result of a partial etch, and they all share a thin film of high-index material. Diffused waveguides are fabricated by diffusing a dopant in the cladding and they typically have very low losses but low contrast as well. As noticed above, the most interesting for quantum applications are those which maximize the lateral confinement, such as the ridge, rib and buried waveguide.

The thickness of a typical Silicon waveguide is usually either 220 or 300 nm, since these are the thicknesses of commonly available SOI wafers. Depending on the desired number of supported modes, the lateral dimensions of the waveguide may then vary: a waveguide supporting a single-TE and a single-TM mode has roughly 450/500 nm width; a single TE-mode waveguide is usually too narrow to be realized with low enough losses. The cross-sections of Silicon Nitride, Silicon Carbide, Hydex and other lower contrast waveguides are generally slightly larger [128], with a consequent scaling of the overall footprint of integrated devices.

The dispersion of the waveguide modes, i.e. the change of the effective index of refraction of the waveguide modes as a function of the radiation wavelength, is an important property to keep into account when applications with large frequency spans are considered. For instance, the dispersion has important consequences on the phase matching of nonlinear optical properties [129]. The waveguide dispersion is determined by the natural material dispersion of the core and cladding materials and by the waveguide cross-section. The latter can be used to engineer the waveguide dispersion for various applications. For instance, optical combs spanning a wide range of frequencies can be realized by engineering a small anomalous dispersion of the waveguide [130].

Many common integrated devices are based on waveguides. **Directional couplers**, integrated versions of beam splitters, are realized when two waveguides are brought close to each other, so that light can jump between them through evanescent coupling.

Phase modulation of the electromagnetic field is realized with the use of **modulators**. Increasing locally the temperature of the sample, an increase in the refractive index can be induced through the thermo-optic effect, thus increasing the optical length of the heated section: this may be realized by passing electrical currents in metal stripes patterned on the top surface of the sample. Moreover, when $\chi^{(2)}$ nonlinearities are available, the index change may be induced with electro-optic modulators [131].

Directional couplers and modulators can then be paired to realize integrated Mach-Zehnder **interferometers**, which can be used to modulate light intensities and to implement optical switches.

Optical nonlinear processes are strongly dependent on the intensity of electromagnetic radiation travelling inside waveguides. One way the intensity of the fields can be enhanced is by using resonant structures.

One of the most important devices in integrated nonlinear optics is the **microresonator**. It is an optical waveguide closed on itself following a circular path. Usually it has a circular shape or it is composed of two semicircular sections connected by straight waveguides; it is referred to as the *microring resonator* in the former case and as the *racetrack resonator* in the latter, because of the obvious similarity with its larger counterpart. Unless differently specified, what applies to the microring resonator applies also to the racetrack, so we may use sometimes the term microring as a synonym of microresonator. Silicon microring resonators used for quantum applications at telecom wavelengths have radii which vary roughly between 5 and 100 μm and Q-factors in the order of 10^5 to 10^6.

Light is coupled into and out of the resonator by evanescent coupling with the use of one or more additional waveguides running next to the ring's waveguide. Neglecting dispersion, the microring resonator exhibits a series of resonances equally spaced in frequency, as easily derived in Section 2.8.

The importance of the microresonator resides in the enormous field enhancement reached inside these objects by resonant fields, i.e. the ratio of the field amplitudes found inside the ring resonator and in the input waveguide. Such enhancement strengthens the interaction between radiation and matter, increasing the efficiency of nonlinear optical processes by many orders of magnitude compared to normal optical waveguides [132]. Four-Wave Mixing, in particular, especially benefits from microring resonators, since phase matching is automatically achieved when using three equally spaced resonances as signal, pump and idler frequencies, as seen in more detail in Paragraph 2.8.2.

The two most common configurations of microring resonators are the *All-Pass* and *Add-Drop*, for which the resonator is coupled to a single waveguide in the former case, and to two waveguides in the latter. The All-Pass resonator removes the resonant frequencies from the coupled waveguide. The Add-Drop exchanges resonant frequencies between the two coupled waveguides and it is particularly interesting for multiplexing applications.

The theoretical description of the microresonator will be given in Section 2.8, while Paragraph 2.8.2 describes in more detail Four-Wave Mixing in microring resonators.

Coupling of light into and out of a sample may be performed with the use of **Bragg grating couplers** [133]: the mode supported by an integrated waveguide is first adiabatically expanded in the horizontal direction with the use of tapers, until its width reaches the one of the mode supported by an optical fiber. Then, light enters a modulated dielectric region, which coherently scatters the radiation out of the sample plane at a determined angle to the normal. At this point light may be coupled to an optical fiber for delivery purposes. Typical coupling efficiencies of uniform grating couplers reach about -1 dB, while apodized designs [134, 135] may reach values closer to unity, at the cost of a reduced coupling bandwidth, and subwavelength structures [135] may also be used to simplify the fabrication process to a single etch step [136].

Another common approach to couple light is the use of **edge-coupling**: light is brought to one edge of the sample with waveguides, where is then coupled to fibers placed just outside the lateral surface of the sample. Inverse tapering of the waveguide [137] and of the fiber tips are used to increase the mode matching and improve the coupling efficiency. Subwavelength structures can be used to further expand the waveguide mode and improve the mode matching with optical fibers [138, 139], reaching efficiencies as high as 90% on a 100 nm bandwidth [140].

Photonic crystals, i.e. periodic dielectric structures, exhibit peculiar optical properties [141, 142]. One of the most common photonic crystal used in integrated optics is the photonic crystal slab [143], which is realized by periodically patterning a thin dielectric film. These objects confine light by total internal reflection in the vertical direction (*index-guiding*), while, at the same time, the destructive interference arising from the scattering by the periodic pattern of the slab forbids the in-plane propagation of radiation for certain frequency intervals, called *photonic bandgaps*. Photonic bandgaps may be present for only TE or TM polarizations, or for both polarizations, in which case they are called complete photonic bandgaps [144]. Photonic crystal slabs have been fabricated in a wide range of platforms [145], including some of the ones discussed above.

Photonic crystal cavities [146] are obtained when a point defect is introduced in the photonic crystal, for instance by removing one or a small number of holes from the lattice. When the energy of the mode associated to the defect lays within the bandgap, it becomes localized because light can propagate in no direction. These bound states exhibit mode volumes smaller than a cubic wavelength and Q-factors exceeding eleven million [147]. Nonlinear optical processes are therefore strongly enhanced, as well as the spontaneous emission rate of emitters embedded in the crystal in correspondence to the maximum of the modal field intensity, as quantified by the Purcell factor

[148].

When a whole line of holes is removed from the lattice, a photonic crystal waveguide is obtained [149]. These waveguides can be engineered to strongly reduce the group velocity of light; the resulting, so-called *slow-light* regime [150, 151], can be used to enhance the interaction between light and matter [152] and can be used to reduce the dimensions of optical components such as optical modulators, or to increase spontaneous emission rates of emitters embedded in the waveguides [153].

Applications of photonic crystal slabs include modulators [154], small filters [155], sensors [156], low-threshold lasers [157] and bistable systems [158].

1.4 Integrated sources of quantum light

Important milestones in experimental quantum optics were and are achieved using bulk sources and setups. Sources of photons for such experiments are typically realized exploiting Spontaneous Parametric Down-conversion (SPDC) in nonlinear crystals. Commonly used materials include Beta Barium Borate (BBO) [159], Potassium Titanyl Phosphate (KTP) [160] and Potassium Dihydrogen Phosphate (KDP) [161] crystals. For instance, a KDP crystal was the source of photons in the first demonstration of bunching effects between identical photons performed by Hong, Ou and Mandel [162].

Regarding pairs of entangled photons, initial experiments relied on electronic cascades in various atomic species. Grangier, Roger and Aspect used sources of entangled photons produced by Calcium radiative cascades to perform the first violations of the Bell inequality [99, 163, 164] and the experimental verification of the antibunching effect of single-photon Fock states [165].

In 1995, Kwiat et al. discovered that type-II SPDC in a nonlinear crystal can be used to realize bright sources of polarization-entangled photon pairs [17]. This kind of sources immediately replaced previous, less efficient ones, and became the workhorse for many quantum optics experiments. For instance, entangled photon pairs prepared in a polarization Bell state have been used to perform the first experimental proof of quantum teleportation [6, 32]. More recently, cascaded BBO crystals have been simultaneously pumped to realize experiments in which entanglement between up to 12 photons has been observed [18, 166].

Bulk optical experiments suffer from various drawbacks. First, experiments with growing number of photons require larger and larger experimental setups, that become increasingly more difficult to realize and keep aligned, occupying large footprints in a laboratory [167]. Secondly, nonlinear optical processes occurring in bulk materials are very weak due to the small intrinsic nonlinearities of transparent optical materials and to the lack of enhancement mechanisms as for integrated devices. Lastly, industrial fabrication in large volumes will benefit from an integrated approach, where hundreds or thousands of devices may be realized on a single wafer.

These reasons motivated the search for integrated optical platforms that could be used for quantum optical experiments. The higher confinement that light experiences in integrated waveguides and resonators largely increases the interaction between light and matter, improving the efficiency of optical nonlinear phenomena. This makes integrated sources of light orders of magnitude more efficient than their bulk counterparts, or it enables the use of nonlinearities of materials that would be otherwise very difficult to exploit in a bulk experimental configuration.

Four-Wave Mixing (FWM), both stimulated and spontaneous, is the nonlinear phenomena of choice when integrated platforms are considered. Optical waveguides are typically more dispersive than bulk materials and nonlinear optical fields are necessarily co-propagating if confinement is to be preserved. This makes phase matching generally harder to obtain in integrated platforms, because orientational and geometrical degrees of freedom are more difficult to exploit effectively compared to bulk configurations. Compared to SPDC, FWM involves fields close in frequency, therefore phase matching is less complicated, since the effect of dispersion is less important in small frequency spans.

First experiments moving towards an integrated approach were performed in low-confinement devices such as fibers. Photon pairs were produced in a Sagnac loop both with single-frequency [168] and double-frequency pump configurations [169]. In ref. [170] a heralded source of photons was realized by pumping a photonic crystal waveguide at 1064 nm and producing pairs around 800 and 1570 nm, achieving heralding rates of 10^5 Hz. Later on, experiments were performed in integrated waveguides and resonant devices.

1.4.1 Silicon

Silicon is an indirect semiconductor with a bandgap of 1.1 eV, thus it is transparent in the near infrared wavelengths, making it well suited for quantum experiments that use photons that can be sent to large distances through optical fibers. Indeed, the majority of the sources based on FWM in Silicon operate around 1550 nm.

The SOI platform benefits from decades-long experience in Silicon fabrication technologies, making it a good choice for systems where the integration between photonic and electronic structures is foreseen [123]. Linear losses inside integrated waveguides in Silicon can be as low as few dB per centimeter.

Silicon is centrosymmetric, therefore the $\chi^{(2)}$ nonlinear coefficient is suppressed; however, the $\chi^{(3)}$ nonlinearity is much higher than in alternative platforms, such as Silicon Nitride [171], resulting in a typical nonlinear waveguide parameter γ of 200 $\mathrm{W}^{-1}\mathrm{m}^{-1}$.

The most notable drawback of Silicon is the presence of fairly high nonlinear optical losses: while a single 1550 nm photon is too weak to excite an electron-hole pair in Silicon, two photons have enough energy to do so. This process is called Two-Photon Absorption (TPA) [171] and it produces direct optical losses in high intensity fields. Moreover, the free charges created by TPA induce additional losses by Free-Carrier Absorption (FCA) on all the fields travelling in the same spatial region of the charges, regardless of their intensity or frequency.

The main kinds of sources of photons based on Silicon can be divided into the following categories: sources based on nanowire waveguides, sources based on resonators (in particular microtoroids and microring resonators), and hybrid approaches such as Coupled-Resonator Optical Waveguides (CROW) [172].

Silicon wire waveguides are effective sources of correlated photons that exploit FWM in millimeter-long devices [173, 174]. The cross-section of Silicon waveguides is usually chosen to allow guided propagation of a single TE mode (and one TM mode) and to exploit the same wafers produced for SOI electronics.

The main advantage of Silicon wire sources, compared to other structures illustrated below, is the ease of realization, since the device is not sensitive to fabrication imperfections. Phase matching for FWM in waveguides happens on a broad range of wavelengths: on the one hand, this allows waveguides to posses a higher flexibility in the design of experiments, since there is no restriction on the frequency of emission of photons, as it happens instead in resonant structures like microtorids and microrings; on the other hand, selective frequency filtering has to be put in place to obtain indistinguishable photons, which results in highly reduced pair production rates. The production of both time-bin [175, 176] and polarization entanglement [177–179] have been experimentally demonstrated with nanowire waveguides.

The main disadvantage of waveguide sources is arguably the small effective nonlinearity achievable in these systems: generally, strong pulsed laser sources have to be used to pump FWM (although continuous wave pumping has been demonstrated [180]), and waveguides have to be millimeters-long [175]. Pairs generation rates are limited to around 10^5 Hz [181]. Although spiral configurations can be used to reduce the footprint of waveguides sources, microring resonators or photonic crystal waveguides represent a better solution in this regard.

Silicon spirals have been used as sources in experiments where the indistinguishabilitly of the generated photon was demonstrated on chip [182].

Increasing the efficiency of FWM, by enhancing the interaction between the fields and the nonlinearity of Silicon, can overcome the limitations of waveguides. This can be achieved by spatially and temporally confining the electromagnetic field in resonant modes, within which each photon dwells for a very large number of optical cycles. The enhancement of nonlinearities in resonant structures is determined by the quality factor of the resonances involved in the nonlinear process and by the optical volume of the mode [132], and is more formally quantified by the Purcell factor [148].

Microring resonators are realized by closing on itself an optical waveguide, while light is coupled into and out of the resonator by evanescent coupling with one or more bus waveguides placed close to the microring. Due to their small bending radius, the footprint of microrings is therefore orders of magnitude smaller than the one of simple nanowire waveguides. Generally, linear losses of about 1 dB/cm limit the Q factor of Silicon microring resonators to about 10^5. Compared to other resonant structures like photonic crystal waveguides, one of the great advantages of microring resonators is that they naturally exhibit a series of approximately equally spaced resonances, so that phase matching for FWM is automatically satisfied, at least for adjacent resonances. The mutual spacing of the resonances (the free spectral range) is influenced by the material and geometric dispersion of the waveguides; however, this is usually not an issue until extremely high Q factors or very distant frequencies are considered. A deeper theoretical description of the microring resonator, that includes the definition of various important figures of merit of this device, can be found in Chapter 3.

Silicon microring resonators have been shown to produce enormous enhancement of the electromagnetic field [132]. The work of ref. [183] demonstrated how stimulated FWM could be achieved with extremely low pumping powers, in the order of milliwatts. Soon after, the emission of correlated photon paris by spontaneous FWM was demonstrated [180, 184] with generation rates as high as 10^7 Hz and Coincidence to Accidental Ratios in the order of 50. More recently, photon pair generation was achieved with pump powers as low as few microwatts [185].

Silicon microrings are excellent sources of time-energy [186] and time-bin [187] entangled photons, as well. The fact that these states are preserved in fiber transmissions compared to polarization entanglement and the lower power consumption of microrings makes them particularly interesting for quantum key distribution protocols implemented in optical networks [97].

Heralded single-photon sources require perfect uncorrelation between the heralding and the heralded photons. An appealing property of the microring resonator is the possibility to dynamically change the type of correlations of the generated photon pair by adjusting the pump's spectral profile [132]: while a narrow continuous wave pump produces time-energy entangled photons, a broader pulsed pump can produce factorized photon states without the need of external frequency filtering. This feature was experimentally demonstrated in [188], where the photon pair correlations exhibited a lower bound on the Schmidt number of 1.03 ± 0.1.

While Silicon microrings possess many appealing properties, they also possess drawbacks. As mentioned, TPA is the main limitation of Silicon devices [171], preventing high power operations. This problem can be partially solved with the fabrication of p-i-n junctions alongside the microring resonator's waveguide that sweep away the charges as soon as they are produced [189]; this solution allowed to achieve higher pumping power and pair emission rates, up to 10^8 Hz, at the cost of a more complex fabrication process. Another disadvantage is the high sensitivity to environmental thermal fluctuations, due to the high thermo-optic effect of Silicon [190], which forces the adoption of thermal stabilization stages and micro-heaters to locally compensate the thermal shift of the refractive index.

Silicon microtoroids, similarly to microring resonators, exploit whispering gallery modes in thin Silicon disks to enhance the production of photon pairs. Very high Q factors are possible for these structures and Coincidence to Accidental Ratios exceed 1000 [191]. Coupling of light usually involves a tapered fiber suspended in air and brought next to the resonator, a more complicated approach than using bus waveguides like in microring resonators systems.

Generation of quantum states of light in Silicon has been achieved also with the use of CROWs: these systems of coupled resonators, forming effectively a photonic crystal waveguide, can be tuned to achieve a slow-light regime, which increases the effective optical nonlinearities. In ref. [192], a Silicon CROW was used to produce pairs at telecom wavelength by Spontaneous FWM with an effective waveguide nonlinear parameter reaching $\gamma \simeq 4100\ \mathrm{m}^{-1}\mathrm{W}^{-1}$. Using a similar approach, emission of correlated photon pairs was obtained by coupling a series of photonic crystal cavities in Silicon [193].

1.4.2 Silicon Nitride and Hydex

The limitation on high power operation given by nonlinear losses in Silicon motivated the search of other platforms immune from this drawback. In the past decade important achievements have been obtained in this regard from devices realized with Silicon Nitride (SiN) and Hydex [117].

Hydex is a form of highly doped silica glass; the doping increases the index of refraction of the material, hence allowing total internal reflection. The exact composition of Hydex is proprietary and not disclosed, however it allows to reduce the detrimental effects of the O-H bonds, the main source of losses at telecom wavelengths, without the need of thermal annealing, maintaining the fabrication process CMOS compatible.

These two glasses possess much lower linear and, more importantly, negligible nonlinear optical losses at telecom wavelengths compared to Silicon, at the expense of a lower intrinsic nonlinearity and refractive index. These properties are consequence of the high electronic bandgap of the two materials; in particular, TPA is suppressed because two telecom photons are too weak to promote electrons to the conduction band. The Kerr coefficient n_2 for the two materials was measured to be $2.4 \cdot 10^{-19}\text{m}^2/\text{W}$ for SiN [194] and $1.15 \cdot 10^{-19}\text{m}^2/\text{W}$ for Hydex [117], which is slightly higher than the one of Silica, about $2.5 \cdot 10^{-20}\text{m}^2/\text{W}$, and much lower than the one of Silicon, about $4.5 \cdot 10^{-18}\text{m}^2/\text{W}$ [171]. The lower refractive index compared to Silicon (2 for SiN and around 1.7 for Hydex) results in a lower transversal confinement of the fields and in larger waveguide cross-sections; the devices' footprint is increased as a consequence of the larger minimum bending radius of the waveguides. The confinement and nonlinearity effects are quantitatively taken into account by the waveguide nonlinear parameter γ, typically equal to 2 $\text{W}^{-1}\text{m}^{-1}$ for SiN [195] and to 0.2 $\text{W}^{-1}\text{m}^{-1}$ for Hydex [117]; because $\chi^{(3)}$ nonlinear phenomena are proportional to γ^2 [132], the overall efficiency of nonlinear phenomena of interest in SiN and Hydex, mainly FWM, is orders of magnitude lower compared to Silicon.

These disadvantages are offset by the absence of nonlinear absorption, by the possibility to effectively shape the modal dispersion by engineering the waveguide cross-section [196], and by the extremely low linear losses achieved in both platforms; losses as low as 7 dB/m in SiN, for instance, recently allowed the realization of 12 million Q-factor microrings [197, 198]. At the cost of increased pumping powers, that can reach hundreds of milliwatts [199] or more, extremely wide bandwidth nonlinear classical and quantum operation can be achieved, as shown for instance in [129], where second and third harmonic generation were achieved. In particular, by careful design, a small anomalous dispersion is used to compensate shifts in the resonances of the microrings induced by strong pumping through the Kerr effect, in a way that a constant free spectral range can be maintained on extremely large frequency spans. This in turn allows cascaded FWM to coherently take place among a large set of resonances, achieving the emission of broad frequency combs, as it was demonstrated in 2010 for both platforms [199, 200]. Optical frequency combs [117, 130, 201] have important applications in metrology, spectroscopy and in fast laser pulse sources, and the possibility of producing them from a compact integrated platform is considered an important breakthrough in the field.

In the past few years, the realization of combs have experienced significant improvement both in SiN [196, 202–204] and Hydex [205, 206]. A significant recent result was the realization of a battery-powered frequency comb based on an integrated SiN chip [207], that highlights the impressive achievements obtained in this field.

On the wake of the classical results on frequency combs, quantum experiments involving large frequency spans or combs have been performed, as well [208]. The wide-band capability of Hydex has been exploited to generate complex quantum states on tens of resonances, comprising both heralded [209] and entangled photons [25, 26]. Similar results have been obtained in SiN [210–212].

An interesting pumping solution was adopted for some of the works based on Hydex [15, 209, 213–215] and SiN [216]: instead of using an external laser to pump FWM, in what is called a *self-pumping* configuration, the microring resonator is closed inside an external fiber cavity that contains an optical amplifier. The consequence is that lasing operation will occur automatically in correspondence with one of the ring resonances; if it happens that the lasing resonance shifts for some reason, the lasing radiation will follow automatically, without requiring an external feedback loop. These experiments were the inspiration for the works described in Chapter 3, where instead of Silicon Nitride and Hydex, Silicon microring resonators were used in a self-pumped configuration, so we refer the reader there for a more detailed discussion on this topic.

1.4.3 Color centers in Diamond and Silicon Carbide

Instead of exploiting directly the material optical nonlinearities, typical photon sources realized with Diamond and Silicon Carbide (SiC) exploit color centers present inside the material, following a different approach with respect to what has been described so far. Defects in the crystalline structure of these materials can result in the formation of electronic levels whose energy falls well inside the electronic bandgap of the materials. Such “deep” electronic levels are therefore well localized, and they are hardly thermally ionized, at variance with “shallow” electronic levels produced, for instance, by donor/acceptor atoms; in the latter case the levels are typically placed much closer to either the conduction or the valence band, and ionization requires much lower thermal energies. Qubits can be encoded in the energy levels of these deep defects, which might show a fine vibrational or spinorial structure, and manipulation and measurements are typically performed using electromagnetic fields, either optical or at microwave and radio frequencies. Otherwise, the defects can be employed as single-photon sources, relying on radiative transitions between their excited and ground states, with applications ranging from quantum computing and quantum communication to quantum metrology.

Among the many color centers found in Diamond, the two most commonly exploited are the negatively charged Nitrogen Vacancy (NV) and the Silicon Vacancy (SiV) [119]. These defects are formed when a Nitrogen or Silicon atom replaces a Carbon atom adjacent to a vacancy. The fluorescence of the NV center is found around 637 nm and its lifetime in bulk Diamond is roughly 12 ns, making it a bright source of single photons for quantum communication [217]. One of the main drawbacks of the NV center is the low fraction of photons emitted into the zero-phonon line at room temperature, limited to 4%, which forces the adoption of enhancement approaches based on nanophotonic structures [218–220], as discussed below. The NV center is also used for magnetometry and sensing applications [221]. The SiV fluorescence is found between 730 and 750 nm, the variability caused by the different local environments the defects may experience, induced by stress in Diamond. The emission of photons in the zero-phonon line at room temperature occurs with efficiency in the order of 70%, making it more viable than the NV center as a single photon source at room temperature, and its lifetime is roughly 1 ns [119].

For these defects, important demonstrations have been performed in recent years, such as of entanglement between defect spins [222] or between the spin and the emitted photon [223] and of two photon interference [224, 225], both at room and cryogenic temperatures. Some other impressive achievements in experimental quantum communications have been obtained with the use of Diamond color centers [226–228].

Diamond NV and SiV color centers may not be the ideal choice for quantum communication application because of the high losses that the emitted photons experience in optical fibers. Conversely, in recent years, some defects in SiC are emerging as possible alternatives to Diamond defects because of their long coherence times and longer emission wavelengths.

Silicon Carbide is a tetrahedral semiconductor composed of Silicon and Carbon atoms. Because of the many possible stacking combinations, more than 200 SiC polytypes are known, among which the three more commonly used for quantum photonic applications are the 3C-SiC, 4H-SiC and 6H-SiC. The bandgap of SiC, although lower than Diamond, is considerably larger than Silicon's, ranging between 2.3 and 3.2 eV, depending on the polytype considered, while its index of refraction is about 2.6. SiC is noncentrosymmetric, and its second-order nonlinearity is high (for instance $\chi^{(2)} \simeq$ 32.8 pm/V for 4H-SiC [229] for static fields) and it is comparable to the one of Lithium Niobate. As well as Diamond, Silicon Carbide is one of the hardest known materials, and it exhibits high thermal conductivity [230].

One of the appealing properties of SiC is its long time use as platform for high power electronics [231]; inches-wide, high quality wafers are readily available from fabrication facilities, and doping techniques and electrical contacts are available.

In recent years, some of the point defects present in SiC, in particular the Silicon Vacancy (V_{Si}^{-}) [232] and the double vacancy ($(V_{\mathrm{Si}}V_{\mathrm{C}})^0$) [233] in 4H-SiC, are emerging as possible alternatives to point defects in Diamond. These defects experience long coherence times of several milliseconds [234], and often operate at room temperature [235, 236].

Moreover, the fluorescence of SiC defects is typically found in the near infrared (around 1100 nm for the double vacancy $V_{\mathrm{Si}}V_{\mathrm{C}}$ and 880 nm for the Silicon Vacancy V_{Si}^{-}), making them more suited for quantum communication and biological applications than Diamond's defects, because of the lower absorption that these wavelengths experience in optical networks and biological materials. The possibility of integrating SiC defects with electronic circuits was demonstrated in ref. [237].

One of the main limitations for both Diamond and Silicon Carbide is the limited brightness achievable with these sources, in the order of 10^6 photons per second. A few orders of magnitude improvement is necessary before they can start to compete with other QKD systems based on the repetition rates of attenuated coherent pulses. The use of nanofabricated optical structures like photonic crystal cavities can increase the brightness of these structures through Purcell enhancement of the spontaneous emission rate, that ultimately limits the defects' brightness, hence showing a possible path for achieving the goal. The same mechanism can be used to enhance radiative transitions, leading to more efficient single-photon emitters.

The first two-dimensional photonic crystal cavity in SiC was demonstrated in 2011 [238], followed by other works, such as [239]; the Q-factor of these cavities remains lower than 10^4, but it was enough to detect considerable fluorescence enhancements [230]. Microdisk resonators were also demonstrated, with Q-factors up to $5 \cdot 10^4$ [240, 241].

1.4.4 Other platforms

There exist a vast number of other integrated platforms that are being investigated as sources of quantum states of light. An example are $\chi^{(2)}$ materials, Lithium Niobate in particular, because of their much higher nonlinearity compared to other $\chi^{(3)}$ platforms like Silicon and Silicon Nitride. Generation of photon pairs in this case is performed, for instance, exploiting Spontaneous Parametric Down-Conversion in periodically poled waveguides [121, 242].

Another important example is represented by self-assembled InAs/GaAs (or close semiconductors) Quantum Dots (QD) [243]: a lower-gap semiconductor surrounded by a higher-gap one, under appropriate conditions on the alignment of the electronic bands of the two materials, can be considered an effective potential well for electrons and holes; this well thus forms discrete, localized electronic states, similarly to the already discussed color centers in Diamond and Silicon Carbide. The shape of the QD and the composition of the semiconductors can be used to engineer the properties of the QD, for instance by changing the distribution of the localized electronic levels. When an electron-hole pair recombines within a quantum dot, an atom-like radiative transmission can occur, resulting in the emission of a single photon.

Although the energy levels of InAs/GaAs QDs are generally shallow, hence requiring operation at cryogenic temperatures, the performance of single-photon emitters based on these QDs is currently very high: the purity of the single-photon states emitted is above 99%. The main challenge that prevents QD from achieving large scale applications and that remains to be solved is to produce a large number of intistinguishable sources of photons. In fact, QDs grow inhomogeneously, and additional selection or tuning processes are needed to achieve good quantum interference between photons produced by different dots.

Nonetheless good results from QD sources include high photon purities [244], high collection efficiencies [245], also aided by nanostructures [245–247], coupling between quantum dots and photonic crystal cavities [29] and the realization of electrically pumped devices [248].

Many other integrated platforms for emission of quantum states of light exist, and it is not our goal to review them here. To this end, we refer the reader to the many review articles present in the literature, among which we cite, for instance, ref. [243].

Chapter 2

Theoretical background

The aim of this chapter is not to give a complete theoretical picture of quantum optics or nonlinear optics; rather, it is an overview of the theoretical concepts that are used in the remaining part of this thesis. For a more detailed overview of the quantum theory of light we refer the reader to *The Quantum Theory of Light* [2] by R. Loudon, while here we illustrate only the most fundamental steps; for a deeper and more complete treatment on the theory of coherence of both classical and quantum fields and on quantum optics in general, we refer the reader to *Optical Coherence and Quantum Optics* by L. Mandel and E. Wolf [249]. While the above textbooks also cover optical nonlinearities, we refer to [250] and [251] for a specific treatment. We assume that the reader is familiar with the theory of Quantum Mechanics and its formalism, while some reference textbooks on the topic are [252, 253].

Section 2.1 outlines the principle of nonlinear optics, focusing in particular on two nonlinear optical phenomena, Parametric Down-Conversion and Four-Wave Mixing, that are of particular importance for the work described in this thesis.

Section 2.2 gives the basic formalism of Quantum Optics used throughout this work; we outline the Second Quantization of light and we give brief descriptions of common categories of light such as chaotic light, coherent light and the Fock number states. We also make a discussion on the time and frequency dependence of ladder operators, useful for describing fields found in the laboratory.

Section 2.3 deals with first- and second-order correlations between beams of light.

Section 2.4 uses the formalism of Quantum Optics to describe three important devices: the Beam Splitter, the Mach-Zehnder interferometer and the Hanbury Brown and Twiss interferometer, focusing also on the difference between their classical and quantum descriptions.

Section 2.5 deals with two-photon states of light, where an introduction to the biphoton wavefunction formalism is performed and more details on the correlation within a bipartite state are given. The time-energy entanglement between photons is described, followed by a detailed theoretical description of the instrument that can be used to prove this kind of entanglement, the Franson interferometer.

Then, the theory of electromagnetic modes in dielectric waveguides is given in Section 2.6, while the expansion to periodic one-dimensional dielectric structures is given in Section 2.7.

The linear theory of the microring resonator is given in Section 2.8, together with the theory of Four-Wave Mixing in this resonant structures.

Finally, the chapter is concluded with Section 2.9, where we describe the theory of loop lasing cavities, useful in Chapter 3.

From now on, the symbol ω is used to refer to angular frequencies, even if at times only the word “frequency” is used.

2.1 Nonlinear phenomena

Nonlinear optical phenomena are those where the response of a material to an incident optical field produces fields at different frequencies with respect to the one of the incident field. Nonlinear optics is treated in detail in a number of textbooks, of which we cite [250] and [251].

Here we will limit the discussion to the description of Parametric Down-Conversion (a $\chi^{(2)}$ phenomenon), and Four-Wave Mixing (a $\chi^{(3)}$ phenomenon), because they are the ones at the heart of what is described in Chapters 3 and 5.

2.1.1 Principle of nonlinear optics

The basic principle of nonlinear optics can be understood by considering the polarization response of a material to an incident electric field.

In a linear material, electric charges are displaced by an incoming field and they start to oscillate around their equilibrium position harmonically, at the same frequency of the incoming electric field; as accelerated charges are sources of the electromagnetic fields, it is understood that these oscillating charges will produce a response field at the same frequency of the incoming field. This is the consequence of the harmonic potential in which the charges live when the displacement from their equilibrium position is small. According to Maxwell's equation, this linear response is described by the following equation

$$\boldsymbol{P}^{(\mathrm{L})}(\boldsymbol{r},t) = \epsilon_0 \chi^{(1)} \boldsymbol{E}(\boldsymbol{r},t) \tag{2.1.1}$$

where the electric polarization field $\boldsymbol{P}$ is proportional to the density of induced dipole moments in the material and where the (L) label underlines that the response is linear.

When the incoming field becomes comparable with the Coulomb field produced by the atom nuclei, however, the electrons are displaced to the point that their potential cannot be considered harmonic anymore. As such, their oscillation will not occur only at the frequency of the incoming field, but other frequencies will appear in their motion; hence, the produced field will posses these new frequencies of the distorted oscillation, as well.

This nonlinear behaviour can be modeled by extending eq. (2.1.1) to include higher order terms that depend nonlinearly on the incident electric field.

$$\boldsymbol{P} = \boldsymbol{P}^{(\mathrm{L})} + \boldsymbol{P}^{(\mathrm{NL})} = \epsilon_0 \big(\chi^{(1)}\boldsymbol{E} + \chi^{(2)}\boldsymbol{EE} + \chi^{(3)}\boldsymbol{EEE} + \dots\big) \tag{2.1.2}$$

where the higher order susceptibility terms ($\chi^{(2)}$, $\chi^{(3)}$, $\dots$) are, in general, tensors that depend on the frequencies and orientation of the incoming fields. While the first-order susceptibility $\chi^{(1)}$ has magnitude in the order of unity, the higher order terms become important when their value becomes comparable to $\chi^{(1)}$, i.e., when $\chi^{(2)}E \sim 1$, $\chi^{(3)}EE \sim 1$ and so on. From the previous argument, we expect this to happen when $E \simeq E_C \simeq 10^{12}$ V/m, where E_C is the bounding Coulomb field. Indeed, for most material used in nonlinear optics we have $\chi^{(2)} \sim 10^{-12}$ m/V and $\chi^{(3)} \sim 10^{-24}$ m^2/V.

The higher order susceptibilities are strongly related to the symmetries of the material they characterize: for instance, even-order susceptibilities ($\chi^{(2)}$, $\chi^{(4)}$, $\dots$) have to vanish for centrosymmetric crystals while odd-order susceptibilities ($\chi^{(1)}$, $\chi^{(3)}$, $\chi^{(5)}$, $\dots$) have not to.

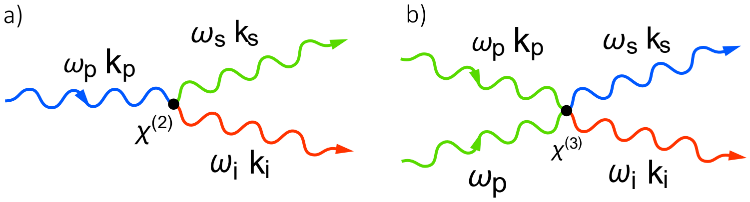

Figure 2.1: Example of nonlinear optical processes involving three and four photons. a) Spontaneous Parametric Down-Conversion b) Spontaneous Four-Wave Mixing.

Nonlinear optical processes can be viewed as scattering events between photons, mediated by the nonlinearities of the optical material, that couple the input and output fields (Figure 2.1).

The energy and momentum of the input and output photons have to be conserved because, throughout the process, the material does not exchange a net amount of energy or momentum with the fields (hence, the term *parametric* process). The conservation of energy naturally translates to a condition on the frequencies of the photons involved: the sum of the angular frequencies of the output photons has to equal the sum of the angular frequencies of the input photons.

$$\sum_{n=\text{input}} \omega_n = \sum_{n=\text{output}} \omega_n \tag{2.1.3}$$

The conservation of momentum translates on the requirement that the sum of the input wavevectors has to equal the sum of the output wavevectors.

$$\sum_{n=\text{input}} \boldsymbol{k}_n = \sum_{n=\text{output}} \boldsymbol{k}_n \tag{2.1.4}$$

This last condition is also known as *phase matching* and it is essential for the efficient generation of fields by nonlinear effects. Phase matching is not straightforward to obtain because, due to the dispersion in optical media, the wavevectors will not match, generally. For instance, in the case of Second-Harmonic Generation, a field at angular frequency 2ω is produced from two fields at angular frequency ω. While obviously the energy conservation condition is fulfilled ($2\omega = \omega + \omega$), the momentum conservation requires that

$$\boldsymbol{k}(2\omega) = \boldsymbol{k}_1(\omega) + \boldsymbol{k}_2(\omega) \tag{2.1.5}$$

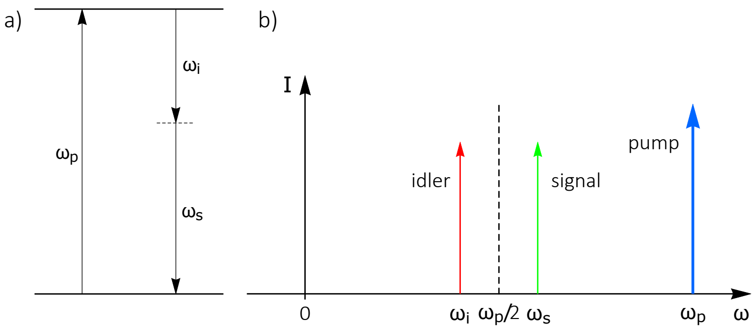

Figure 2.2: a) Level scheme of Parametric Down-Conversion. b) Pictorial frequency-axis representation of Parametric Down-Conversion.

where $k_1(\omega) = k_2(\omega) = \omega n(\omega)/c$ and $k(2\omega) = 2\omega n(2\omega)/c$. Now, assuming parallel propagation, the phase matching condition requires that $n(2\omega) = n(\omega)$ which is not usually the case. In practice, phase matching is obtained by carefully choosing the orientation of the nonlinear crystal, when they are birefringent, and by choosing the direction of propagation of the fields involved in the nonlinear process.

2.1.2 Parametric Down-Conversion

One important $\chi^{(2)}$ nonlinear process that is often encountered in nonlinear optical experiments is Parametric Down-Conversion (PDC). The classical process involves two input fields, the *pump* and the *signal* fields, oscillating at angular frequencies ω_p and ω_s respectively; these two fields interact in a nonlinear medium to produce a third field, called *idler*, at a third frequency $\omega_i = \omega_p - \omega_s$. For obvious reasons, the classical process is also called Difference-Frequency Generation. If placed on a frequency axis, we see that ω_s and ω_i will lay at symmetric positions with respect to half the pump frequency $\omega_p/2$ (Figure 2.2-b):

$$\omega_s - \omega_p/2 = \omega_p/2 - \omega_i \tag{2.1.6}$$

When described quantumly, the process can be viewed as a pump photon at frequency ω_p being annihilated to produce a pair of photons (signal and idler) whose frequencies add up to the pump frequency (Figure 2.2-a). When the pump spontaneously annihilates, the process is called Spontaneous Parametric Down-Conversion (SpPDC); when a photon at angular frequency ω_s stimulates the creation of a pair, the process is called Stimulated Parametric Down-Conversion (StPDC).

If we call $\hat{a}_p^\dagger$, $\hat{a}_s^\dagger$ and $\hat{a}_i^\dagger$ the creation operators for the field oscillating at frequencies ω_p, ω_s and ω_i, under phase-matching conditions, the relevant Hamiltonian that describes PDC is the following

$$\begin{aligned}\mathcal{H}_{\text{PDC}} = \hbar\omega_p(\hat{a}_p^\dagger\hat{a}_p + \frac{1}{2}) + \hbar\omega_s(\hat{a}_s^\dagger\hat{a}_s + \frac{1}{2}) + \hbar\omega_i(\hat{a}_i^\dagger\hat{a}_i + \frac{1}{2}) + \\ + \hbar g(\hat{a}_s^\dagger\hat{a}_i^\dagger\hat{a}_p + \hat{a}_s\hat{a}_i\hat{a}_p^\dagger)\end{aligned} \tag{2.1.7}$$

where g is a coefficient that takes into account the efficiency of the process and it depends on the nonlinear susceptibility $\chi^{(2)}$. The last term of the equation is responsible for the nonlinear coupling of the three fields and it can be obtained by applying perturbation theory of quantum mechanics to the quantized Maxwell's equations for fields propagating in media. The complete derivation is out of the scope of this work, however we refer the reader to Chapter 22 of [249] for further details.

By taking the exponential of eq. (2.1.7), the quantum evolution operator for the PDC interaction can be obtained:

$$\hat{\mathcal{U}}_{\text{PDC}} = e^{-i\hbar u(\hat{a}_s^\dagger\hat{a}_i^\dagger\hat{a}_p + \hat{a}_s\hat{a}_i\hat{a}_p^\dagger)} \tag{2.1.8}$$

where u is proportional to g and to the interaction time.

When a very strong coherent beam is used to pump the process, the $\hat{a}_p$ operator can be replaced with a complex number α that takes into account the phase and amplitude of the beam. This replacement can be performed because $\hat{a}_p^\dagger \left|\alpha\right\rangle_p \simeq \alpha^* \left|\alpha\right\rangle_p$ when $\alpha \gg 1$. Therefore, the PDC operator takes the form

$$\hat{\mathcal{U}}_{\text{PDC}} \simeq e^{-i\hbar u(\alpha\hat{a}_s^\dagger\hat{a}_i^\dagger + \alpha^*\hat{a}_s\hat{a}_i)} \tag{2.1.9}$$

When the above operator acts on a signal-idler vacuum and on a coherent pulse, i.e. without a field stimulating the nonlinear process, the following series is produced

$$\hat{\mathcal{U}}_{\text{PDC}} \left|\alpha\right\rangle_p \left|0\right\rangle_s \left|0\right\rangle_i \simeq \left|\alpha\right\rangle_p \left(\left|0\right\rangle_{s,i} + \gamma \left|1\right\rangle_s \left|1\right\rangle_i + \frac{\gamma^2}{2} \left|2\right\rangle_s \left|2\right\rangle_i + \dots\right) \tag{2.1.10}$$

where usually $\gamma \ll 1$. It is seen that most of the times the signal and idler fields remain in the vacuum state, while a small number of times a coincident

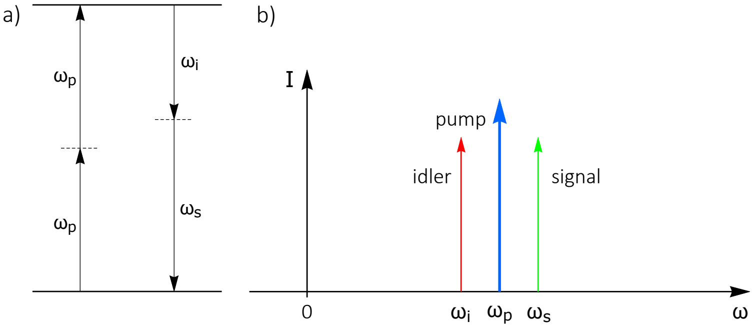

Figure 2.3: a) Level scheme of Degenerate Four-Wave Mixing. b) Pictorial frequency-axis representation of Degenerate Four-Wave Mixing.

pair of photon is produced. If $|\gamma|$ is indeed much smaller than 1, then the higher order terms can be neglected. This is usually the case when the nonlinear process is pumped with a continuous-wave laser, but the higher order terms may not be neglected when a pulsed laser is used or when the nonlinear process occurs in a confining optical cavity.

2.1.3 Four-Wave Mixing

An example of third-order nonlinear process is Four-Wave Mixing (FWM). Here, three fields combine together in a nonlinear material to produce a fourth field at a different frequency. In particular, we will focus on the particular case in which two of the input fields have the same angular frequency, which we will call *pump* frequency ω_p. The other input field is then called *signal*, while the produced field is called *idler* and these two fields oscillate at angular frequencies ω_s and ω_i respectively. When two fields have the same frequency, StFWM is often called Degenerate Four-Wave Mixing (DFWM).

From the conservation of the energy, eq. (2.1.3), it is straightforward to notice that the produced signal and idler frequencies will lay symmetrically with respect to the pump frequency (Figure 2.3-b).

$$\omega_s - \omega_p = \omega_p - \omega_i \tag{2.1.11}$$

Phase matching analogously becomes

$$2\boldsymbol{k}_p = \boldsymbol{k}_s + \boldsymbol{k}_i \tag{2.1.12}$$

When described quantumly, the process annihilates two pump photons to produce a pair of signal and idler photons (Figure 2.3-a). Again, if there is no stimulating field at ω_s the process is called Spontaneous Four-Wave Mixing (SpFWM), while it is called Stimulated Four-Wave Mixing (StFWM) otherwise.

Analogously to PDC, the relevant quantum operator that describes the annihilation and creation of photons during FWM is the following

$$\hat{\mathcal{U}}_{\mathrm{DFWM}} = e^{-i\hbar v\left((\hat{a}_p)^2\hat{a}_s^\dagger\hat{a}_s^\dagger+(\hat{a}_p^\dagger)^2\hat{a}_s\hat{a}_i\right)} \tag{2.1.13}$$

where the second power of the pump operator comes from the fact that we have two degenerate fields, while the v coefficient has the same meaning as u for PDC, that is, it is dependent on the third-order nonlinear susceptibility $\chi^{(3)}$ and to the interaction time. Again, when the pump field is a strong coherent beam, the pump operator can be replaced with a complex number α and the operator will reduce to the same form of the PDC operator

$$\hat{\mathcal{U}}_{\mathrm{DFWM}} \simeq e^{-i\hbar v(\alpha^2\hat{a}_s^\dagger\hat{a}_s^\dagger-(\alpha^*)^2\hat{a}_s\hat{a}_i)} \tag{2.1.14}$$

producing a series analogous to eq. (2.1.10) when the operator acts on the signal and idler vacuum.

2.2 Quantum states of light

2.2.1 Second Quantization

The fundamental concept on which the theory of Quantum Optics is based is the Second Quantization of light. Here we outline very briefly the standard quantization procedure that leads to the definition of the photon ladder operators and notable quantum states of light, such as the photon number states, that are used throughout the rest of the thesis.

The standard procedure for the Second Quantization of light expresses the classical electromagnetic fields, as described by Maxwell equations and through the scalar and vector potentials ϕ and $\boldsymbol{A}$, in the form of a harmonic oscillator, which is then assumed to be quantized.

Classically, electric and magnetic fields $\boldsymbol{E}$ and $\boldsymbol{B}$ are governed by Maxwell's equations (in vacuum):

$$\begin{cases} \boldsymbol{\nabla} \cdot \boldsymbol{E} = 0 \\ \boldsymbol{\nabla} \cdot \boldsymbol{B} = 0 \\ \boldsymbol{\nabla} \times \boldsymbol{E} = -\frac{\partial \boldsymbol{B}}{\partial t} \\ \boldsymbol{\nabla} \times \boldsymbol{B} = \mu_0 \epsilon_0 \frac{\partial \boldsymbol{E}}{\partial t} \end{cases} \tag{2.2.1}$$

where ϵ_0 and μ_0 are the vacuum electric permittivity and magnetic permeability.

By the properties of vector calculus, the Maxwell equations can be expressed in terms of the scalar and vector potentials ϕ and $\boldsymbol{A}$, by exploiting the following relations

$$\begin{cases} \boldsymbol{B} = \boldsymbol{\nabla} \times \boldsymbol{A} \\ \boldsymbol{E} = -\boldsymbol{\nabla}\phi - \frac{\partial \boldsymbol{A}}{\partial t} \end{cases} \tag{2.2.2}$$

that also hold for any other pair of potentials $(\phi', \boldsymbol{A}')$ related to $(\phi, \boldsymbol{A})$ by the following gauge transformation:

$$\begin{cases} \boldsymbol{A} = \boldsymbol{A}' - \boldsymbol{\nabla}\chi \\ \phi = \psi' + \frac{\partial \chi}{\partial t} \end{cases} \tag{2.2.3}$$

where χ is an arbitrary scalar function of position and time. We exploit this freedom to choose a vector potential $\boldsymbol{A}$ such that

$$\boldsymbol{\nabla} \cdot \boldsymbol{A} = 0 \qquad \text{(Coulomb gauge)} \tag{2.2.4}$$

This choice and relations (2.2.2) allow to rewrite the Maxwell equations in the following form:

$$\begin{cases} \boldsymbol{\nabla}\phi = 0 \\ -\nabla^2 \boldsymbol{A} + \frac{1}{c^2} \frac{\partial^2 \boldsymbol{A}}{\partial t^2} = 0 \end{cases} \tag{2.2.5}$$

where the second one is a wave equation for the vector potential $\boldsymbol{A}$. As such, the vector potential oscillates in time and in space sinusoidally, as an harmonic oscillator. More formally, we consider now a cubic cavity of side L, with periodic boundary conditions, in which the field $\boldsymbol{A}$ can oscillate.

In general, the field will be described by a superposition of modes that can oscillate in the cavity as:

$$\boldsymbol{A}(\boldsymbol{r},t)=\sum_{\boldsymbol{k},\lambda}\boldsymbol{e}_{\boldsymbol{k},\lambda}A_{\boldsymbol{k},\lambda}(\boldsymbol{r},t) \tag{2.2.6}$$

where $\lambda = 1, 2$ is the index associated with the polarization of the modes, $\boldsymbol{k}$ is the wavevector associated with the mode and $\boldsymbol{e}_{\boldsymbol{k},\lambda}$ is the unit vector that takes into account the polarization of the field. From the periodic boundary conditions it follows that

$$\boldsymbol{k}=(k_x,k_y,k_z),\quad k_x=\frac{2\pi m_x}{L},\quad k_y=\frac{2\pi m_y}{L},\quad k_z=\frac{2\pi m_z}{L} \tag{2.2.7}$$

where m_α $(\alpha = x, y, z)$ are integers. Each of the modes $A(\boldsymbol{r},t)_{\boldsymbol{k},\lambda}$ is independent of the others and it separately solves the wave equation. Moreover, the dependences on space and time can be separated.

Without performing the whole derivation, the final solution is expressed as

$$A_{\boldsymbol{k},\lambda}(\boldsymbol{r},t)=A_{\boldsymbol{k},\lambda}e^{-i\omega_{\boldsymbol{k}}t+i\boldsymbol{k}\cdot\boldsymbol{r}}+A^*_{\boldsymbol{k},\lambda}e^{+i\omega_{\boldsymbol{k}}t-i\boldsymbol{k}\cdot\boldsymbol{r}} \tag{2.2.8}$$

where $\omega_{\boldsymbol{k}} = c/k$ is the frequency associated to the wavevector $\boldsymbol{k}$. From the previous expression it is possible to derive the electromagnetic fields associated to each mode $(\boldsymbol{k},\lambda)$:

$$\begin{cases}E_{\boldsymbol{k},\lambda}=i\omega_{\boldsymbol{k}}\big(A_{\boldsymbol{k},\lambda}e^{-i\omega_{\boldsymbol{k}}t+i\boldsymbol{k}\cdot\boldsymbol{r}}-A^*_{\boldsymbol{k},\lambda}e^{+i\omega_{\boldsymbol{k}}t-i\boldsymbol{k}\cdot\boldsymbol{r}}\big)\\ B_{\boldsymbol{k},\lambda}=ik\big(A_{\boldsymbol{k},\lambda}e^{-i\omega_{\boldsymbol{k}}t+i\boldsymbol{k}\cdot\boldsymbol{r}}-A^*_{\boldsymbol{k},\lambda}e^{+i\omega_{\boldsymbol{k}}t-i\boldsymbol{k}\cdot\boldsymbol{r}}\big)\end{cases} \tag{2.2.9}$$

and of the associated energy

$$\mathbb{E}_{\boldsymbol{k},\lambda}=\epsilon_0L^3\omega_{\boldsymbol{k}}^2(A_{\boldsymbol{k},\lambda}A^*_{\boldsymbol{k},\lambda}-A^*_{\boldsymbol{k},\lambda}A_{\boldsymbol{k},\lambda}) \tag{2.2.10}$$

It is left implicit that the polarization of the fields follows the usual rules of plane-wave propagation.

The canonical Second Quantization is performed when it is assumed that the vector potential $\boldsymbol{A}$ is actually a quantum operator:

$$\boldsymbol{A}(\boldsymbol{r},t)\longrightarrow\hat{\boldsymbol{A}}(\boldsymbol{r},t) \tag{2.2.11}$$

In particular, each of the modes $A_{\boldsymbol{k},\lambda}$ is an independent harmonic oscillator, and each of these modes is then quantized. The substitution formally reads

$$\begin{cases} A_{\boldsymbol{k},\lambda} \longrightarrow (\hbar/2\epsilon_0 L^3 \omega_{\boldsymbol{k}})^{1/2} \hat{a}_{\boldsymbol{k},\lambda} \\ A^*_{\boldsymbol{k},\lambda} \longrightarrow (\hbar/2\epsilon_0 L^3 \omega_{\boldsymbol{k}})^{1/2} \hat{a}^\dagger_{\boldsymbol{k},\lambda} \end{cases} \tag{2.2.12}$$

where $\hat{a}_{\boldsymbol{k},\lambda}$ and $\hat{a}^\dagger_{\boldsymbol{k},\lambda}$ are the destruction and creation operators of the now quantum harmonic oscillator associated to the mode $(\boldsymbol{k}, \lambda)$.

These ladder operators are analogous to the operators of the quantum harmonic oscillator and they share the same properties. The canonical commutation relation is expanded to take into account the independence between different modes of the cavity:

$$[\hat{a}_{\boldsymbol{k},\lambda}, \hat{a}^\dagger_{\boldsymbol{k}',\lambda'}] = \delta_{\boldsymbol{k},\boldsymbol{k}'} \delta_{\lambda,\lambda'} \tag{2.2.13}$$

and the Fock states for the mode $(\boldsymbol{k}, \lambda)$, that form a complete basis for that mode, are defined in terms of the ladder operators

$$\begin{aligned} \hat{a}_{\boldsymbol{k},\lambda} \left| n_{\boldsymbol{k},\lambda} \right\rangle &= \sqrt{n_{\boldsymbol{k},\lambda}} \left| n_{\boldsymbol{k},\lambda} - 1 \right\rangle \\ \hat{a}^\dagger_{\boldsymbol{k},\lambda} \left| n_{\boldsymbol{k},\lambda} \right\rangle &= \sqrt{n_{\boldsymbol{k},\lambda} + 1} \left| n_{\boldsymbol{k},\lambda} + 1 \right\rangle \end{aligned} \tag{2.2.14}$$

More in general, the basis vectors of the field comprising all the modes of the cavity will be given by the tensor product of the basis vectors associated to the individual modes

$$\left| n_{\boldsymbol{k}_1,1}, n_{\boldsymbol{k}_1,2}, n_{\boldsymbol{k}_2,1}, n_{\boldsymbol{k}_2,2}, \ldots \right\rangle = \left| n_{\boldsymbol{k}_1,1} \right\rangle \left| n_{\boldsymbol{k}_1,2} \right\rangle \left| n_{\boldsymbol{k}_2,1} \right\rangle \left| n_{\boldsymbol{k}_2,2} \right\rangle \ldots \tag{2.2.15}$$

while the Hamiltonian of the whole system is expressed in terms of the Hamiltonians of the single systems

$$\hat{\mathcal{H}} = \sum_{\boldsymbol{k},\lambda} \hat{\mathcal{H}}_{\boldsymbol{k},\lambda} = \sum_{\boldsymbol{k},\lambda} \hbar \omega_{\boldsymbol{k},\lambda} (\hat{a}^\dagger_{\boldsymbol{k},\lambda} \hat{a}_{\boldsymbol{k},\lambda} + \frac{1}{2}) \tag{2.2.16}$$

The formalism of the quantum harmonic oscillator is a well known topic of Quantum Mechanics and it will not be further reviewed here. The topic is covered by a number of textbooks, among which we cite [252, 253].

From now, until stated otherwise, we will focus our attention to a single mode of the electromagnetic field. We will assume that all the other modes are in the vacuum state, so that we can simplify the notation: with the symbol $|n\rangle$ we will now represent the field of the single mode $(\boldsymbol{k}_i\lambda_i)$ to be in the number state n, retrieving the familiar notation of the canonical quantum harmonic oscillator:

$$|\psi\rangle = |\ldots, 0_{\boldsymbol{k}_{i-1},2}, n_{\boldsymbol{k}_i,1}, 0_{\boldsymbol{k}_i,2}\ldots\rangle = \frac{(\hat{a}^{\dagger}_{\boldsymbol{k}_0,\lambda_0})^n}{\sqrt{n!}}\,|0\rangle \longrightarrow |n\rangle = \frac{(\hat{a}^{\dagger})^n}{\sqrt{n!}}\,|0\rangle \tag{2.2.17}$$

We will refer to states of light described by this kind of wavefunction as *single-mode states.*

Other useful operators that can be used to calculate important properties of quantum states of light are the field operators. They are obtained from $\hat{\boldsymbol{A}}$ using the same relations that connect the classical electromagnetic fields and the vector potential. For a given mode of the cavity we have

$$\hat{\boldsymbol{E}}(\boldsymbol{r},t) = \hat{\boldsymbol{E}}^{+}(\boldsymbol{r},t) + \hat{\boldsymbol{E}}^{-}(\boldsymbol{r},t) \tag{2.2.18}$$

where

$$\begin{aligned}\hat{\boldsymbol{E}}^{+}(\boldsymbol{r},t) &= \boldsymbol{e}\,(\hbar\omega/2\epsilon_0 L^3)^{1/2}\hat{a}e^{-i\omega t+i\boldsymbol{k}\cdot\boldsymbol{r}-i\pi/2}\\ \hat{\boldsymbol{E}}^{-}(\boldsymbol{r},t) &= \boldsymbol{e}\,(\hbar\omega/2\epsilon_0 L^3)^{1/2}\hat{a}^{\dagger}e^{+i\omega t-i\boldsymbol{k}\cdot\boldsymbol{r}+i\pi/2}\end{aligned} \tag{2.2.19}$$

These two operators are known as the *positive frequency* and *negative frequency* field operators. The whole electric field operators will be given by the usual sum over all the possible modes of the cavity expressed as in the previous equations.

Analogously, for the magnetic field we have operators with very similar forms:

$$\hat{\boldsymbol{B}}(\boldsymbol{r},t) = \hat{\boldsymbol{B}}^{+}(\boldsymbol{r},t) + \hat{\boldsymbol{B}}^{-}(\boldsymbol{r},t) \tag{2.2.20}$$

with

$$\begin{aligned}\hat{\boldsymbol{B}}^{+}(\boldsymbol{r},t) &= \boldsymbol{k}\times\boldsymbol{e}\,(\hbar/2\epsilon_0\omega L^3)^{1/2}\hat{a}e^{-i\omega t+i\boldsymbol{k}\cdot\boldsymbol{r}-i\pi/2}\\ \hat{\boldsymbol{B}}^{-}(\boldsymbol{r},t) &= \boldsymbol{k}\times\boldsymbol{e}\,(\hbar/2\epsilon_0\omega L^3)^{1/2}\hat{a}^{\dagger}e^{+i\omega t-i\boldsymbol{k}\cdot\boldsymbol{r}+i\pi/2}\end{aligned} \tag{2.2.21}$$

As a final consideration, in the case of the quantization in the cube cavity, the polarization relation between the field is fixed by the fact that the modes are plane waves; this also sets the relations between the amplitudes of the magnetic field and of the vector potential operators. As such, it is customary to consider only the scalar part of the electric field operator, dropping the pesky square root factor that sets the amplitude of the electric field. Hence, a convenient expression to which the electric field operator reduces is

$$\hat{E}(\boldsymbol{r},t) = \hat{E}(\boldsymbol{r},t)^{+} + \hat{E}(\boldsymbol{r},t)^{-} = \frac{1}{2}\hat{a}e^{-i\xi} + \frac{1}{2}\hat{a}^{\dagger}e^{+i\xi} \tag{2.2.22}$$

where $\xi = \omega t - \boldsymbol{k} \cdot \boldsymbol{r} + \pi/2$ captures the spatial and temporal dependence of the field operator and where it is intended that the original vectorial field operator is given by

$$\hat{\boldsymbol{E}}(\boldsymbol{r}, t) = 2\,\boldsymbol{e}\,(\hbar\omega/2\epsilon_0 L^3)^{1/2} \hat{E}(\boldsymbol{r}, t) \tag{2.2.23}$$

The *quadrature operators* $\hat{X}$ and $\hat{Y}$ are naturally defined as

$$\begin{aligned} \hat{X} &= \frac{\hat{a} + \hat{a}^\dagger}{2} \\ \hat{Y} &= \frac{\hat{a} - \hat{a}^\dagger}{2i} \end{aligned} \tag{2.2.24}$$

and the scalar field operator can be rewritten equivalently as

$$\hat{E}(\xi) = \hat{X} \cos\xi + \hat{Y} \sin\xi \tag{2.2.25}$$

2.2.2 Notable states of light

Here we will briefly introduce the formalism used to describe three important kinds of light that can be frequently encountered during experiments of quantum optics: *number states*, *chaotic light*, *coherent light.* Another important kind of light, with peculiarly quantum properties, is squeezed light, but it will not be recalled here.

Number states

Number states are those states of light for which the field wavefunction is exactly equal to a Fock state. In the single-mode formalism introduced at the end of the previous section, these states are simply described by the simple expression

$$|\psi\rangle = |n\rangle \tag{2.2.26}$$

Despite the simple definition, these states possess some peculiar characteristics that are quite different with respect to the ones of classical fields. In particular, whenever the number of photons of these states is measured, the outcome is known precisely

$$\langle n \rangle = \langle n|\, \hat{n}\, |n\rangle = \langle n|\, \hat{a}^\dagger \hat{a}\, |n\rangle = n \tag{2.2.27}$$

where we introduced the number operator $\hat{n} = \hat{a}^\dagger \hat{a}$. The measurement is precise in the sense that there is no variation in the outcomes of repeated measurements, since the standard deviation of the measurement is equal to zero:

$$\langle \Delta n^2 \rangle = \langle n^2 \rangle - \langle n \rangle^2 = \langle n|\, \hat{n}\, \hat{n}\, |n\rangle - n^2 = n^2 - n^2 = 0 \tag{2.2.28}$$

The probability distribution of finding m photons in a number state $|n\rangle$ is obviously the Kronecker delta:

$$P(m) = \delta_{n,m} \tag{2.2.29}$$

On the other hand, the expectation value of the electric field is equal to zero for any value of ξ

$$\langle \hat{E} \rangle = 0 \tag{2.2.30}$$

and its uncertainty is equal to

$$\langle (\Delta \hat{E})^2 \rangle = \frac{1}{2}\left(n + \frac{1}{2}\right) \tag{2.2.31}$$

When the field is represented in terms of the quadrature expectation values (Figure 2.4), number states can be represented as an infinitely thin circle centered on the origin, regardless of the value of ξ. In other words, a perfect knowledge of the field amplitude is paired with a complete lack of knowledge on the phase of the field.

Coherent states

Coherent states are often considered a good representation of laser radiation. Indeed, as we will see in the following, their characteristics are very close to the ones of the coherent light described by classical theory. They also give a rather insightful picture of the origin of the shot noise in coherent beams of light.

The coherent state is defined in terms of the Fock number states as

$$|\alpha\rangle = e^{-\frac{1}{2}|\alpha|^2} \sum_{n=0}^{\infty} \frac{\alpha^n}{\sqrt{n!}} |n\rangle \tag{2.2.32}$$

where α is a complex number that indicates the amplitude and phase of the field. Equivalently, the coherent state can be defined as the eigenstate of the destruction operator $\hat{a}$, having eigenvalue α:

$$\hat{a}\, |\alpha\rangle = \alpha\, |\alpha\rangle \tag{2.2.33}$$

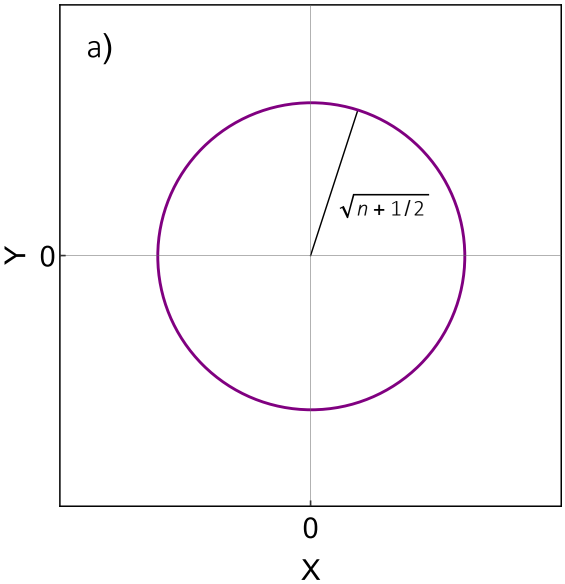

Figure 2.4: Quadrature representation of a number state. There is no uncertainty in the amplitude of the field, but complete uncertainty on its phase.

The two definitions are equivalent and they can be derived from one another.

The mean number of photons of the coherent state $\langle n \rangle$ is equal to $|\alpha|^2$, as it can be easily verified by the direct evaluation of $\langle n \rangle = \langle \alpha | \hat{n} | \alpha \rangle$. At variance with the number state, the uncertainty in the number of photons of the coherent state is now grater than zero:

$$\Delta n = \sqrt{\langle n \rangle} = |\alpha| \tag{2.2.34}$$

As the uncertainty scales sublinearly with the mean number of photons of the coherent state, it becomes less and less important as $|\alpha|^2$ increases. This concept can be captured by the Signal-to-Noise Ratio (SNR):

$$\text{SNR} = \frac{\Delta n}{\langle n \rangle} = \frac{1}{\sqrt{\langle n \rangle}} \tag{2.2.35}$$

And the analogy with the SNR of a classical coherent beam affected by shot noise is clear

$$\text{SNR} = \frac{\Delta I}{I} = \frac{1}{\sqrt{I}} \tag{2.2.36}$$

The probability distribution of finding n photons in the coherent state α is the Poisson distribution

$$P(n) = e^{-\langle n \rangle} \frac{\langle n \rangle^n}{n!} \tag{2.2.37}$$

Another convenient representation of the coherent state is given in terms of the exponential of the operator $\hat{a}$:

$$|\alpha\rangle = e^{-\frac{1}{2}|\alpha|^2} \sum_{n=0}^{\infty} \frac{(\alpha \hat{a}^\dagger)^n}{n!} |0\rangle = e^{\alpha \hat{a}^\dagger - \frac{1}{2}|\alpha|^2} |0\rangle = e^{\alpha \hat{a}^\dagger - \alpha^* \hat{a}} |0\rangle \tag{2.2.38}$$

where the last equality has been obtained thanks to the Baker-Campbell-Hausdorff relation. The operator that multiplies vacuum in the previous expression is also called *displacement operator*, and it is often indicated with $\hat{\mathcal{D}}(\alpha)$.

With the use of the properties of the displacement operator, not given here, it is easy to derive a series of properties of the coherent state that clarify the meaning of the complex number α. In fact, the expectation value of the scalar field operator is given by

$$\langle E \rangle = \langle \alpha | \hat{E}(\xi) | \alpha \rangle = |\alpha| \cos \xi - \theta, \qquad \theta = \arg \alpha \tag{2.2.39}$$

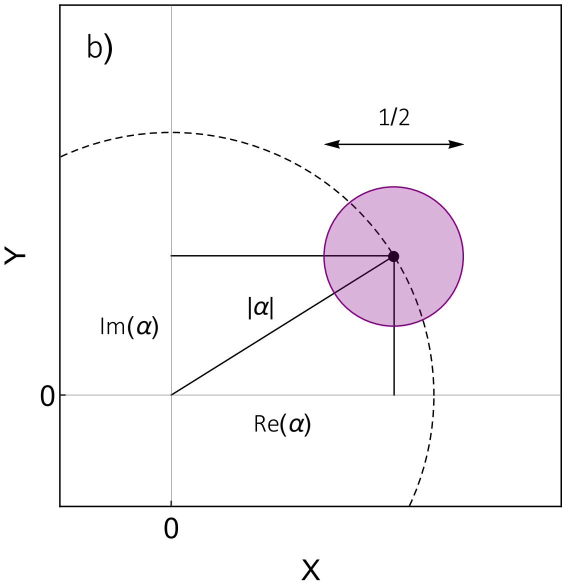

Figure 2.5: Quadrature representation of a coherent state. The circle represents the spread of a gaussian wavefunction.

highlighting the role of $\arg\alpha$ as the phase of the field.

The uncertainty on the quadrature operators, which gives a measure of the horizontal and vertical spread of the wavefunction in the quadrature space, has the same value irrespectively of the value of α:

$$\begin{aligned}(\Delta X)^2 &= \langle(\Delta\hat{X})^2\rangle = \frac{1}{4} \\ (\Delta Y)^2 &= \langle(\Delta\hat{Y})^2\rangle = \frac{1}{4}\end{aligned} \tag{2.2.40}$$

and it can be represented as a gaussian wavefunction displaced from the origin by the amount α (as seen pictorially in Figure 2.5). From the picture it is now evident that the displacement operator does indeed what its name suggests: it displaces the vacuum field by the complex number α; the vacuum field is indeed a coherent state, since it is a trivial eigenstate of the destruction operator with zero eigenvalue: $\hat{a}\,|0\rangle = 0\,|0\rangle$.

Chaotic light

The light of a beam is said to be *chaotic* when it is given by the superposition of fields produced by a large number of independent emitters; this uncoordination is the cause of the peculiar statistical properties of this kind of light.

The number of photons found in a chaotic light beam follows the geometric distribution:

$$P(n) = \frac{\langle n\rangle^n}{(1+\langle n\rangle)^{n+1}} \tag{2.2.41}$$

The distribution is the consequence of the Plank law, for which chaotic light is also called *thermal light*, that affirms that the probability to exite n photons in a cavity at temperature T is

$$P(n) = \frac{e^{-(n+1/2)\hbar\omega/k_B T}}{\sum_n e^{-(n+1/2)\hbar\omega/k_B T}} \tag{2.2.42}$$

where k_B is the Boltzmann constant. Consequently, the average number of photons $\langle n\rangle$ found in a beam of thermal light is given by

$$\langle n\rangle = \frac{1}{\exp(\frac{\hbar\omega}{k_B T}) - 1} \tag{2.2.43}$$

While the coherent state is a coherent superposition of photon number states, chaotic light is, instead, a statistical mixture because the emitters are incoherent. As such, the state of chaotic light will be given in terms of a mixture of coherent states [254], or Fock states, as for the density operator $\hat{\rho}$:

$$\hat{\rho} = \sum_n P(n)\,|n\rangle\langle n| \tag{2.2.44}$$

The uncertainty in the measured photon number is given given by

$$\Delta n^2 = \langle n\rangle^2 + \langle n\rangle \tag{2.2.45}$$

where the additional $\langle n\rangle^2$ term indicates that the noise of thermal light is higher than for coherent states.

When the variance of the number of photons for a state is equal to $\langle n\rangle$, the state is said to be *Poissonian*; if it is higher or lower than $\langle n\rangle$, it is said to be *super-Poissonian* or *sub-Poissonian*, respectively.

2.2.3 Frequency and time dependence of ladder operators

In this section we will introduce frequency- and time-dependent creation and destruction operators as they are a useful instrument to describe and understand the behaviour of light in certain situations in which the field cannot be considered confined in an optical cavity. As we will see in Paragraph 2.5.3, for instance, the Franson experiment can be understood in terms of these operators, and the resulting picture will be easier to understand.

In a closed cavity, only a discrete set of modes is able to oscillate (eq. (2.2.8)) and each of these modes corresponds to a quantum oscillator. The general state for single-mode light in this scenario is given by a superposition of states across all the number states associated with the mode.

$$|\psi\rangle = \sum_n c_{k,n} |n\rangle_k \tag{2.2.46}$$

where k is the discrete label that identifies the mode. When the field propagates in free space the picture is analogous, but now the possible modes form a continuum. The frequency-dependent ladder operators are the extension of the ladder operators of the cavity modes to the continuous case. Instead of having a discrete quantum number k, we will now have a continuous quantum number ω.

For instance, the superposition of single photons on different cavity modes is translated to the continuous case according to

$$|\psi\rangle = \sum_n c_n \hat{a}^\dagger_{k_n} |0\rangle \quad \longrightarrow \quad |\psi\rangle = \int \mu(\omega)\hat{a}^\dagger(\omega)\, d\omega\, |0\rangle \tag{2.2.47}$$

and $\hat{a}^\dagger(\omega)$ can be considered the operator that creates a photon on a field mode that is infinitely extended in space (and time) and that oscillates exactly at frequency ω. We will indicate this state with $|\psi(\omega)\rangle$, the result of the creation operator $\hat{a}^\dagger(\omega)$ acting on the vacuum:

$$\hat{a}^\dagger_{k_n} |0\rangle = |1\rangle_n \quad \longrightarrow \quad \hat{a}^\dagger(\omega)\,|0\rangle = |\psi(\omega)\rangle \tag{2.2.48}$$

The commutation relations naturally extend to the continuum of modes, as well

$$[\hat{a}_{k_n}, \hat{a}^\dagger_{k_m}] = \delta_{k_n,k_m} \quad \longrightarrow \quad [\hat{a}(\omega), \hat{a}^\dagger(\omega')] = \delta(\omega - \omega') \tag{2.2.49}$$

and from the previous expression it is easily demonstrated that the normalization condition has to be

$$\langle\psi|\psi\rangle = \sum_n |c_n|^2 = 1 \quad\longrightarrow\quad \langle\psi|\psi\rangle = \int |\mu(\omega)|^2\, d\omega = 1 \tag{2.2.50}$$

The time-dependent ladder operator can be approximately defined in terms of the Fourier transform of $\hat{a}(\omega)$, so that the two operators form a Fourier conjugate pair:

$$\hat{a}(t) = \frac{1}{\sqrt{2\pi}}\int \hat{a}(\omega)e^{-i\omega t}\, d\omega, \qquad \hat{a}(\omega) = \frac{1}{\sqrt{2\pi}}\int \hat{a}(t)e^{i\omega t}\, dt \tag{2.2.51}$$

from which it is easily seen that the field state has the dual description

$$|\psi\rangle = \int \mu(\omega)\hat{a}^\dagger(\omega)\, d\omega\, |0\rangle = \int \mu(t)\hat{a}^\dagger(t)\, dt\, |0\rangle \tag{2.2.52}$$

where

$$\mu(t) = \frac{1}{\sqrt{2\pi}}\int \mu(\omega)e^{-i\omega t}\, d\omega, \qquad \mu(\omega) = \frac{1}{\sqrt{2\pi}}\int \mu(t)e^{i\omega t}\, dt \tag{2.2.53}$$

Finally, it is possible to estimate the average number of photons present in the beam at time t with the use of the *mean photon flux* operator, defined as

$$\hat{f}(t) = \hat{a}^\dagger(t)\hat{a}(t) \tag{2.2.54}$$

so that the mean photon flux will be given by its expectation value

$$f(t) = \langle\hat{f}(t)\rangle = \langle\hat{a}^\dagger(t)\hat{a}(t)\rangle = |\mu(t)|^2 \tag{2.2.55}$$

For a detailed discussion about the time and frequency dependent operators and about the detection of photons we refer to the theory of optical detection, discussed again, for instance, in reference [2].

2.3 Field correlations

There are two kinds of correlations that are of interest when performing optical experiments. Correlations between fields *amplitudes*, and correlations between *intensities*. This section discusses these two kind of correlations both for the classical and quantum cases.

2.3.1 First-order correlation function

First-order correlations are the ones that involve field amplitudes. These correlations give rise to direct interference effects.

In general, we can define a function that measures the degree of first-order correlation of a field at two different space-time points; the study of this function can give important information about the behaviour of light inside devices that exploit interference between fields. This function, called *first-order correlation function* is a normalized expression that measures the extent to which two fields are capable of interfering with each other.

The first-order correlation function for classical fields is defined as

$$g^{(1)}(\boldsymbol{r}_1, t_1;\, \boldsymbol{r}_2, t_2) := \frac{\langle E^*(\boldsymbol{r}_1, t_1)E(\boldsymbol{r}_2, t_2)\rangle}{\sqrt{\langle E^*(\boldsymbol{r}_1, t_1)E(\boldsymbol{r}_1, t_1)\rangle\langle E^*(\boldsymbol{r}_2, t_2)E(\boldsymbol{r}_2, t_2)\rangle}} \tag{2.3.1}$$

where the angled brackets indicate the expectation value of the inner quantity over a large number of realizations of the same experiment. The brackets disappear if the fields are deterministic, but here we may deal also with chaotic light that is described classically with the mathematics of the random process.

The most general definition of the first-order correlation function includes the polarization and the direction of propagation of fields, but here we will assume co-polarized and co-propagating fields for simplicity.

This first definition of the correlation function deals with different fields in different space-time coordinates, but it is usual to encounter situations in which the expression can be simplified. For instance, we may deal with the same field at different space-time points, or with the same field in the same point but at different time coordinates. In this latter case the $g^{(1)}$ function only depends on $\boldsymbol{r}$, t_1 and t_2 and we say that we are considering the *time-correlations* of the field. In writing the simplified first-order correlation function we now leave implicit the dependence on $\boldsymbol{r}$:

$$g^{(1)}(t_1, t_2) = \frac{\langle E^*(t_1)E(t_2)\rangle}{\sqrt{\langle E^*(t_1)E(t_1)\rangle\langle E^*(t_2)E(t_2)\rangle}} \tag{2.3.2}$$

If the field is stationary, the correlations will depend only on the time difference $\tau = t_2 - t_1$ and not on the absolute times t_1 and t_2; this is the simplest case and the definition of first-order correlation function reduces to

$$g^{(1)}(\tau) = \frac{\langle E^*(t)E(t+\tau)\rangle}{\langle E^*(t)E(t)\rangle} \tag{2.3.3}$$

As it is evident from this last expression, the first-order correlation function is a normalized measure of how much the field E would constructively interfere with a delayed copied of itself.

From the mathematical properties of the ensemble average it is possible to derive the following properties for $g^{(1)}(\tau)$

$$g^{(1)}(0) = 1 \qquad \lim_{\tau \to \infty} g^{(1)}(\tau) = 0 \tag{2.3.4}$$

The definition of the first-order correlation function for quantum fields is analogous to its classical counterpart, where the expression of the field amplitudes are replaced with the quantum operators defined in Paragraph 2.2.1.

$$g^{(1)}(\boldsymbol{r}_1, t_1;\, \boldsymbol{r}_2, t_2) = \frac{\langle \hat{E}^-(\boldsymbol{r}_1, t_1)\hat{E}^+(\boldsymbol{r}_2, t_2)\rangle}{\sqrt{\langle \hat{E}^-(\boldsymbol{r}_1, t_1)\hat{E}^+(\boldsymbol{r}_1, t_1)\rangle\langle \hat{E}^-(\boldsymbol{r}_2, t_2)\hat{E}^+(\boldsymbol{r}_2, t_2)\rangle}} \tag{2.3.5}$$

and the simpler version for stationary fields is

$$g^{(1)}(\tau) = \frac{\langle \hat{E}^-(t)\hat{E}^+(t+\tau)\rangle}{\langle \hat{E}^-(t)\hat{E}^+(t)\rangle} \tag{2.3.6}$$

Expressing the last expression in terms of ladder operators one gets

$$g^{(1)}(\tau) = \frac{\langle \hat{a}^\dagger(t)\hat{a}(t+\tau)\rangle}{\langle \hat{a}^\dagger(t)\hat{a}(t)\rangle} \tag{2.3.7}$$

where the time dependence follows the discussion of Paragraph 2.2.3. The previous expression has the same properties (2.3.4), similarly to its classical counerpart.

2.3.2 Second-order correlation function

As mentioned, the second-order correlations are those that happen between field intensities. Some striking consequences of the second-order correlations are discovered when, for instance, single photon states are sent to the input of a beam splitter, as will be seen in Paragraph 2.4.3.

Analogously to the first-order correlation function, a second-order correlation function can be defined, as follows, for classical fields:

$$g^{(2)}_{a,b}(\boldsymbol{r}_1, t_1; \boldsymbol{r}_2, t_2) := \frac{\langle E^*_a(\boldsymbol{r}_1, t_1) E^*_b(\boldsymbol{r}_2, t_2) E_b(\boldsymbol{r}_2, t_2) E_a(\boldsymbol{r}_1, t_1)\rangle}{\langle E^*_a(\boldsymbol{r}_1, t_1) E_a(\boldsymbol{r}_1, t_1)\rangle \langle E^*_b(\boldsymbol{r}_2, t_2) E_b(\boldsymbol{r}_2, t_2)\rangle} \tag{2.3.8}$$

where we still assumed co-propagating and co-polarized fields; we also have now two indexes, a and b, that label which of two field modes are considered for the correlations. When the two modes are different the function is named second-order *cross*-correlation function; when they are the same, we have the second-order *auto*-correlation function.

Similarly to the previous paragraph, the expression of $g^{(2)}$ can be simplified when we consider the same spacial point $\boldsymbol{r}$ for the two fields and when we assume stationarity, so that only the time difference $\tau = t_2 - t_1$ will be relevant:

$$g^{(2)}_{a,b}(\tau) = \frac{\langle E^*_a(t) E^*_b(t+\tau) E_b(t+\tau) E_a(t)\rangle}{\langle E^*_a(t) E_a(t)\rangle \langle E^*_b(t) E_b(t)\rangle} \tag{2.3.9}$$

The second-order correlation function can also be given in terms of intensities

$$g^{(2)}_{a,b}(\tau) = \frac{\langle I_a(t) I_b(t+\tau)\rangle}{\langle I_a(t)\rangle \langle I_b(t)\rangle} \tag{2.3.10}$$

where the intensity is averaged over the optical cycle. Again, from the properties of the ensamble average, the following properties hold for the second-order correlation function

$$\begin{cases} 1 \leq g^{(2)}(0) \leq \infty \\ 0 \leq g^{(2)}(\tau) \leq g^{(2)}(0) \qquad \tau \neq 0 \end{cases} \tag{2.3.11}$$

which, however, hold for classical fields only.

The quantum version of the second-order function is obtained when the amplitudes are replaced with field operators. We show only the most simple version of it, where the replacement to be done in eq. (2.3.8) is now straightforward:

$$g^{(2)}_{a,b}(\tau) = \frac{\langle \hat{E}^-_a(t) \hat{E}^-_b(t+\tau) \hat{E}^+_b(t+\tau) \hat{E}^+_a(t)\rangle}{\langle \hat{E}^-_a(t) \hat{E}^+_a(t)\rangle \langle \hat{E}^-_b(t) \hat{E}^+_b(t)\rangle} \tag{2.3.12}$$

Notice that now the order of the operators is important since, in the case of the auto-correlation function, the $\hat{E}^+$ and $\hat{E}^-$ operators do not commute.

When ladder operators are used instead of the field operators, this other expression is obtained

$$g^{(2)}_{a,b}(\tau) = \frac{\langle \hat{a}^\dagger(t)\hat{b}^\dagger(t+\tau)\hat{b}(t+\tau)\hat{a}(t)\rangle}{\langle \hat{a}^\dagger(t)\hat{a}(t)\rangle\langle \hat{b}^\dagger(t)\hat{b}(t)\rangle} \tag{2.3.13}$$

where $\hat{a}(t)$ and $\hat{b}(t)$ are the field destruction operators of modes $E_a(t)$ and $E_b(t)$ and, again, they commute only if a and b are different modes.

In the case of quantum fields, the $g^{(2)}(\tau)$ function is a measure of the likelihood that two photons can be detected with a τ time delay. When $g^{(2)}(0) > 1$ we say that the light is *bunched* because the probability of detecting two photons at small time intervals will be higher than for longer time intervals. For instance, this is the case of thermal light, for which $g^{(2)}(0) = 2$. On the other hand, if $g^{(2)}(0) < 1$ light is called *antibunched*, and the probability of detecting photons at small time intervals will be small. This is particularly significant, because only quantum states of light can feature antibunching. In particular, $g^{(2)}$ values smaller than 1/2 cannot be explained by classical theories of light. Coherent light is an example for which $g^{(2)}(\tau) = 1$, and therefore the probability of detecting a second photon is not dependent on the time elapsed from the previous detection.

2.4 Devices

Here we will describe three important components used in optical experiments, the beam splitter, the Mach-Zehnder interferometer and the Hanbury Brown and Twiss interferometer. We will also focus on the importance of the $g^{(1)}$ and $g^{(2)}$ functions in the description of these devices.

2.4.1 The beam splitter

The beam splitter is a device that couples two input light modes and two output light modes (Figure 2.6). In general, the power incident on the first input mode of the beam splitter, as the name of the device suggests, is split between the two output modes, and the same is true for the other input. If we assume that no losses are present, the input-output relations of the the beam splitter can be described by 2 × 2 matrix, $\mathcal{U}_{\text{bs}}$, that has to be unitary as imposed by the conservation of the energy.

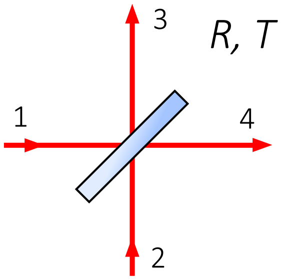

Figure 2.6: The beam splitter.

The classical description of the beam splitter involves the field amplitudes at the input and output of the device and is summarized by the following equation

$$\begin{pmatrix} E_3 \\ E_4 \end{pmatrix} = \mathcal{U}_{\text{bs}} \begin{pmatrix} E_1 \\ E_2 \end{pmatrix} = \begin{pmatrix} \mathcal{T} & \mathcal{R} \\ \mathcal{R}' & \mathcal{T}' \end{pmatrix} \begin{pmatrix} E_1 \\ E_2 \end{pmatrix} \tag{2.4.1}$$

where $\mathcal{R}$, $\mathcal{R}'$, $\mathcal{T}$ and $\mathcal{T}'$ are complex numbers. The beam splitter matrix $\mathcal{U}_{\text{bs}}$ has to be unitary, so its coefficients must fulfill the following equations:

$$\begin{aligned} \mathcal{T} &= Te^{i\alpha}, \qquad & \mathcal{R} &= Re^{i\beta} \\ \mathcal{R}' &= Re^{i\gamma}, \qquad & \mathcal{T}' &= Te^{i\delta} \end{aligned} \tag{2.4.2}$$

where R and T are real, and where

$$\begin{cases} R^2 + T^2 = 1 \\ \mathcal{R}^* \mathcal{T}' + \mathcal{R}' \mathcal{T}^* = 0 \end{cases} \tag{2.4.3}$$

When $R = T = 1/\sqrt{2}$ the beam splitter is said to be *balanced* or, equivalently, that it is a 50:50 beam splitter, because the power at either of the input modes is split equally between the output modes. The relations (2.4.3) do not impose a unique choice of the phases α, β, γ and δ, but an infinite set of matrices can describe a balanced beam splitter; among these matrices two common choices are

$$\mathcal{U}_{\text{bs}} = \frac{1}{\sqrt{2}} \begin{pmatrix} 1 & 1 \\ 1 & -1 \end{pmatrix} \qquad \mathcal{U}_{\text{bs}} = \frac{1}{\sqrt{2}} \begin{pmatrix} 1 & i \\ i & 1 \end{pmatrix} \tag{2.4.4}$$

Unless otherwise specified, we will use the second matrix when modeling the balanced beam splitter.

When the beam splitter is described quantum mechanically, the same above matrices relate the ladder operators for the input and output fields rather then the field amplitudes, as in

$$\begin{pmatrix} \hat{a}_3^\dagger \\ \hat{a}_4^\dagger \end{pmatrix} = \begin{pmatrix} \mathcal{T} & \mathcal{R} \\ \mathcal{R}' & \mathcal{T}' \end{pmatrix} \begin{pmatrix} \hat{a}_1^\dagger \\ \hat{a}_2^\dagger \end{pmatrix} = \mathcal{U}_{\mathrm{bs}} \begin{pmatrix} \hat{a}_1^\dagger \\ \hat{a}_2^\dagger \end{pmatrix} \tag{2.4.5}$$

where $\mathcal{R}$ and $\mathcal{T}$ still have to fulfill the unitarity conditions (2.4.3). Replacing the ladder operators with the field operators leads to the following equivalent result:

$$\begin{cases} \hat{E}_3(\xi) = T\hat{E}_1(\xi+\alpha) + R\hat{E}_2(\xi+\beta) \\ \hat{E}_4(\xi) = R\hat{E}_1(\xi+\gamma) + T\hat{E}_2(\xi+\delta) \end{cases} \tag{2.4.6}$$

While the equations for the classical and quantum description of the beam splitter look formally very similar, the overall picture is quite different, as it will be detailed later, in Section 2.4.3. Before discussing these differences, we will first give the formal description of the Mach-Zehnder interferometer.

2.4.2 The Mach-Zehnder interferometer

The Mach-Zehnder interferometer is schematized in Figure 2.7. As it can be seen there, the two input modes interact at a first beam splitter, they travel two paths that are in general of different lengths and then they interact again at a second beam splitter.

The unitary matrix $\mathcal{U}_{\mathrm{mzi}}$ describing the evolution of the fields between the input and output ports for the Mach-Zehnder interferometer is the following

$$\begin{aligned} \mathcal{U}_{\mathrm{mzi}} = \mathcal{U}_{\mathrm{bs},2}\mathcal{U}_{\mathrm{ps}}\mathcal{U}_{\mathrm{bs},1} = \begin{pmatrix} \mathcal{T}_2 & \mathcal{R}_2 \\ \mathcal{R}_2 & \mathcal{T}_2 \end{pmatrix} \begin{pmatrix} e^{i\phi_1} & 0 \\ 0 & e^{i\phi_2} \end{pmatrix} \begin{pmatrix} \mathcal{T}_1 & \mathcal{R}_1 \\ \mathcal{R}_1 & \mathcal{T}_1 \end{pmatrix} = \\ = \begin{pmatrix} e^{i\phi_2}\mathcal{R}_1\mathcal{R}_2 + e^{i\phi_1}\mathcal{T}_1\mathcal{T}_2 & e^{i\phi_2}\mathcal{T}_1\mathcal{R}_2 + e^{i\phi_1}\mathcal{R}_1\mathcal{T}_1 \\ e^{i\phi_1}\mathcal{T}_1\mathcal{R}_2 + e^{i\phi_1}\mathcal{R}_1\mathcal{T}_2 & e^{i\phi_1}\mathcal{R}_1\mathcal{R}_2 + e^{i\phi_2}\mathcal{T}_1\mathcal{T}_2 \end{pmatrix} \end{aligned} \tag{2.4.7}$$

where for simplicity we chose $\alpha = \delta$ and $\beta = \gamma$ for the individual beam splitter matrices, and where $\mathcal{U}_{\mathrm{ps}}$ is a unitary matrix that describes the phase shifts acquired by the fields as they propagate between the two beam splitters, so that $\phi_1 = kz_1 = \omega t_1$ and $\phi_2 = kz_2 = \omega t_2$, where t_1 and t_2 are the

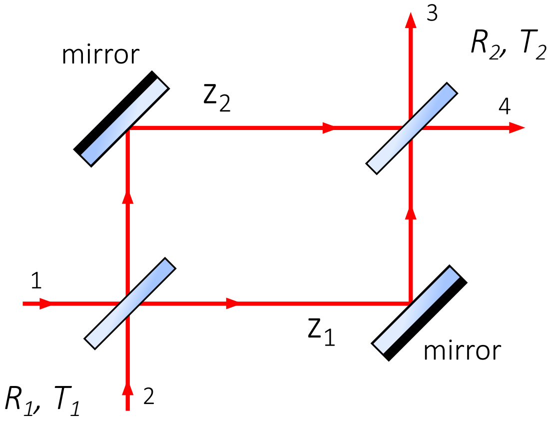

Figure 2.7: The Mach-Zehnder inteferometer.

times it takes the field to travel the two paths. Depending on the values of $\mathcal{T}_1$, $\mathcal{R}_1$, $\mathcal{T}_2$ and $\mathcal{R}_2$ the maximum visibility of the Mach-Zehnder can vary between zero and one. As it is seen in the description, the two beam splitters can be different, in general, however if we assume equal and balanced beam splitters instead, the Mach-Zehnder unitary matrix reduces to

$$\mathcal{U}_{\mathrm{mzi}} = \frac{1}{2}\begin{pmatrix} e^{i\phi_1} - e^{i\phi_2} & i(e^{i\phi_1} + e^{i\phi_2}) \\ i(e^{i\phi_1} + e^{i\phi_2}) & e^{i\phi_2} - e^{i\phi_1} \end{pmatrix} \tag{2.4.8}$$

Just like the beam splitter, the classical and quantum descriptions of the interferometer have the same unitary matrices, but in the first case the input and output field amplitudes are related, while in the second case the ladder operators are related instead.

$$\begin{pmatrix} E_3 \\ E_4 \end{pmatrix} = \mathcal{U}_{\mathrm{mzi}} \begin{pmatrix} E_1 \\ E_2 \end{pmatrix} \qquad \begin{pmatrix} \hat{a}_3 \\ \hat{a}_4 \end{pmatrix} = \mathcal{U}_{\mathrm{mzi}} \begin{pmatrix} \hat{a}_1 \\ \hat{a}_2 \end{pmatrix} \tag{2.4.9}$$

Experimentally, a quantity of interest is the intensity of the fields at the output of the interferometer. In particular, by taking the squared absolute value of the elements of the $\mathcal{U}_{\mathrm{mzi}}$ unitary matrix, one can determine the ratios between the input and output intensities of the device. If we assume no field at the second input port (i.e. $E_2 = 0$ and $E_1 = E$) and we assume to have a stationary field at the first port, we can easily arrive to the following equation that relates the input and output intensity:

$$\begin{aligned} I_3 &= \left(\frac{1}{2} - \frac{1}{2}\cos(\phi_1 - \phi_2)\right) I_1 \\ I_4 &= \left(\frac{1}{2} + \frac{1}{2}\cos(\phi_1 - \phi_2)\right) I_1 \end{aligned} \tag{2.4.10}$$

that holds for deterministic sinusoidal fields. When chaotic light is sent into the device, a description in terms of the expectation values of the field is more appropriate, and one arrives to

$$\langle E_4^*(t)E_4(t)\rangle = \frac{1}{4}(\langle E^*(t_1)E(t_1)\rangle + \langle E^*(t_2)E(t_2)\rangle + 2\,\mathrm{Re}\langle E^*(t_1)E(t_2)\rangle) \tag{2.4.11}$$

It is easily seen that the first two factors between parentheses are given by the field traveling in the two interferometer's paths while the last term, that involves the product of the input field at two different time instants, is the one producing the fringes at the output of the interferometer. With little further manipulation of the expression, one can recognize the first-order correlation function in the last term of the previous equation. If we assume stationary fields we have

$$\frac{\langle I_4\rangle}{\langle I_1\rangle} = \frac{\langle E_4^*(t)E_4(t)\rangle}{\langle E^*(t)E(t)\rangle} = \frac{1}{2} + \frac{1}{2}\,\mathrm{Re}\,g^{(1)}(\tau) \tag{2.4.12}$$

It is now apparent that the role of the first-order correlation function $g^{(1)}$ is to give a normalized description of the direct interference effects that are present in the interferometer. In general, whenever interference arises from two fields, a first-order correlation function can be used to describe such interference. In particular, the modulus $|g^{(1)}|$ of the function corresponds to the maximum visibility of the fringes that will be obtained between fields at the space-time points indicated in the function.

These considerations about the first-order correlation function apply to both the classical and quantum descriptions of the Mach-Zehnder interferometer, after performing the usual substitution of the classical amplitudes with the quantum operators.

2.4.3 The Hanbury Brown and Twiss interferometer

Let us go back now to the description of the behaviour of the beam splitter. While the Mach-Zehnder interferometer provided an example of the use of the

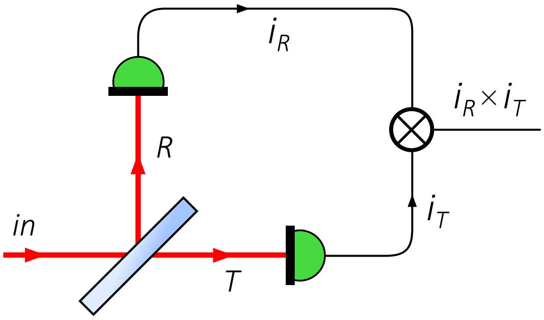

Figure 2.8: The Hanbury-Brown and Twiss inteferometer.

$g^{(1)}$ function, the beam splitter provides interesting insight on the meaning of $g^{(2)}$.

Consider a single input mode ("in") entering a beam splitter and its two output modes ("T" and "R"), as detailed in Figure 2.8. Consider also two detectors at the outputs of the beam splitter; classically, the detectors would produce currents (i_{T} and i_{R}) proportional to the intensity of the inpinging classical fields (I_{T} and I_{R}); quantumly they would produce electrical pulses when a photon is absorbed, a process that is proportional to the mean photon flux $f(t) = \langle \hat{a}^\dagger(t)\hat{a}(t)\rangle$. When the two signals produced by the detectors are multiplied together with a mixer, the signal obtained will be proportional to the product of I_R and I_T, which is reminiscent of the numerator of the second-order correlation function, as in eq. (2.3.10). This scheme is known as the *Hanbury Brown and Twiss interferometer* [255], and indeed it can be used to measure the second-order autocorrelation of an input field.

Indeed, from equations (2.3.13) and (2.4.5), it can be demonstrated that, when the beam splitter is balanced, the cross-correlation function at the output of the beam splitter $g^{(2)}_{\mathrm{R,T}}(\tau)$ is equal to the auto-correlation function of the input field $g^{(2)}_{\mathrm{in,in}}(\tau) = g^{(2)}_{\mathrm{R,T}}(\tau)$.

Let us consider a single photon at the input of the balanced beam splitter, so that $|\psi\rangle_{\mathrm{in}} = \hat{a}^\dagger_{\mathrm{in}}\,|0\rangle$; the input-output relations described above imply that input state will be equal to the following output state

$$|\psi\rangle_{\mathrm{out}} = \frac{1}{\sqrt{2}}(\hat{a}^\dagger_{\mathrm{T}} + i\hat{a}^\dagger_{\mathrm{R}})\,|0\rangle = \frac{1}{\sqrt{2}}(|1\rangle_{\mathrm{T}} + i\,|1\rangle_{\mathrm{R}}) \tag{2.4.13}$$

The quantum superposition of the output states implies that the photon will be detected *either* at detector T or at detector R; the coincident detection of two photons at the two detectors is not a possibility. This anti-correlation of the photon state is reflected by the value of the second-order correlation function that is equal to zero at zero time delay.

$$g^{(2)}(0) = 0 \qquad \text{(single photon)} \tag{2.4.14}$$

and we see that the field of a single photon is perfectly antibunched at zero-time delay.

This is in contrast with the classical result, where the input field is split equally on the two output paths and the detectors will produce equal currents proportional to half the input intensity. The classical result can be described with the quantum formalism assuming that a coherent state of complex amplitude α is present at the input of the beam splitter:

$$|\psi\rangle_{\text{in}} = |\alpha\rangle = \hat{\mathcal{D}}_{\text{in}}(\alpha)\,|0\rangle \tag{2.4.15}$$

From the properties of the displacement operator it is possible to demonstrate that at the output of the beam splitter, the output state is factorized:

$$\hat{\mathcal{D}}_{\text{in}}(\alpha) = \hat{\mathcal{D}}(\beta)_{\text{T}}\hat{\mathcal{D}}(\gamma)_{\text{R}} \tag{2.4.16}$$

so that

$$|\psi\rangle_{\text{out}} = \mathcal{D}(\beta)_{\text{T}}\mathcal{D}(\gamma)_{\text{R}}\,|0\rangle = |\beta\rangle_{\text{T}}\,|\gamma\rangle_{\text{R}} \tag{2.4.17}$$

where $\beta = \mathcal{T}\alpha$ and $\gamma = \mathcal{R}\alpha$. The second-order correlation function of a coherent state is then found equal to 1 when the beam splitter is balanced.

$$g^{(2)}(0) = 1 \qquad \text{(coherent state)} \tag{2.4.18}$$

This same prediction would be made if a classical continuous-wave field was used instead of the quantum coherent state.

More in general, the $g^{(2)}$ function depends on τ (i.e. on the path lengths between the beam splitter and the detectors). In the case of a single photon, the $g^{(2)}$ function approaches 1 in the limit of large positive and negative delay and it features a dip with minimum at zero time delay. The width of the dip is determined by the coherence time of the field arriving at the input of the detectors.

When Fock states other than $|1\rangle$ are sent at the input of the beam splitter, $g^{(2)}(0)$ remains smaller than one, but it will increase following

$$g^{(2)}(0) = 1 - \frac{1}{n} \tag{2.4.19}$$

Therefore, in this case, the value at zero time-delay of the second-order wavefunction can be taken as a measure of the fidelity of the photon at the input of the interferometer with the single photon Fock state $|1\rangle$.

In essence, the importance of the Hanbury Brown and Twiss interferometer resides in its ability to measure the bunching properties of light.

2.5 Bipartite states

When the formalism of Quantum Mechanics was expanded to take into account the collective behaviour of more than one particle, its predictions were considered wild and surprising. In particular, as the Einstein-Podolsky-Rosen paradox [256] highlights, two distant particles can feature correlations that cannot be predicted classically.

This section introduces a formalism to describe the time and frequency correlations of two photon pair states in terms of continuous-mode operators introduced in Paragraph 2.2.3. Then, the time-energy entanglement is introduced and discussed, followed by the description of the Franson interferometer, an instrument that can be used to test whether two photons are time-energy entangled.

2.5.1 The biphoton wavefunction

Building on the formalism that described the frequency and time dependences of ladder operators, here we introduce the quantum description of a photon-pair state, whose correlations have no equivalent classical analogue. In this section we will only describe the formalism for photons traveling in distinct modes, as this is the case encountered in the following chapters of the thesis.

The definition of the two-photon wavepacket is the following:

$$|1_a, 1_b\rangle = \hat{P}^{\dagger}_{a,b}\,|0\rangle = \int_{-\infty}^{\infty}\int_{-\infty}^{\infty} \beta(\omega,\omega')\hat{a}^{\dagger}(\omega)\hat{b}^{\dagger}(\omega')\,d\omega\,d\omega'\,|0\rangle \tag{2.5.1}$$

where $\hat{a}^\dagger(\omega)$ and $\hat{b}^\dagger(\omega)$ are the (commuting) creation operators that generate a field at frequency ω on two different modes labeled a and b, while the so-called *biphoton creation operator* $\hat{P}^\dagger_{a,b}$ creates the biphoton state. The complex function $\beta(\omega,\omega')$ is the *biphoton wavefunction*, and it can be interpreted as the function that describes which are the frequency components of the biphoton state. Given the basis modes a and b, the biphoton wavefunction keeps track of all the information needed to describe the state and the correlations between the two photons. The wavepacket has to be normalized, from which it follows that the biphoton wavefunction has to be normalized, as well:

$$\int_{-\infty}^{\infty}\int_{-\infty}^{\infty} |\beta(\omega,\omega')|^2 \, d\omega \, d\omega' = 1 \tag{2.5.2}$$

and the relation is analogous to eq. (2.2.50).

The biphoton wavepacket can also be defined in terms of time coordinates as

$$|1_a, 1_b\rangle = \int_{-\infty}^{\infty}\int_{-\infty}^{\infty} \beta(t,t')\hat{a}^\dagger(t)\hat{b}^\dagger(t') \, dt \, dt' \, |0\rangle \tag{2.5.3}$$

where $\hat{a}^\dagger(t)$ and $\hat{b}^\dagger(t)$ are the commuting creation operators that generate a field at time t, and where $\beta(t,t')$ is still normalized, according to

$$\int_{-\infty}^{\infty}\int_{-\infty}^{\infty} |\beta(t,t')|^2 \, dt \, dt' = 1 \tag{2.5.4}$$

Just like for the creation operators themselves, the Fourier transform can be used to obtain with a good approximation the time representation of the biphoton wavefunction from its frequency representation and vice versa. In particular, we may write

$$\beta(t,t') = \frac{1}{2\pi}\int_{-\infty}^{\infty}\int_{-\infty}^{\infty} \beta(\omega,\omega')e^{-i(\omega t+\omega' t')} \, d\omega \, d\omega' \tag{2.5.5}$$

so that

$$|1_a, 1_b\rangle = \int_{-\infty}^{\infty}\int_{-\infty}^{\infty} \beta(t,t')\hat{a}^\dagger(t)\hat{b}^\dagger(t') \, dt \, dt' \, |0\rangle \tag{2.5.6}$$

From the properties of continuous-mode operators, in particular the commutation relation $[\hat{a}(t), \hat{a}^\dagger(t')] = \delta(t-t')$, it is also possible to derive the mean photon fluxes for the single a or b modes in terms of the marginal density of the biphoton wavefunction:

$$\begin{aligned} f_a(t) &= \langle \hat{a}^\dagger(t)\hat{a}(t)\rangle = \int |\beta(t,t')|^2\, dt' \\ f_b(t) &= \langle \hat{b}^\dagger(t)\hat{b}(t)\rangle = \int |\beta(t',t)|^2\, dt' \end{aligned} \tag{2.5.7}$$

The use of these expression is particularly useful when one derives an expression for the second-order correlation function in the case of two-photon states. In fact, the cross-correlation function between the fields a and b becomes equal to

$$g^{(2)}_{a,b}(t_1,t_2) = \frac{|\beta(t_1,t_2)|^2}{f_a(t_1)\, f_b(t_2)} \tag{2.5.8}$$

Instead, the autocorrelation functions for either beam a or b produces a zero output irrespective of the values of t_1 and t_2, as expected for a state that is defined to have exactly one photon for each of the beams:

$$g^{(2)}_{a,a}(t_1,t_2) = g^{(2)}_{b,b}(t_1,t_2) = 0 \tag{2.5.9}$$

The squared absolute value of the biphoton wavefunction is a quantity of particular experimental significance, and it is called *Joint Spectral Density* (JSD)

$$J(\omega,\omega') := |\beta(\omega,\omega')|^2 \tag{2.5.10}$$

The JSD is easier to measure with respect to the biphoton wavefunction. In fact, in order to obtain the true biphoton wavefunction, the experiment has to be able to distinguish the phase of the photons under analysis, while the measurement of the JSD only involves intensities or, equivalently, photon rates. In fact, it can be considered the extension to the two-photon state of eqs. (2.2.54) and (2.2.55) because

$$J(\omega,\omega') = \langle \hat{a}^\dagger(\omega_1)\hat{a}(\omega_1)\hat{b}^\dagger(\omega_2)\hat{b}(\omega_2)\rangle \tag{2.5.11}$$

This can be exemplified when one considers what happens when the biphoton wavepacket is filtered before detection. Suppose that R_0 is the rate at which photon pair states are produced. When the photons a and b are sent to ideal single photon detectors the coincidence rate will be R_0. Now, suppose that two filters centered at ω_1 and ω_2 and with $\delta\omega$ resolution are placed before the single photon detectors that collect photons a and b. The total photon rate R_1 that reaches the detectors, given by

$$R_{1,\delta\omega}(\omega_1,\omega_2) = R_0 \int_{\omega_1-\delta\omega/2}^{\omega_1+\delta\omega/2} \int_{\omega_2-\delta\omega/2}^{\omega_2+\delta\omega/2} J(\omega,\omega')\, d\omega\, d\omega' \tag{2.5.12}$$

will be smaller than the original one. However, if the resolution $\delta\omega$ of the experiment is much better than the fine details of the biphoton wavefunction, the photon rate $R_{1,\delta\omega}(\omega_1,\omega_2)$ will approximately give the intensity of the biphoton wavefunction at the point (ω_1,ω_2):

$$J(\omega_1,\omega_2) \simeq \frac{R_{1,\delta\omega}(\omega_1,\omega_2)}{(\delta\omega)^2\, R_0} \tag{2.5.13}$$

The issue with this approach is that to have high enough resolutions, the frequency filtering has to be highly selective, and this reduces dramatically the pair rates that are detected past the filtering stage. The acquisition times to obtain a complete JSD become rapidly unfeasible as the resolution is increased.

A workaround to easily obtain the (complete) biphoton wavefunction exists when the photon pair is produced by a nonlinear parametric process, such as in the case of Spontaneous Parametric Down-Conversion or Spontaneous Four-Wave Mixing, for which the biphoton wavefunction for the spontaneous nonlinear process is obtained in terms of the efficiency of the corresponding stimulated nonlinear process. This approach, called Stimulated Emission Tomography, is described in more detail in reference [257].

2.5.2 Time-energy entanglement

The biphoton wavefunction plays a key role in describing the correlations present between the two photons of the pair, as evident, for instance, in equation (2.5.8).

Indeed, the shape of the biphoton wavefunction determines whether or not two photons are considered entangled. In particular, in this section we will give the definition of time-energy entanglement and we will give the definition of Schmidt number, a figure of merit typically used to quantify the degree of entanglement that exists between two photons.

Time-energy entanglement can be considered the extension to the continuous domain of time-bin entanglement [23], already discussed in Section 1.2, where a superposition of well-separated time bins is replaced with a superposition of a continuum of time modes.

Time-energy entanglement

Time-energy entanglement occurs when two photons have a well-determined value of their total energy, but an undetermined value of the individual energies. If this is the case, the measurement of the energy of one photon implies perfect knowledge of the energy of the other photon. The ideal time-energy entangled state is described by the following expression

$$|\psi\rangle = \int_{-\infty}^{\infty} f(\omega)\hat{a}^{\dagger}(\omega_0+\omega)\hat{b}^{\dagger}(\omega_0-\omega)\,d\omega\,|0\rangle \tag{2.5.14}$$

where $\int_{-\infty}^{\infty}|f(\omega)|^2 d\omega = 1$. Equivalently, the state can be expressed more explicitly in terms of the biphoton wavefunction as

$$|\psi\rangle = \int_{-\infty}^{\infty}\int_{-\infty}^{\infty} f(\omega_1-\omega_2)\delta(\omega_{\mathrm{tot}}-(\omega_1+\omega_2))\,\hat{a}^{\dagger}(\omega_1)\hat{b}^{\dagger}(\omega_2)\,d\omega_1\,d\omega_2\,|0\rangle \tag{2.5.15}$$

More in general, the value of the total energy $\hbar\omega_{\mathrm{tot}}$ will possess a given degree of uncertainty so that the delta function of the previous equation will be replaced by a function with a non-infinitesimal domain, as in the following example

$$\beta(\omega_1,\omega_2) = \frac{1}{\sqrt{2\pi\sigma_+\sigma_-}}\exp\left(-\frac{(\omega_1+\omega_2-2\omega_0)^2}{4\sigma_+^2}\right)\exp\left(-\frac{(\omega_2-\omega_1)^2}{4\sigma_-^2}\right) \tag{2.5.16}$$

where we assume that the uncertainty on the total energy σ_+ is much smaller than the uncertainty on the photons' individual energies σ_-. When looking at the representation of this state, as in Figure 2.9, it is now evident that there are strong correlations between the frequencies of the photons: if one of the photons is found to have energy ω_a, then the other will be found in a small range of frequencies $\Delta\omega$ around $2\omega_0-\omega_a$.

As the name suggests, time-energy entanglement possesses time-correlations as well as energy correlations. This is seen by taking the Fourier transform, eq. (2.5.5), of the biphoton wavefunction (2.5.16), that produces the following expression:

$$\begin{aligned}\beta(t_1,t_2) &= \mathcal{F}\{\beta(\omega_1,\omega_2)\} = \\ &= \frac{1}{\sqrt{2\pi\tau_+\tau_-}}\exp\left(-i\omega_0(t_1+t_2)-\frac{(t_1+t_2)^2}{2\tau_+^2}-\frac{(t_2-t_1)^2}{2\tau_-^2}\right)\end{aligned} \tag{2.5.17}$$

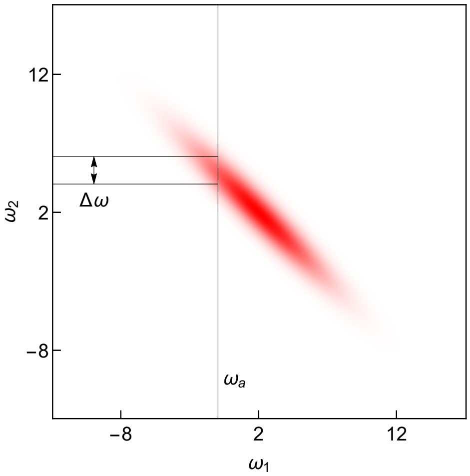

Figure 2.9: Frequency representation of a time-energy entangled biphoton state. The picture shows the real part of eq. (2.5.16), with $\omega_0 = 2$, $\sigma_+ = 1/2$ and $\sigma_- = 3$.

where $\tau_\pm = 2/\sigma_\pm$. This wavefunction is depicted in Figure 2.10. Small uncertainty in frequencies become large uncertainties in time and vice versa and the times of arrival of the two photons are strongly correlated: although the arrival time of the single photon is not perfectly determined, the second photon always arrives within a short time interval around the detection time of the first one.

Time-energy entanglement is lost when the knowledge of the frequency of one photon does not convey any information on the other photon. This is the case when the biphoton wavefunction can be factorized into the product of functions for the two different modes

$$\beta(\omega_1, \omega_2) = \gamma_a(\omega_1)\,\gamma_b(\omega_2) \tag{2.5.18}$$

For example, eq. (2.5.16) becomes factorisable when the uncertainties σ_+ and σ_- become equal.

An example of such a factorized state is depicted in Figure 2.11. No frequency correlations are present between the two photons. Regarding the time dependent wavefunction, the Fourier transform of the factorized state is the product of the Fourier transforms of the individual γ_i functions and

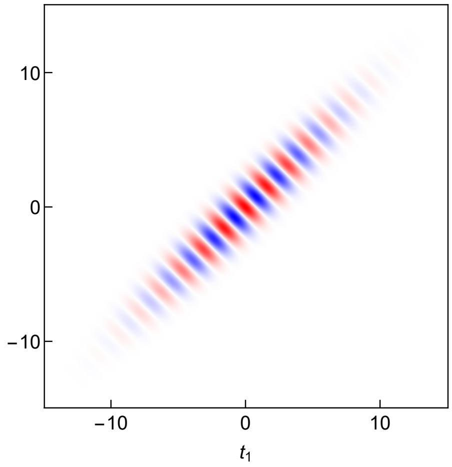

Figure 2.10: Time representation of a time-energy entangled biphoton state. The picture shows the real part of eq. (2.5.17), with $\omega_0 = 2$, $\tau_+ = 4$ and $\tau_- = 2/3$.

hence no time-correlations are present, either (Figure 2.12).

$$\beta(t_1, t_2) = \gamma_a(t_1)\,\gamma_b(t_2), \qquad \gamma_i(t) = \frac{1}{2\pi}\int \gamma_i(\omega_i)e^{-i\omega t}\,d\omega \tag{2.5.19}$$

Schmidt decomposition

Although an infinite number of frequency (or time) modes are involved in the energy-time entangled state, the degree of entanglement is limited. Here we introduce a way to quantify the degree of entanglement of such state: the Schmidt number.

It is well known that the degree of purity of a quantum mixture can be obtained in terms of the coefficients of the expansion of the density operator $\hat{\rho}$ over a basis of pure states $\{|\psi_n\rangle\langle\psi_n|\}$. If

$$\hat{\rho} = \sum_n p_n\,|\psi_n\rangle\langle\psi_n|\,, \tag{2.5.20}$$

the purity of the mixture is defined as the trace of the squared density operator:

$$P = \mathrm{Tr}\,\hat{\rho}^2 = \sum_n \langle\psi_n|\,\hat{\rho}^2\,|\psi_n\rangle = \sum_n p_n^2 \tag{2.5.21}$$

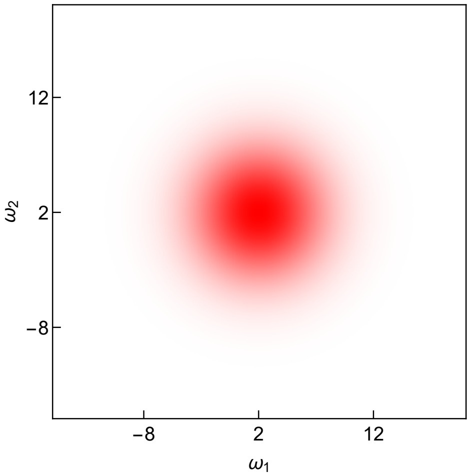

Figure 2.11: Frequency representation of a factorized biphoton state. The picture shows the real part of eq. (2.5.16), with $\omega_0 = 2$, $\sigma_+ = \sqrt{2}$ and $\sigma_- = \sqrt{2}$.

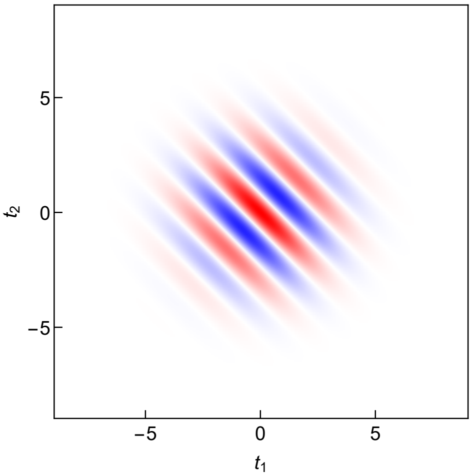

Figure 2.12: Time representation of a factorized biphoton state. The picture shows the real part of eq. (2.5.17), with $\omega_0 = 2$, $\tau_+ = \sqrt{2}$ and $\tau_- = \sqrt{2}$.

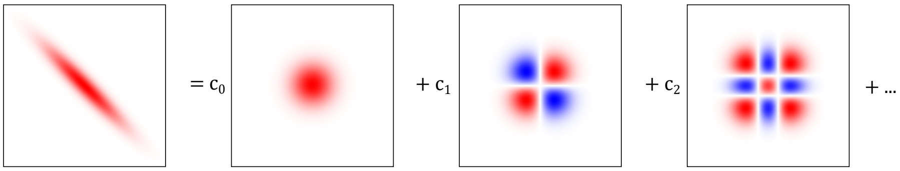

Figure 2.13: Example of Schmidt decomposition. The modes on the right are all factorized. The biphoton wavefunction on the left has Schmidt number $S = 3.08$.

and the purity does not depend on the chosen basis for the expansion since the trace operation is invariant under unitary transformations. A similar procedure can be exploited to define the degree of entanglement of a biphoton wavepacket, that is based on the Schmidt decomposition of the biphoton wavefunction [258, 259].

Let us consider a biphoton wavefunction of two frequencies $\beta(\omega_1, \omega_2)$. It is always possible to decompose such a function into a superposition of factorisable functions of variables ω_1 and ω_2:

$$\beta(\omega_1, \omega_2) = \sum_n c_n \mu_n(\omega_1) \nu_n(\omega_2) \tag{2.5.22}$$

where the two sets $\{\mu_n\}$ and $\{\nu_n\}$ are orthonormal bases of the a and b modes' Hilbert spaces and where $|c_n|^2$ is the probability to find a photon in the n-th factorized state. An example of such decomposition is pictured in Figure 2.13.

The bases can be found in term of the biphoton wavefunction itself as they are the solutions of the following integral equations:

$$\begin{aligned} \int K_1(\omega, \omega') \mu(\omega') \, d\omega' &= c_n^2 \mu(\omega) \\ \int K_2(\omega, \omega') \nu(\omega') \, d\omega' &= c_n^2 \nu(\omega) \end{aligned} \tag{2.5.23}$$

where the eigenvalues c_n^2 are a discrete set and K_1 and K_2 are obtained from $\beta(\omega_1, \omega_2)$:

$$\begin{aligned} K_1(\omega, \omega') &= \int \beta(\omega, \omega_2) \beta^*(\omega', \omega_2) \, d\omega_2 \\ K_2(\omega, \omega') &= \int \beta(\omega_1, \omega') \beta^*(\omega_1, \omega') \, d\omega_1 \end{aligned} \tag{2.5.24}$$

If the original β function is factorisable, then it is always possible to find a single pair of functions $(\mu(\omega_1), \nu(\omega_2))$ that factorizes β. In this case the decomposition is trivial and we have a single coefficient of the expansion different from zero:

$$\beta(\omega_1, \omega_2) = \mu(\omega_1)\nu(\omega_2) \tag{2.5.25}$$

If the biphoton wavefunction is not factorisable, a higher number of coefficients of the expansion will be different from zero. The Schmidt number is defined according to

$$S = \frac{1}{\sum_n c_n^4} \tag{2.5.26}$$

If a single mode is present in the expansion, S takes the smallest possible value of 1; as the weight of the higher modes of the decomposition increases, the denominator of S will become smaller and the Schmidt number will increase.

We also report another measure of the degree of entanglement that is often used, the entropy of entanglement:

$$E = -\sum_n c_n^2 \log_2 \left(c_n^2\right) \tag{2.5.27}$$

The same decomposition procedure can be performed for the time-dependent biphoton wavefunction $\beta(t_1, t_2)$; the time and frequency biphoton wavefunctions are Fourier transform of each other, and it can be demonstrated that the coefficients of the expansions are the same for the two functions:

$$\beta(\omega_1, \omega_2) = \sum_n c_n \mu_n(\omega_1)\nu_n(\omega_2) \Longleftrightarrow \beta(t_1, t_2) = \sum_n c_n \mu_n(t_1)\nu_n(t_2) \tag{2.5.28}$$

where $\mu_n(\omega)$ and $\mu_n(t)$ are Fourier transforms of each other, as well as $\nu_n(\omega)$ and $\nu_n(t)$.

Purity of marginal biphoton states

Many quantum experiments require that quantum interference phenomena between different photons, such as the Hong Ou Mandel effect [162], are perfectly visible. This implies that the photons produced by different sources have to be mutually indistinguishable.

Heralded single photon sources operate by emitting pairs of photons and by detecting one of the two photons to herald the presence of the other one. In order to produce indistinguishable photons, however, no correlation has to be present in the biphoton state before the heralding measurement is performed. In fact, as described with the formalism of the density operator, the state resulting from the detection measurement is equal to the marginal state of the global density operator. If the initial biphoton state is correlated, the resulting marginal state will be mixed. Using the Schmidt decomposition, the discussion on the purity of multipartite states of Section 1.1 can be expanded to the continuous variables case discussed here.

From the definition of the biphoton wavefunction (2.5.1) and from the Schmidt decomposition of the biphoton wavefunction (2.5.22), we may write

$$|\psi\rangle = \sum_n c_n \, |\mu_n\rangle |\nu_n\rangle \tag{2.5.29}$$

where

$$|\mu_n\rangle = \int \mu_m(\omega) \hat{a}^\dagger(\omega) \, d\omega \, |0\rangle \, , \quad |\nu_n\rangle = \int \nu_m(\omega) \hat{b}^\dagger(\omega) \, d\omega \, |0\rangle \tag{2.5.30}$$

Then, the density operator associated to $|\psi\rangle$ is given by

$$\hat{\rho} = |\psi\rangle\langle\psi| = \sum_{n,m} c_n^* c_m \, |\mu_n\rangle |\nu_n\rangle \langle\mu_m| \langle\nu_m| \tag{2.5.31}$$

The marginal states $\hat{\rho}_A$ and $\hat{\rho}_B$ are given in terms of the partial traces of the density operator $\hat{\rho}$. Since $\{|\mu_n\rangle\}$ and $\{|\nu_n\rangle\}$ are orthonormal bases of the individual photons' Hilbert spaces, we may write

$$\hat{\rho}_A = \mathrm{Tr}_B\{\hat{\rho}\} = \sum_l \langle\nu_l| \left(\sum_{m,n} c_m^* c_n \, |\mu_n\rangle |\nu_n\rangle \langle\mu_m| \langle\nu_m| \right) |\nu_l\rangle = \sum_n |c_n|^2 \, |\mu_n\rangle\langle\mu_n| \tag{2.5.32}$$

and analogously

$$\hat{\rho}_B = \mathrm{Tr}_A\{\hat{\rho}\} = \sum_n |c_n|^2 \, |\nu_n\rangle\langle\nu_n| \tag{2.5.33}$$

The two marginal states $\hat{\rho}_A$ and $\hat{\rho}_B$ are therefore *mixtures* unless only a single coefficient c_n is different from zero, that is, only if the original biphoton wavefunction is factorized.

If two such mixtures are made to interfere at a beam splitter, the visibility of the resulting Hong Ou Mandel dip is reduced, since photons on one given frequency mode from the first source may interfere with photons on a different frequency mode from the second source.

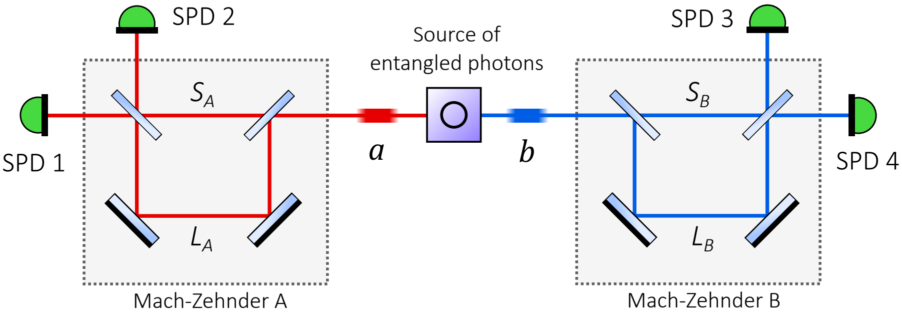

Figure 2.14: The Franson interferometer. The two photons emerging from a source of time-energy entangled photon pars are sent individually to different Mach-Zehnders interferometers. The Mach-Zehnders are unbalanced and as the lengths of the arms are changed, the biphoton state exhibits nonlocal behaviour.

2.5.3 The Franson interferometer

Time-energy entanglement was first proposed by Franson in ref. [260]. There, he also proposed an instrument capable of detecting the nonlocal properties of time-energy entangled states, and he demonstrated that these states cannot be described with hidden-variables theories, violating an appropriate Bell inequality.

The Franson interferometer, depicted in Figure 2.14, is composed of two Mach-Zehnder interferometers through which each of the photons of the pair travels. If the coherence length of the individual photons is much shorter than the unbalance of the interferometer, they will not experience interference at the output beam splitter, and a superposition state of the photon travelling at different times will be produced, analogously to the time-bin qubit state described in Section 1.1; the superposition is actually coherent as long as the coherence of the global wavefunction is longer than the interferometers.

When coincidence measurements are performed on the photons that travelled through the interferometer, three outcomes are possible, represented by three equally spaced coincidence peaks as a function of the relative delay: the central peak corresponds to the cases in which the photons both travel through the short or long path of their respective interferometer, while the lateral ones correspond to the cases in which the photons take different paths.

Since the absolute time of emission of the pair is unknown, the two cases corresponding to the central peak are indistinguishable and they exhibit nonlocal quantum interference effects, which depend on the *sum* of the phases of the distant interferometers.

This scenario is analogous to EPR experiments [99, 256], where the time-bin degree of freedom takes the place of polarization and where the phases of the interferometers take the role of the angles of the polarizers used to analyze the nonlocal state. As such, the modulated central peak produces a nonlocal interference fringe analogous to the Bell fringe of EPR experiments, violating any local hidden-variable theory.

In the original proposal by Franson, time-energy entangled photons are produced by an atomic cascade. The two photons are emitted by the subsequent decay of an electron from an excited level to an intermediate metastable level, and then to the ground state. The lifetime of the metastable level is assumed to be much shorter than the lifetime of the excited level. As a consequence, although the emission time of both the photons has large uncertainty, comparable to the lifetime of the excited level, the second photon will be emitted within a short time interval of the first, ensuring a strong positive correlation on the emission time of the two photons of the pair. By the same token, the energy uncertainty of the metastable level will be much larger than the one of the ground and excited states: the total energy of the pair will be well defined, while the individual energies of the photons will be uncertain and anti-correlated. These features are at the core of time-energy entanglement, as was discussed in the previous Paragraph 2.5.2.

Analogous correlations are produced, for instance, when the photon pair is emitted by Spontaneous Four-Wave Mixing from microring resonators pumped with a continuous wave laser: the total energy is well defined by the total energy of the two annihilated pump photons, while the individual energies of the signal and idler photons are uncertain due to the width of the ring resonances.

In this section we will use the formalism of ladder operators introduced in the previous sections of the chapter to describe the behaviour of a pair of time-energy entangled photon pairs as it travels through the Franson interferometer. We will first describe the evolution of the ladder operators through the interferometers, followed by the description of the evolution of the full biphoton wavepacket. Then we will discuss how the biphoton wavefunction is analyzed in terms of relative time of arrival of the photons, and finally we will consider the nonlocal interference effects and the requirements for their observation.

Evolution of creation operators

Consider the scheme of the Franson interferometer shown in Figure 2.14. A pair of unbalanced Mach-Zehnder interferometers (MZI) is used to analyze the biphoton state produced by a source of time-energy entangled photons. Each of the photons of the source, that we will label with a and b, is sent individually to the two interferometers. The MZIs, labeled A and B, are unbalanced and we call S_A, L_A, S_B and L_B the short and long paths of MZI A and B respectively.

As it was shown in the previous section, the two photon state can be described in terms of the biphoton wavefunction $\beta(t_1, t_2)$ and, in the case of time-energy entanglement, the wavefunction is wider in the $t_1 + t_2$ direction than in the $t_2 - t_1$ direction; assuming eq (2.5.17) as the expression for the time-energy entangled photons, we impose $\tau_+ > \tau_-$.

The effect of each MZI can be modeled, irrespectively of the shape of $\beta(t_1, t_2)$, by considering the evolution of the creation operators $\hat{a}^\dagger(t)$ and $\hat{b}^\dagger(t)$. Once we know the new form of these operators past the interferometers, it will be possibile to understand how the biphoton state is evolved.

Consider MZI A. The lengths of the short and long arms are L_A and S_A and we assume that both the beam splitters have $\mathcal{R}_A$ and $\mathcal{T}_A$ coefficients. We first apply the unitary transformations of each component of the Mach-Zehnder to $\hat{a}^\dagger$. The beam splitter is modeled by equation (2.4.5) and we get

$$\mathcal{U}_{\text{bs,A}}\hat{a}^\dagger(t) = \mathcal{T}_A\hat{a}^\dagger_S(t) + \mathcal{R}_A\hat{a}^\dagger_L(t) \tag{2.5.34}$$

where indexes S and L indicate the short and long paths of the interferometer respectively. Then, we consider the propagation along the two arms

$$\begin{aligned} \mathcal{U}_{\text{prop}}(S_A)\hat{a}^\dagger_L(t) &= \hat{a}^\dagger_L(t + t_{S,A}), \quad t_{S,A} = \frac{S_A}{c} \\ \mathcal{U}_{\text{prop}}(L_A)\hat{a}^\dagger_S(t) &= \hat{a}^\dagger_S(t + t_{L,A}), \quad t_{L,A} = \frac{L_A}{c} \end{aligned} \tag{2.5.35}$$

and finally we have the effect of the second beam splitter:

$$\begin{aligned} \mathcal{U}_{\text{bs}}\hat{a}^\dagger_L(t + t_{S,1}) &= \mathcal{T}_A\hat{a}^\dagger_1(t + t_{S,1}) + \mathcal{R}_A\hat{a}^\dagger_2(t + t_{S,1}) \\ \mathcal{U}_{\text{bs}}\hat{a}^\dagger_L(t + t_{L,1}) &= \mathcal{T}_A\hat{a}^\dagger_2(t + t_{L,1}) + \mathcal{R}_A\hat{a}^\dagger_2(t + t_{S,1}) \end{aligned} \tag{2.5.36}$$

where indexes 1 and 2 indicate the two output ports of the MZI. The effect of the whole MZI is obtained combining the previous expressions:

$$\begin{aligned}\mathcal{U}_{\mathrm{MZI},A}(S_A,L_A)\hat{a}^\dagger(t) = \mathcal{T}_A^2\hat{a}_1^\dagger(t+t_{S,A}) + \mathcal{R}_A^2\hat{a}_1^\dagger(t+t_{L,A}) + \\ + \mathcal{R}_A\mathcal{T}_A\hat{a}_2^\dagger(t+t_{S,A}) + \mathcal{R}_A\mathcal{T}_A\hat{a}_2^\dagger(t+t_{L,A})\end{aligned} \tag{2.5.37}$$

Of course, MZI A has no effect on $\hat{b}^\dagger(t)$:

$$\mathcal{U}_{\mathrm{MZI},A}(S_A,L_A)\hat{b}^\dagger(t) = \hat{b}^\dagger(t) \tag{2.5.38}$$

The second MZI has an analogous effect on $\hat{b}^\dagger(t)$ as MZI A has on $\hat{a}^\dagger(t)$:

$$\begin{aligned}\mathcal{U}_{\mathrm{MZI},B}(S_B,L_B)\hat{b}^\dagger(t) = \mathcal{T}_B^2\hat{b}_3^\dagger(t+t_{S,B}) + \mathcal{R}_B^2\hat{b}_3^\dagger(t+t_{L,B}) + \\ + \mathcal{R}_B\mathcal{T}_B\hat{b}_4^\dagger(t+t_{S,B}) + \mathcal{R}_B\mathcal{T}_B\hat{b}_4^\dagger(t+t_{L,B})\end{aligned} \tag{2.5.39}$$

and again

$$\mathcal{U}_{\mathrm{MZI},B}(S_B,L_B)\hat{a}^\dagger(t) = \hat{a}^\dagger(t) \tag{2.5.40}$$

where indexes 3 and 4 indicate the output ports of MZI B, while $t_{S,B} = S_B/c$ and $t_{L,B} = L_B/c$.

Evolution of biphoton state

We can combine equations (2.5.37) to (2.5.40), to describe what happens to the complete biphoton wavepacket. The output state $|\psi_{\mathrm{out}}\rangle$ is obtained by applying the unitaries to the input state $|\psi_{\mathrm{in}}\rangle$ produced by the source of entangled photons:

$$|\psi_{\mathrm{out}}\rangle = \mathcal{U}_{\mathrm{MZI},A}(S_A,L_A)\mathcal{U}_{\mathrm{MZI},B}(S_B,L_B)\,|\psi_{\mathrm{in}}\rangle \tag{2.5.41}$$

with

$$|\psi_{\mathrm{in}}\rangle = \int\int \beta(t_1,t_2)\hat{a}^\dagger(t_1)\hat{b}^\dagger(t_2)\,dt_1\,dt_2\,|0\rangle \tag{2.5.42}$$

Due to the cross-products, we get a fairly long expression:

$$\begin{aligned}|\psi_{\mathrm{out}}\rangle &= \int\int \beta(t_1,t_2)(\hat{P}_{1,3}^\dagger + \hat{P}_{1,4}^\dagger + \hat{P}_{2,3}^\dagger + \hat{P}_{2,4}^\dagger)\,dt_1, dt_2\,|0\rangle \\ &= |\psi_{1,3}\rangle + |\psi_{1,4}\rangle + |\psi_{2,3}\rangle + |\psi_{2,4}\rangle\end{aligned} \tag{2.5.43}$$

where the four $\hat{P}^\dagger_{i,j}$ operators represent the terms involving ports i and j:

$$\begin{aligned}\hat{P}^\dagger_{1,3} = {} & \mathcal{T}_A^2\mathcal{T}_B^2\hat{a}_1^\dagger(t+t_{S,A})\hat{b}_3^\dagger(t+t_{S,B}) + \mathcal{R}_A^2\mathcal{R}_B^2\hat{a}_1^\dagger(t+t_{L,A})\hat{b}_3^\dagger(t+t_{L,B}) + \\ & + \mathcal{T}_A^2\mathcal{R}_B^2\hat{a}_1^\dagger(t+t_{S,A})\hat{b}_3^\dagger(t+t_{L,B}) + \mathcal{R}_A^2\mathcal{T}_B^2\hat{a}_1^\dagger(t+t_{L,A})\hat{b}_3^\dagger(t+t_{S,B})\end{aligned} \tag{2.5.44}$$

$$\begin{aligned}\hat{P}^\dagger_{1,4} = {} & \mathcal{T}_A^2\mathcal{T}_B\mathcal{R}_B\hat{a}_1^\dagger(t+t_{S,A})\hat{b}_4^\dagger(t+t_{S,B}) + \mathcal{R}_A^2\mathcal{T}_B\mathcal{R}_B\hat{a}_1^\dagger(t+t_{L,A})\hat{b}_4^\dagger(t+t_{L,B}) + \\ & + \mathcal{T}_A^2\mathcal{T}_B\mathcal{R}_B\hat{a}_1^\dagger(t+t_{S,A})\hat{b}_4^\dagger(t+t_{L,B}) + \mathcal{R}_A^2\mathcal{T}_B\mathcal{R}_B\hat{a}_1^\dagger(t+t_{L,A})\hat{b}_4^\dagger(t+t_{S,B})\end{aligned} \tag{2.5.45}$$

$$\begin{aligned}\hat{P}^\dagger_{2,3} = {} & \mathcal{T}_A\mathcal{R}_A\mathcal{T}_B^2\hat{a}_2^\dagger(t+t_{S,A})\hat{b}_3^\dagger(t+t_{S,B}) + \mathcal{T}_A\mathcal{R}_A\mathcal{R}_B^2\hat{a}_2^\dagger(t+t_{L,A})\hat{b}_3^\dagger(t+t_{L,B}) + \\ & + \mathcal{T}_A\mathcal{R}_A\mathcal{R}_B^2\hat{a}_2^\dagger(t+t_{S,A})\hat{b}_3^\dagger(t+t_{L,B}) + \mathcal{T}_A\mathcal{R}_A\mathcal{T}_B^2\hat{a}_2^\dagger(t+t_{L,A})\hat{b}_3^\dagger(t+t_{S,B})\end{aligned} \tag{2.5.46}$$

$$\begin{aligned}\hat{P}^\dagger_{2,4} = {} & \mathcal{T}_A\mathcal{R}_A\mathcal{T}_B\mathcal{R}_B\hat{a}_2^\dagger(t+t_{S,A})\hat{b}_4^\dagger(t+t_{S,B}) + \mathcal{T}_A\mathcal{R}_A\mathcal{T}_B\mathcal{R}_B\hat{a}_2^\dagger(t+t_{L,A})\hat{b}_4^\dagger(t+t_{L,B}) + \\ & + \mathcal{T}_A\mathcal{R}_A\mathcal{T}_B\mathcal{R}_B\hat{a}_2^\dagger(t+t_{S,A})\hat{b}_4^\dagger(t+t_{L,B}) + \mathcal{T}_A\mathcal{R}_A\mathcal{T}_B\mathcal{R}_B\hat{a}_2^\dagger(t+t_{L,A})\hat{b}_4^\dagger(t+t_{S,B})\end{aligned} \tag{2.5.47}$$

Let us consider only the first one of these expressions, eq. (2.5.44), i.e., let us look at light exiting from ports 1 and 3; the behaviour for the other combinations of ports is analogous. First of all, we can simplify the expression by assuming that all beam splitters are balanced ($\mathcal{T} = 1/\sqrt{2}$, $\mathcal{R} = i/\sqrt{2}$).

$$\begin{aligned}\hat{P}^\dagger_{1,3} = {} & \frac{1}{4}(\hat{a}_1^\dagger(t+t_{S,A})\hat{b}_3^\dagger(t+t_{S,B}) + \hat{a}_1^\dagger(t+t_{L,A})\hat{b}_3^\dagger(t+t_{L,B}) + \\ & - \hat{a}_1^\dagger(t+t_{S,A})\hat{b}_3^\dagger(t+t_{L,B}) - \hat{a}_1^\dagger(t+t_{L,A})\hat{b}_3^\dagger(t+t_{S,B}))\end{aligned} \tag{2.5.48}$$

and then, performing changes of variables inside the integral $\int\int \beta(t_1,t_2)\hat{P}_{1,3}dt_1, dt_2$ we can rewrite $|\psi_{1,3}\rangle$ as

$$\begin{gathered}|\psi_{1,3}\rangle = \frac{1}{4}\int\int(\beta(t_1-t_{S,A},t_2-t_{S,B}) + \beta(t_1-t_{S,A},t_2-t_{L,B}) + \\ -\beta(t_1-t_{L,A},t_2-t_{S,B}) - \beta(t_1-t_{L,A},t_2-t_{L,B}))\hat{a}_1^\dagger(t_1)\hat{b}_3^\dagger(t_2)\,dt_1dt_2\,|0\rangle\end{gathered} \tag{2.5.49}$$

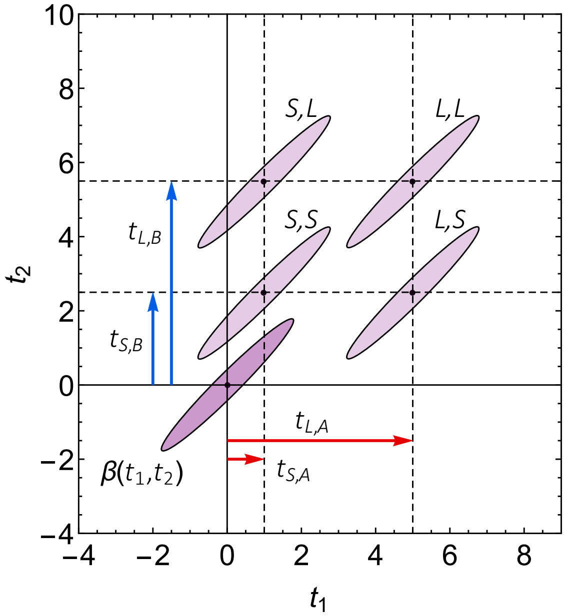

Figure 2.15: Effect of two interferometers on a biphoton wavefunction. The darker region represent the biphoton of time-energy entangled photons at the input of the interferometer, while the lighter regions represent the output wavefunction.

so that we can define a new biphoton wavefunction

$$\begin{aligned}\beta_{1,3}(t_1,t_2) &= \frac{1}{4}(\beta(t_1-t_{S,A},t_2-t_{S,B})+\beta(t_1-t_{S,A},t_2-t_{L,B})+\\ &\quad-\ \beta(t_1-t_{L,A},t_2-t_{S,B})-\beta(t_1-t_{L,A},t_2-t_{L,B}))\\ &= \frac{1}{4}(\beta_{S,S}(t_1,t_2)+\beta_{S,L}(t_1,t_2)-\beta_{L,S}(t_1,t_2)-\beta_{L,L}(t_1,t_2))\end{aligned} \tag{2.5.50}$$

The effect of eq. (2.5.49) is schematized in Figure 2.15: the original β wavefunction is split into four parts and it is translated in the (t_1,t_2) space by time intervals equal to the travelling time of the photons in the arms of the interferometer.

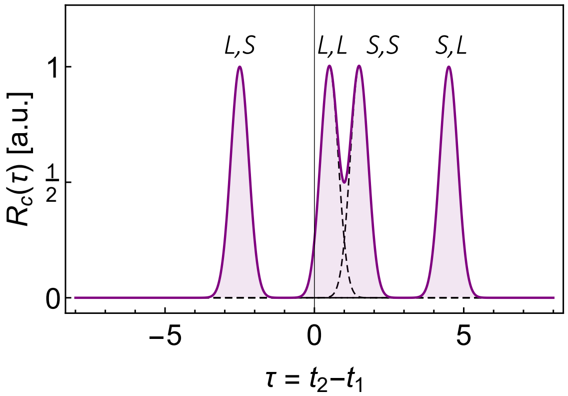

Figure 2.16: Coincidence rate as a function of time delay between detectors 1 and 3 if the biphoton function depicted in Figure 2.15 is produced by the Franson interferometer.

Delay measurements

In real experiments it is often the case that the absolute time of emission of the photon pair is unknown. In such cases it is possible to measure, instead, the relative time of arrival of photons a and b by looking, for instance, at the reaction times of detectors SPD 1 and 3 of Figure 2.14. Therefore, effectively, the experiment will detect the rate of coincidences R_c as a function of $t_2 - t_1$. Similarly to eq. (2.5.7), such rate is proportional to the marginal state of the biphoton wavefunction along the $t_1 + t_2$ direction. If we define $\tau = t_2 - t_1$ and $t_0 = (t_1 + t_2)/2$ we have

$$R_c(\tau) = R_0 \int \left| \beta(t_0 - \frac{\tau}{2}, t_0 + \frac{\tau}{2}) \right|^2 dt_0 \tag{2.5.51}$$

where R_0 is the rate of emission of pairs by the source.

The result of such a measurement for the biphoton state depicted in Figure 2.15 is presented in Figure 2.16, where it is assumed that the four parts of the biphoton wavefunction have a gaussian envelope and that their overlap is negligible.

Nonlocal effects

So far we did not see any nonlocal effect because we assumed that the overlap between the different parts of the biphoton wavefunction is negligible. We now assume that the unbalance of the two interferometers is the same but for a small quantity for each of them, so that we can define the unbalance times as

$$\begin{aligned} \Delta t_A &= t_{A,L} - t_{A,S} = \Delta t + \delta t_A, \quad \delta t_A \ll \Delta t_A \\ \Delta t_B &= t_{B,L} - t_{B,S} = \Delta t + \delta t_B, \quad \delta t_B \ll \Delta t_B \end{aligned} \tag{2.5.52}$$

We assume that the total time it takes light to travel in the interferometer is much larger than the width of the biphoton wavefunction in the $t_1 + t_2$ direction (i.e. $\tau_+ \gg t_{i,L}$, with $i = A, B$); at the same time we assume that the width of the wavefunction along $t_2 - t_1$ is much smaller than the unbalance time of the interferometers (i.e. $\tau_- \ll \Delta t_i$). These two requirements are equivalent to imposing that the coherence length of the single photons is much smaller than the unbalance $(L_i - S_i)$ and that the coherence length of the whole wavepacket is much larger than the dimension of each interferometer (L_i). When parametric processes are the sources of the biphoton wavepacket, the last requirement corresponds to the coherence length of the pump beam being much longer than the length of the MZIs.

Under these assumptions the biphoton wavefunction $\beta_{1,3}$ is better described by Figure 2.17: there is now an almost complete overlap between $\beta_{S,S}$ and $\beta_{L,L}$. We can now write

$$\begin{aligned} \beta_{S,S}(t_1, t_2) &= \beta(t_1, t_2) \\ \beta_{S,L}(t_1, t_2) &= \beta(t_1, t_2 - \Delta t - \delta t_B) \\ \beta_{L,S}(t_1, t_2) &= \beta(t_1 - \Delta t - \delta t_A, t_2) \\ \beta_{L,L}(t_1, t_2) &= \beta(t_1 - \Delta t - \delta t_A, t_2 - \Delta t - \delta t_B) \end{aligned} \tag{2.5.53}$$

where we implicitly assumed, without loss of generality, that $t_{S,A} = t_{S,B} = 0$. The key point to understand the Franson interferometer follows by realizing that, approximately, the following relation holds

$$\beta_{L,L}(t_1, t_2) \simeq e^{-i\omega\Delta t} e^{-i\omega(\delta t_A + \delta t_B)} \beta_{S,S}(t_1, t_2) \tag{2.5.54}$$

In fact, after replacing $i\omega\delta t_{A/B}$ with $\phi_{A/B}$ we have

$$|\psi_{1,3}\rangle = \frac{1}{4}\Big(|\psi_{S,L}\rangle + |\psi_{L,S}\rangle + e^{-i\omega\Delta t} \int\!\!\int \beta(t_1, t_2)(1 + e^{-i(\phi_A + \phi_B)}) \hat{a}^\dagger(t_1) \hat{b}^\dagger(t_2) \Big) |0\rangle \tag{2.5.55}$$

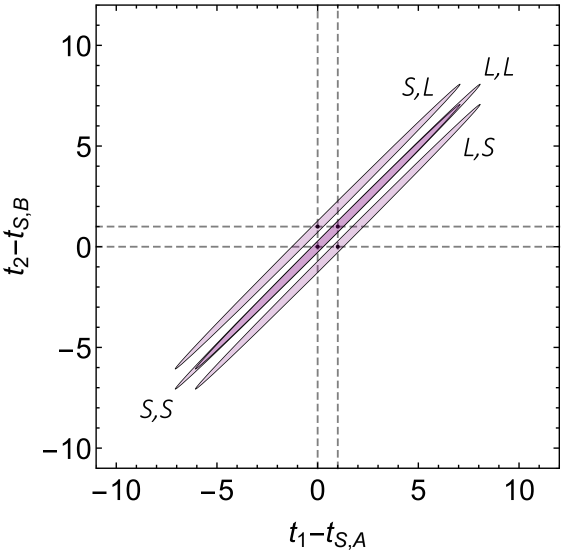

Figure 2.17: Effect of a Franson interferometer on a biphoton wavefunction. The darker region represent the biphoton of time-energy entangled photons at the input of the interferometer, while the lighter regions represent the output wavefunction.

and we see that the central part of the wavepacket is a superposition of two β functions that depend on the configuration of *both* the interferometers (i.e. $\phi_A + \phi_B$). In particular, we have that

$$|\beta_{1,3}(t_1,t_2)|^2 = \frac{1}{16}(|\beta_{S,L}(t_1,t_2)|^2 + |\beta_{L,S}(t_1,t_2)|^2) + \\ + \frac{1}{4}|\beta_{S,S}(t_1,t_2)|^2 \cos^2\left(\frac{\phi_A+\phi_B}{2}\right) \tag{2.5.56}$$

When considering the coincidence rates as a function of time delay $R(\tau)$, we see from eqs. (2.5.51) and (2.5.56) that the experimental setup will see three equally spaced peaks: the central one corresponds to wavefunctions S, S and L, L; the two lateral ones correspond to S, L and L, S. The intensity of the central peak R_c will vary cosinusoidally with $\phi_A + \phi_B$ between zero and four times the intensity of the lateral peak, forming an interference fringe described by

$$R_c(\phi_A+\phi_B) = \frac{1}{4}R_0 \cos^2\left(\frac{\phi_A+\phi_B}{2}\right) \tag{2.5.57}$$

The two extremes of this oscillations are shown in Figure 2.18.

Since eq. (2.5.57) has the same form of the fringe obtained for Bell-type experiments that involve polarization entanglement, it cannot be explained with local hidden-variable theories, in agreement with the Bell theorem [99]. In particular, the Bell inequality is violated when the visibility of the fringe exceeds $1/\sqrt{2} \simeq 0.707$.

As a final comment, one can notice that when the $\phi_A + \phi_B$ is such that the central peak vanishes, whenever the a photon takes the long path, the b photon takes the short path and vice versa, a clear signature of entanglement.

2.6 Dielectric waveguides

Here we give an overview of the modal theory of light travelling in dielectric wire waveguides. In particular, we consider how the discrete spectrum of modes of a lossless dielectric waveguide results from an eigenvalue problem, and how the symmetry of the structure gives rise to mode classification.

In Section 2.7, the theory is further expanded to describe one-dimensional periodic structures.

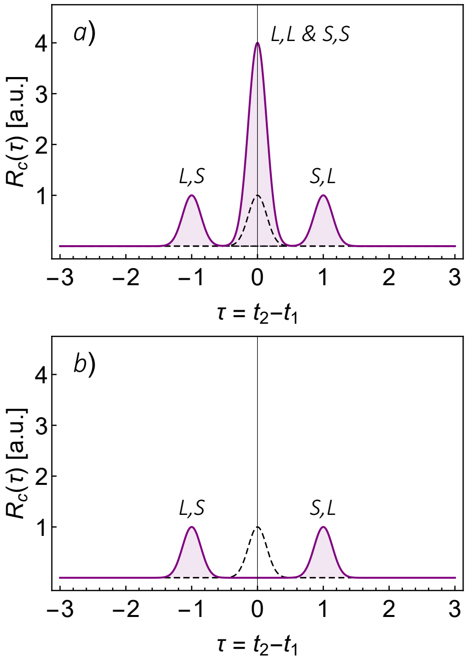

Figure 2.18: Coincidence rate as a function of time delay between detectors 1 and 3 if the biphoton function depicted in Figure 2.17 is produced by the Franson interferometer. a) Constructive interference between $\beta_{S,S}$ and $\beta_{L,L}$. b) Destructive interference between $\beta_{S,S}$ and $\beta_{L,L}$.

2.6.1 Confinement and eigenmodes

The (relative) dielectric function $\epsilon(\boldsymbol{r})$ of a generic linear lossless dielectric medium is real in all space. Under this assumption, and from the linearity of Maxwell's equations, the generic space and time dependent electromagnetic fields can be replaced with fields oscillating at a single frequency ω

$$\begin{cases} \boldsymbol{E}(\boldsymbol{r},t) \\ \boldsymbol{D}(\boldsymbol{r},t) \\ \boldsymbol{B}(\boldsymbol{r},t) \\ \boldsymbol{H}(\boldsymbol{r},t) \end{cases} \longrightarrow \begin{cases} \boldsymbol{E}(\boldsymbol{r})e^{-i\omega t} \\ \boldsymbol{D}(\boldsymbol{r})e^{-i\omega t} \\ \boldsymbol{B}(\boldsymbol{r})e^{-i\omega t} \\ \boldsymbol{H}(\boldsymbol{r})e^{-i\omega t} \end{cases} \tag{2.6.1}$$

In this picture, $\boldsymbol{D}$ and $\boldsymbol{H}$ are the displacement and magnetizing fields, introduced to take into account the effect of propagation of light in a dielectric medium. The generic solution to the Maxwell problem will be given by a linear superposition of modes at different frequencies, hence Maxwell's equations are transformed as well

$$\begin{cases} \boldsymbol{\nabla}\cdot\boldsymbol{B}(\boldsymbol{r},t) = 0 \\ \boldsymbol{\nabla}\cdot\boldsymbol{D}(\boldsymbol{r},t) = 0 \\ \boldsymbol{\nabla}\times\boldsymbol{E}(\boldsymbol{r},t) + \frac{\partial \boldsymbol{B}(\boldsymbol{r},t)}{\partial t} = 0 \\ \boldsymbol{\nabla}\times\boldsymbol{B}(\boldsymbol{r},t) - \frac{\partial \boldsymbol{D}(\boldsymbol{r},t)}{\partial t} = 0 \end{cases} \longrightarrow \begin{cases} \boldsymbol{\nabla}\cdot\boldsymbol{H}(\boldsymbol{r}) = 0 \\ \boldsymbol{\nabla}\cdot(\epsilon(\boldsymbol{r})\boldsymbol{E}(\boldsymbol{r})) = 0 \\ \boldsymbol{\nabla}\times\boldsymbol{E} - i\omega\mu_0\boldsymbol{H}(\boldsymbol{r}) = 0 \\ \boldsymbol{\nabla}\times\boldsymbol{H}(\boldsymbol{r}) + i\omega\epsilon_0\epsilon(\boldsymbol{r})\boldsymbol{E}(\boldsymbol{r}) = 0 \end{cases} \tag{2.6.2}$$

The solutions to Maxwell's equations can be found by restating them as an eigenvalue problem for the electric or the magnetic fields. In particular, a common eigenvalue equation usually employed to describe uniform and periodic dielectric structures is the following:

$$\boldsymbol{\nabla}\times\left(\frac{1}{\epsilon(\boldsymbol{r})}\boldsymbol{\nabla}\times\boldsymbol{H}(\boldsymbol{r})\right) = \left(\frac{\omega}{c}\right)^2 \boldsymbol{H}(\boldsymbol{r}) \tag{2.6.3}$$

This equation can be restated in terms of the (hermitian) operator

$$\hat{\Theta} = \boldsymbol{\nabla}\times\left(\frac{1}{\epsilon(\boldsymbol{r})}\boldsymbol{\nabla}\times(\cdot)\right) \tag{2.6.4}$$

so that the new form is

$$\hat{\Theta}\boldsymbol{H}(\boldsymbol{r}) = \left(\frac{\omega}{c}\right)^2 \boldsymbol{H}(\boldsymbol{r}) \tag{2.6.5}$$

This equation, together with

$$\boldsymbol{\nabla} \cdot \boldsymbol{H}(\boldsymbol{r}) = 0, \quad \boldsymbol{\nabla} \cdot (\epsilon(\boldsymbol{r})\boldsymbol{E}(\boldsymbol{r})) = 0 \tag{2.6.6}$$

is sufficient to determine the solutions to Maxwell's equation for a given linear, transparent dielectric structure, in terms of a set of eigenstates $\{\boldsymbol{H}_i\}$ and eigenvelues $\{\omega_i^2/c^2\}$, albeit usually numerical calculations have to be performed to obtain their explicit expression. The eigenproblem can be put in different forms, but the one given here is often used as the basis of simulations because of reasons of numerical stability that are out of the scope of the present work.

This formulation of electromagnetism is very similar to Quantum Mechanics [252, 253]. The Schrödinger equation plays the role of eq. (2.6.5), while wavefunctions ψ and the energies E are the associated eigenstates and eigenvalues. The analogy is best summarized by the following equations:

$$\begin{aligned} \hat{\Theta} = \boldsymbol{\nabla} \times \left(\frac{1}{\epsilon(\boldsymbol{r})}\boldsymbol{\nabla} \times (\cdot)\right) \quad &\leftrightarrow \quad \hat{H} = \left(\frac{-\hbar^2\nabla^2}{2m} + V(\boldsymbol{r})\right)(\cdot) \\ \hat{\Theta}\boldsymbol{H}(\boldsymbol{r}) = \left(\frac{\omega}{c}\right)^2 \boldsymbol{H}(\boldsymbol{r}) \quad &\leftrightarrow \quad \hat{H}\psi(\boldsymbol{r}) = E\psi(\boldsymbol{r}) \\ (\boldsymbol{H}(\boldsymbol{r}), \omega^2/c^2) \quad &\leftrightarrow \quad (\psi(\boldsymbol{r}), E) \end{aligned} \tag{2.6.7}$$

As such, the eigenproblem formulation of electromagnetism shares many of the properties found in Quantum Mechanics, such as the normalization of the fields, commutators and so on.

When a homogeneous medium is considered, for which the dielectric function is constant in space $\epsilon(\boldsymbol{r}) = \epsilon$, the solutions of eq. (2.6.5) are simple plane waves:

$$\boldsymbol{H}_{\boldsymbol{k}}(\boldsymbol{r}) = \boldsymbol{H}_0 e^{i\boldsymbol{k}\boldsymbol{r}} \tag{2.6.8}$$

where the polarization of the field $\boldsymbol{H}_0$ is orthogonal to the propagation direction $\boldsymbol{k}$ from eq (2.6.6), and where $\boldsymbol{k}$ labels the eigenstate and it is related to the eigenvalue by $k(\omega) = \epsilon^2\omega/c$. The inverse expression

$$\omega(\boldsymbol{k}) = \frac{c|\boldsymbol{k}|}{\sqrt{\epsilon}} \tag{2.6.9}$$

is also called *dispersion relation*. The vector $\boldsymbol{k}$ is particularly important because it is a conserved quantity of the field solutions, i.e., when the complete solution $\boldsymbol{H}(\boldsymbol{r}, t)$ evolves in time, its wavevector $\boldsymbol{k}$ does not change. This is the direct consequence of the translational symmetry that the homogeneous medium has; it can be understood in terms of the Noether's theorem, so that $\boldsymbol{k}$ is the conserved quantity associated to the commutation relation $[\hat{T}_{\boldsymbol{d}}, \hat{\Theta}] = 0$, where $\hat{T}_{\boldsymbol{d}}$ is the translation operator that shifts functions of the space coordinate $\boldsymbol{r}$ by the vector $\boldsymbol{d}$, as in

$$\hat{T}_{\boldsymbol{d}}\boldsymbol{H}(\boldsymbol{r}) = \boldsymbol{H}(\boldsymbol{r} - \boldsymbol{d}) \tag{2.6.10}$$

Consider now a dielectric structure that is not uniform, but translationally invariant in only one direction, say z. The dielectric function associated to this structure will be invariant under changes of the z coordinate

$$\epsilon(\boldsymbol{r}) = \epsilon(x, y) \tag{2.6.11}$$

Compared to the homogeneous medium case, here the translational symmetry is found only along z, hence only the z component of $\boldsymbol{k}$ (k_z) will be conserved in this case. The other components of $\boldsymbol{k}$ are not conserved quantities anymore, because of the lack of symmetry in the associated directions. As such, from now on we will replace k_z with k to simplify notation. The general form of the solutions to this problem is

$$\boldsymbol{H}_{k,n}(\boldsymbol{r}) = \boldsymbol{h}_{k,n}(x, y)e^{ikz} \tag{2.6.12}$$

the function $\boldsymbol{h}_{k,n}(x, y)$ being determined by the specific shape of the dielectric function $\epsilon(x, y)$. In this case, an additional label n is necessary to classify the modes because, in general, an infinite number of different solutions are found for each value of k. Typically, for each k all the modes are classified in terms of increasing energy, and the collection of the angular frequencies of all the modes associated with a particular label n is called the n-th *photonic band* of the dielectric structure, and it is indicated with $\omega_n(k)$. The collection of all the bands $\omega_n(k)$ associated to a dielectric structure is called *band structure*, and it can be used to determine most of the properties of light propagating in the structure.

Two classes of modes can be identified in this situation: they are the *guided modes* and *radiative modes*, that differ in the fact that in the former case most of the energy is found on or around the high-ϵ regions of the structure, while in the latter the energy is radiated away. The radiative modes form a continuum, so that n is a continuous variable in this case, and they are found at energies above the ones of the so-called *light-line*, which is identified by the relation

$$\omega(k) = \frac{kc}{\epsilon^2} \tag{2.6.13}$$

where ϵ is assumed to be the dielectric constant of the surrounding material. The guided modes form instead a discrete set, and they are found below the light-line; the discrete nature of guided modes is a direct consequence of the transversal confinement given by the waveguide.

Guided modes can be classified according to polarization. It is common to encounter waveguides whose cross-section is rectangular. In that case we can find a first series of modes, called *quasi-Transverse-Electric* (quasi-TE or simply TE), for which the electric field is mainly polarized in the horizontal direction and the magnetic field in the vertical direction. The other series exhibits the electric and magnetic fields mainly polarized in the vertical and horizontal direction respectively, and they are called *quasi-Transverse-Magnetic* (quasi-TM or TM). The names Transverse-Electric/Magnetic are derived from the modes supported by a dielectric infinite slab, where indeed the polarization of the electric and magnetic fields are transverse with respect to the propagation direction.

In general, whenever a particular symmetry is present in the system, the Noether's theorem assures that the solutions of the eigenproblem can be further classified. When the waveguide cross-section is rectangular, the system is symmetric in the horizontal and vertical directions, hence two additional indexes can be used to classify the modes sustained by the waveguide depending on the horizontal and vertical symmetry that they exhibit. So, for instance the fundamental TE mode will be classified with TE_{00}, while higher modes are TE_{01}, TE_{10}, TE_{11} and so on. A similar classification holds for TM modes.

2.7 One-dimensional periodic structures

The theory of light propagation in confining and periodic structures is well known and found in a number of textbooks (such as [16] and [142]). Here we will review those concepts useful to understand the experimental work described in the following chapters.

2.7.1 Theory

Given the analogy between the Schrödinger equation and the eigenproblem formulation of Maxwell equations, it is not surprising that periodic dielectric structures share many of the properties of systems of quantum particles described by periodic potentials, such as atomic crystals. Here we briefly review these features for the specific case of one-dimensional photonic crystals, i.e. dielectric structures described by a dielectric function periodic in one direction.

Consider a dielectric function periodic along the z direction. If a is the periodicity of the structure, the dielectric function will fulfill the following condition

$$\hat{T}_{m\,a\hat{z}}\epsilon(x,y,z) = \epsilon(x,y,z+m\,a) = \epsilon(x,y,z) \tag{2.7.1}$$

where $\hat{T}_{m\,a\hat{z}}$ is the translation operator with $\boldsymbol{d} = m\,a\hat{z}$ and m is an integer number. The *unit cell* is the region of the structure that, periodically repeated in space, gives rise to the periodic dielectric structure. For a one-dimensional photonic crystal periodic along z, the unit cell is any region of the structure found between two planes orthogonal to z and spaced by a.

Due to the symmetry of the system, it has to be that $\hat{\Theta}$ and $\hat{T}_{ma\hat{z}}$ commute.

$$[\hat{\Theta}, \hat{T}_{ma\hat{z}}] = 0 \tag{2.7.2}$$

Plane waves propagating along z are still eigenvectors of this "discrete" translation operator, with the difference that now multiple eigenstates have the same eigenvalue, and are therefore degenerate. In fact, replacing again k_z with k,

$$\hat{T}_{ma\hat{z}}e^{i\left(k+n\frac{2\pi}{a}\right)z} = e^{i\left(k+n\frac{2\pi}{a}\right)(z-ma)} = e^{-ik(ma)}e^{i\left(k+n\frac{2\pi}{a}\right)z} \quad \forall n \tag{2.7.3}$$

Without getting into the details, it is understood that the final solutions will be given in terms of a linear superposition of all these degenerate modes

$$\boldsymbol{u}_{k,n}(x,y,z) = \sum_m c_{k,n}(x,y)e^{im\frac{2\pi}{a}z} \tag{2.7.4}$$

where it is evident that $\boldsymbol{u}_{k,n}$ has the same periodicity of the dielectric function and that the expansion itself depends on the transverse coordinates x and y. The magnetic field is given by

$$\boldsymbol{H}_{k,n} = e^{ikz}\boldsymbol{u}_{k,n}(\boldsymbol{r}) \tag{2.7.5}$$

and is therefore expressed in terms of a plane wave propagating along z, modulated by a periodic function that takes into account the periodicity of the underlying structure itself. This result is known as the Bloch theorem, while $\boldsymbol{u}$ is known as the Bloch function. As for the uniform structure described in the previous paragraph, the eigenvalues associated with each eigenstate, $\omega_n(k)$, and the Bloch function depend ultimately on the particular form of the dielectric function $\epsilon(\boldsymbol{r})$, and they are usually evaluated numerically.

We can make some additional remarks regarding eq. (2.7.5). First, any fields with wavevectors $k + m\,2\pi/a$ and k are physically identical; in particular, from eq. (2.7.4) it is easy to see that the Bloch function $\boldsymbol{u}_{k,n}$ does not change, as well as the eigenvalue $\omega_n(k)$. This implies that for a one-dimensional photonic crystal, the band structure found in any interval $(k, k + 2\pi/a)$ will be periodically repeated in the whole k-space. Therefore, by convention, only the interval $(-\pi/a, \pi/a)$ is taken into account, and it is called *First Brillouin Zone*. Moreover, as it can be seen by replacing k with $-k$ in eqs. (2.7.4) and (2.7.5), flipping the sign of k corresponds to obtaining the same field travelling in the opposite direction (or backward in time).

Figure 2.19 shows a periodic dielectric structure and its associated band structure in the first Brillouin zone. There exist frequency ranges, called *photonic bandgaps*, in which no photonic TE or TM state exists. These regions are particularly important because they represent energies at which light cannot propagate. Such feature is used, for instance, to realize very selective filters, as it will be seen in Section 4.2. In particular, in Paragraph 2.7.2 we will estimate the energy and width of the photonic bandgap of the most simple one-dimensional photonic crystal, the multilayer. Although *complete* photonic bandgaps may exist, i.e., regions where both TE and TM light cannot propagate, it is more common to encounter dielectric structures where the bandgap is either TE or TM, such as the case of the device illustrated in Figure 2.19.

Because of the scale invariance of Maxwell's equations, it is usually convenient to plot the photonic band structure in terms of adimensional frequency $(\omega a/2\pi c)$ and wavevector $(ka/2\pi)$.

The definition of group velocity for a photonic state in a photonic crystal is defined in terms of the derivative of the photonic bands:

$$\boldsymbol{v}_n(k) = \frac{d\omega_n(k)}{dz}\hat{\boldsymbol{z}} \tag{2.7.6}$$

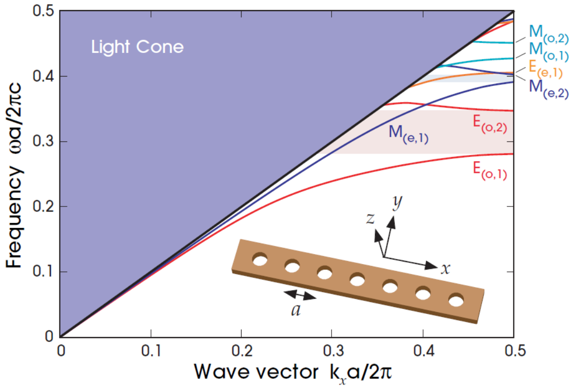

Figure 2.19: Photonic band structure on the first Brillouin zone of the dielectric structure depicted. Labels E and M correspond to TE and TM modes as defined in the main text. The shaded regions on the right are the photonic bandgaps. Figure reproduced from ref. [142].

The expression can be derived from the expressions of energy density and of the Poynting vector. Due to symmetry reasons, similarly to electronic crystals, the group velocity of light vanishes at the edges of the Brillouin zone, where the photonic bands flatten out.

The region of the photonic band structure found below the bandgap is sometimes called the *subwavelength* region [135]. Light in the modes found in this region, in fact, have wavelengths comparable or larger than the periodicity of the photonic crystal; in particular, in the limit of very low energy, the wavelength becomes so large that the dielectric medium can be considered effectively uniform along the propagation (which is the reason why the dispersion of the first photonic band becomes linear near $k = 0$). If this concept is applied to the example periodic structure of Figure 2.19, the result is an approximation of a uniform dielectric waveguide, whose effective core index of refraction is given by the particular arrangement of the subwavelength structures.

It might seem surprising that light can be guided by such complex structures, considering that it has to encounter countless dielectric interfaces along the propagation. In fact, when light encounters obstacles with dimensions comparable to its wavelength it usually scatters away. However, as the existence of the first photonic band demonstrates, this is not the case when the structures are periodic, because unscattered light propagation is a lossless solution of the eigenproblem (2.6.5). Ideally, as long as the periodicity is preserved, light will propagate without scattering losses. Equivalently, one can consider the absence of scattering as the result of perfect destructive interference from all the single scattering events caused by the interfaces.

This scenario is similar to the propagation of light in a common crystal: diffraction of light occurs only at those frequencies for which the wavelength is comparable with the crystal lattice spacing, i.e. in the X-rays, while scattering is completely absent for longer optical wavelengths. The counter-intuitive part is realizing that scattering does not occur even just below the bandgap, where the wavelength is indeed comparable to the lattice spacing.

While the fabrication of subwavelength structures is clearly more difficult than the one of standard uniform waveguides, the advantage resides in the additional design degrees of freedom that they allow. For instance, changing the radius of the holes of the structure shown in Figure 2.19 allows to change the effective index of refraction of propagating light while maintaining the same waveguide cross-section.

Further discussion on this topic is found in Section 4.1 of Chapter 4, where the design process for suspended subwavelength waveguides is illustrated.

2.7.2 The multilayer

The multilayer is a dielectric structure comprising a series of infinite layers with changing refractive index and, sometimes, thickness. When the repetition is periodic, the multilayer becomes the simplest example of one-dimensional photonic crystal. In particular, here we assume that the unit cell is composed of two layers with thicknesses d_1 and d_2 (so that the total period is $a = d_1 + d_2$) and with refractive indexes n_1 and n_2, as illustrated in Figure 2.20. Although it is possible to describe light propagating in every direction, here we are only interested in the propagation normal to the interfaces, since this is the useful scenario for the remaining part of the chapter. Moreover, we will not perform the complete mathematical derivations, already detailed elsewhere [16, 142], but we will only report the relevant results.

The band structure of a generic multilayer is shown in Figure 2.21. The structure is not very different from the ones shown previously, apart from the fact that the TE and TM photonic bands are degenerate due to the cylindrical symmetry of the system.

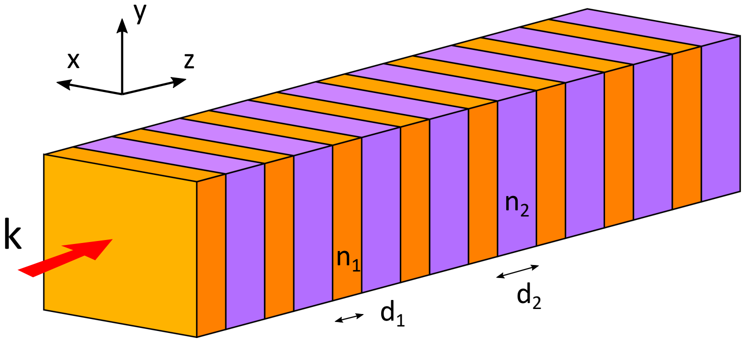

Figure 2.20: Schematic representation of a section of a multilayer. The simplest multilayer is a periodic repetition of infinite dielectric layers with alternating thickness and index of refraction.

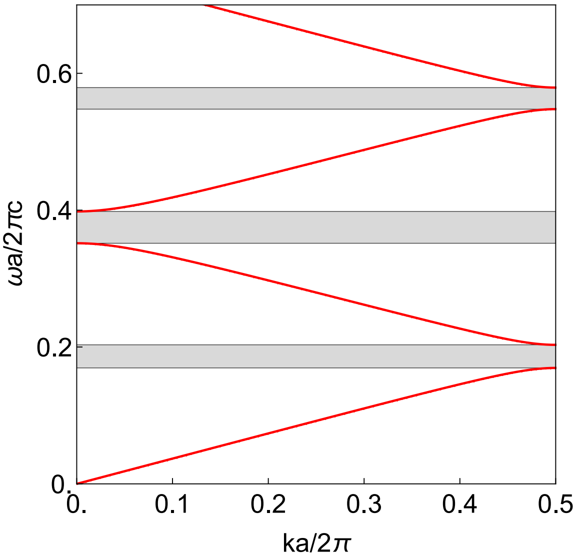

Figure 2.21: Band structure of a multilayer with layer thicknesses $d_1 = 1\ \mu$m and $d_2 = 2\ \mu$m ($a = 3\ \mu$m) and with refractive indexes $n_1 = 2$ and $n_2 = 3$. The gray bands are the photonic bandgaps.

The size $\Delta\omega$ and position ω_{bg} of the photonic bandgaps are particularly interesting properties. The general dispersion relation for the multilayer can be obtained using the transfer matrix method [16], and it is given by the following equation:

$$\cos(ka) = \cos(k_1 d_1)\cos(k_2 d_2) - \frac{1}{2}\left(\frac{n_2}{n_1} + \frac{n_1}{n_2}\right)\sin(k_1 d_1)\sin(k_2 d_2) \tag{2.7.7}$$

where $k_{1/2} = \omega n_{1/2}/c$. The dispersion relation is not analytical, and the bandgap properties cannot be determined exactly for any choice of layers; however, specific formulas can be derived for special cases.

For instance, when the two layers have similar refractive indexes, or when the thickness of one of the layers is very small, the bandgap size is approximately described by the following equation

$$\frac{\Delta\omega}{\omega_{\mathrm{bg}}} \simeq \frac{\epsilon_2 - \epsilon_1}{\epsilon}\frac{\sin(\pi d_1 a)}{\pi} \tag{2.7.8}$$

where $\epsilon_{1/2} = \sqrt{n_{1/2}}$ and $\epsilon = (\epsilon_1 + \epsilon_2)/2$. This situation corresponds to a small perturbation introduced to a uniform dielectric medium.

Another important special case is the *Quarter-Wave Stack* (QWS). Given fixed refractive indexes n_1 and n_2, the QWS is the structure that maximizes the bandgap centered at a given angular frequency ω_{bg}. In particular, say $\omega_{\mathrm{bg}} = 2\pi c/\lambda_0$ is the frequency where we want the bandgap to appear: choosing the individual layers to have thickness equal to a quarter wavelength

$$d_1 = \frac{\lambda_0}{4n_1}, \quad d_2 = \frac{\lambda_0}{4n_2} \tag{2.7.9}$$

assures that the bandgap will be found around ω_{bg} and that the size is the maximum possible given the indexes n_1 and n_2. In particular, the bandgap size can be derived from eq. (2.7.7)

$$\frac{\Delta\omega}{\omega_{\mathrm{bg}}} = \frac{4}{\pi}\arcsin\left(\frac{n_2 - n_1}{n_2 + n_1}\right) \tag{2.7.10}$$

while the bandgap position is derived directly from (2.7.9)

$$\omega_{\mathrm{bg}} = \frac{\pi c}{2a}\left(\frac{1}{n_1} + \frac{1}{n_2}\right) \tag{2.7.11}$$

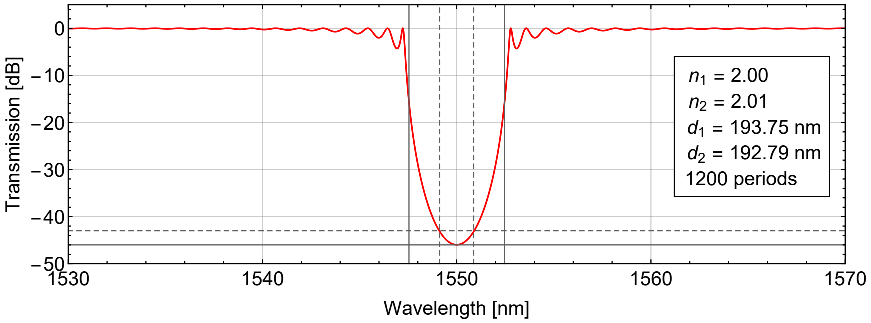

Figure 2.22: Transmission of a quarter-wave stack whose parameters are specified in the inset of the picture. The continuous and dashed vertical gray lines represent the width of the stop-band of an infinite multilayer (4.92 nm) and the 3-dB bandwidth (1.75 nm) respectively.

More in general, in the case of the QWS, a bandgap opens in correspondence of odd multiples of ω_{bg}.

Another property of interest of the multilayer is the transmission function. In the case of the infinite stack, the multilayer is perfectly transparent for all the frequencies outside the bandgaps, while it acts as a perfect mirror for the frequencies within. Real devices, however, have a limited number of periods N. The transmission can be calculated employing the same transfer matrix approaches used to derive eq. (2.7.7); Figure 2.22 shows the transmission of a low contrast, 1200 periods QWS.

We define the 3-dB bandwidth ($\Delta\omega_{3dB}$) as the range of angular frequencies where the attenuation is within 3 dB from the maximum attenuation at the center of the stop-band; this figure of merit is often more meaningful than the complete stop-band of the multilayer. It can be demonstrated that, when plotted in logarithmic scale, the bottom of the transmission curve has a parabolic shape, which is independent on the number of periods N, when N is large. Thus, the ratio between the 3-dB bandwidth and the size of the bandgap turns out to be constant, roughly equal to

$$\Delta\omega_{3dB} \simeq 35.58\% \, \Delta\omega_{\text{bg}} \tag{2.7.12}$$

When using the multilayer as an attenuator, we are often interested in the number of periods required to achieve the level of attenuation we require. Again, for a QWS, using the transfer matrix method at the bandgap center, it is possible to calculate without approximations the minimum transmission T as a function of the number of periods N:

$$T_N = \frac{1}{\cosh^2(\log(\frac{n_2}{n_1})N)} \simeq 4\left(1 - \frac{\Delta n}{n}\right)^{2N} \tag{2.7.13}$$

where the approximation holds for large N and small contrast $\Delta n/n$, where $\Delta n = n_2 - n_1$ and where $n = (n_1 + n_2)/2$ is the average index of the multilayer.

Notice that the size of the stop-band (either the complete bandgap or the 3-dB bandwidth) does not depend on the number of periods. Instead, manipulating eq. (2.7.10), we can obtain an expression for the contrast required to obtain a given stop-band:

$$\frac{\Delta n}{n} = 2\sin\left(\frac{\pi}{4}\frac{\Delta\omega}{\omega_{\mathrm{bg}}}\right) \tag{2.7.14}$$

2.8 Microring resonators

A microring resonator has a simple description: it is a dielectric waveguide closed on itself.

Light can be brought into and out of the resonator by means of other waveguides that pass roughly within one wavelength from the resonator. Optical power is then transferred from the waveguides to the resonator or vice versa through evanescent waves, in a manner analogous to a directional coupler.

Once radiation is coupled in the resonator, it travels around and, due to interference, only those frequencies for which an integer number of wavelength fits inside the resonator length will be sustained by the resonator. The field of such frequencies, however, will be enhanced compared to the one travelling in the external waveguide, and in general they will experience higher optical nonlinearities, the very reason why these devices are interesting for nonlinear optics applications.

The microring resonator sustains a discrete spectrum of resonances. When dispersion is negligible, as it is usually the case for limited frequency spans, these resonances are equally spaced, which is another advantage of this device when it is exploited to enhance Four-Wave Mixing, as discussed in Paragraph 2.8.2.

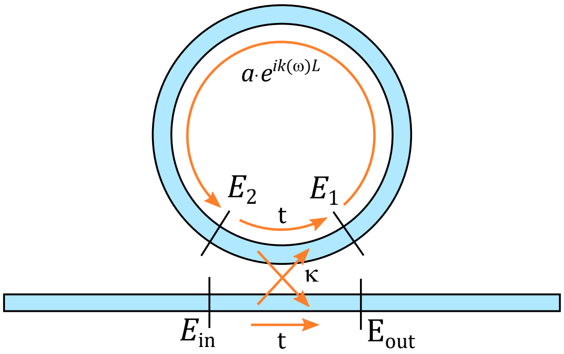

Figure 2.23: Scheme of the All-Pass microring resonator. Light is coupled from a bus straight waveguide to the microring resonator at the point of minimum distance. The coupling region is described as a beam splitter.

In this section the transmission function of the All-Pass ring is derived from a simple circuital model of the microring. Then the transmission function for the Add-Drop is illustrated and the two are discussed in their main points. We will report the definitions and derivations of various important figures of merit useful to characterize microrings for nonlinear photonic applications. Lastly, we illustrate how both Stimulated and Spontaneous Four-Wave Mixing occur in microresonators.

2.8.1 Linear theory

Consider Figure 2.23. We assume that a straight optical waveguide is placed close to a circular microring resonator, of length L; the waveguide is guiding a field of amplitude E_{in} and we assume that no exchange of energy occurs between the waveguide and the ring but at the point of minimum distance: this region, that will be referred to as the *point coupler*, effectively acts as a beam splitter, so that a fraction κ^2 of the power carried by the input field is transferred from the waveguide to the ring, while the other fraction is transmitted forward. This is known as the All-Pass microring configuration. We assume that the point coupler is lossless, while we will assume that some losses are present in the microring resonator.

Given these assumptions we can describe the relations between the fields at the different points marked in Figure 2.23 and from there we can derive the transmission $E_{\text{out}}/E_{\text{in}}$ of the system.

First, we assume that the unitary matrix that describes the point coupler has the following form:

$$\mathcal{U}_{PC} = \begin{pmatrix} t & i\kappa \\ i\kappa & t \end{pmatrix} \tag{2.8.1}$$

where t and κ are real and where, to preserve unitariety, $t^2 + \kappa^2 = 1$. The relations between the field amplitudes at the input and output of the point coupler are then

$$\begin{pmatrix} E_{\text{in}} \\ E_2 \end{pmatrix} = \begin{pmatrix} t & i\kappa \\ i\kappa & t \end{pmatrix} \begin{pmatrix} E_{\text{out}} \\ E_1 \end{pmatrix} \tag{2.8.2}$$

The relation between the amplitudes E_1 and E_2 is found taking into account the propagation along the ring:

$$E_2 = ae^{ik(\omega)L} E_1 \tag{2.8.3}$$

where a is a real constant smaller than 1 that takes into account the losses experienced by the field travelling in the resonator and $k(\omega)$ is the wavevector of the light mode travelling in the ring at angular frequency ω.

Putting together equations (2.8.2) and (2.8.3) it is easy to derive the formula that relates the input and output field amplitudes

$$E_{\text{out}}/E_{\text{in}} = \frac{t - ae^{ik(\omega)L}}{1 - tae^{ik(\omega)L}} \tag{2.8.4}$$

and by taking the absolute square value of the previous equation we obtain the power transmission $T(\omega) = |E_{\text{out}}/E_{\text{in}}|^2$ of the All-Pass microring resonator:

$$T(\omega) = \frac{t^2 + a^2 - 2at\cos\left(k(\omega)L\right)}{1 + a^2t^2 - 2at\cos\left(k(\omega)L\right)} \tag{2.8.5}$$

Figure 2.24 shows a plot of the previous equation. The transmission function is composed of a series of dips, spaced 2π radians from each other. The width of the dips is determined by the amount of losses experienced by light travelling in the microring, either through intrinsic propagation losses or through the coupling point. When the losses are small, the dips are well separated and they can be approximated with a Lorentzian function. By small losses it is meant that the energy lost per roundtrip is much smaller compared to the energy stored in the ring, a situation formalized by

$$1 - a \ll 1, \qquad \kappa^2 \ll 1 \tag{2.8.6}$$

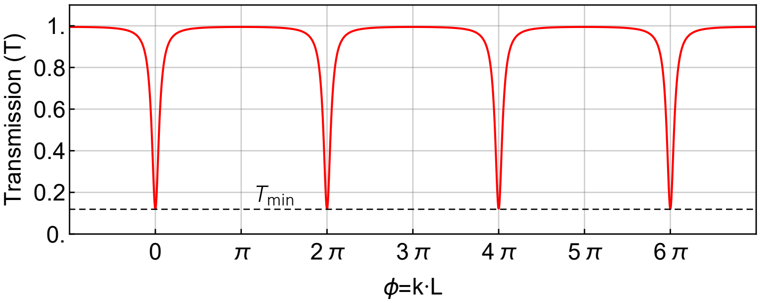

Figure 2.24: Transmission function of an All-Pass microring resonator. The microring resonances are equally spaced in phase.

The minimum value of the transmission, $T_{\min}$, is obtained when the argument of the cosine function is a multiple of 2π:

$$T_{\min} = \frac{(t-a)^2}{(1-at)^2} \tag{2.8.7}$$

In general, $T_{\min}$ is not equal to zero unless t equals a or, in other words, when the light coupled in the resonator equals the losses along the resonator itself; this is known as the *critical coupling* condition or, equivalently, it is said that the ring is *critically coupled*. In critical coupling the light at the resonance frequency that is transmitted past the point coupler undergoes perfect destructive interference with the light outcoupled from the ring itself, and the device reaches the maximum filtering power.

The *Add-Drop* configuration is obtained when two waveguides are coupled to the microring resonator. A representation of an Add-Drop microring is shown in Figure 2.25: two point-coupling sections are now present in the ring, and the coupling can in general be different for the two waveguides. The scheme shows equally spaced coupling points, but the distance may vary, as well. The four input/output ports of the Add-Drop ring are conventionally named “In”, “Through”, “Add” and “Drop” because, while non-resonant wavelengths are routed directly from In to Through (and from add Add to Drop), resonant wavelengths are instead “dropped” from the input waveguide to the Drop port and are “added” from the Add port to the Through port.

The transmission function of the Add-Drop ring between ports In and Through has the same shape of the All-Pass ring (Figure 2.24) because the

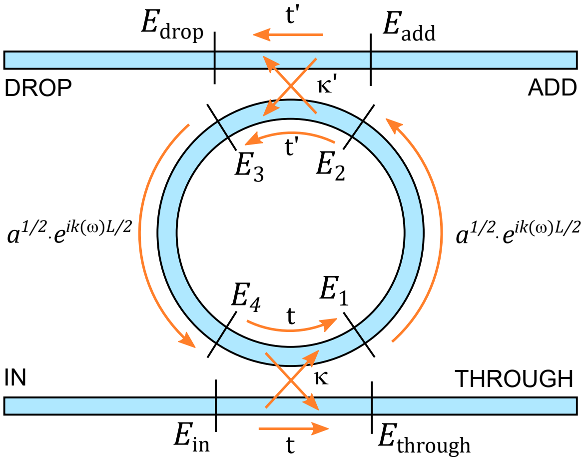

Figure 2.25: Scheme of the Add-Drop microring resonator. The ring is coupled to waveguides in two different points, which are modeled with beam splitters, possibly different.

other coupling point behaves as an effective additional channel for losses. Indeed, the explicit expression $T_{\text{I,T}}$ is obtained by replacing at' to a in eqs. (2.8.4) and (2.8.5).

$$E_{\text{through}}/E_{\text{in}} = \frac{t - at'e^{ik(\omega)L}}{1 - att'e^{ik(\omega)L}} \tag{2.8.8}$$

$$T_{\text{I-T}}(\omega) = \frac{t^2 + a^2t'^2 - 2att'\cos\left(k(\omega)L\right)}{1 + a^2t^2t'^2 - 2att'\cos\left(k(\omega)L\right)} \tag{2.8.9}$$

As such, the critical coupling condition requires that the coupling of a waveguide to the ring is equal to the total effective losses seen from that waveguide, which comprise both the ring intrinsic losses of the ring and the outcoupling losses to the second waveguide ($t = at'$). Consequently, the transmissions from In to Through and from Add to Drop can both be in critical coupling only if the ring intrinsic losses are negligible compared to the coupling losses. In such case, the transmission function from In to Drop will be simply given by $T_{\text{I-D}}(\omega) = 1 - T_{\text{I-T}}(\omega)$.

In general, the transmission of the device from In to Drop is represented by a comb of positive resonances, as seen in Figure 2.26, whose peaks reach

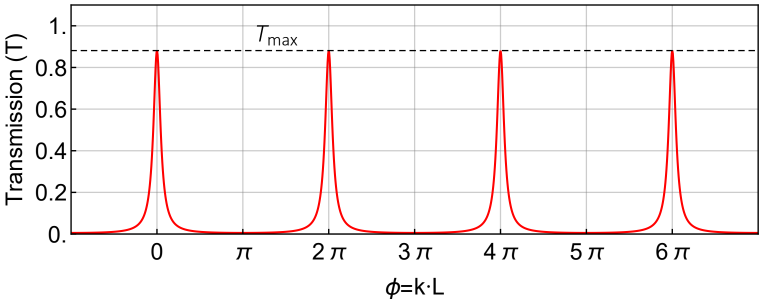

Figure 2.26: Transmission from the In (Add) port to the Drop (Through) port of an Add-Drop microring resonator.

unity only if the add-drop microring is critically coupled.

Naturally, the transmission function of a ring can be obtained experimentally by measuring the transmission of radiation incoming at the input port of the system to the output port. In the following, from equations (2.8.5) and (2.8.9), we will derive the expression of some of the important figures of merit that characterize the microring resonator. These figures can be measured experimentally, and their expressions that we are about to derive can be used to estimate those physical parameters of the ring that determine its performance as a nonlinear optical component.

Free Spectral Range (FSR)

The *Free Spectral Range* is the spectral distance between two adjacent resonances and it can be derived by calculating the distance between two minima of expression (2.8.5). We will derive the expression of the FSR with respect to the wavelength λ or to the frequency ω.

Assuming that the dispersion $k(\omega)$ is linear with the frequency, an assumption that is approximately true for a small range of frequencies, we see that the transmission function is composed, in general, by a series of equally spaced dips, that correspond to the resonances of the resonator.

More in general, $k(\omega)$ can be expanded in Taylor series around a central frequency ω_0 in terms of the phase and group indexes of light at angular frequency ω_0:

$$k(\omega) \simeq k(\omega_0) + \frac{dk(\omega)}{d\omega}(\omega - \omega_0) = \frac{\omega_0}{c}n(\omega_0) + \frac{(\omega - \omega_0)}{c}n_g(\omega_0) \qquad (2.8.10)$$

then, if ω_0 corresponds to the frequency of one resonance, the distance $\Delta\omega$ between two adjacent resonances can be found imposing that one more wavelength fits within the microring circumference L at the new frequency, ω_1, that is, that the difference between $k(\omega_1)L$ and $k(\omega_0)L$ equals 2π:

$$2\pi = (k(\omega_1) - k(\omega_0))L = \frac{(\omega_1 - \omega_0)}{c}n_g(\omega_0)L = \frac{\Delta\omega}{c}n_g(\omega_0)L \qquad (2.8.11)$$

Then the frequency Free Spectral Range ($\mathrm{FSR}_\omega = \Delta\omega$) is given by

$$\mathrm{FSR}_\omega = \frac{2\pi c}{n_g L} \qquad (2.8.12)$$

When FSR_ω is much smaller than the absolute frequency ω, as is often the case, we can obtain the same expression in terms of wavelength by assuming $\Delta\lambda/\lambda = \Delta\omega/\omega$:

$$\mathrm{FSR}_\lambda = \frac{\lambda^2}{n_g L} \qquad (2.8.13)$$

The FSR has a dependence on the frequency/wavelength through n_g, and the expression for the Add-Drop ring has the same.

Quality factor (Q)

Another important figure of merit is the *Quality factor* (Q), or *Q-factor*, a measure of the amount of losses that light experiences when travelling inside the microring. More formally, the Q-factor of a resonant cavity is defined as 2π times the ratio between the total energy stored inside the resonator and the fraction of that energy that is lost in the next optical cycle. It can be shown that the Q-factor is also equal to the ratio between the frequency (wavelength) of a resonance and its FWHM bandwidth $\delta\omega$ ($\delta\lambda$):

$$Q := 2\pi\frac{\mathbb{E}}{\mathbb{E}_{\mathrm{lost}}} = \frac{\omega}{\delta\omega} = \frac{\lambda}{\delta\lambda} \qquad (2.8.14)$$

Let us first assume that the microring resonator is not connected to the outside world through waveguides. In this case, if radiation is travelling inside the ring, it will be dissipated only through the intrinsic losses of the resonator itself. The quality factor will then be a representation of the intrinsic losses of the resonator, and it is therefore called *intrinsic quality factor* (Q_0). It is easy to derive an expression for Q_0 from the first definition: we assume that the energy stored inside the cavity will decay in time with a certain time constant τ that is linked to the losses: $\mathbb{E}(t) = \mathbb{E}_0 \exp(-t/\tau)$. After an optical period δt has passed we will have

$$\mathbb{E}_{\text{lost}} = \mathbb{E}_0 - \mathbb{E}(\delta t) \simeq \mathbb{E}_0 \frac{\delta t}{\tau} \tag{2.8.15}$$

While $\delta t = 2\pi/\omega$, we can link τ to a by defining the *power* attenuation coefficient, α:

$$a^2 = e^{-\alpha L} = e^{-T_{\text{rt}}/\tau} \tag{2.8.16}$$

where T_{rt} is the roundtrip time of the field travelling in the microring, equal to $n_g L/c$. From the previous equations it is then straightforward to obtain

$$Q_0 = \frac{\omega n_g}{c\,\alpha} = \frac{2\pi n_g}{\lambda\alpha} \tag{2.8.17}$$

By extension, the point coupler can be regarded as an additional channel of losses: when the losses are small, we have that the intrinsic roundtrip energy losses are approximately equal to αL, so that we can rewrite Q_0 as

$$Q_0 = \frac{2\pi n_g L}{\lambda(\alpha L)} \tag{2.8.18}$$

and by analogy we can define the *coupling quality factor* Q_c as:

$$Q_c = \frac{2\pi n_g L}{\lambda\kappa^2} \tag{2.8.19}$$

In practice we are modeling the point coupler as if it was introducing κ^2/L losses per unit length. Finally, Q_0 and Q_c will contribute to the global quality factor Q:

$$Q = \left(\frac{1}{Q_0} + \frac{1}{Q_c}\right)^{-1} = \frac{2\pi\, n_g L/\lambda}{(\kappa^2 + \alpha L)} \tag{2.8.20}$$

so that the Q-factor is equal to 2π times the ratio between the optical length expressed in unit wavelengths and the total losses per roundtrip. The expression for Q in terms of angular frequency is easily derived:

$$Q = \frac{\omega L/v_g}{(\kappa^2 + \alpha L)} \tag{2.8.21}$$

If more than one waveguide is coupled to the ring, the expression is trivially extended to

$$Q = \frac{\omega L/v_g}{(\sum_i \kappa_i^2 + \alpha L)} \tag{2.8.22}$$

where i labels each coupled waveguide.

As the name suggests, the *Full Width at Half Maximum* (FWHM) is the width of a resonance taken at half the depth of the dip. Sometimes the expression *Full Width at Half Dip* is used instead.

From the definition (2.8.14) and final expressions (2.8.20) and (2.8.21) that we obtained for the Q-factor, it is straightforward to derive an expressions for the FWHM:

$$\mathrm{FWHM}_\lambda = \delta\lambda = \frac{\lambda^2}{2\pi n_g L}(K + \alpha L) \tag{2.8.23}$$

and

$$\mathrm{FWHM}_\omega = \delta\omega = \frac{v_g}{L}(K + \alpha L) \tag{2.8.24}$$

where K indicates $\sum_i \kappa_i$. These expression could be equivalently derived from equation (2.8.5), by performing the Taylor expansion around a minimum of the transmission T, under the low loss approximation, and by finding the values of $k(\omega)L$ for which $T(\omega) = T_{\mathrm{min}} + (1/2)(1 - T_{\mathrm{min}})$.

Field enhancement F

Another important quantity of interest is the *Field enhancement* ($F(k)$), defined as the ratio between the amplitudes of the fields inside and at the input of the ring (that is, $F(k) = |E_1/E_{\mathrm{in}}|$).

$$F(k) = \left| \frac{\kappa}{1 - ate^{ikL}} \right| \tag{2.8.25}$$

The maximum field enhancement (F) is found on resonance

$$F = \frac{\kappa}{1 - at} \tag{2.8.26}$$

The field enhancement is a key property of resonator structures, as nonlinear optical processes are strongly dependent on this factor, as it will be evident in Paragraph 2.8.2. Usually, one refers to the maximum field enhancement when the expression “field enhancement” is used. When the ring is critically coupled ($t = a$), a convenient expression of the field enhancement can be obtained

$$F = \frac{\kappa}{1 - t^2} = \frac{1}{\kappa} \tag{2.8.27}$$

and then, from eq. (2.8.21) it is possible to express F in terms of the quality factor of the ring and of its geometrical parameters:

$$F = \sqrt{\frac{2 v_g Q}{\omega L}} \tag{2.8.28}$$

where critical coupling implies that $\kappa^2 + \alpha L \simeq 2\kappa^2$. This last expression is valid for critically coupled Add-Drop rings, as well, as it can be seen by repeating the derivation replacing a with at' and assuming $t \simeq t'$ and $a = 1$ for critical coupling.

The field enhancement can easily reach high values. A critically coupled Silicon ring ($n_g = 4$), 10 μm in radius and with a modest Q-factor of 20’000 at 1550 nm exhibits a field enhancement $F \simeq 16$.

Finesse $\mathcal{F}$

The *Finesse* ($\mathcal{F}$) of a microring is defined as the ratio between the FSR and the FWHM.

$$\mathcal{F} = \frac{\mathrm{FSR}}{\mathrm{FWHM}} \tag{2.8.29}$$

The Finesse is trivially derived from the definition and it has a simple expression related to losses and coupling:

$$\mathcal{F} = \frac{2\pi}{K + \alpha L} \tag{2.8.30}$$

When the ring is in critical coupling the Finesse is a direct experimental measurement of the squared field enhancement of the resonator, since the expressions differ only by a π factor:

$$\mathcal{F} = \frac{\pi}{\kappa^2} = \pi \mathrm{F}^2 \tag{2.8.31}$$

2.8.2 Stimulated and Spontaneous Four-Wave Mixing in microring resonators

The extremely high field enhancement achievable by microring resonators makes nonlinear optical processes enormously more efficient than in normal waveguides. Here we briefly discuss how Four-Wave Mixing (FWM) occurs in microring resonators. We first model Stimulated Four-Wave Mixing (StFWM) in waveguides and in microrings, doing a comparison in the efficiencies of these two devices, followed by the description of Spontaneous Four-Wave Mixing (SpFWM) in microresonators.

Stimulated Four-Wave Mixing

Suppose that a strong pump beam, with complex amplitude A_p is travelling in a waveguide together with weak signal and idler beams of complex amplitude A_s and A_i, so that $|A_s|, |A_i| \ll |A_p|$; we assume negligible loss experienced by the pump, either through attenuation or by nonlinear transfer of energy to the other beams, so that the amplitude of the pump remains much larger than the others (undepleted pump approximation). Under these assumptions, and assuming energy conservation and phase matching, eqs. (2.1.11) and (2.1.12), the evolution of the three field amplitudes is given by the following coupled differential equations, as described in ref. [261]

$$\begin{aligned} A_p &= (i\beta_p - \frac{\alpha_p}{2})A_p \\ A_s &= (i\beta_s - \frac{\alpha_s}{2})A_s + \gamma A_p^2 A_i^* \\ A_i &= (i\beta_i - \frac{\alpha_i}{2})A_i + \gamma A_p^2 A_s^* \end{aligned} \tag{2.8.32}$$

where β_p, β_s and β_i are the field propagation constants and α_p, α_s and α_i are the power attenuation coefficients; the nonlinear coupling coefficient γ is given by

$$\gamma = \frac{n_2 \omega}{c A_{\text{eff}}} \tag{2.8.33}$$

where n_2 is the Kerr coefficient of the medium, A_{eff} is the effective area of the mode travelling in the waveguide and ω is the frequency of the beams.

When considering StFWM in microring resonators, the field enhancement properties of the microresonator force the use of frequencies within the resonances of the ring, as the other frequencies exhibit field enhancements lesser than 1. Under this condition, the conservation of the energy forces the choice of signal and idler resonances that are symmetrically placed with respect to the pump resonance. Luckily, when dispersion is negligible, these resonances also satisfy the phase matching condition as it can be understood, for instance, by the derivation of the FSR above, where we have seen that the phase difference between adjacent resonances is always equal to 2π.

By applying the previous expressions to the point coupler model of the ring resonator, and assuming that no idler field is initially present, it is possible to derive the following expression for the idler power produced inside the microring resonator

$$P_i^{(\mathrm{st})} = (\gamma L)^2 \, |F_p(k_p)|^4 |F_s(k_s)|^2 |F_i(k_i)|^2 \, P_p^2 P_s \tag{2.8.34}$$

where P_p and P_s are the pump and signal powers at the input of the ring and $P_i^{(\mathrm{st})}$ is the generated idler power at the output of the ring. As it is seen, the generated idler power is strongly dependent on the field enhancement at the three involved frequencies and it scales quadratically with the pump power. In order to maximize the efficiency of the nonlinear process, it is natural to choose the central frequencies of three equally spaced resonances of the microresonator. Assuming that the field enhancement is the same for the three resonances, we get

$$P_i^{(\mathrm{st})} = (\gamma L)^2 \, |F|^8 \, P_p^2 P_s \tag{2.8.35}$$

Assuming critical coupling, equation (2.8.34) can be restated by using eq. (2.8.28):

$$P_i^{(\mathrm{st})} = (\gamma L)^2 \left(\frac{2 v_g}{L} \right)^4 \frac{Q_p^2 Q_s Q_i}{\omega_p^2 \omega_s \omega_i} P_p^2 P_s \tag{2.8.36}$$

while assuming equal resonances and close frequencies

$$P_i^{(\mathrm{st})} = (\gamma L)^2 \left(\frac{2 v_g Q}{\omega L} \right)^4 P_p^2 P_s \tag{2.8.37}$$

It is seen that StFWM scales in terms of the intrinsic parameters of microresonators as $P_i^{(\mathrm{st})} \propto Q^4/L^2$; if the effective mode area from eq. (2.8.33) is used to define an effective mode volume for the resonator (i.e. $V = L A_{\mathrm{eff}}$), then the scaling goes as $P_i^{(\mathrm{st})} \propto Q^4/V^2$.

Spontaneous Four-Wave Mixing

Here we review the quantum treatment of Spontaneous Four-Wave Mixing, that can be found in more detail in ref. [132].

The quantum mechanical behaviour of the ring-waveguide system can be understood in terms of the separated ring and waveguide Hamiltonians which interact through a coupling Hamiltonian that models the effect of the point coupler.

The waveguide Hamiltonian is the following

$$\hat{\mathcal{H}}^{\mathrm{wg}} = \sum_{\mu} \left[\begin{array}{c} \hbar\omega_{\mu} \int dz\, \hat{\psi}^{\dagger}_{\mu}(z)\hat{\psi}_{\mu}(z) + \\ \frac{i}{2}\hbar v_{\mu} \int dz \left(\frac{\partial \hat{\psi}^{\dagger}_{\mu}(z)}{\partial z} \hat{\psi}_{\mu}(z) - h.c. \right) \end{array} \right] \tag{2.8.38}$$

where z is the propagation coordinate along the waveguide, equal to 0 at the coupling point, where μ labels the particular waveguide mode at frequency ω_{μ} and having group velocity v_{μ}, while $\hat{\psi}^{\dagger}_{\mu}(z)$ represents the waveguide field operator. The Hamiltonian also takes into account the dispersion of the waveguide.

The ring Hamiltonian is given by the following expression:

$$\hat{\mathcal{H}}^{\mathrm{R}} = \sum_{\mu} \hbar\omega_{\mu}\hat{b}^{\dagger}_{\mu}\hat{b}_{\mu} - \sum_{\mu_1,\mu_2,\mu_3,\mu_4} S_{\mu_1,\mu_2,\mu_3,\mu_4}\hat{b}^{\dagger}_{\mu_1}\hat{b}^{\dagger}_{\mu_2}\hat{b}_{\mu_3}\hat{b}_{\mu_4} \tag{2.8.39}$$

The $\hat{b}^{\dagger}_{\mu}$ and $\hat{b}_{\mu}$ are the ladder operators for the ring mode at frequency ω_{μ}. The term on the left is hence the usual harmonic term for the electromagnetic field, eq. (2.2.16), while the second term represents the nonlinear interactions occurring among the fields in the ring; the coefficient $S_{\mu_1,\mu_2,\mu_3,\mu_4}$ takes into account the nonlinearity of the medium and the energy and momentum conservation conditions on the fields at frequencies ω_{μ_1} through ω_{μ_4}. When $\mu_3 = \mu_4$ we recognize a term similar to the degenerate FWM operator of eq. (2.1.13).

Finally, the coupling term is given by

$$\hat{\mathcal{H}}^{\mathrm{cp}} = \sqrt{2\pi}\hbar \sum_{\mu} [c_{\mu}\hat{b}^{\dagger}_{\mu}\hat{\psi}_{\mu}(0) + h.c.] \tag{2.8.40}$$

where c_{μ} is the ring-waveguide coupling constant, while the whole Hamiltonian is the sum of previous equations

$$\hat{\mathcal{H}} = \hat{\mathcal{H}}^{\mathrm{wg}} + \hat{\mathcal{H}}^{\mathrm{R}} + \hat{\mathcal{H}}^{\mathrm{cp}} \tag{2.8.41}$$

The actual process of SpFWM is modelled by applying the above Hamiltonians to the input state; such state assumes that the pump field is in a strong coherent beam and that all the other fields are in the vacuum state (signal and idler included). The resulting generated state, neglecting the residual pump, will have the following form

$$|\psi_{\text{out}}\rangle = e^{\xi \hat{P}^{\dagger}_{s,i} - \xi^{*} \hat{P}_{s,i}} |0\rangle \tag{2.8.42}$$

where $\mu = s$ and $\mu = i$ are the labels for the signal and idler field modes, ξ is a complex number proportional to the mean number of pump photons, and where

$$\hat{P}^{\dagger}_{s,i} = \int\int \beta(\omega_s, \omega_i)\, b^{\dagger}(\omega_s) b^{\dagger}(\omega_i)\, d\omega_s d\omega_i \tag{2.8.43}$$

is the biphoton creation operator, as defined in eq. (2.5.1), so that $\hat{P}^{\dagger}_{s,i} |0\rangle = |1_s, 1_i\rangle$; the form of the biphoton wavefunction $\beta(\omega_s, \omega_i)$ depends on the spectral properties of the pump and of the ring resonances, and on phase matching and energy conservation condition. When the pump beam is sufficiently weak, so that $|\xi| \ll 1$, the generated state is approximately equal to

$$|\psi_{\text{out}}\rangle \simeq |0\rangle + \xi\, |1_s, 1_i\rangle \tag{2.8.44}$$

so that the term $|\xi|^2$ can be interpreted as the probability of producing a pair of photons.

The above expressions are sufficient to derive an equation analogous to eq. (2.8.37) for spontaneous FWM in microring resonators. Assuming equal and close resonances,

$$\begin{aligned} P_i^{(\text{sp})} = P_s^{(\text{sp})} &= (\gamma L)^2 |F|^6 \frac{\hbar\omega v_g}{2L} P_p^2 = \\ &= (\gamma L)^2 \left(\frac{2 v_g Q}{\omega L}\right)^3 \frac{\hbar\omega v_g}{2L} P_p^2 \end{aligned} \tag{2.8.45}$$

Apart from a reduced dependence on the field enhancement F, the main difference with the equations for StFWM is the power term $P_{\text{vac}} = \hbar\omega v_g/2L$. While the classical description of FWM prevents the signal and idler fields from being generated out of a single pump beam, the quantum description of SpFWM allows this process, which can be viewed as the result of vacuum fluctuations actually stimulating FWM. Under this interpretation, the term P_{vac} is the power of such vacuum fluctuations and it replaces the P_s term of eq. (2.8.37). Because this term does not depend on the Q-factor of the ring, the scaling of StFWM is now $P_i^{(\text{sp})} \propto Q^3/V^2$. Summarizing:

$$P_i^{(\text{st})} \propto \frac{Q^4}{V^2}, \qquad P_i^{(\text{sp})} \propto \frac{Q^3}{V^2} \tag{2.8.46}$$

Pump influence on photon pair correlations

Intuitively, the changing spectral correlation of fields emitted by Four-Wave Mixing described in ref. [132] can be understood as follows.

Figure 2.27-a represents a microring resonator being pumped by a continuous wave laser at the center of the pumping resonance: the pump field has a very narrow frequency spectrum compared to the pump resonance, hence it is represented in the figure by a green arrow. Consider now the signal resonance: if a continuous-wave field is present slightly detuned from the center of the resonance (blue arrow in the figure), the conservation of the energy requires that the associated idler field will also be detuned from the center of the idler resonance, as well (red arrow), by the same amount and towards the opposite side. There is a strong correlation between the idler and signal frequencies because their Four-Wave Mixing interaction is mediated by a pump field with very narrow frequency spread: for each signal frequency, there is only a very narrow span of idler frequencies that will fulfill the conservation of the energy with the pump field. This results in a strongly correlated Joint Spectral Density, as pictured in Figure 2.27-b.

By the same token, if the pump field has a broad frequency spectrum (green curve in Figure 2.27-c), a single signal frequency will be able to achieve energy conservation with a broad span of idler frequencies: for instance, the particular signal frequency identified by the blue arrow in Figure 2.27-c will be able to interact with the idler frequencies i_1 or i_2 through the pumping frequencies p_1 or p_2, respectively; the interaction of the signal field with the whole collection of pump frequencies (green curve) will result in a broad idler spectrum (blue curve). This discussion is applicable also to the case of a signal frequency detuned from the center of the resonance, or, symmetrically, to the case of the idler field. In the end, under approproate pumping conditions, there is no correlation between the signal and idler fields, and the resulting Joint Spectral Density will be factorisable, as depicted in Figure 2.27-d.

2.9 Rigrod model of lasing cavities

A useful model that describes the radiation produced by a loop laser cavity is the Rigrod model [262], that has been used to theoretically describe the behaviour of the fiber loop cavities described in Chapter 3. Here the Rigrod

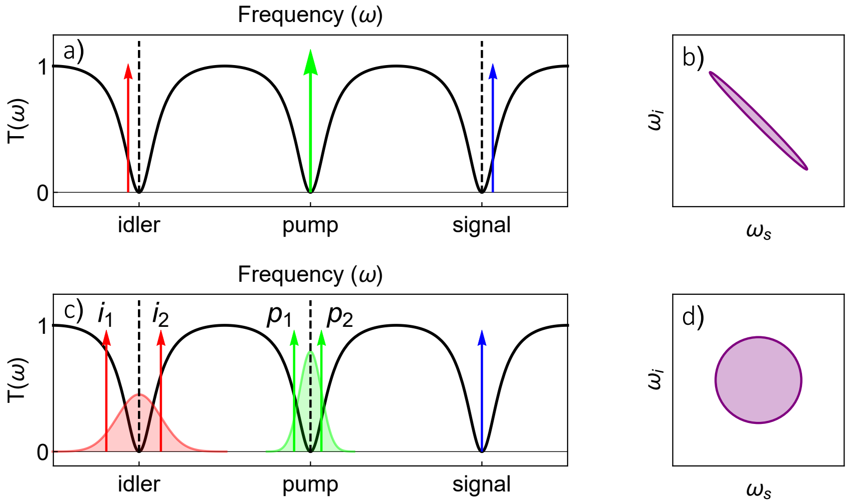

Figure 2.27: Schematic representation of the effect of the pumping scheme on the Joint Spectral Density (JSD) of photon pairs emitted by microring resonators. A spectrally narrow pump field (a) results in a correlated JSD (b); A broad pump field (c) results in an uncorrelated JSD (d).

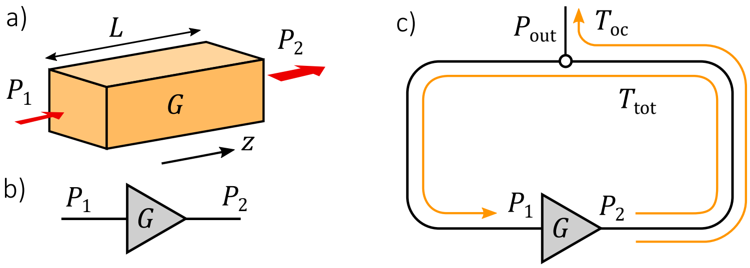

Figure 2.28: Rigrod model of the fiber lasing cavity. a) Representation of a gain medium. b) Symbolic representation of an amplifier. c) Symbolic representation of the lasing cavity.

model is derived and briefly discussed.

We first start by giving a model of an amplifying medium; then we will obtain the complete Rigrod model by closing the medium in a cavity.

Consider a medium capable of light amplification, of total length L (Figure 2.28-a). We assume that the medium is a four-level system, that it is pumped with a constant current and that it experiences gain saturation; we assume that its saturation power is P_s.

To model amplification, we consider what happens in each infinitesimal slice dz of the medium, where we have that the power at the input of the slice $P(z)$ will be amplified according to

$$\frac{dP(z)}{dz} = \alpha(z)P(z), \qquad \alpha(z) = \frac{\alpha_0}{1 + P(z)/P_s} \tag{2.9.1}$$

where α_0 is the unsaturated gain of the medium when $P(z)$ is much smaller than P_s. Rearranging the terms of the previous equation we realize that it can be integrated

$$\left(\frac{1}{P} + \frac{1}{P_s}\right) dP = \alpha_0 dz \tag{2.9.2}$$

and if we call P_1 and P_2 the power at the input and the output of the medium we have

$$\int_{P_1}^{P_2} \left(\frac{1}{P} + \frac{1}{P_s}\right) dP = \int_0^L \alpha_0 dz \tag{2.9.3}$$

so that

$$\ln \frac{P_2}{P_1} + \frac{P_2 - P_1}{P_s} = L\alpha_0 \tag{2.9.4}$$

we then define the small signal gain, $g_0 = L\alpha_0$, and the total gain of the medium, $G = e^g = P_2/P_1$.

Now we close the medium in a cavity (2.28-c). We suppose that the cavity has transmission T_{tot} between the output of the amplifier and the input of the amplifier. It follows that, when the cavity is in a stationary state, the gain G has to be equal to the inverse of T_{tot}:

$$\ln G + \frac{G - 1}{P_s} P_1 = g_0 \tag{2.9.5}$$

and therefore

$$P_2 = G\, P_1 = T_{\text{tot}} P_s \frac{G}{G - 1}(g_0 - g) = P_s \frac{T_{\text{tot}}}{1 - T_{\text{tot}}}(g_0 - g) \tag{2.9.6}$$

Finally, in general, the power will be extracted from the cavity through an output coupler. We assume that T_{oc} is the total transmission between the output of the amplifier and the point at which the power is measured; we then arrive to our final formula:

$$P_{\text{out}} = T_{\text{oc}} P_s \frac{T_{\text{tot}}}{1 - T_{\text{tot}}}(g_0 - g) \tag{2.9.7}$$

If we assume that the gain of the medium is directly proportional to the current supplied to it, that is

$$g_0 = kI, \tag{2.9.8}$$

then almost no power is emitted below the threshold current, I_{th}, while the power will increase linearly for currents above I_{th}; the threshold current, obtained by imposing the condition $g_0 = g$ depends on the total transmission T_{tot}, while the slope of the curve, also called *slope efficiency*, depends on both T_{tot} and P_s. In general, the gain of the medium will depend nonlinearly on the supplied current and some saturation effects may be present.

Chapter 3

Correlated photon pair emission from self-pumped Silicon microresonators

The importance of the microresonator, as discussed in Section 2.8, resides in the enormous field enhancement that these objects are capable to achieve. Such enhancement increases the interaction between radiation and matter, allowing them to reach performances that would be extremely difficult to achieve in similar non-resonant structures. The practical result is that the efficiency of optical nonlinear processes like Parametric Down-Conversion and Four-Wave Mixing will be orders of magnitude higher inside microresonators compared to normal optical waveguides, when the same input power is used.

Four-Wave Mixing, in particular, is the main nonlinear process that is used to generate photon pair states in microring resonators. A strong laser pump is coupled to one of the ring resonances and signal-idler photon pairs are produced in adjacent resonances. However, the resonances of the ring can shift due to, for instance, thermal ambient fluctuations that drive the thermo-optic effect. Thus, if the pump is not kept continuously in resonance the efficiency of Four-Wave Mixing may be reduced. External tunable laser sources can be employed for this purpose, but they are usually expensive and sometimes an active feedback system has to be put in place; these drawbacks make micorings less appealing for industrial applications.

A solution that allows a ring to be pumped without an external tunable

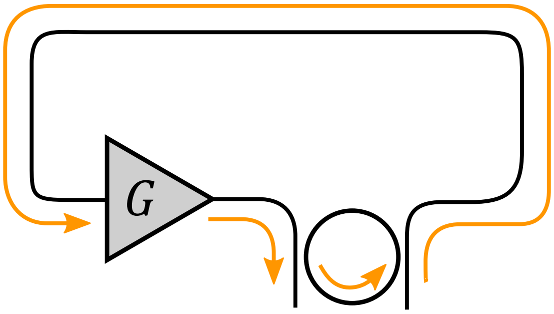

Figure 3.1: Basic scheme of the self-pumping configuration.

laser is obtained when the resonator, in the add-drop configuration, is closed on itself in a loop cavity that contains an optical amplifier [213], as illustrated in Figure 3.1. The transmission between the Input and Drop ports of a ring in the Add-Drop configuration is allowed only for the discrete sets of frequencies corresponding to the ring resonances. Since the ring acts as a frequency selective element, the gain of the amplifier is modulated by the ring and lasing activity will occur automatically on one or more of these resonant frequencies. Simple additional filtering can be used to obtain lasing on a single ring resonance.

This configuration, called *self-pumping* configuration, has several advantages: an external tunable source is no longer necessary, because the amplifier produces lasing radiation on a ring resonance automatically, and it may be electrically pumped; moreover, was the ring resonance to shift for any reason, the lasing radiation would follow. For instance, the system will be more resilient to thermal noise fluctuations, especially for high-Q resonators; as the optical power coupled to the ring is increased, the thermo-optic effect redshifts the resonances of the ring, but also in this case the pump would automatically follow.

This chapter describes how the emission of correlated photon pairs by a Silicon racetrack microresonator can be performed with the use of a self-pumping configuration. Section 3.1 describes how the self-pumped cavity has been realized and characterized and how the correlations between the generated photons could be controlled changing the current supplied to the amplifier. Section 3.2 describes how the cavity was modified to produce highly correlated pairs of time-energy entangled photons. The chapter is concluded by Section 3.3, that gives the perspectives of these projects, suggesting how this research line could proceed in the future towards a higher degree of integration.

3.1 Multi-mode cavity

Here we present the proofs of principle of a source of heralded single photons and a source of entangled photon pairs, working around the standard 1550 nm telecom wavelength, and based on a self-pumped Silicon on Insulator (SOI) Add-Drop racetrack microresonator with a Q-factor roughly equal to 20'000. The racetrack was closed in a fiber loop cavity and was electrically pumped by an optical amplifier. Throughout this chapter we will also refer to the microresonator using the terms “microring” or “ring”, while we will always refer to the fiber loop cavity when using the term “cavity”.

The work was based on previous works from Morandotti's group. [213–215] and it is the continuation of a project started by M. Previde Massara et al. [263].

3.1.1 Setup and linear characterization

Consider the experimental setup shown in Figure 3.2. An SOI racetrack microresonator, 69.4 μm in radius and in the Add-Drop configuration, is optically connected to the external environment through waveguides that route the light to grating couplers. The maximum transmission of the couplers at 1550 nm was 35%.

The light outcoupled from the Drop port of the ring is routed externally through polarization maintaining (PM) fiber components to the Input port of the same ring, thus forming a closed loop cavity. In particular, coupling to the sample is performed using an array of PM fibers.

The external cavity contains an electrically pumped optical amplifier (Thorlabs BOA-1004P), that provides the optical gain necessary to reach lasing operation. The isolator was needed to prevent lasing on the standing-wave modes of the external cavity that were formed between the input and output grating couplers, and to ensure that radiation travelled counter-clockwise only.

The two identical Band-Pass Filters (BPF), 10 nm in bandwidth, select

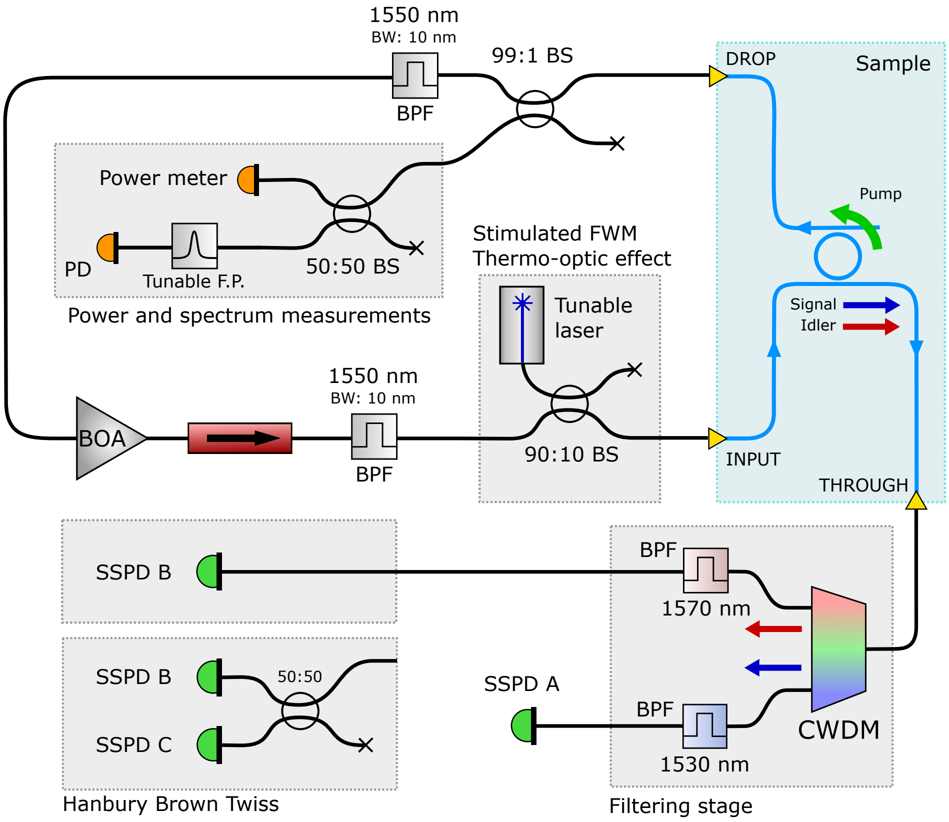

Figure 3.2: Experimental setup of the multi-mode self-pumped cavity. BS: Beam Splitter; PD: Photodiode; F.P.: Fabri-Perot filter; SSPD: Superconducting Single-Photon Detector; BPF: Band-Pass Filter; BW: Bandwidth; CWDM: Coarse Wavelength Division Multiplexer

the ring resonance used for pumping. The BPF at the input of the sample also rejects the Amplified Spontaneous Emission (ASE) emitted from the amplifier before it reaches the ring: the ASE is orders of magnitude brighter than the spontaneously generated photons in the ring and it would mask the dim signals. The other BPF, on the other hand, also suppresses the spontaneously generated photons that are coupled back in the cavity before they reach the amplifier, where they would induce Stimulated FWM and subsequently destroy the Spontaneous FWM signals in the ring.

The 99:1 Beam Splitter (BS) included in the cavity extracts a small fraction of the traveling radiation for monitoring purposes: half of the extracted radiation is measured by a power meter to monitor the power level of the cavity, while the other half is sent to a photodiode preceded by a scanning fiber Fabri-Perot filter (FP) (Micron Optics FFP-TF2, 240 pm FSR, 1 pm bandwidth), that allowed us to monitor the spectral shape of the lasing line.

The signals generated in the ring were extracted from the Through port and routed to either power meters, photodiodes or Superconducting Single-Photon Detectors (SSPD), as detailed in the following paragraphs.

The Coarse Wavelength Division Multiplexer (CWDM) along this output line served two purposes: to spatially separate the signal and idler frequencies, and to partially suppress the pump. The CWDM separates incoming light into 10 nm channels and the rejection between adjacent channels is in excess of 30 dB. Still the rejection was not sufficient to completely suppress the pump radiation below the signal and idler power level, so further filtering was performed by additional BPFs.

Finally, when needed, a 90:10 BS is inserted in the cavity to route the radiation from an external tunable laser to the ring to measure transmission or to perform measurements of Stimulated FWM.

The total length of the cavity was estimated to be equal to 16.2 m, and its group index was assumed to be equal to the phase index of Silica (1.44). Hence, the FSR between the longitudinal modes of the cavity was estimated to be 103 fm (12.8 MHz).

Linear characterization

The transmission measurements of the ring resonances chosen for the generation of photon pairs are reported in Figure 3.3. Following the standard nomenclature for Four Wave Mixing, the three resonances were labeled *pump* ($\lambda_p = 1547.6$ nm), *signal* ($\lambda_s = 1530.4$ nm) and *idler* ($\lambda_i = 1565.9$ nm). The

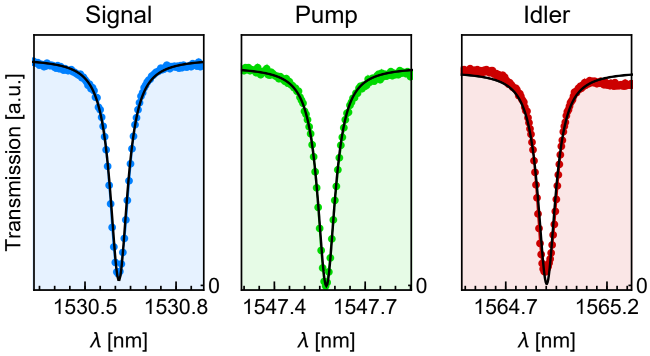

Figure 3.3: Measured transmission and Lorentzian fit of the three microresonator resonances chosen to produce photon pairs by Four-Wave Mixing. The resonances' Q-factors are equal to 21'900, 22'100 and 14'900 respectively.

redmost resonance had a slightly larger width, and a slight splitting can be recognized, suggesting that a defect is present in the ring. The resolution of the measurement was 5 pm, and from the Lorentzian fit of the resonances the value of the Q-factor was extracted: the three resonances had 22'100, 21'900, and 14'900 Q-factors, respectively. The three resonances are two FSRs apart, and the FSR of the ring was measured to be 8.6 nm; the group index of the ring waveguide was estimated to be 4.32. The minimum transmission of all the resonances reaches values close to zero at the frequencies of interest, hence the ring is close to be critically coupled.

From this measurement the coupling efficiency of the grating couplers was obtained: 35% loss per pass (-4.5 dB), and it was estimated that the ring attenuated the pump by 15 dB at the Through port of the ring. Moreover, we estimated that the power measured at the power meter was 565 times smaller than the power at the Input port of the ring.

Lasing characterization

The lasing activity of the cavity was modeled using the Rigrod model, described in Section 2.9; eq. (2.9.7) is reported here, where the output power of the cavity is related to the amplifier current (I):

$$P_{\mathrm{out}} = T_{\mathrm{oc}} P_s \frac{T_{\mathrm{tot}}}{1 - T_{\mathrm{tot}}} (g_0(I) - g) \tag{3.1.1}$$

First of all, the small signal gain $g_0(I)$ was measured using two independent techniques. First, the amplifier is kept in an open configuration and a small signal P_{in} is sent at its input. Then, the output power P_{out} is recorded as a function of the current I supplied to the amplifier, after the ASE is filtered out by a BPF centered on the signal wavelength. By taking the ratio between the output and input signals, the gain G is obtained, and as long as P_{out} is kept much lower than the saturation power P_s of the amplifier, an estimation of g_0 is obtained by taking the logarithm of G:

$$g_0(I) \simeq \log\left(G(I)\right) = \log\left(\frac{P_{\mathrm{out}}(I)}{P_{\mathrm{in}}}\right), \qquad P_{\mathrm{out}}(I) \ll P_s \tag{3.1.2}$$

In our case, three different input powers (24.2 μW, 55.1 μW and 101.5 μW) were used to measure $g(I) = \log G(I)$ and the result is reported in Figure 3.4.

The second measurement technique, instead, extracts the value of g_0 from the threshold current of the lasing cavity. At threshold, in fact, the value of the gain of the amplifier g, is exactly equal to the small signal gain g_0, as it is evident when we impose a zero output of the cavity in eq. (3.1.1); moreover, the gain of the amplifier is linked to the cavity roundtrip transmission by the stationarity condition: $G = T_{\mathrm{tot}}^{-1}$. Hence, it is evident that by knowing the value of the roundtrip transmission T_{tot} and the associated threshold current I_{th} the value of $g_0(I_{\mathrm{th}})$ is obtained.

First, the total transmission T_{tot} from the output to the input of the amplifier using a tunable laser was measured to be $T_{\mathrm{tot}} = 8.95\%$ (-10.5 dB) and it was mainly due to losses introduced by the sample's grating couplers (-4.5 dB each) and by the BPFs (-0.5 dB each). Additional losses were introduced using a variable attenuator, that was characterized in advance, placed along the closed cavity. Then, the threshold current was obtained by measuring the output power of the cavity as a function of the amplifier current, and by taking a linear fit of the first points above threshold, as shown in Figure 3.5.

The values of g_0 obtained with this second method are reported as the red curve (triangles) of Figure 3.4; the curves from the two methods agree very well.

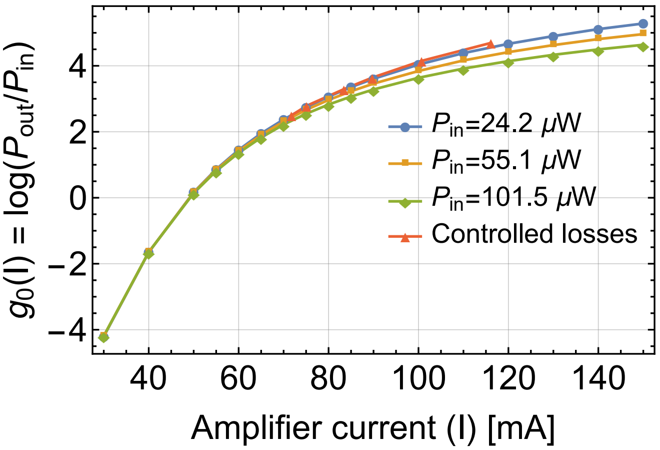

Figure 3.4: Measurement of the small signal gain of the optical amplifier inserted in the cavity. The first three curves have been obtained from an input-output small signal gain measurement, while the last one (red triangles), has been obtained by closing the amplifier inside the cavity and introducing controlled losses in the loop.

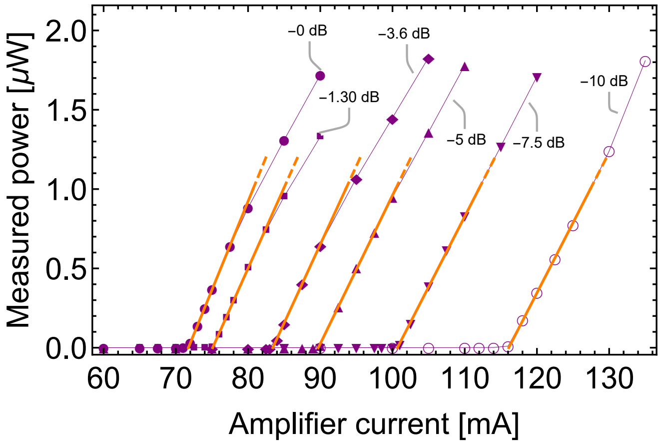

Figure 3.5: Output power of the fiber loop cavity as a function of the amplifier current. With increasing additional losses introduced in the loop, as labeled in the plot, the threshold current increases. The values for the threshold current used in the Rigrod model have been extracted from the linear fits shown (orange lines).

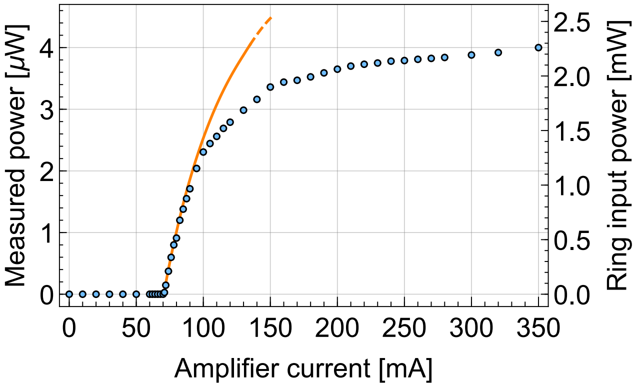

Figure 3.6: Output power of the fiber loop cavity as a function of the amplifier current. The orange line is the expected output as predicted by the Rigrod model of the cavity. Deviation from the expected behaviour occurs for currents in excess of 100 mA.

Finally, the lasing curve of the cavity was taken and compared to the expected output predicted by the Rigrod model. Figure 3.6 reports the experimental data (blue dots) and the lasing model (orange curve).

The agreement between theory and experiment is very good for currents above threshold up to roughly 100 mA. When the current is increased, however, the output of the cavity is inferior with respect to the expected one and saturation occurs.

Thermo-Optic Effect and Two-Photon Absorption

In order to investigate the saturation effect, a systematic analysis of the behaviour of the cavity line and the ring resonance as a function of the cavity power was performed. A tunable laser, connected to the cavity through a 90:10 BS, as detailed in Figure 3.2, was used to measure the transmission of the signal resonance while the cavity was closed and lasing. The transmission measurement, as a function of the optical power at the input of the ring, is reported in Figure 3.7. The resonance is redshifted as the input power is increased; moreover, the Q-factor of the ring is decreased, as well as the visibility of the resonance. This behaviour is consistent with a thermally induced increase of the ring's mode effective index (Thermo-Optic Effect)

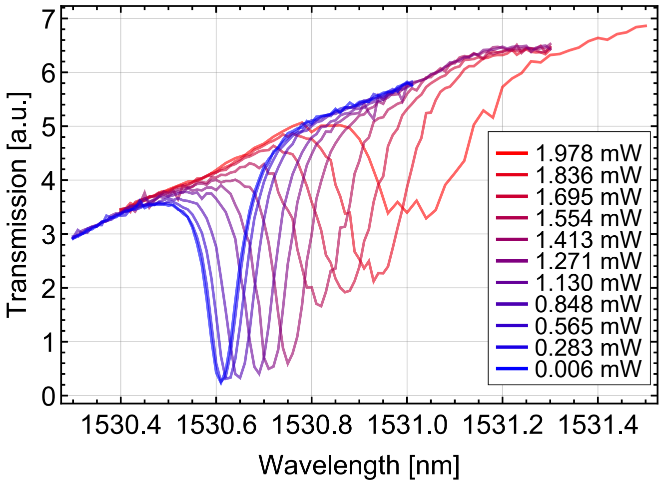

Figure 3.7: Idler resonance transmission as a function of coupled pump power. The thermo-optic effect redshifts the resonance, while Two-Photon Absorption decreases the Q-factor of the ring by inducing Free-Carrier Absorption. The legend refers to the optical power at the input of the microring.

and by an increase of the losses caused by Free-Carrier Absorption induced by Two-Photon Absorption (TPA), that also progressively drive the ring out of the critical coupling condition.

At the same time, the spectral shape of the cavity line was monitored by a photodiode preceded by a tunable FP and connected to the 99:1 BS at the output of the sample; the oscilloscope traces taken from the photodiode are shown in Figure 3.8. The curves have been corrected for the distortion induced by the nonlinear response of the piezoelectric actuators used to tune the FP. At low powers, the lasing line is narrower and aligned with the wavelength of the cold ring (a relative misalignment of 4 pm is attributed to the use of independent techniques to measure the ring resonance and the laser lines); at higher powers the curves are redshifted and broadened to a large extent.

Figure 3.9 compares the redshift of the lasing lines and of the ring resonance: at every given power, the lasing lines of the cavity have been blueshifted back by the same amount that the ring resonance is redshifted; this way, if the redshift of the lasing lines was equal to the one of the ring, in the plot they would all align back at the wavelength of the cold ring reso-

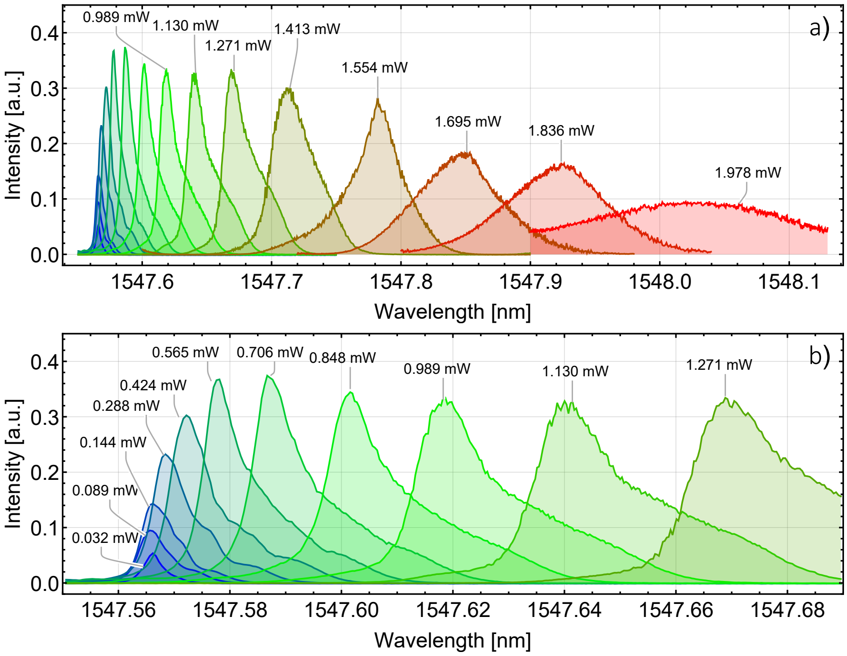

Figure 3.8: Lasing curves of the cavity line as a function of the microring's input power; the labels for each curve refer to the optical power at the input of the ring. The lines are redshifted together with the ring resonance due to the thermo-optic effect. Some curves are cropped because the measurement was taken with a tunable Fabri-Perot filter that had 240 pm Free Spectral Range. a) All the lines. b) The lines corresponding to the lowest imput power, more in detail.

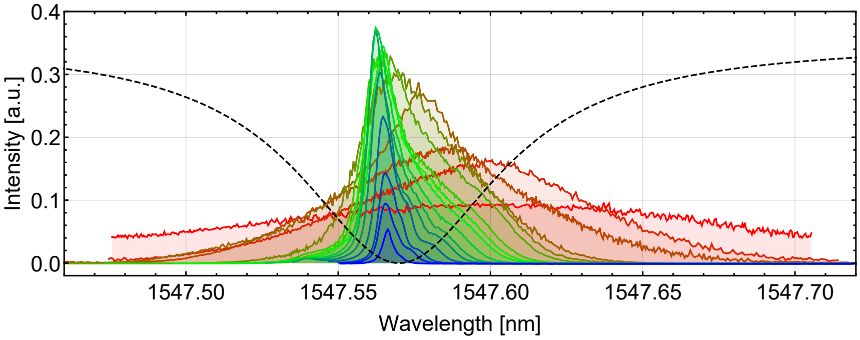

Figure 3.9: When the lasing lines of Figure 3.8 are blueshifted by the redshift of the ring resonance shown in Figure 3.7, they align together on the center of the ring resonance. The black dashed line is the outline of the cold microring pump resonance, centered at 1547.57 nm, as obtained from the fit of the resonance transmission measurement.

nance. Indeed, this happens for most of the lines at lower power, proving that lasing occurs in correspondence with the center of the ring resonance, where the roundtrip transmission of the cavity is maximum. This is significant of the capability that the loop cavity has in following the ring resonance as it shifts. Only few high-power lines experience a further redshift compared to the ring resonance.

The analysis of the lasing line behavior explains well the saturation effect seen in the lasing curve of the cavity. Figure 3.7 shows that the Q-factor of the ring resonance starts to degrade when the power at the input of the ring exceeds roughly 1.3 mW, that corresponds to the power at which the saturation of the lasing line starts to occur, as well. Therefore, in this regime losses are higher than what has been assumed for the Rigrod model and the lasing line sits below the one predicted.

On the other hand, the broadening of the lasing spectrum is not completely understood. We tentatively attribute the cause to the combination of gain saturation effects occurring in the amplifier and to the onset of TPA in the microring resonator.

3.1.2 Nonlinear characterization

The nonlinear properties of the ring have been characterized, as well. In particular, the Stimulated Four-Wave Mixing (StFWM) and Spontaneous Four-Wave Mixing (SpFWM) nonlinear processes have been characterized.

In order to verify that Four-Wave Mixing (FWM) is the main nonlinear process that happens inside the microring resonator, we verified that the scaling of the power of the signals generated nonlinearly was the one expected. As described by eqs. (2.8.36) and (2.8.45) in Paragraph 2.8.2, the expected scaling for StFWM is quadratic with the pump power and linear with the stimulating signal power, while the expected scaling for SpFWM is quadratic with the pump.

The measurement of StFWM was performed by connecting to the cavity a tunable laser that sent the stimulating signal through the 90:10 BS at the input of the sample. The output signals were collected from the Through port of the ring, they were sent to the CWDM for spatial demultiplexing and filtering and they were acquired by a power meter.

Figures 3.10-a and 3.10-b show how the idler signal scales with the pump and with the signal. In both cases the scaling is in agreement with eqs. (2.8.36) and (2.8.45), but a saturation effect is present at higher powers.

3.1.3 Emission of photon pairs and time correlation

In the case of continuous wave pumping, the photon pairs produced in a microring are expected to be emitted simultaneously, within about the dwelling time of the light circulating in the microring. The correlations were analyzed by sending the signal and idler photons at the output of the frequency filtering stage to two Superconducting Single-Photon Detectors (SSPD A and B in Figure 3.2); the detectors (Photon Spot) are helium cooled to 0.7 K by a closed-cycle helium cryostat, they had 75% and 80% efficiency, respectively, and they exhibited a time jitter of 37 ps. The electrical pulses emitted by the detectors are sent via coaxial cables to time-tagging electronics (PicoQuand HydraHarp 400) and the obtained acquisition log was analyzed at a later time.

Figure 3.11 shows the rate of coincident events between SSPDs A and B as a function of relative delay, for two particular ring pumping powers. A clear peak is observed, having about 120 ps FWHM, highlighting the coincident emission of the pairs; indeed, from the dwelling time of the photons within

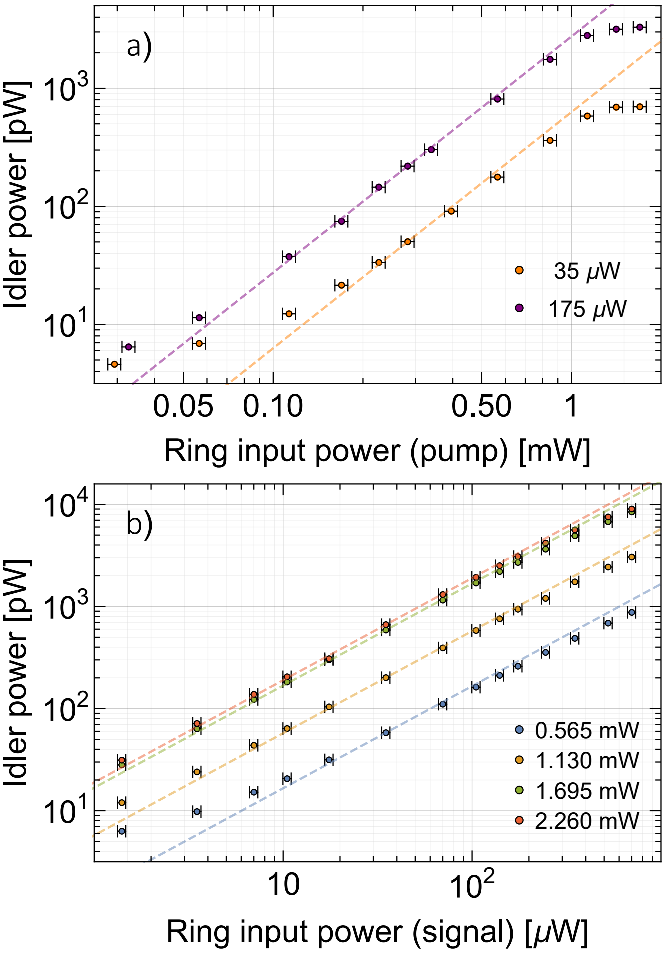

Figure 3.10: a) Stimulted Four-Wave Mixing scaling at varying pump power and fixed signal power (labeled in the Figure); dashed lines represent perfect quadratic scaling. b) Stimulted Four-Wave Mixing scaling at varying signal power and fixed pump power (labeled in the Figure); dashed lines represent perfect linear scaling.

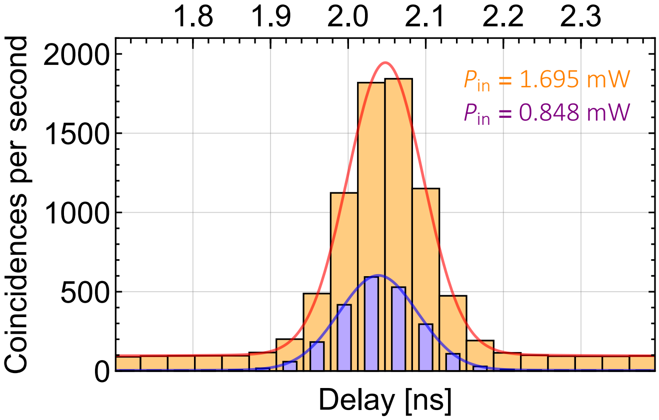

Figure 3.11: Coincidence histograms for two ring input pump powers (labeled). The data are the result of one minute acquisition time; time bins ($\delta\tau$) are 35 ps wide in both cases. The red and blue curves are the fits of the data, as detailed in the text.

the ring (16 ps) and from the detectors' response (37 ps), the system would be unable to resolve emission events closer than 57 ps in time, which is on the same order of magnitude of the observed value, and much lower than the mean interval between singles' detections, as reported below. For different input pump powers similar peaks were observed.

All the peaks were fitted with the weighted sum of a Lorentzian and a Gaussian curve (p and $1-p$ weights respectively). In particular, if $L_{d\tau}(\tau)$ and $G_{d\tau}(\tau)$ are the two normalized functions, centered at zero time delay, where $d\tau$ indicates their FWHM, the fitting function $h_{d\tau}(\tau)$ was defined as

$$h_{d\tau}(\tau) = B + A(p\,L_{d\tau}(\tau - \tau_0) + (1-p)\,G_{d\tau}(\tau - \tau_0)) \tag{3.1.3}$$

where τ_0 indicates the position of the peak. Figure 3.11 shows an example of data fitting performed with the curve defined above.

The total coincidence rates were obtained from the area under the fitting curve (A), after the subtraction of the background (B), which was obtained from the same fit. In particular, the coincidence rate R is obtained from

$$R = \frac{A}{T\delta\tau} \tag{3.1.4}$$

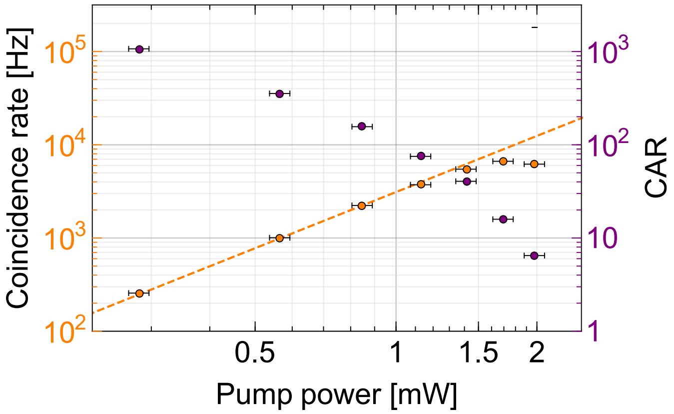

Figure 3.12: Left scale: coincidence rate (R) as function of the ring input power. The scaling is quadratic, as expected by the theory of Spontaneous Four-Wave Mixing in microring resonators. The dashed line represents perfect quadratic scaling. Right scale: Coincidence to Accidental Ratio extracted from the fit of the coincidence peaks; the definition used is given in the text.

where T is the acquisition time (60 s) and $\delta\tau$ is the time bin of the histogram (35 ps). The scaling of the coincidence rate is shown in Figure 3.12. The quadratic slope still confirms the absence of other parasitic fluorescence effects.

From the total transmission losses between the microring resonator and the SSPDs we could estimate the pair generation rate inside the microring. The losses between the Through port of the ring (past the grating coupler) and the input of the SSPDs were directly measured to be -4.39 dB and -5.76 dB for the signal and idler wavelengths respectively; taking into account additional -3 dB outcoupling losses between the ring and the bus waveguide (for each beam), -4.5 dB for the grating couplers transmissions (for each beam) and the efficiency of the SSPDs, the losses for the coincidence signal totaled -27.5 dB. Hence, from the maximum coincidence rate measured (6650 coincidences per second at 1.695 mW ring input power) we estimated a maximum internal generation rate of 3.69 MHz.

Figure 3.12 also shows the Coincidence to Accidental Ratio (CAR) for each of the acquisitions; the CAR was defined as the ratio between the

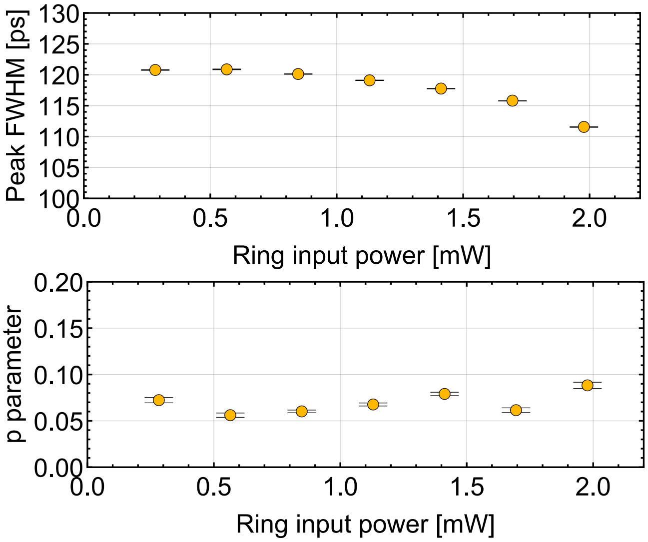

Figure 3.13: Top: FWHM of the coincidence peaks ($d\tau$) as obtained from the fit of the data. Bottom: relative weight of the Gaussian (p = 0) and Lorentzian (p = 1) for the best fit curves, as detailed in the text.

total coincidence rate under the FWHM of the peak and the background coincidences over the same interval. At low powers the CAR is high, while at higher powers the CAR is degraded indicating that multiple emission of pairs is reducing the quality of the generated quantum state.

Figure 3.13 shows the variations of the parameters of the peak as extracted from the fits. The width of the peak is slightly decreased as the pump power increases, in agreement with an increasing resonance width at higher power, and the overall shape is close to a pure gaussian.

Frequency correlations

As detailed previously in Paragraph 2.8.2, when the bandwidth of the pumping field is comparable to the linewidth of the microring's resonance, the biphoton wavefunction produced by SpFWM becomes less correlated; in this instance, the figure of merit for the degree of correlation is the Schmidt number (K), discussed in Paragraph 2.5.2.

Indeed, as outlined in the previous paragraphs, the bandwidth of the cavity lasing line is much broader than for the ideal continuous wave laser, thus a weakly-correlated photon pair state is expected to be produced.

The degree of frequency correlation for the photons produced by the cavity has been investigated experimentally with the use of Stimulated Emission Tomography (SET) [257] for different cavity powers, and then compared with numerical simulations. As explained in more detail in ref. [257], the spectral correlations between signal and idler fields obtained by stimulated FWM are the same of spontaneously generated signal and idler photon pairs. The stimulated process, however, is orders of magnitude brighter than the spontaneous counterpart, and measurement times can be reduced accordingly.

The setup used to perform the SET measurement is illustrated in Figure 3.14. As previously, the signal field was produced by the tunable laser source coupled to the ring through the 90:10 BS, while the FWM output fields were analyzed by a tunable FP filter and single photon detectors. The tunable FP, preceded by an isolator, was put at the output of the Through port of the microring, before the CWDM, so that all the pump, signal and idler fields could be spectrally filtered before being separated at the demultiplexer and sent to three SSPDs. Appropriate attenuation of the fields ensured that the SPDs would not be blinded by the strong classical fields.

The measurement proceeded by stepping the tunable laser across the signal resonance of the ring with 1 pm steps, while a function generator was continuously applying voltage ramps to control the FP and scan the produced output field. The pulses produced by the SSPDs were sent to time-tagging electronics, and the log was subsequently analyzed at the end of the acquisition phase. In order to correctly assign the pulses to the correct pixel of the image, both the laser and the function generator sent electronic marker signals to the time-tagging electronics for synchronization, with nanosecond resolution.

Figure 3.15 (a, b and c) shows the Joint Spectral Density (JSD) of the biphoton wavefunction retrieved from the SET measurement. The resolution of the vertical axis is given by the 1 pm laser steps, while the horizontal resolution is given by the 1 pm FWHM of the FP. The total acquisition time for each of the images shown was 240 seconds. Originally the pictures were distorted because of the hysteresis present in the response of the FP to the applied voltage. These distortions were compensated by correcting the lowest-power picture to show an antidiagonal JSD, and then applying the same correction to the pictures at higher powers.

At a later time, the pump beam outcoupled from the 99:1 BS was scanned

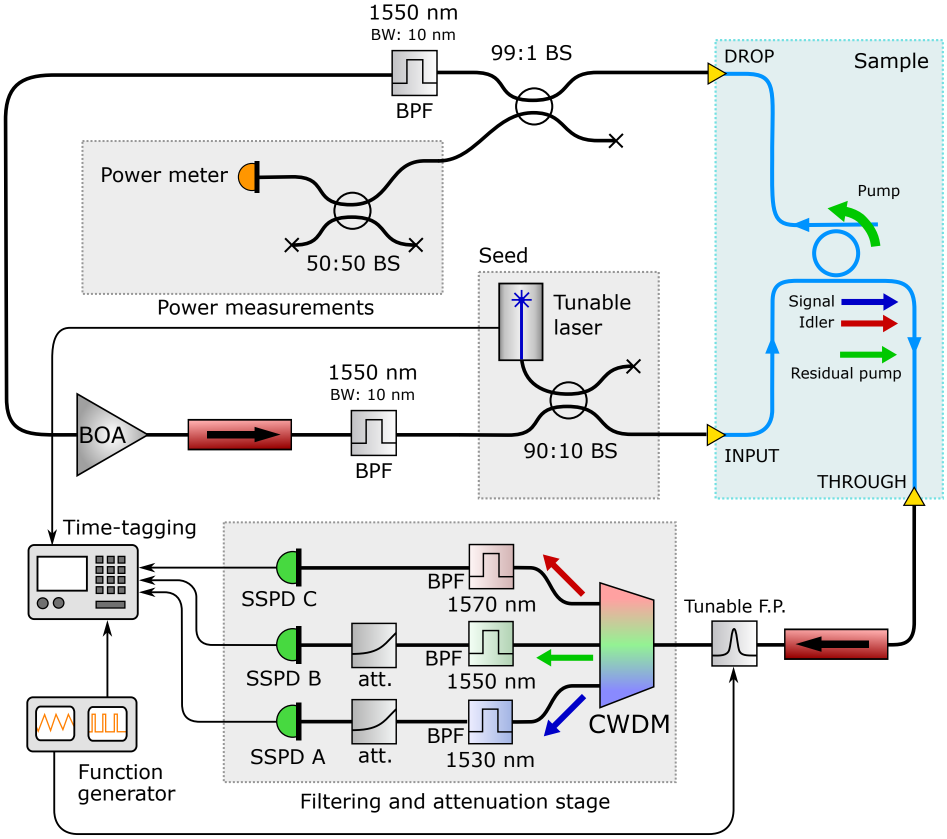

Figure 3.14: Experimental setup used to perform the Stimulated Emission Tomography of the fields emitted by the cavity. BS: Beam Splitter; PD: Photodiode; F.P.: Fabri-Perot filter; SSPD: Superconducting Single-Photon Detector; BPF: Band-Pass Filter; BW: Bandwidth; CWDM: Coarse Wavelength Division Multiplexer; att.: attenuator

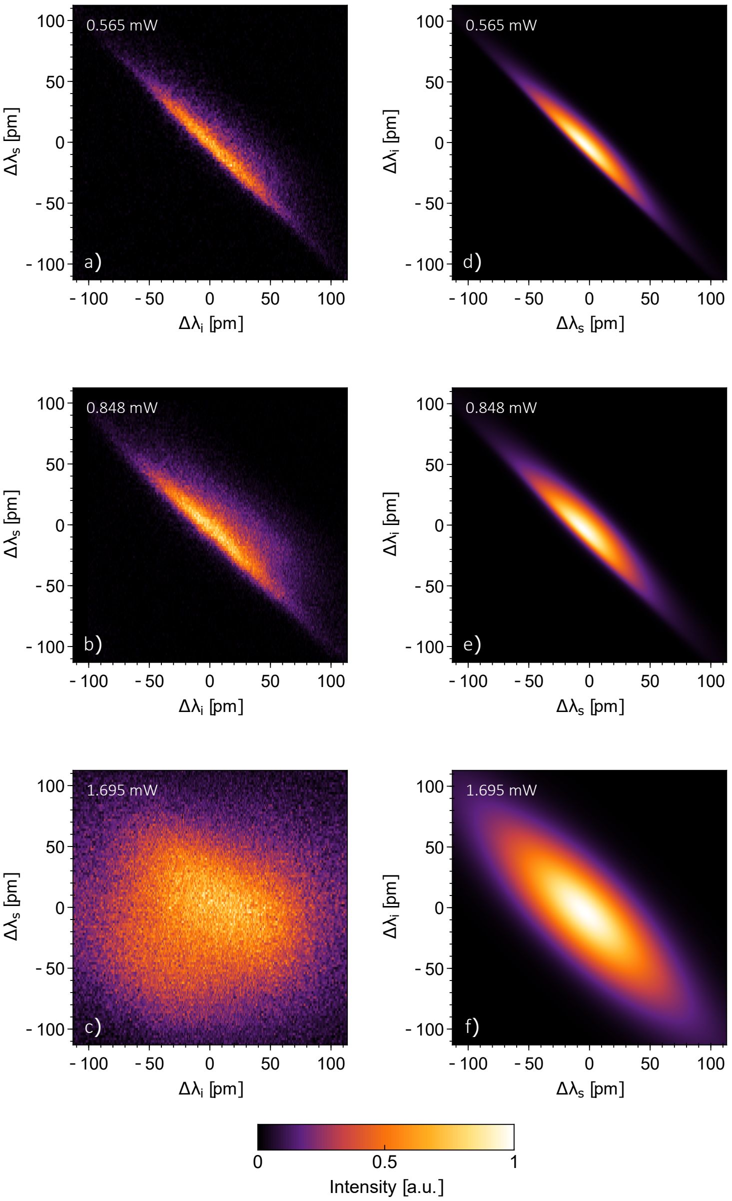

Figure 3.15: Joint Spectral Density of the emitted photon pairs obtained from Stimulated Emission Tomography measurements. a-c) Experimental results. d-f) Predictions by numerical simulations.

with the same FP filter and sent to a photodiode, so that the pump spectral shape that produced the JSD images was available, as well. In principle, as originally intended, the Through-port pump signal could have been used at the same time of the signal and idler fields, however the pump field at the Through port of the Add-Drop ring, being a residual field, was more unstable than at the pump at the Drop port.

This measurement was the one that actually produced Figure 3.8 and, together with the measurements of the thermo-optic shift shown in Figure 3.7 (including the relative redshift of the pump field and resonance, and the decreasing quality factor of the ring), it was used to numerically simulate the expected JSD at a given ring pump power.

The experimental data and theoretical predictions agree very well at lower pump powers, while the experimental JSD is broader than expected at higher powers. In particular, broader pump spectral shapes are expected to produce rounder JSD figures, and this is indeed the case for our experiment. The Schmidt number associated to the various theoretical JSDs varied between 4.07 at lower powers and 1.92 at higher powers.

Further investigation is necessary to understand the origin of the discrepancy between the theory predictions and experimental data. As before, we tentatively attribute the cause to an interplay of different phenomena: saturation effects in the optical amplifier at higher cavity powers which seem to be responsible for the broadening of the pump radiation; moreover, the fact that the redshift of the cavity radiation is even stronger than the redshift of the ring resonance itself at high power (Figure 3.9) suggests that the thermo-optic effect might play an important role in the broadening of the JSD at higher powers, as well.

Second-order correlations

The last figure of merit assessed was the degree of second-order correlation of the photon state, which is obtained from the $g^{(2)}(\tau)$ autocorrelation function of the heralded beam, as discussed in Section 2.3. Experimentally, as pictured in Figure 3.2, the $g^{(2)}(\tau)$ function was obtained from a Hanbury Brown and Twiss (HBT) interferometer connected to the idler arm and to SSPDs B and C, while the signal arm was being heralded by SSPD A.

For two different cavity power levels (0.847 mW and 1.695 mW at the ring input) the field produced by the cavity during one hour acquisition windows was analyzed and the results are reported in Figure 3.16. A clear dip is ob-

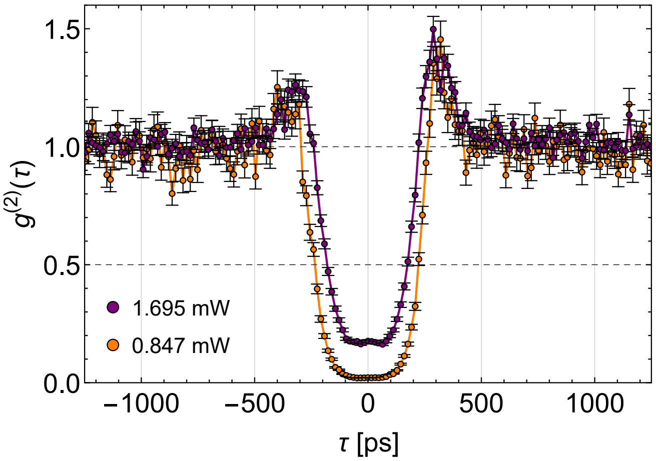

Figure 3.16: Autocorrelation function of the heralded idler beam for two different ring input powers (legend). Acquisition time was one hour. The error bars represent uncertainty due to Poissonian statistic. The zero of the delay was set at the center of the dip and the shift was consistent with the difference in path length between the beam splitter and the single photon detectors.

served in the heralded coincidences between SSPDs B and C, demonstrating antibunching for the photon state at the input of the HBT interferometer. At both powers the minimum of the $g^{(2)}(\tau)$ function is well below 0.5, confirming the quantum nature of the field produced in the ring.

A series of shorter acquisitions (10 minutes each) has been taken, as well, to observe the variation of the minimum value of the autocorrelation function as the power in the cavity is increased. The results of the analysis is reported in Figure 3.17. Although antibunching is present for all the powers investigated, the minimum of $g^{(2)}$ rises above 0.5 at the highest pumping powers, and the purity of the state is reduced. The lowest value of $g^{(2)}$ we obtained was $(15 \pm 7.5) \cdot 10^{-3}$ for 0.565 mW power at the ring input.

3.2 Single-mode cavity

As far as we have seen in the characterization described in Section 3.1, the bandwidth of the cavity laser radiation was much larger than the one for the

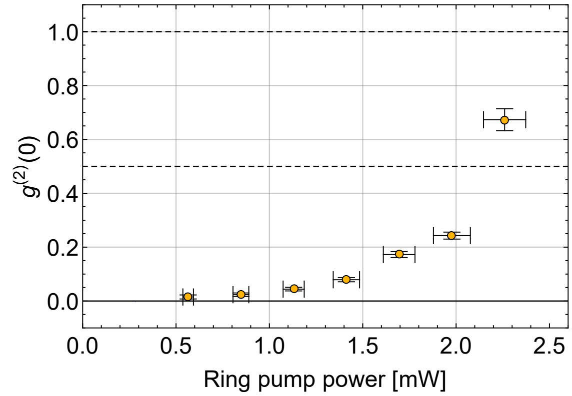

Figure 3.17: Minimum value of the autocorrelation function of the heralded idler field. Each point was obtained after 10 minutes acquisition. Below the value of 0.5 the nature of the field is considered quantum and not explainable by semi-classical theories of light.

ideal continuous-wave laser.

However, during the characterization process of the cavity, it was fairly common to see for brief moments the spectrum of the pump becoming as narrow as the resolution of the scanning Fabri-Perot filter allowed to resolve (smaller than 1 pm), suggesting that the cavity was lasing on a single longitudinal mode. If that was actually the case, then it was reasonable to assume that the ring was producing highly entangled photon pairs, since now the spectrum of the pump was much narrower than the ring resonance.

These brief "jumps" were the inspiration for the work described in this section. Here we describe how we managed to stabilize the cavity to work on a single longitudinal mode for longer time spans; the improved stability of the cavity, in turn, allowed us to indeed demonstrate the emission of time-energy entangled photons by violation of the Bell inequality using a Franson interferometer [260].

Since we used the same microring and since the cavity is essentially identical but for a tunable Fabri-Perot filter inserted along the loop, here I will report only the relevant measurements and differences compared to the cavity described in the previous section.

3.2.1 Setup and linear characterization

The updated setup for the single-mode cavity is reported in Figure 3.18. The microring used for the cavity was the same described in Section 3.1; the configuration of the cavity is essentially identical to the one already described, but with two main differences: the loop now contains a tunable Fabri-Perot filter (FP), that has 240 pm FSR and 1 pm linewidth; moreover, since the FP was not polarization maintaining, a polarization controller was inserted before the filter in order to maximize the roundtrip transmission and to lower the threshold current of the cavity. The second difference was the replacement of the tunable FP filter on the measuring arm at the output of the 99:1 BS with another FP filter with smaller FSR (10 pm) and linewidth (0.1 pm). The Franson interferometer shown in the setup was not connected but for the measurement of entanglement, which is described later on.

The insertion of the FP filter inside the cavity provided the system with a device that sharply selected the frequency of operation. Only a few modes of the cavity, roughly 16.2 m long, are present within the FWHM of the FP line at any given time, since the FSR of the cavity was measured to be 94 fm, as shown later on. In order to obtain lasing on a single longitudinal mode for times long enough to take the measurements presented in the following paragraphs, we had to take particular care in attaching all the fibers to the optical table and the whole setup had to be covered with a box to prevent air currents from disturbing the cavity. Moreover, as many components as possible were polarization maintaining.

Although it allowed to achieve single-mode operation, the introduction of the FP filter prevented the lasing radiation to automatically follow the ring resonance as it shifted. Every time the amplifier current was modified, the position of the FP line had to be manually adjusted and aligned on the center of the microring resonance to optimize the output power produced by the lasing cavity. In general, a fine manual adjustment of the FP filter is needed to make the cavity operate on a single longitudinal mode.

Lasing characterization

The lasing curve of the single-mode cavity is reported in Figure 3.19. The behaviour is still similar to the one of the multi-mode cavity, but, due to the FP filter transmission not exceeding 25%, the threshold current was higher (101.2 mA) and the slope efficiency (16.36 nW/mA) was smaller. Each of

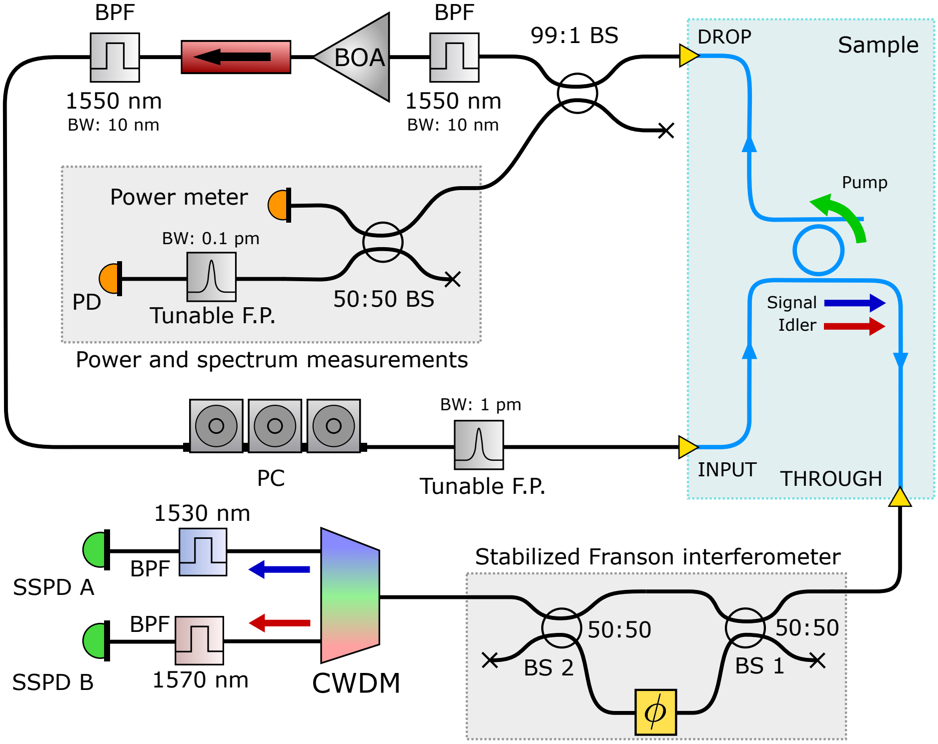

Figure 3.18: Experimental setup of the single-mode cavity. BS: Beam Splitter; PD: Photodiode; F.P.: Fabri-Perot filter; SSPD: Superconducting Single-Photon Detector; BPF: Band-Pass Filter; PC: Polarization Controller; BW: Bandwidth; CWDM: Coarse Wavelength Division Multiplexer.

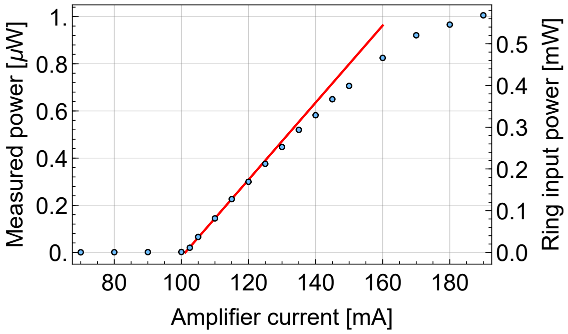

Figure 3.19: Lasing curve of the single-mode cavity. Each point has been recorded after tuning the intra-cavity Fabri-Perot filter to achieve single-mode operation. The threshold current (101.2 mA) and the slope efficiency (16.36 nW/mA) were extracted from the linear fit shown in the plot.

the points of the curve was taken after a fine tuning of the intra-cavity FP filter. While the cavity was stable for many minutes for the lower points, the stability for the highest point of the curve did not exceed few seconds of operation.

In order to estimate the bandwidth of the cavity radiation, we performed a heterodyne measurement by beating the cavity line with the line of a tunable laser (Santec TSL-710), used as local oscillator, locked to an ultrastable reference laser (Orbits Lightwave Ethernal). The two fields have been sent to balanced photodetectors, and the spectrum analyzer used to analyze the RF signal (Tektronix MDO-3034, custom) had 3 GHz bandwidth.

Figure 3.20-a shows the spectrum of the acquired heterodyne signal. A sharp peak is visible, whose width is estimated to be smaller than 300 kHz. This value is much smaller than the FSR of the fiber loop cavity, and no other peaks are present in its vicinity, proving that the operation of the cavity is indeed single moded. From the width of the peak we can set a lower bound on the coherence length of the cavity radiation of 300 m.

As the time-stability of the cavity was not perfect, by perturbing the system slightly or by detuning the FP line from the center of the microring resonance it was possible, at times, to induce the cavity to work in a multimode regime. Figure 3.20-b shows the heterodyne spectrum of the cavity working in such regime, where a comb of few equally spaced peaks is visible.

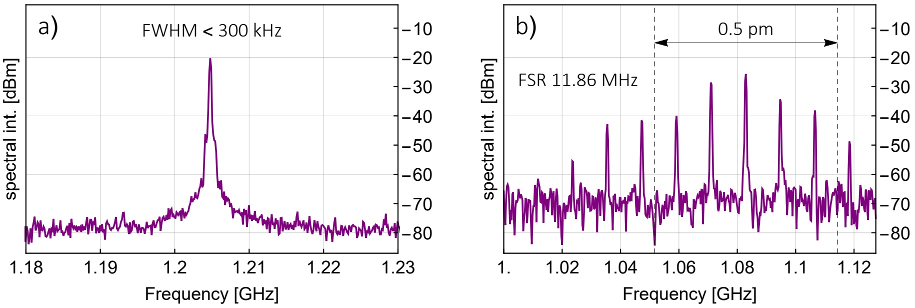

Figure 3.20: Heterodyne measurements of the cavity radiation. a) Single-mode regime of the laser cavity (133 kHz resolution). b) Multi-mode regime of the laser cavity (133 kHz resolution): the FSR between the modes is 11.86 MHz.

The FSR of this comb (11.86 MHz / 94 fm) corresponds to a 17.4 m long fiber cavity and it is consistent with the actual length of the cavity (16.2 m) and expected FSR (12.8 MHZ / 103 fm); the width of the comb spanned roughly 1 pm, as shown in the figure, which is comparable with the bandwidth of the intra-cavity FP filter.

3.2.2 Nonlinear characterization and emission of photon pairs

As well as for the multi-mode cavity, a characterization of the power scaling of FWM has been performed for the single-mode cavity. The top panel of Figure 3.21 shows the acquisition performed by a spectrometer followed by a linear CCD camera of the line produced by SpFWM on the signal resonance of the ring; the signal is acquired after the filtering stage shown in Figure 3.18, past the output of the CWDM's 1530 nm channel and past the BPF (while the Franson interferometer was not connected). The graph shows that all the other FWM lines have been suppressed, and that the pump beam has been completely rejected. A similar peak was observed in correspondence with the idler resonance's wavelength when the other output port of the filtering stage was connected to the spectrometer.

The bottom panel of Figure 3.21 shows that the power scaling of SpFWM is quadratic, as expected. The data for this figure has been obtained by subtracting the luminescence background visible within the pass band of the BPF and by taking the total of the subtracted counts.

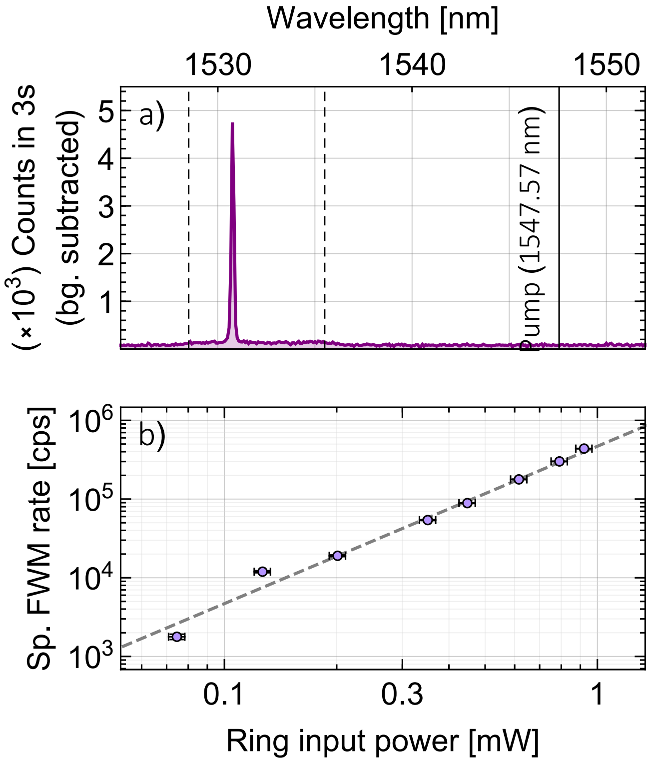

Figure 3.21: Spontaneous Four-Wave Mixing produced by the single-mode fiber loop cavity. Top: Spontaneous Four-Wave mixing field produced at the signal microring resonance, measured past the 1530 nm channel of the CWDM and BPF. The pump is completely rejected. The dashed lines represent the transmission window of the BPF. Bottom: power scaling of the signal field. The dashed line represents a prefect quadratic scaling; the vertical scale has been adjusted so that the data points represent the actual rate of signal photons incident at the input port of the spectrometer.

The time correlations of the spontaneously generated fields have been characterized using the same experimental and numerical techniques as described for the multi-mode cavity, in the previous section: the signal and idler fields have been sent to different SSPDs, the generated electrical pulses have been analyzed with time-tagging electronics, and the time logs have been numerically analyzed afterwards.

The left panel of Figure 3.22 shows one histogram of the coincidences detected as a function of the time delay between the two fields, where a clear peak is visible. The peak has been fitted with the same function described in the previous section and exhibited 108 ps FWHM for all the ring input powers investigated, and it was mostly gaussian in shape. The right panel of Figure 3.22 shows the scaling of the area under the fitted curve, background subtracted (left scale) and the CAR for the same peaks (right scale); again, the scaling is quadratic, as predicted by theoretical models of SpFWM in microring resonators, and the CAR is decreased at higher ring input powers.

3.2.3 Entanglement verification

The verification of entanglement has been performed by sending the photon pairs through a Franson interferometer. The details of the Franson measurement have been described in Paragraph 2.5.3 of Chapter 2, while here we will recall the most important points of that discussion.

In a Franson experiment, the photons of a signal-idler pair are sent to different unbalanced interferometers, and they are independently detected by SSPDs. Assuming to know the time at which the pair has been emitted, four different situations are observed, depending on whether each of the photon has taken the long (L) or short (S) path of its interferometer.

In general, however, the emission time of the photon pair is unknown, so if the two MZIs have identical unbalance, cases $\mathrm{S}_s\mathrm{S}_i$ and $\mathrm{L}_s\mathrm{L}_i$ are indistinguishable, where s and i label the signal and idler photon. When the photons are time-energy entangled and they fulfill appropriate coherence requirements, the indistinguishability leads to nonlocal quantum interference effects on the global biphoton wavefunction.

In particular, when the relative arrival times between the signal and idler photons are analyzed, three coincidence peaks are observed. The central peak corresponds to the indistinguishable cases and it is customary to choose the time reference of the two axes so that the central peak has zero time delay; the lateral peaks then correspond to the signal photon arriving earlier than

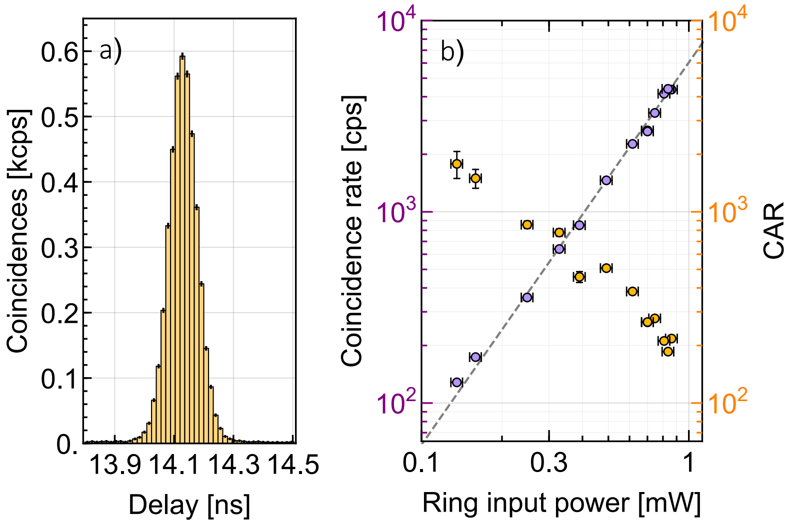

Figure 3.22: Time correlations between the signal and idler fields produced by Spontaneous Four-Wave Mixing by the single-mode cavity. a) Coincidence histogram as a function of the time delay between signal and idler field for 0.86 mW optical pump power at the ring input port. The time bin used for the analysis was 16 ps and the error bars represent Poissonian uncertainty on the bin counts. b) Left scale: power scaling of the intensity of the peak at different input powers; right scale: Coincidence to Accidental Ratio of the peak for the same input powers.

the idler beam on this reference frame ($\mathrm{S}_s\mathrm{L}_i$), or vice versa ($\mathrm{L}_s\mathrm{S}_i$). Obviously, the distance between the three peaks will correspond to the unbalance time of the two MZIs; it is clear that in order to distinguish the central peak from the lateral ones the time width of the peaks has to be much shorter than the delay due to the unbalance of the MZIs; this requires that the coherence length of the single photons has to be much shorter than the unbalance of the MZIs.

The intensity of the central peak will change depending on the global status of the MZIs; the total coincidence rate R_c of the central peak, in fact, depends on the sum of the phases of the two interferometers, that we will call ϕ_s and ϕ_i, following the relation

$$R_c = \frac{1}{4} R_0 \cos^2\left(\frac{A + \phi_s + \phi_i}{2}\right) \tag{3.2.1}$$

where R_0 is the original coincidence rate of the pairs when the photons are not traveling through MZIs and A is a phase factor that depends, for instance, on the total path between the pair source and the interferometers.

Having two different MZIs is a necessary condition if one wants to violate the Bell inequality by closing the nonlocality loop, out of the scope of this experiment. Therefore, we chose to use a single MZI instead, for simplicity; the two photons are still propagating independently and the phase delay they will acquire in the interferometer will be approximately the same

$$\phi_s \simeq \phi_i \simeq \phi \tag{3.2.2}$$

where ϕ is the phase introduced by the single MZI. The central peak coincidence rate will then be dependent on ϕ:

$$R_c = \frac{1}{4} R_0 \cos^2\left(\frac{A}{2} + \phi\right) \tag{3.2.3}$$

Moreover, the use of a single MZI ensures that the two photons will experience the same unbalance apart from a negligible difference due to the dispersion of the fibers used in the interferometer.

The setup used to perform the Franson experiment is the one illustrated above (Figure 3.18). The MZI used in our experiment was realized with polarization maintaining fiber components. The phase shifter arm was 2 m longer than the short arm, corresponding to an additional delay of 9.67 ns assuming 1.45 as the group velocity of optical fibers. The MZI was stabilized by a counterpropagating laser beam produced by a laser diode locked to a stable reference laser (Orbits Lightwave Ethernal), similarly to the heterodyne measurement described above; the system allowed to set the phase shift induced by the phase shifter with a precision much better than 1 degree. The splitting ratio of the BSs varied with wavelength. They were balanced at 1550 nm, but they exhibited different ratios at the signal and idler wavelengths. In particular, BS 1 was 56:44 at the signal wavelength and 43:57 at the idler wavelength, while BS 2 was 58:42 and 40:60 at the two wavelengths, respectively.

The photon pairs generated in the ring were collected from the Through port of the sample and they were routed to one input port of the MZI. After traveling through the interferometer, they were collected by one of the two output ports and sent to SSPDs; the filtering of the pump and the separation of the two frequencies was performed past the interferometer.

The reaction times of SSPDs have been recorded for eighty different phase settings of the interferometer; the measurement was performed in 160 s and the time acquisition window for each setting was 1.7 s long. The results of the measurement are illustrated in Figure 3.23. The top panels show the coincidence histogram for four different settings of the phase of the interferometer. The three peaks are clearly visible and spaced apart by the expected time delay, and it is clearly seen that the central peak intensity changes in the different configurations. The different height of the lateral peaks is due to the unbalance of the BSs at the signal and idler wavelengths.

Each of the points of the lower panel (left scale) represents the total coincidences under the FWHM of the central peak of the histograms described above, and the expected sinusoidal fringe is clearly visible in the plot. The visibility of the fringe, $93.9\% \pm 0.9\%$, was extracted from the sinusoidal fit of the experimental points, and it violated the Bell inequality boundary [99] (70.7%) by 26 standard deviations.

While the vertical error bars represent poissonian noise, the horizontal error bars are due to the small frequency shift that the cavity pump radiation experiences within time scales comparable with the total acquisition time of the fringe. The estimation was performed by scanning multiple times the MZI as the pump beam emitted by the cavity was travelling through it. The series of fringes obtained is reported in the top panel of Figure 3.24; the

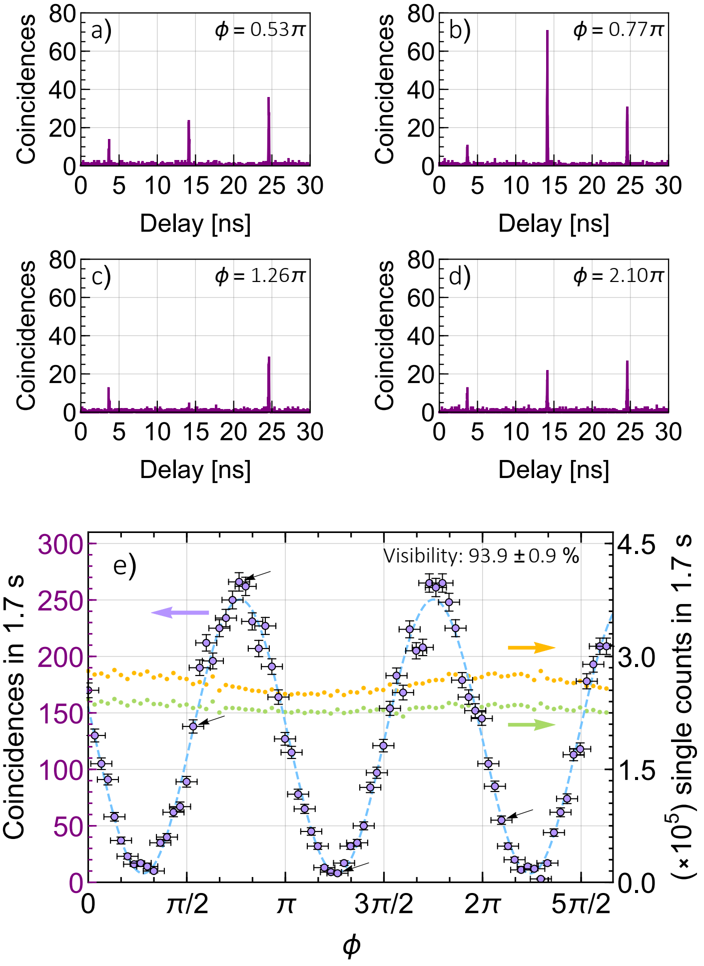

Figure 3.23: Results of the measurement performed with the Franson interferometer. a) to d) Coincidence histograms for four different phase settings (labeled) of the Franson interferometer. The acquisition window is 1.7 s and the time bin is 16 ps. e) Left scale: Total coincidence counts under the FWHM of the central peak (not background subtracted); the dashed line is a sinusoidal fit of the data. Right scale: signal and idler single counts over the same acquisition windows. Black arrows indicate the data points corresponding to the histograms shown in figures a) to d).

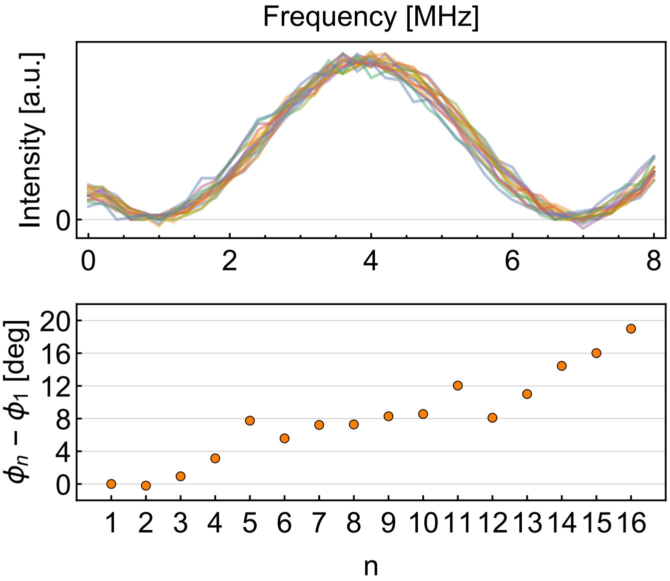

Figure 3.24: Top) Sixteen repeated acquisitions of of the residual pump signal emitted from the Through port of the sample; all the lines have been acquired in 160 s. Bottom). Phase of the sinusoidal function used to fit the curves of the top panel; a drift occurred in time.

curves were fitted with the following function

$$t(f) = B + A \sin\left(2\pi(\frac{f}{f_0}) + \phi\right) \tag{3.2.4}$$

where f_0 is the period of the fringe and ϕ is the phase term used to take into account the drift of the individual fringe. The horizontal error bars of Figure 3.23 were estimated in turn from the size of the ensemble of phases obtained from such fits, shown in the bottom panel of Figure 3.24.

Panel e) of Figure 3.23 (right scale) also shows the singles' rates of the signal and idler fields that were extracted from the analysis of the same experimental data that produced the coincidence fringe. These data show that the fluctuations between different acquisitions of the fields produced by the cavity were small, and that no mode-jumps happened throughout the whole duration of the experiment; this was confirmed also by inspecting the spectrum of the cavity laser line measured at the output of the 99:1 BS, that was kept under direct visual observation on a monitor screen throughout the acquisition.

Ideally, the small sinusoidal modulation of the signal and idler rates should be absent, and it was due to a difference in the transmissions of the long and short arms at the signal and idler wavelengths; the coherence length of the photons ($\sim$ 15 mm) was too short to be responsible for this effect. In any case, it is interesting to notice from this data set that, as expected, the modulation of the correlated events has half the periodicity of the modulations of the uncorrelated events, in accordance with equation (3.2.3).

3.3 Perspectives

The works on the single- and multi-mode cavities described in Sections 3.1 and 3.2 represent, respectively, the first demonstration of emission of photon pairs by SpFWM and of entangled photon pairs by a self-pumped Silicon microresonator. These are proof of principle experiments where a laser cavity has been realized using bulk components and where only Four-Wave Mixing has been realized inside an integrated device.

Table 3.1 reports a sammary of the performance of various sources of photon pairs based on microresonators reported so far. The work described in this Chapter compares well with the state of the art. In particular, the visibility of the Franson fringe is comparable with the other ones reported, and we notice that the Coincidence to Accidental Ratios exhibit very high values, especially if related to the pump powers employed; this is due to the high performance of the superconducting single-photon detectors used.

Apart from an obvious reduction in the required footprint, the realization of a completely integrated self-pumped device capable of emitting time-energy entangled photons would represent a big improvement for various reasons. In fact, the small Free Spectral Range of the fiber loop cavity prevented the achievement of single-mode operation without the addition of a Fabri-Perot filter inside the cavity: this not only increased the complexity of the setup, but also removed the advantage of the self-pumping configuration, since the tuning of the Fabri-Perot had to be adjusted whenever the current supplied to the amplifier changed. Complete integration would reduce considerably the optical length of the cavity, increasing accordingly

Work	Platf.	r / L [μm]		Q	P_p [mW]	R [Hz]	CAR	V
[180]	Si	5	-	$7.9 \cdot 10^3$	0.2	$2 \cdot 10^5$	220	-
					2.0	$7.5 \cdot 10^6$	16	-
[184]	Si	-	43	$1 \cdot 10^4$	0.4	$3 \cdot 10^5$	30	-
[189]	Si	-	73	$3.75 \cdot 10^4$	0.019	$8.27 \cdot 10^5$	602	-
					4.8	$1.23 \cdot 10^8$	37	-
[264]	Si	15	-	$4 \cdot 10^4$	0.3	$1 \cdot 10^6$	>50	-
[265]	Si	-	132.5	$8.1 \cdot 10^4$	0.1	$1.4 \cdot 10^4$	180	-
[187]	Si	7	-	$2 \cdot 10^4$	0.41	$2.1 \cdot 10^7$	350	-
[123]	Si	22	-	$3.1 \cdot 10^4$	0.005	165	37	-
					0.32	$3 \cdot 10^5$	35	-
[123]	Si	20	-	$2.5 \cdot 10^5$	0.008	$5.7 \cdot 10^4$	22	-
		20	-	$9.5 \cdot 10^4$	0.008	$4.7 \cdot 10^5$	60	-
		10	-	$9.4 \cdot 10^4$	0.079	$8.3 \cdot 10^4$	65	-
[209]	Hydex	135	-	$1.375 \cdot 10^6$	30	$3 \cdot 10^5$	12	-
[186]	Si	10	-	$1.5 \cdot 10^4$	0.25	$4 \cdot 10^5$	132	$94.8\% \pm 3.8\%$
					1.00	$4.8 \cdot 10^5$	64	$91.8\% \pm 1.9\%$
					1.5	$1.4 \cdot 10^6$	45	$89.3\% \pm 2.6\%$
[266]	Si	-	132.5	$1.3 \cdot 10^5$	3.16	n/a	80	$92.0\% \pm 1.3\%$
[267]	Si	60	-	$4 \cdot 10^4$	0.5	$2 \cdot 10^6$	n/a	$99.2\% \pm 2.3\%$
[210]	SiN	60	-	$1.1 \cdot 10^6$	2.4	n/a	52	$92.0\% \pm 13\%$
[211]	SiN	350	-	$2 \cdot 10^6$	n/a	n/a	n/a	$93.0\% \pm 13\%$
[212]	SiN	25	-	$1 \cdot 10^6$	0.146	$6.2 \cdot 10^4$	423	$82.7\% \pm 0.2\%$
					0.046	$4.8 \cdot 10^3$	2200	
					0.023	$1.2 \cdot 10^3$	3780	
M.M.	Si	-	64.9	$2 \cdot 10^4$	1.70	$3.7 \cdot 10^6$	17	-
					0.28	$1.42 \cdot 10^5$	1069	-
S.M.	Si	-	64.9	$2 \cdot 10^4$	1.5	$2.9 \cdot 10^6$	185	-
					0.65	n/a	n/a	$93.9\% \pm 0.9\%$
					0.24	$8.4 \cdot 10^4$	1781	-

Table 3.1: Performance of various sources of photon pairs based on microresonators. The first, middle and last sections refer respectively to sources of photon pairs, sources of pairs where Franson experiments have been performed and to the work described in this Chapter. r: ring radius, Q: quality factor, P_p: pump power, R: pair generation rate, CAR: Coincidence to Accidental Ratio, V: Franson fringe visibility, M.M.: Multi-mode cavity, S.M.: Single-Mode cavity.

the Free Spectral Range between adjacent modes. It is then reasonable to assume that single mode operation would be reached with the microring as the only frequency selective element of the cavity.

Moreover, an integrated design would reduce the overall roundtrip losses experienced by the cavity field, since they are currently determined mostly by the grating couplers losses. The threshold current would be reduced, lowering the electrical power consumption of the device, and the birefringence naturally present in integrated waveguides would lift the need for polarization control.

Additional challenges would have to be solved, however. First of all, being an indirect semiconductor, Silicon cannot be used as a gain medium for lasing, therefore more involved integration processes would have to be used to achieve lasing operation. For instance, III-V gain media can be integrated on top of Silicon waveguides to provide optical gain at telecom wavelengths [268, 269].

Moreover, the two Band-Pass Filters rejecting the Amplified Spontaneous Emission produced by the amplifier and the photon pairs coupled back into the cavity will still be required in an integrated version of the cavity. Highly filtering devices such as integrated distributed Bragg reflectors could be used to implement the filtering of the residual pump on the output port of the resonator, but they would not be useful to reject the ASE and the cavity-coupled signal-idler photons, since circulators would have to be added to redirect the reflected pump radiation into the cavity.

Assuming these challenges are solved, a straightforward application of such a device would be an extremely compact, cheap and low-power source of time-energy entangled photon pairs, that could be used to implement quantum communication protocols for long distance key distribution, as discussed already in Chapter 1.

Chapter 4

Periodic structures in high-bandgap materials

Periodic dielectric structures are of paramount importance in the fields of classical and quantum photonics. The combination of the countless reflection and refraction events that light undergoes when it encounters dielectric interfaces can produce interesting phenomena, such as the emergence of a photonic bandgap. These phenomena are best described by the theory of photonic crystals, as already discussed in Section 2.7.

The two experimental works described in this chapter are based on periodic dielectric structures, where the optical properties emerging from their periodicity are key features of their design. The works are the result of the collaboration between the University of Pavia and the group of Alberto Politi, the Quantum nanoPhotonic Lab, at the University of Southampton. The Author visited the Politi's group between April and December 2018.

Section 4.1 describes the design of a photonic platform based on Silicon Carbide suspended subwavelength waveguides for operation at 1550 nm. Suspending waveguides in air is needed when a higher contrast between the guiding dielectric material and the cladding is required, or when, for some reason, the cladding material is deleterious for light propagation.

In the case of the work described here, a Silicon Carbide film is grown on Silicon, which makes impossible to exploit total internal reflection to guide light; in fact, Silicon has a higher index of refraction than Silicon Carbide. Moreover, the use of subwavelength structures simplifies the fabrication process by allowing the use of a single Silicon Carbide etching step to define all the geometries of the photonic platform. In Section 4.1, the description of the photonic platform and of its design process is followed by the description of the fabrication and characterization of the first Silicon Carbide devices used to test the platform.

Integrated filters capable of attenuating radiation selectively by more than 100 dB in a waveguide are a key requirement for the realization of integrated sources of photon pairs based on Four-Wave Mixing in microring resonators. Section 4.2 introduces a novel design for a high-attenuation integrated Bragg filter, where the periodic modulation is introduced by external dielectric structures rather than by direct modulation of either the refractive index of the waveguide or of its width, as performed normally. Finally, the first transmission measurements of a Silicon Nitride test sample are reported.

The performance of the preliminary test samples described in this chapter cannot be considered successful. Nonetheless, we believe that these results are a proof of principle of the ideas illustrated in this chapter and that great improvements can be obtained with further experimental investigation.

4.1 Silicon Carbide suspended subwavelength waveguides

Silicon Carbide (SiC) is a promising material for quantum optics applications, due to the presence of a broad range of color centers active in the near infrared. As detailed in Chapter 1, these color centers can be used as sources of single photons or as systems where to encode qubits. The realization of a scalable photonic platform capable of exploiting these features is thus highly desirable, but the required fabrication of optical nanostructures in thin SiC films remains challenging.

For instance, the heteroepitaxial growth of 3C-SiC can be performed on Silicon, which however is a higher index material, preventing the use of Total Internal Reflection (TIR); moreover, even if Silicon is removed afterwards, the crystalline mismatch between the two materials implies that SiC close to the interface is rich of defects and it is therefore of poor optical quality, with losses in the order of 30 dB/cm. This problem can be solved in principle by employing wafer bonding techniques [270]: the top surface of SiC is bonded to another lower index wafer, while, after Silicon is removed, the remaining

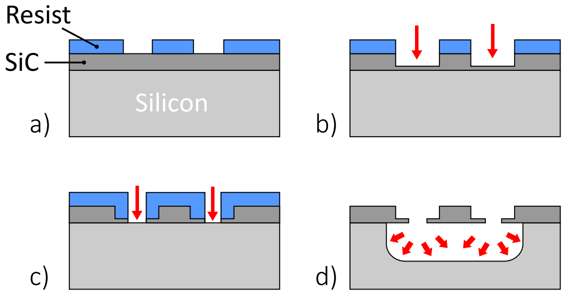

Figure 4.1: Schematic representation of the fabrication of Silicon Carbide (SiC) suspended waveguides. a) A thin film of SiC is grown on a Silicon Substrate and covered with resist for e-beam patterning. b) A chemical etch defines the lateral geometry of the waveguide, leaving a thin film of SiC. c) A second e-beam patterning and etch cycle opens holes to the substrate. d) Under-etching of the substrate completes the process.

low quality interface can be thinned down by etching. This leaves a high-quality thin film of SiC on a substrate with a lower index of refraction for further processing, at the cost of a more complicated fabrication.

The heteroepitaxial growth of 4H-SiC provides higher quality thin films, but exploits Smart-cut processes [271], which increase losses due to the required implantation of dopants.

Another approach relies on the suspension of thin films in air by under-etching part of the Silicon substrate underneath SiC. This approach, illustrated schematically in Figure 4.1, requires that holes are etched in the SiC to access the underlying substrate, after which a second under-etch step removes the substrate. While a single etch step in SiC is sufficient to realize photonic crystal cavities [120, 238], since they are naturally connected to the rest of the SiC layer, ridge waveguides cannot be suspended in this way. Rib waveguides can be realized, but two SiC etching processes are necessary instead: the first step, by partially etching the SiC layer, defines the lateral structures and leaves a very thin film for connecting the waveguide to the rest of the layer; the second etch step opens the holes to access the substrate [272].

The approach described in this section allows the realization of suspended waveguides with a single etch step, by exploiting subwavelength structures, and it is based on previous works realized in Silicon [273, 274] and Germa-

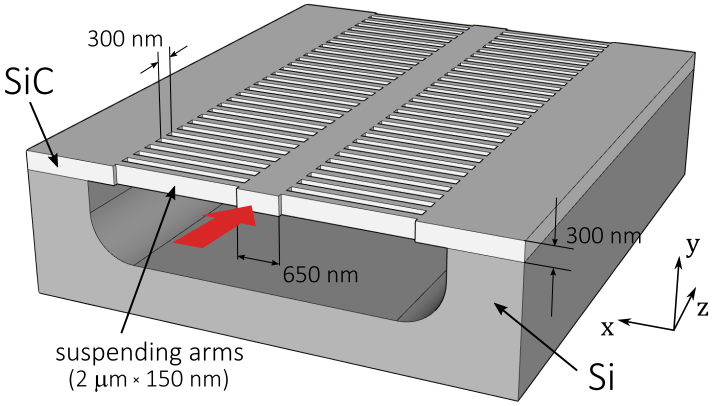

Figure 4.2: Schematic representation of the Silicon Carbide suspended subwavelength waveguides. The structure is periodic along the propagation direction (z), with a periodicity much smaller than the wavelength of light (300 nm). Light is guided along the central rod (red arrow), which is suspended in air and connected by lateral arms to the rest of the Silicon Carbide layer.

nium [275].

Although frequencies closer to the fluorescence of SiC color centers would be more interesting, the choice of 1550 nm as the working wavelength was motivated by the consequent relaxation on fabrication requirements that longer wavelengths allow. Naturally, provided that the fabrication is good enough to address smaller geometrical features, the scale invariance of Maxwell's equations implies that this design can be applied to shorter wavelengths by scaling down all the dimensions listed in the following paragraphs.

4.1.1 Waveguide

The geometrical structure of the suspended waveguide is shown in Figure 4.2, while the relevant dimensions are listed in Table 4.1. Light travels along the central SiC rod, suspended in air with the use of a periodic array of lateral arms that connects the rod to the rest of the SiC layer.

The waveguide is essentially a one-dimensional photonic crystal, whose band structure, calculated with the MIT Photonics Bands [276] software

Dimension	Length [nm]
Periodicity (a)	300
Film thickness (h)	300
Waveguide width (W_{wg})	650
Arm length (L_a)	150
Hole length (L_h)	150
Arm/hole width (W_a/W_h)	2000

Table 4.1: Proposed dimensions for a single TE-TM subwavelength SiC waveguide. We assume a value of 2.6 for the index of refraction of SiC.

suite, is illustrated in Figure 4.3. The SiC film (h) is 300 nm thick, while the periodicity of the structure (a), equal to 300 nm, was chosen to put the photonic bandgap of TE-like modes well above the energy of 1550 nm radiation, ensuring that the structure is effectively subwavelength. The goal in the choice of the dimensions of the structures, as illustrated in the following, was to allow the maximum possible confinement of light while keeping the structure single-TE/single-TM.

Light is confined in the vertical direction by Total Internal Reflection (TIR). Under strong subwavelength conditions, the lateral arms act as an effective homogeneous medium, whose bulk effective index of refraction n_e is intermediate between the one of air and SiC, as illustrated in Figure 4.4. Therefore, effectively, light is confined in the lateral direction by TIR, as well.

Estimation of the effective index

The refractive index of this effective medium has been estimated by considering an air-SiC multilayer, with layer thicknesses equal to the ones of the holes and of the arms. Let us label the length of the arms and of the holes with L_a and L_h, so that $a = L_a + L_h$. Using the notation introduced for the multilayer in Paragraph 2.7.2, the layers 1 and 2 have thicknesses $d_1 = L_a$ and $d_2 = L_h$, and refractive indexes $n_1 = n_{\mathrm{SiC}} = 2.6$ and $n_2 = 1$ (air). Making use of the dispersion relation of the multilayer, eq. (2.7.7), one can calculate the effective index of the Bloch mode travelling in the structure ($n = ck/\omega$). Figure 4.5 shows the effective index of light travelling in the multilayer as a function of the filling factor $f_{\mathrm{wg}} = L_a/a$ and with constant

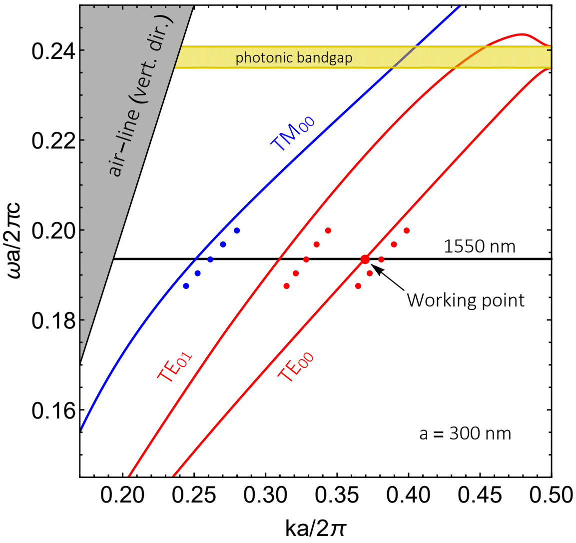

Figure 4.3: Calculated band structure of the suspended subwavelength waveguide proposed in this section. Continuous lines have been obtained with the MPB software suite. Dots are obtained from eigensolver simulations of the cross-section of the waveguide under the homogeneous medium approximation, as described in the main text.

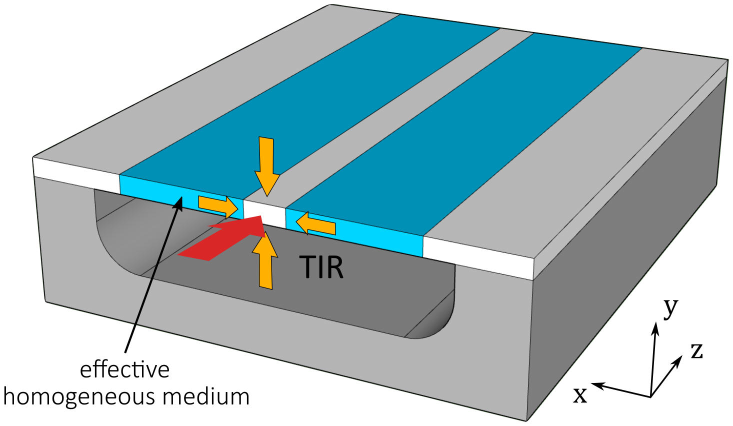

Figure 4.4: The blue region represent the homogeneous medium approximation of the lateral arms used to calculate the light confinement on the central waveguide. Red arrow indicate light propagation; orange arrows indicate Total Internal Reflection (TIR)

periodicity $a = 300$ nm.

At higher values of f_{wg}, light is more confined into the high-index layers of the multilayer, effectively lowering the bandgap energy, and preventing propagation at 1550 nm, as highlighted by the missing values of the effective index. At lower values of f_{wg}, the lower index of refraction increases the contrast with the core waveguide index (n_{SiC}), but the arms become thinner, weakening the structure. To ensure the sufficient mechanical stability of the structure, the minimum dimensions of the arms have been chosen to be above the one of similar works performed in SOI platforms, where they employed 100 nm thick arms [273]. Hence, as a compromise between confinement and minimum dimensions of the arms, we chose $f_{\text{wg}} = 0.5$ (corresponding to $L_a = L_h = 150$ nm), resulting in an effective index $n_e = 2.144$.

Waveguide width

While the behaviour of light in the waveguide can be predicted from its band structure, the effective index approach allows the use of quick standard numerical techniques, such as the simulation of the waveguide modes by eigensolvers. Figure 4.6 shows the modes supported by our structure at

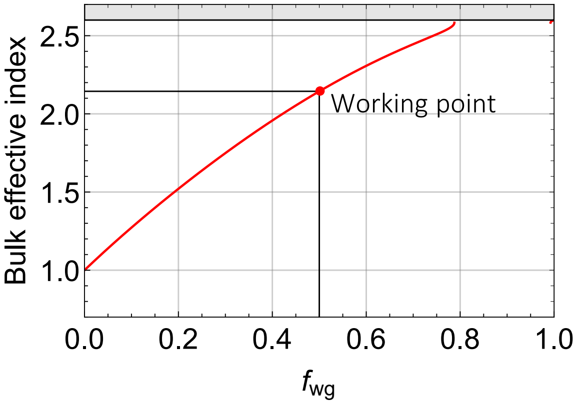

Figure 4.5: Effective index of the arm region under the effective homogeneous medium approximation.

1550 nm when the lateral arms are replaced by the homogeneous medium with $n_e = 2.144$, as calculated with Lumerical MODE.

Using this kind of simulations, in order to maximize the confinement of the fundamental TE mode, the waveguide width W_{wg} has been increased until the second TE mode became just loosely bound at 1550 nm. In a real device this second TE mode is likely to experience extremely high losses, since a very small amount of disorder would be sufficient to couple it to radiative modes and because the delocalization of the mode makes it more sensitive to the roughness on the surfaces of the lateral arms; at the same time, disorder and roughness would be less detrimental to the fundamental TE mode because of the higher confinement achieved.

The validity of the effective medium approach is underlined by Figure 4.3: the effective index of the eigenmodes compares well with the photonic bands calculated with MPB. In particular, at 1550 nm, the eigensolvers and the photonic bands predict $n = 1.967$ and $n = 1.907$, respectively, for the effective index of the fundamental TE mode.

Arms width

The lateral arm section is 2 μm wide per side and, again, it is the result of a compromise. In fact, the width is short enough to ensure the sufficient mechanical strength of the structure, while it is large enough to suppress

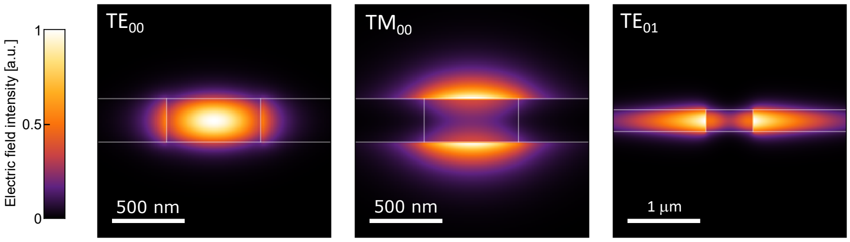

Figure 4.6: Modes sustained by the suspended waveguide at 1550 nm, as calculated by an eigensolver (Lumerical MODE) under the homogeneous medium approximation on the lateral arms. The TE_{01} mode is very loosely bound.

the coupling between the fundamental TE mode of the waveguide and the slab modes of the remaining SiC layer. The coupling is estimated using the effective index approach and Coupled-Mode Theory [16]: the coupling coefficient between two identical SiC waveguides, 650 nm wide and 300 nm thick and spaced by 2 μm of effective homogeneous material, results to be 15 m^{-1}, compared to the modal wavevector of the fundamental TE mode, $k = 1.27 \cdot 10^6\ \mathrm{m}^{-1}$.

Limitations

The main limitation of subwavelength waveguides is the loss introduced by surface roughness [277, 278] and by perturbation in the periodicity of the structure. Compared to standard ridge and rib waveguides, the lateral arms make the structure more complex and they make light travel through a much higher number of interfaces, increasing the detrimental effect of roughness. Perturbations in the periodicity of subwavelength structures, on the other hand, increase scattering losses: as explained in Section 2.7, lossless propagation relies on the destructive interference among the scattering events of all the periodically spaced subwavelength structures. Indeed, the work of ref. [279], where the effect of disorder in structures similar to the one considered here has been numerically studied, suggests that losses remain at a reasonable level if the jitter in the placement of the lateral arms does not exceed about 5 nm. In general the effect of surface roughness can be mitigated by maximizing the confinement of the fundamental mode, while the effect of disorder is lowered by choosing a working point far below the bandgap, as we have done here.

4.1.2 Other structures

Additional components are required in order to obtain a complete photonic platform. Most important functions are the coupling of light between the platform and the outside world, and the modulation of light propagating in the medium.

In the following part of this paragraph we will first describe how bends, directional couplers and microresonators can be realized with this platform, followed by the proposed design for a uniform grating coupler and by the estimation of the performance of an electro-optic modulator that exploits the strong $\chi^{(2)}$ nonlinearity of SiC.

Bends and directional couplers

The first extension to the platform comes by the introduction of bends, whose design is straightforward. Of course, the spacing between the periods have to remain as close as possible to the one chosen for the straight waveguide. For our platform, the minimum bending radius is chosen from the eigensolver simulation of the bent waveguide using the effective medium approach: a radius of 10 μm introduces a loss of around 20 dB/cm.

The design becomes more complicated when two waveguides are brought close together to realize, for instance, a directional coupler. In that case the lateral arm sections of the two waveguides will overlap and care has to be taken to ensure that the arms connect properly, especially around bent sections. Figure 4.7 shows some example designs of directional couplers, where the orange rectangles represent the holes to be etched in SiC. These designs can also be used to realize microresonators by closing one of the waveguides on itself, either in a ring or in a racetrack configuration.

Figure 4.7-a shows the easiest way a directional coupler can be realized; the straight part of this design might be removed, leaving two circular sections. A pulley-type coupler is shown in Figure 4.7-b, which can be used, for example, to obtain a strong coupling between a bus waveguide and a microring resonator realized by closing the inner bend waveguide. Figure 4.7-c shows that the design of directional couplers based on bent and straight waveguides is possible, although more complicated. Particular care has to

be taken in connecting the arms along the parabolic boundary between the straight and circular waveguides. Since there is no possibility to keep the exact same periodicity for both the straight and bent waveguide at small radii, the design is valid only at larger radii.

The correct behaviour of all these structures have been simulated with 3D-FDTD techniques, both using the complete description of the arms and under the homogeneous medium approximation.

Electro-optic modulators

A fundamental function necessary for scalable photonic platforms is the modulator, with which more complex devices like integrated Mach-Zehnder interferometers can be realized. Here we give an estimate of the performance of an electro-optic modulator that exploits the high $\chi^{(2)}$ nonlinearity of SiC.

The modulator may be realized with metal pads placed at the sides of a waveguide. A voltage difference applied to the pads will produce an electric field across the waveguide; the electro-optic effect [250], in turn, will induce a change in the refractive index of the material $n_{\mathrm{SiC}} = \sqrt{1+\chi^{(1)}}$ according to

$$n(E) = \sqrt{1+\chi^{(1)}+2\chi^{(2)}E} \simeq n_{\mathrm{SiC}} + \chi^{(2)}E \tag{4.1.1}$$

Given the width of the arms at the sides of the waveguide (2 μm per side), we model the electro-optic modulator as a 6 μm spaced parallel-plate capacitor [131]. Then, the standard voltage-length figure of merit is obtained after requiring a π phase shift:

$$L_\pi V_\pi \simeq \frac{\lambda_0 n_{\mathrm{SiC}} W}{2\chi^{(2)}} \tag{4.1.2}$$

where L_π is the total length of the modulator, V_π is the applied voltage and W is the distance between the plates.

The $\chi^{(2)}_{zzz}$ coefficient of 4H-SiC, equal to 32.8 pm/V, is particularly useful since the TE polarization would be the most affected by a transverse-polarized modulating field. The figure of merit of a modulator exploiting this coefficient would be

$$L_\pi V_\pi \simeq 36.9\ \mathrm{V}\cdot\mathrm{cm} \tag{4.1.3}$$

which is not far from the state of the art of Lithium Niobate modulators [280].

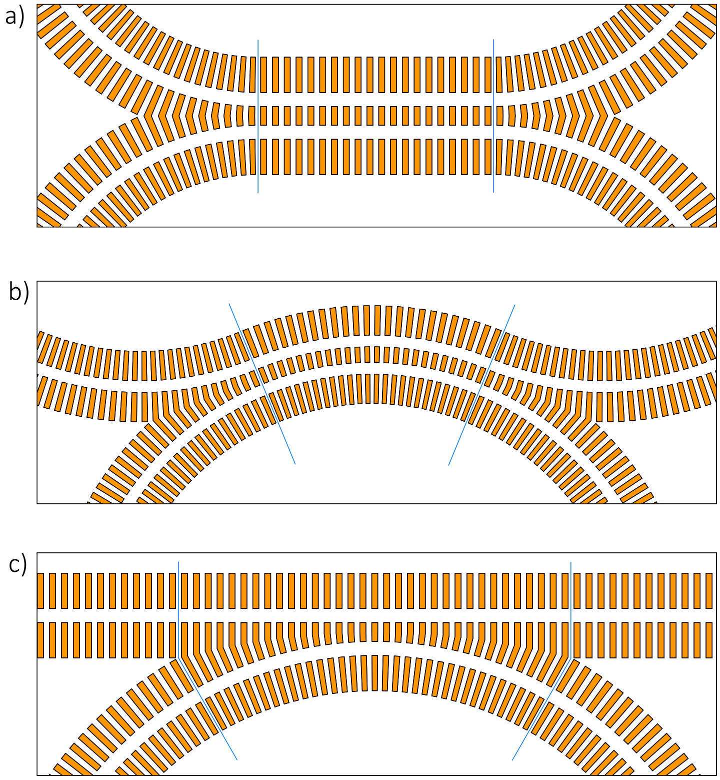

Figure 4.7: Schematic representation of subwavelength geometries for directional couplers (DC). Orange rectangles represent holes to be etched in the SiC film. Blue lines help identify different regions. a) DC based on parallel waveguides. b) DC based on concentric bends (pulley coupler). c) Straight-bent waveguide DC.

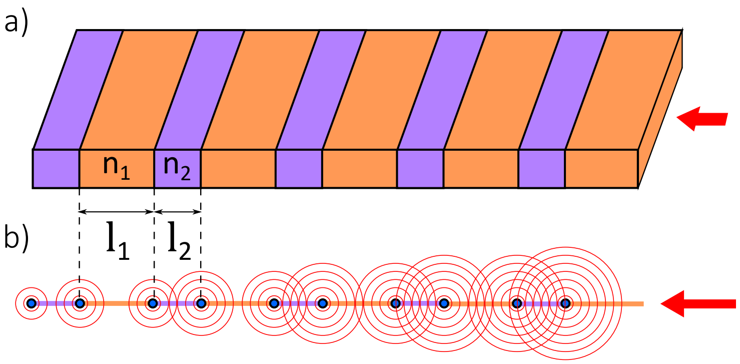

Figure 4.8: a) Schematic representation of a uniform grating coupler. b) A grating coupler can be modeled as an array of scattering points in correspondence to the interfaces of the original coupler.

This is the estimate for a modulator realized along waveguides. Making use of resonating structures, like microring resonators, can improve the performance of electro-optic modulators and reduce dramatically the footprint of such devices [281].

4.1.3 Grating coupler

Unless generation, manipulation and detection of light is performed on the same device, coupling of light with the external environment is another fundamental function to be implemented in a photonic platform. Subwavelength structures can be used to realize grating couplers, and various designs have been proposed and realized in the past [136, 282, 283], involving both uniform couplers and more complex, apodized designs.

Similarly to the waveguide, the subwavelength structures are used to implement an effective homogeneous medium, whose index of refraction can be controlled by geometric design. The advantages of using subwavelength designs is the same as for waveguides: only a single etch step is required to define the final geometry, and the index of refraction can change in different parts of the sample.

One way standard uniform grating couplers are realized is by alternating periodically, along the propagation direction, layers with different refractive indexes, as shown in Figure 4.8-a, so that the light impinging at a certain

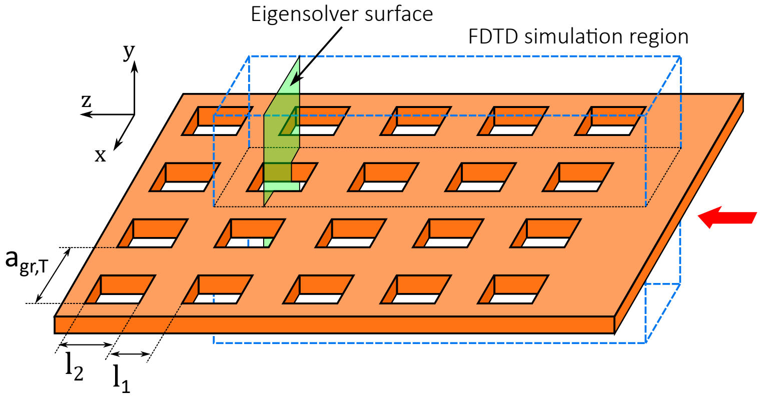

Figure 4.9: Schematic representation of a subwavelength grating coupler. The low index grooves of traditional uniform gratings are replaced with a series of subwavelength holes implementing an effective lower refractive index.

angle is scattered horizontally into the guiding slab, and vice versa. Figure 4.9 shows how subwavelength structures can be used to realize a uniform grating coupler: the lower index material (which we will call "groove") of the standard grating is replaced by a an array of holes, with transverse periodicity $a_{\mathrm{gr,T}}$ smaller than the wavelength of light. The effective index of the groove is controlled by setting the ratio between the void and filled parts of the grating.

The design parameters of the proposed uniform grating coupler are shown in Table 4.2, while in the following we report the design process that determined them, following closely ref. [282].

Theoretical model

The simplest model of a grating coupler is the one reported in Figure 4.8-b. The light travelling horizontally in the slab undergoes a series of scattering events upon the encounter of the dielectric interfaces between the high and low-index materials. This scenario can be modeled by an array of isotropic antennas, corresponding to the interfaces, whose phase relationship is set by the phase acquired by light that travels in the slab. In particular, the phase delay between two adjacent antennas $\delta\phi_{i,i+1}$ will be determined by vacuum

Film thickness (h)	300 nm
Longitudinal period ($a_{\mathrm{gr,L}}$)	1230 nm *
Longit. filling factor ($f_{\mathrm{gr,L}}$)	32.4% *
Number of periods	13
Transverse period ($a_{\mathrm{gr,T}}$)	300 nm
Transv. filling factor ($f_{\mathrm{gr,T}}$)	50%
Transverse length (W_{gr})	12 μm
Maximum transmission:	41.8% (-3.8 dB)
1 dB bandwidth:	75 nm

Table 4.2: Proposed dimensions and properties for a TE SiC subwavelength grating coupler operating around 1550 nm. The index of SiC is assumed to be 2.6. The values marked with * are obtained by numerical optimization.

wavelength of light, λ_0, and by the optical length between the two points:

$$\delta\phi_{i,i+1} = \frac{2\pi}{\lambda_0} n_{i,i+1} \Delta L_{i,i+1} \tag{4.1.4}$$

where $n_{i,i+1}$ is the *effective* index of the light mode travelling in the slab between interfaces i and $i+1$, and where $\Delta L_{i,i+1}$ is the distance between the two interfaces.

Along these lines, a uniform grating coupler optimized for coupling radiation coming at an angle α to the normal can be designed by choosing the lengths of the high and low index regions (l_2 and l_1) so that the antennas produce constructive interference in the direction identified by α. The result is summarized by the following equations

$$l_1 = \frac{\lambda_0}{2(n_1 - n_c \sin\alpha)}, \quad l_2 = \frac{\lambda_0}{2(n_2 - n_c \sin\alpha)} \tag{4.1.5}$$

where n_c is the index of refraction of the surrounding material and where n_1 and n_2 are the low and high effective indexes of light travelling in the slab.

Estimation of the effective index

In the case of the SiC subwavelength grating coupler, $n_c = 1$ (air), and $n_2 = 1.967$ is the effective index of the fundamental TE mode of light travelling in a 300 nm thick SiC slab. Similarly, n_1 is the effective index of the

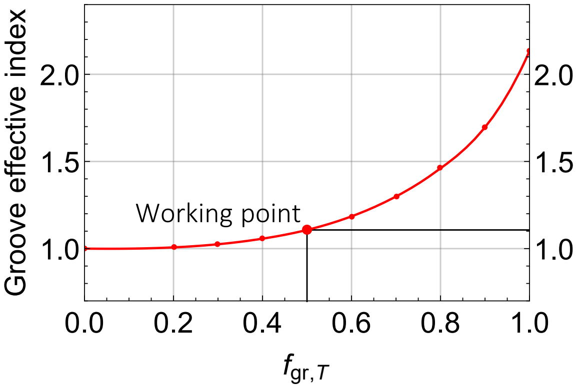

Figure 4.10: Effective index of the groove region of the subwavelength grating coupler.

fundamental TE mode of a slab made of the effective homogeneous material. The subwavelength arms of the grating grooves are longitudinally oriented with respect to the propagation direction of light in the slab, hence modeling cannot be performed with the multilayer approach described earlier.

After choosing 300 nm as the transverse periodicity of the subwavelength groove ($a_{\mathrm{gr,T}}$), its effective index was estimated using an eigensolver: n_1 was identified with the effective index of the fundamental TE mode supported by the structure identified by the green surface shown in Figure 4.9; periodic boundary conditions were used in the horizontal transverse direction. Figure 4.10 shows the effective index of the mode as a function of the horizontal filling factor $f_{\mathrm{gr,T}}$ of the subwavelength groove: as expected, at $f_{\mathrm{gr,T}} = 0$ the effective index equals the one of air (1), while at $f_{\mathrm{gr,T}} = 1$ it reduces to the one of the SiC slab (n_2). Notice that due to the continuity conditions of the electromagnetic fields at the interface, at a given filling factor the effective index is much lower for the groove than for the waveguide lateral arms (Figure 4.5). Minimum feature size requirements led to the choice of $f_{\mathrm{gr,T}} = 0.5$ and a corresponding $n_1 = 1.11$.

Using these values as effective indexes in eqs. (4.1.5), the predicted length of the high and low index regions of the uniform grating couplers are $l_1 = 798.3$ nm and $l_2 = 424.0$ nm, with a periodicity of $a_{\mathrm{gr,L}} = l_1 + l_2 = 1222.3$ nm and longitudinal filling factor $f_{\mathrm{gr,L}} = 34.7\%$.

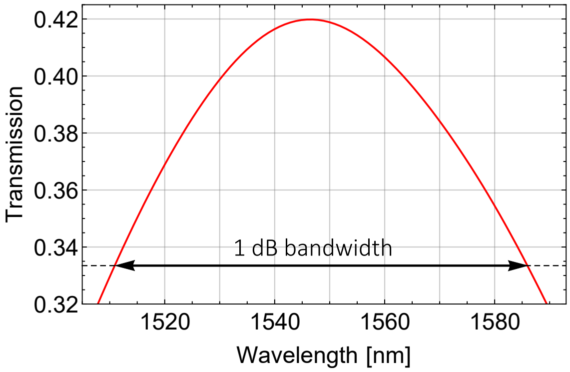

Figure 4.11: Simulated transmission of the proposed grating couper.

Numerical simulation and optimization

The dimensions of the grating coupler reported in Table 4.2 are actually the result of optimization algorithms and FDTD simulations: a single longitudinal line (dashed box in Figure 4.9) was simulated in a three-dimensional manner, using periodic boundary conditions in the transverse dimensions, setting l_1 and l_2 as free parameters and initialized with the values obtained above. The results of the simulations are very close to the results expected from the theoretical modeling of the grating coupler we just described.

Figure 4.11 shows the simulated coupling efficiency of the grating coupler as a function of wavelength. The maximum coupling efficiency at 1550 nm, $\eta_{\max} = 41.8\%$, is close to the maximum of 0.5 achievable with a vertically symmetric design, while the 1-dB bandwidth reaches 75 nm. Achieving a higher maximum efficiency, at the cost of a smaller bandwidth, is likely possible with the use of apodized designs.

The total width and length of the grating coupler were chosen to maximize the coupling efficiency with the gaussian mode of a standard telecom optical fiber.

4.1.4 Slow-light

Being one-dimensional photonic crystals, the SiC suspended waveguides described here can be adapted for slow-light operation [150]. As described in Section 2.7, the photonic band structure close to the edge of the Brillouin zone becomes gradually flat and, according to eq. (2.7.6), the group index diverges.

Higher group indexes of light increase the interaction between radiation and matter. The length of electro-optical modulators, for instance, is reduced linearly with the increase of the group index and the emission of radiation from embedded dipoles into guided waveguide modes occurs at a higher efficiency and speed. The latter effects are particularly important for the realization of deterministic sources of single photons, since any losses decrease their quality by introducing randomness and because faster emission corresponds to higher repetition rates. The Purcell Factor (PF) [148] is a measure of the enhancement of the spontaneous emission rate that a dipole experiences when it is embedded into various nanostructures. For instance, as described in ref. [153], the PF can be defined for travelling modal fields in photonic crystal waveguides as

$$\mathrm{PF} = \frac{3\pi c^3 a}{V_{\mathrm{eff}} \omega n^3 v_g} \tag{4.1.6}$$

where c is the speed of light, n is the refractive index of the host medium, v_g is the group velocity of light at the position of the dipole, and where V_{eff} is an effective mode volume defined in terms of the modal field as

$$V_{\mathrm{eff}} = \frac{1}{\max(\epsilon(\boldsymbol{r})|\boldsymbol{e}(\boldsymbol{r})|^2)} \tag{4.1.7}$$

where $\epsilon(\boldsymbol{r})$ is the dielectric function defining the waveguide structure, $\boldsymbol{e}(\boldsymbol{r})$ is the modal field associated to it, and $\boldsymbol{r}$ is allowed to vary over the whole unit cell.

Our platform can achieve slow-light operation naturally by increasing the periodicity of the waveguides. In fact, as seen for instance for the multilayer, according to eq. (2.7.11), increasing the periodicity lowers the bandgap, moving it closer to the working energy, so that the working point lives on a flatter region of the fundamental TE mode dispersion.

Figure 4.12 shows the change in the group velocity as a function of an increased periodicity a' of the system, when all the other geometric parameters are kept equal (in particular, the longitudinal filling factor f_{wg} is kept equal to 0.5). Using the MPB software suite [276], the plot was obtained by calculation of the group velocity of the fundamental TE mode of the waveguides at 1550 nm at increasing values of a'. The modal fields obtained from the same simulations were also employed to calculate the PF from equation

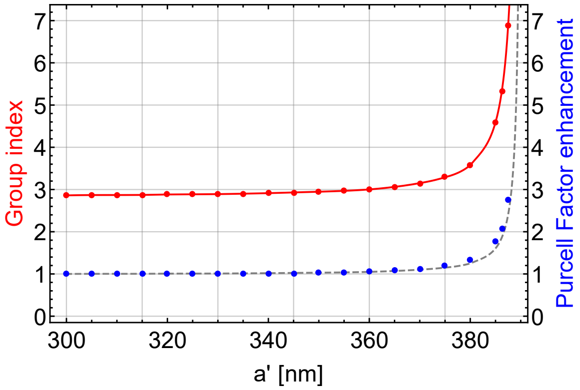

Figure 4.12: Red (dots and line): group velocity of the suspended waveguide as a function of the increased periodicity a'; blue (dots): enhancement of the Purcell factor of the suspended waveguide as a function of the increased periodicity a'. The dashed line represents the enhancement of the group index alone, i.e. $n_g(a')/n_g(a)$.

(4.1.6) as a function of a'. Figure 4.12 also reports the enhancement of the PF, i.e. $\mathrm{PF}(a')/\mathrm{PF}(a)$, with $a = 300$ nm. The enhancement is mostly determined by the decrease of the group velocity v_g (dashed line), since the change in the effective mode volume V_{eff} is almost completely compensated by the increase of a at the numerator of eq. (4.1.6).

Mode-matching is important to reduce unwanted reflections at the transition between normal and slow-light regimes [150]. In our platform the cross-sections of the modal fields of normal and slow-light waveguides is mostly the same, hence the transition region is easily realized by a simple adiabatic change in the periodicity of the waveguide. The absence of unwanted reflections in this case was confirmed by 3D-FDTD simulations.

4.1.5 Experimental realization

Two 3C-SiC samples have been fabricated and measured in order to test the platform and, in particular, to determine the optical losses of light travelling in the suspended waveguides.

The general sample design comprises a series of devices containing microring resonators similar to the one schematically pictured in Figure 4.13: once a microring resonator is known to be either in the overcoupling or un-

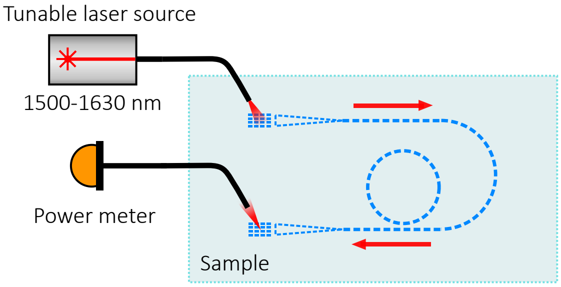

Figure 4.13: Schematic representation of the fabricated samples and measurement setup. Dashed lines represent suspended waveguides.

dercoupling regime, a transmission measurement is sufficient to determine the attenuation coefficient of light travelling inside the ring. In particular, from eqs. (2.8.5) and (2.8.20), the value of the resonance Q-factor and minimum transmission can be used to determine the attenuation coefficient α. This is a particularly convenient measurement of the intrinsic waveguide losses, since it does not depend on the total waveguide length nor on the coupling efficiency to the sample, that might be difficult to properly estimate experimentally due to possible misalignments. The microrings are coupled to U-shaped bus waveguides which bring light from and to grating couplers spaced by 250 μm, for coupling to standard fiber arrays.

Figure 4.13 also schematically represents the setup used to perform transmission measurements: radiation from a tunable infrared laser source (Santec TSL-510) is launched inside the sample and the outcoupled radiation is measured with a power meter.

Two samples were fabricated using a lithographic procedure similar to the one reported in ref. [272]. Scanning Electron Microscope (SEM) images of the first fabrication iteration, shown in Figure 4.14, highlighted the presence of detrimental fabrication defects, most likely determined by the use of 100 nm arms in the design and by a strong over-etch of the SiC film. It was not possible to measure any transmitted radiation through this first sample.

The second sample fabrication resulted in a 260 nm thick SiC layer, hence two sets of devices were designed where the nominal width of the waveguide was increased from 650 nm to 750 and 800 nm. Moreover, in order to compensate for over-etching, a preemptive offset was introduced in the design of the etching geometries. The radius of the microring was chosen to be 80 μm in order to have a negligible contribution from bending losses.

The gaps at the coupling point between the bus and ring waveguides were chosen to allow measurements assuming a large uncertainty in the intrinsic losses of SiC. In particular, considering 750 nm wide waveguides, a gap of 350 nm would result in a critically coupled ring with propagation losses equal to 25.5 dB/cm, while a gap of 800 nm would result in critical coupling with 0.675 dB/cm losses. By the same token, with 800 nm wide waveguides, critical coupling occurs with 39.1 dB/cm losses for a 350 nm gap and with 0.686 dB/cm losses for a 800 nm gap.

The SEM images of the newly fabricated sample (Figure 4.15) show that the waveguides were free from the macroscopic defects affecting the first iteration. Transmission measurements of the second sample, however, revealed very high propagation losses. The total overall transmission of the sample was very low, in the order of 10^{-4}; moreover, only rings with the smallest gaps exhibited discernible resonances in the transmission measurements, as seen for instance in Figure 4.16. Values of the measured Q-factors of the visible resonances, which assume the under-coupling condition, ranged between roughly 5000 and 7000, resulting in propagation losses in excess of 100 dB/cm.

The very high losses, as explained at the beginning of this section, are attributed mainly to the very low quality of the lower surface of the 3C-SiC thin film, which is originally grown heteroepitaxially on Silicon, with crystalline mismatch; nonetheless, the role of disorder and surface roughness may also play an important role. In any case, the measured losses are consistent with the ones of previous suspended SiC waveguides realized with a similar fabrication process, where losses around 30 dB/cm were obtained [272, 284], and could be lowered only when large cross-section waveguides were employed [272].

4.2 Silicon Nitride integrated Bragg filters based on external geometries

As described in Chapter 3, Four-Wave Mixing in microring resonators can be used to produce quantum states of light in the form of signal-idler photon pairs emitted from resonances adjacent to the pump one. The process relies on strong coherent pump beams, with powers in the order of $1 \cdot 10^{-3}$ W; on the other hand, the pair generation rate obtained with Silicon mi-

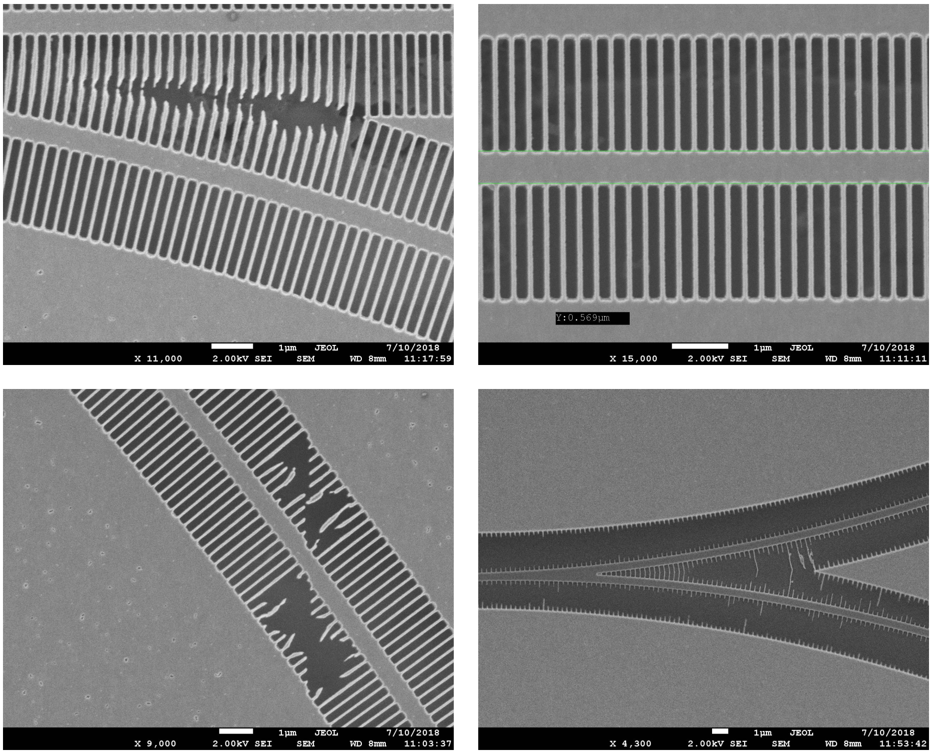

Figure 4.14: Scanning electron microscope images of the first fabricated sample, exhibiting defects. Top-left) Coupling region between a microring and a straight waveguide. Top-right) straight waveguide: the width of the waveguide and the thickness of the arms was smaller than expected. Bottom-left) Defects caused by stitching. Bottom-right) A Y-splitter: most of the arms are missing or broken.

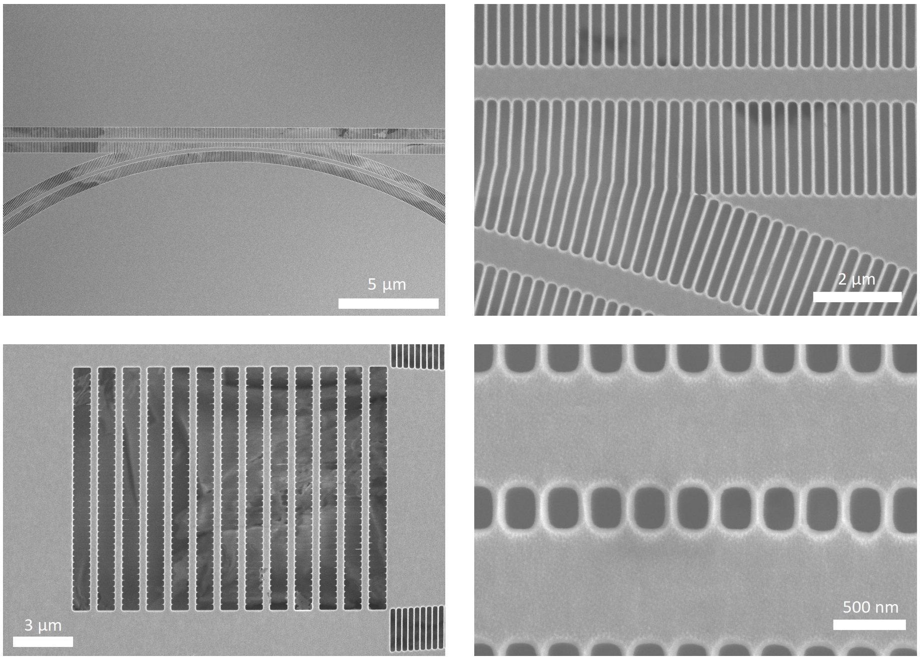

Figure 4.15: Scanning electron microscope images of the second fabricated sample. Top-left) Microring-waveguide coupling region. Top-right) Detail of microring coupling region. Bottom-left) Grating coupler: the longitudinal arms are absent. Bottom-right) Gap between bus waveguide and microring.

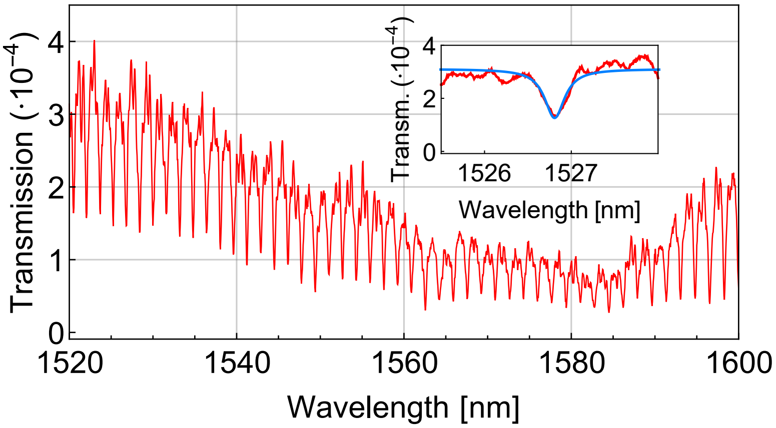

Figure 4.16: Transmission measurement (50 pm resolution) of a Silicon Carbide microring based on 800 nm wide waveguides and with 250 nm gap. Inset (10 pm resolution): a Q-factor of 5400 was extracted from the the Lorentzian fit shown by the blue line.

crorings, for instance, does not exceed 10^8 pairs/s, even when using charge sweeping techniques [189], so that the actual generated power is in the order of $10 \cdot 10^{-12}$ W. The ideal critically coupled microring resonator completely suppresses the pump beam in continuous-wave operation; real attenuations, however, are in the order of 30 dB or less. This is due, for instance, to the residual transmission of a real ring, never perfectly critically coupled, or by the spectrum of the laser source being broad, especially for pulsed operation. Hence, in the best case scenario, the strength of the pump beam is five orders of magnitude larger than the generated fields, and usually it is far stronger. This implies that selective attenuations of 100 dB or more have to be performed on the pump radiation [264, 285]; in addition, signal and idler frequencies typically lie few nanometers apart from the pump frequency, requiring a strongly selective filter.

While usually this can be achieved fairly easily outside the sample using bulk optical components (such as diffraction gratings and dielectric filters), the realization of a scalable photonic platform requires an integrated approach. Promising paths are based on integrated Bragg filters [264], cascaded Mach-Zehnder interferometers [285] or coupled ring resonators (Coupled-Resonator Optical Waveguide, CROW) [286].

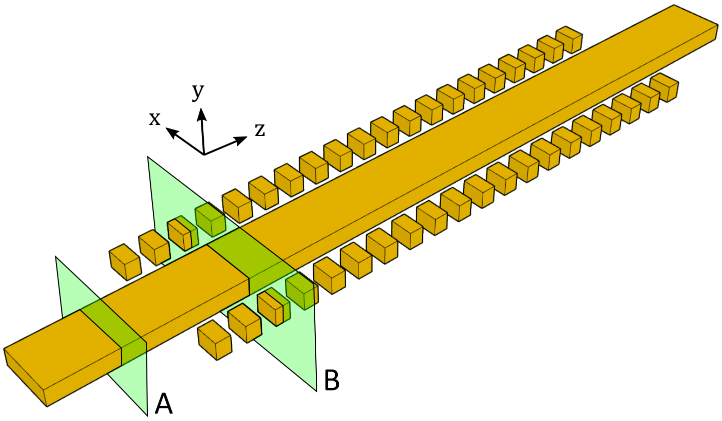

Figure 4.17: Scheme of the pillar-based integrated Bragg filter. The surfaces A and B identify the cross-sections where eigensolver simulations have been performed.

The present section concerns the study and preliminary realization of a novel integrated Bragg filter for attenuating 1600 nm radiation, where the periodic modulation of the effective index of refraction travelling in a waveguide is not performed by modulating the width or the refractive index of the waveguide itself, as usually done, but by the presence of external geometric structures that interact with the lateral tails of the traveling mode. Since integrated Bragg gratings have to be millimeters to centimeters long in order to achieve the required attenuations, losses play an important role on the device performance; this kind of geometry allows to maintain a constant cross-section of the central waveguide, reducing the contribution of surface roughness and disorder introduced by standard geometry/index modulations.

4.2.1 Design

The scheme of the proposed geometry of the integrated Bragg filter is shown in Figure 4.17.

Two approaches have been followed to determine the appropriate dimensions of the structure. The first relied on modeling the effect of the external pillars as a perturbation of the fundamental mode of the central waveguide, and approximating the structure with a multilayer; the second approach relied on the calculation of the band structure of the Bragg filter, treated as a one-dimensional photonic crystal. Although the former approach is easier to use to determine the properties of the fundamental stop-band, the latter is necessary to obtain insight on additional features absent in standard filters based on the modulation of the waveguide cross-section, such as possible couplings between the fundamental and higher order modes.

The behaviour of light traveling in the structure can be approximated with a multilayer. The low index layer, n_1, corresponds to the effective index of light travelling in the original central waveguide (surface A of Figure 4.17); the high index, n_2, corresponds to the effective index of light travelling in a system composed of three waveguides (surface B of Figure 4.17): the central one is equal to the previous case, while the two lateral waveguides are obtained by extending the transverse cross-section of the pillars along the propagation direction. The thickness l_1 and l_2 of the layers are respectively equal to the distance between adjacent pillars along the propagation direction (z), and to the length of the pillars.

The values of the individual effective indexes (and thus the index contrast $\Delta n/n$, where $\Delta n = |n_2 - n_1|$ and $n = (n_1 + n_2)/2$) will be influenced by the transverse dimensions of the structures; the lengths l_1 and l_2 of the two different sections will be determined in turn from the indexes n_1 and n_2 so that they are both quarter-wave layers. As discussed in Section 2.7, the quarter-wave stack is the multilayer that maximizes the width of the photonic bandgap for a given index contrast, hence introducing the strongest attenuation in the middle of the bandgap. Usually the difference between the indexes will be small, so that with a very good approximation $n_1 \simeq n_2 \simeq n$ and $l_1 \simeq l_2 \simeq \lambda/(4n)$. The two indexes can be easily obtained, using an eigensolver, from the effective index of the fundamental TE mode supported by the cross-sections A and B of Figure 4.17. Once the indexes are known, all the properties of the stop-band can be easily calculated using the equations of the multilayer outlined in the previous section. This simple approach, however, fails to take into account effects related to higher order modes, as we are about to discuss.

Ideally, as shown in eq. (2.7.13), the largest possible contrast would be preferable to maximize the attenuation within the bandgap and to minimize the length of the filter. Using the present geometry, this can be accomplished by either bringing the pillars closer to the central waveguide, or by increasing the width of the pillars themselves. In the former case, the minimum gap between the waveguide and the pillars is set by the resolution of the lithographic process that is used to fabricate the device, usually above 100 nm for optical lithography. In the latter case, the additional light confinement given by the increased width of the pillars would bring higher-order TE and TM modes closer in energy to the fundamental TE mode. This is a particularly important issue: disorder, surface roughness and the periodicity of the structure itself may couple the fundamental TE mode to these other modes, inducing a significant transfer of energy, especially in millimeter-long devices.

In order to correctly take into account the effect of higher order modes, an approach based on perturbation theory [16] can be employed. In general, the dielectric function associated with the Bragg filter is given by a term that is uniform along the propagation direction, and a term that takes into account the periodicity of the structure:

$$\epsilon(x, y, z) = \epsilon(x, y) + \Delta\epsilon(x, y, z) \tag{4.2.1}$$

When the second term represents a small perturbation, the first term can be used to calculate the set of eigenmodes of the uniform structure; then, the second term may perturbatively induce coupling between the co-propagating or counter-propagating eigenmodes of the uniform structure, as described in detail in ref. [16] and as we will briefly describe here.

Consider the pillar structure. If $\epsilon_2 = \sqrt{n_{\text{core}}}$ and $\epsilon_1 = \sqrt{n_{\text{clad}}}$ are the dielectric constants associated to the high and low refractive indexes of the structure materials, we have that

$$\begin{cases} \epsilon(x, y) = \epsilon_2 \quad (x, y) \in A \\ \epsilon(x, y) = \frac{\epsilon_2 + \epsilon_1}{2} \quad (x, y) \in B \\ \epsilon(x, y) = \epsilon_1 \quad \text{otherwise} \end{cases} \tag{4.2.2}$$

where A and B are the regions highlighted in Figure 4.18, while $\Delta\epsilon(x, y, z)$ will be different from zero only in region B, and alternating between $\pm(\epsilon_2 - \epsilon_1)/2 = \pm\Delta\epsilon/2$ depending on whether the point (x, y, z) falls within a pillar or in the region between adjacent pillars.

Regarding the uniform part, the TE eigenmodes are schematically represented in Figure 4.18; the TM eigenmodes will have a similar intensity profile and slightly different dispersions. Assuming $l_1 = l_2$, the function $\Delta\epsilon(x, y, z)$

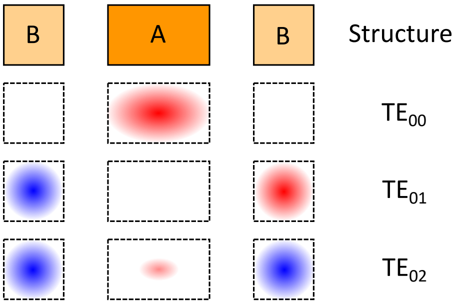

Figure 4.18: Top: scheme of the uniform structure used to calculate the eigenmodes of the Bragg filter; the background has refractive index $n_{\mathrm{clad}} = 1.44$, region A and B have refractive indexes $n_A = n_{\mathrm{core}} = 2$ and $n_B = 1.743$, as described in the text. The first three supported modes are schematically represented below, with red and blue representing positive and negative horizontal electric field component.

is modulated with a square wave, and it can be expanded in Fourier series:

$$\Delta\epsilon(x, y, z) = \sum_{m=1}^{\infty} c_n f(x, y) \sin\left((2m-1)\frac{2\pi}{a}z\right) \tag{4.2.3}$$

where $c_m = 1/(2m-1)$. Without getting into the mathematical details, which involve overlap integrals between the different modes, the first spatial harmonic ($m = 1$) of the dielectric function may couple modes that differ by the wavenumber $K = 2\pi/a$, where a is the periodicity of the structure. Analogously, higher spatial harmonics couple modes differing by $3K$, $5K$, and so on; these higher contributions are typically negligible both because the amplitude coefficients c_m decrease rapidly with m, and because, for the structure considered here, the eigenmodes' wavenumbers actually differ by about K, as seen shortly.

Figure 4.19 shows schematically the dispersion of the first three TE eigenmodes of the Bragg waveguide propagating both in the forward and backward direction. The thick blue arrow represents the strongest coupling contribution from the periodicity of the Bragg, responsible for the opening of the main filter stop-band: the forward propagating fundamental TE mode, with wavenumber $k = \pi/a$ for a quarter-wave stack, is coupled to its backward propagating counterpart, as expected from a Bragg filter (indeed, K is ex-

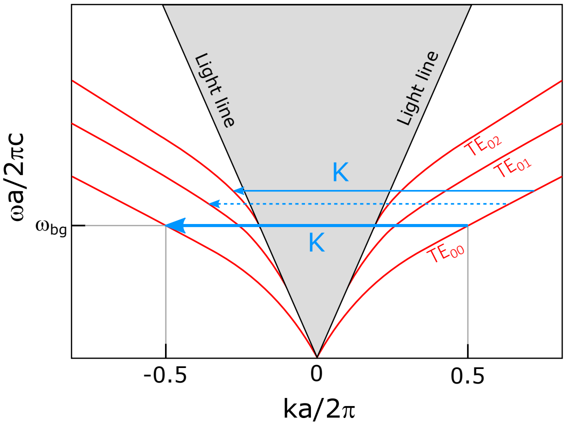

Figure 4.19: Schematic representation of the TE band structure associated to the uniform part of the Bragg grating. Blue arrows represent possible couplings introduced by the dielectric periodicity which may open photonic bandgaps; dashing indicate the the coupling is forbidden by symmetry.

actly equal to the difference between k and $-k$).

At higher energies, however, additional couplings are possible. In particular, since at the input of the filter light is propagating in the fundamental mode, we are interested in the coupling processes that transfer energy to other modes. Such processes are highlighted by the other arrows in Figure 4.19. When these processes happen, the main consequence is the appearance of additional stop-bands at shorter wavelengths (higher frequencies), whose width is proportional to the coupling strength. Notice, however, that the symmetry of the modes plays an important role: the coupling strength between TE and TM modes and between TE modes with different even/odd symmetry will be equal to zero, because of the overlap integrals mentioned before will vanish, forbidding the process. Coupling processes mediated by higher spacial harmonics (3K, 5K, and so on), not shown in the figure, occur at much higher frequencies than the ones we are interested in here.

At the end of the day, in our case, the only additional coupling process of concern is the one that couples the fundamental TE mode to the backward propagating third, even, TE mode (indicated by the other continuous blue arrow) because it may be responsible for the appearance of a second stop-band close to the fundamental one. Indeed, although not meant to be used as a filter, the structure fabricated and characterized in ref. [287], similar to the one considered in this section, exhibits an additional stop-band at shorter wavelengths.

Figure 4.20 shows some example band structures of some Bragg filters designed here. The photonic bandgap, at the right edge of the Brillouin zone, is small and below the resolution of the plot; the crossing between the fundamental and second TE mode occurs at wavelengths shorter than the fundamental wavelength by more than 50 nm, and it is suppressed because of the modes' different symmetry (notice that the anticrossing seen in the central and right plots is only apparent, and given by the low horizontal resolution of the simulations). The anticrossing of interest, the one between the fundamental and third TE mode, does not happen below the light-line for the waveguides shown in Figure 4.20, and it is always more than 100 nm away even for the most confining fabricated waveguides. Therefore, should the filter be used in conjunction with typical microring resonators, additional stop-bands would be far enough not to interfere with signal and idler photons generated by Four-Wave Mixing, since their frequencies usually lay closer to the pump one; the stop-bands might represent a more serious issue for applications involving wider frequency spans, such as optical frequency combs.

An additional, very similar structure was studied, as well: instead of placing isolated pillars at the side of the central waveguide, the pillars may be all connected together, forming a dielectric comb-like structure, as illustrated in Figure 4.21. This second filter may be more robust against adhesion problems affecting individual pillars and it works similarly to the one described above; on the other hand, it is slightly more confining and additional stop-bands may be brought closer to the fundamental one.

4.2.2 Experimental realization

While the filter described here can be realized in any standard photonic platform, the considerations made in the previous paragraph have been applied to design Silicon Nitride (SiN) devices, because of the possibility of fabricating and characterizing a test sample. This sample has been fabricated without the use of an annealing process to reduce losses due to OH imputites; this was the reason to target attenuation of 1600 nm radiation instead of the more usual 1550 nm wavelength.

Tables 4.3 and 4.4 give the design parameters of some of the Bragg filters

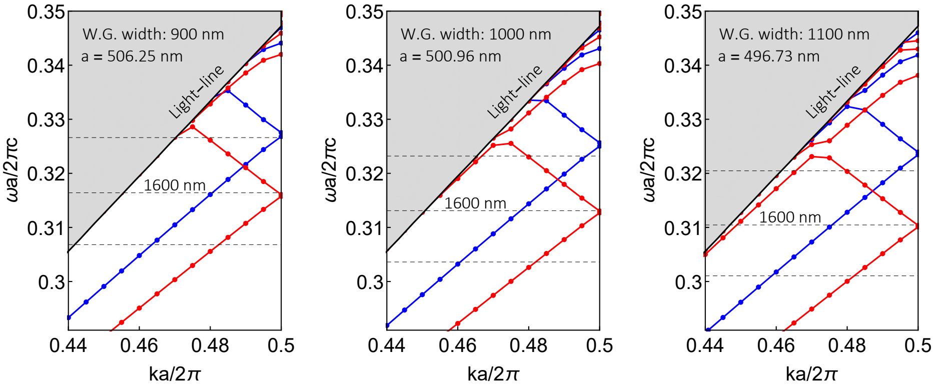

Figure 4.20: Simulated band structures of three different pillar-based Bragg filters. Red: TE bands; Blue: TM bands. The anticrossing between the fundamental mode and the second TE mode is an artifact given by the low resolution of the simulation, as it is forbidden by the symmetry of the two modes. The real anticrossing of interest would be the one between the fundamntal and third TE modes, but it is above the light-line. Dashed lines represent the energy of 1550, 1600 and 1650 nm radiation.

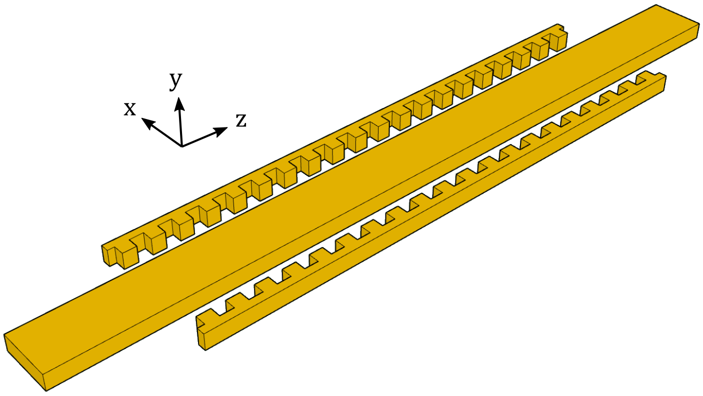

Figure 4.21: Scheme of the comb-based integrated Bragg filter.

Device	WG. width [nm]	a [nm]	gap [nm]	Periods	Stop-band [pm]
A22	1000	500.96	300	2100	3130
A32	1100	496.73	300	2500	2650
B7	950	503.60	300	2400	2800
B19	1050	498.62	350	4800	1370

Table 4.3: Design parameters of filters whose measurement are reported in Figures 4.23 and 4.24. A and B refer to comb-like filters and pillar-based filters. The number of periods targets 50 dB attenuation. Group A devices have 150 nm wide comb rods and 200 nm wide extrusions (total comb width equal to 350 nm)The pillar width of group B devices is 400 nm.

Device	WG. width [nm]	a [nm]	mod. width [nm]	Periods	Stop-band [pm]
C2	800	512.50	30	1900	3400
C3	800	512.50	50	1100	6100

Table 4.4: Parameters of width-modulation filters whose measurement are reported in Figure 4.25. The number of periods targets 50 dB attenuation.

that have been fabricated. Groups A, B and C refer to comb-like filters, pillar filters and traditional width-modulation filters, respectively. The parameters of all the fabricated devices are found in Appendix A.

Various waveguide widths have been taken into account due to the different degree of confinement they provided. Although the geometries of the actual sample were defined with electron beam lithography, the minimum feature size, set often by the minimum gap between the central waveguide and the pillars, was kept above the limits for optical lithography. The tables include also the estimation of the photonic bandgap, while the 3 dB stop-band, defined as the range of wavelengths for which the total attenuation is within 3 dB from the maximum attenuation at the center of the stop-band, is always equal to 35.58% of the photonic bandgap. In order to reduce the footprint of each device, the filters included in the sample targeted a moderate 50 dB attenuation: a large number of devices was preferred to higher attenuations in order to simplify measurements and to sample a larger parameter space with this first fabricated sample. Traditional filters based on modulation of the waveguide cross-section were fabricated, as well, for comparison.

Figure 4.22 shows the schematic representation of one of the fabricated

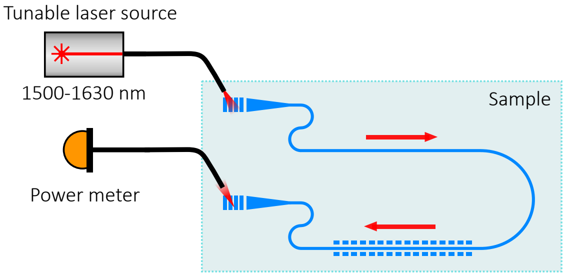

Figure 4.22: Schematic representation of the fabricated devices and measurement setup. The S-shaped waveguides are used to eliminate higher-order modes, as described in the main text.

devices and the setup used to perform transmission measurements. Light is coupled with uniform grating couplers, while tapers adiabatically transform the grating mode to the one of the waveguides. As the waveguides composing the Bragg filters were often multi-moded, high order modes were filtered by the S-shaped waveguides sections: both the tight bends and the narrow width of the waveguides (800 nm) ensure the guided propagation of the fundamental TE mode only. The fabrication steps can be found in ref. [288].

Preliminary transmission measurements were performed with an experimental setup very similar to the one described in Section 4.1. Representative examples of transmission measurements are shown in Figures 4.23, 4.24 and 4.25. While the filter stop-band is clearly discernible in all the measurements, the real behaviour of the filter differs from the expected one. The stop-band appears at shorter wavelengths than expected (we targeted 1600 nm), and it typically has maximum attenuation lower than 40 dB. The black lines overlaid on the experimental data represent the expected complete and 3-dB stop-bands: although the stop-band size corresponds roughly to the one expected, the transmission curve does not posses the clear shape expected from theory, as in Figure 2.22 of Paragraph 2.7.2. Finally, the power transmitted at frequencies outside the stop-bands is roughly one thousand times lower than the power at the input of the sample (not shown in the transmission plots), which, however, did not seem to depend on the length of the measured device. No additional stop-band was observed at shorter wavelengths in the whole tunability range of the laser source (1500-1630 nm).

All-Pass microring resonators have been included in the sample, as well,

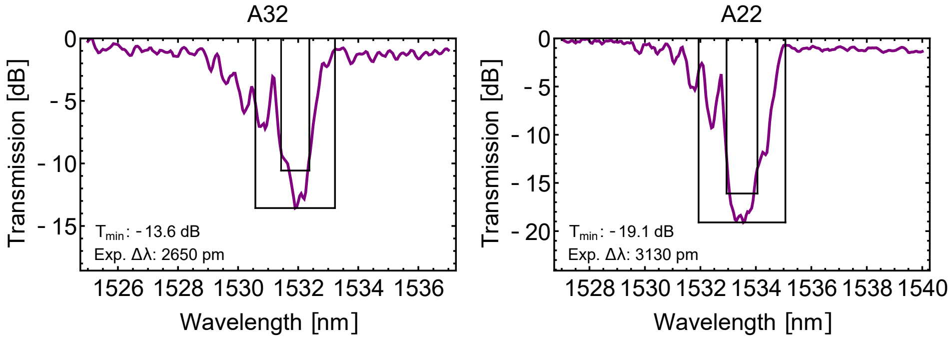

Figure 4.23: Representative transmission measurements of comb-like filters. The black vertical lines represent the expected full stop-band and 3-dB bandwidth of the nominal design. The 0 dB level corresponds to the maximum measured transmission to highlight the effect of the filter.

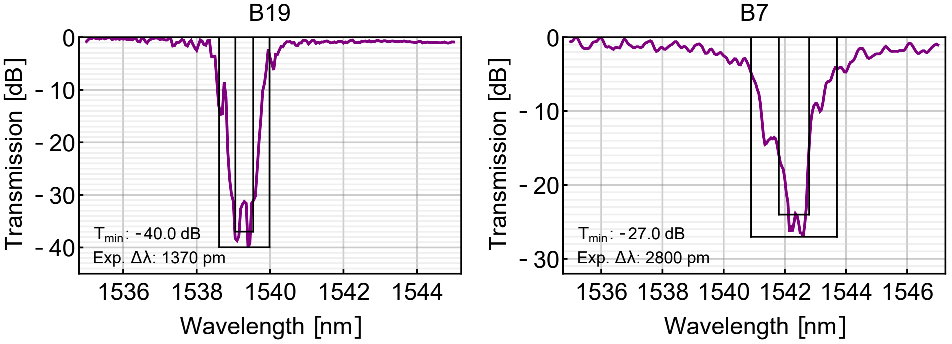

Figure 4.24: Representative transmission measurements of pillar-based filters. The black vertical lines represent the expected full stop-band and 3-dB bandwidth of the nominal design. The 0 dB level corresponds to the maximum measured transmission to highlight the effect of the filter.

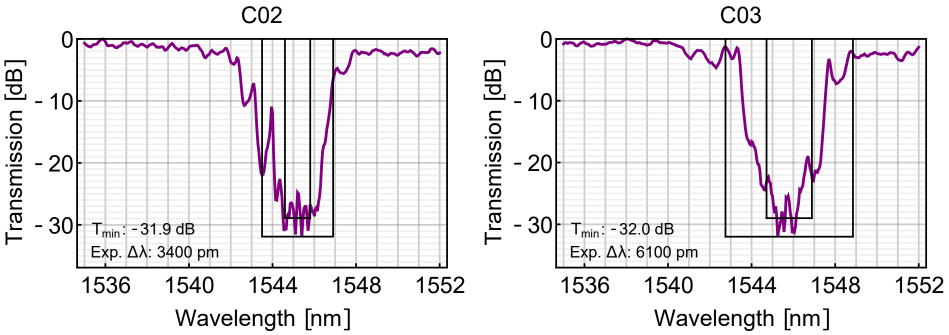

Figure 4.25: Representative transmission measurements of width-modulation filters. The black vertical lines represent the expected full stop-band and 3-dB bandwidth of the nominal design. The 0 dB level corresponds to the maximum measured transmission to highlight the effect of the filter.

and connected to grating couplers with a U-shaped waveguide, similarly to the scheme used for the suspended waveguides (Figure 4.13), but with the addition of the same S-shaped filters used for the Bragg filter devices. Although the overall transmission through the sample was equally low for the rings and for the Bragg filter devices, the resonances at 1540 nm were close to critical coupling and exhibited Q-factors of 40’000, corresponding to an attenuation coefficient $\alpha = 0.93$ dB/cm. These measurements imply that losses are not caused by normal waveguides; it is also unlikely that the Bragg filters themselves caused the issue, because the overall transmission of ring devices was low and similar to filter devices, despite the absence of the Bragg filters themselves.

While measurements of the thickness of SiN showed that the layer was thinner than expected, which could explain the shift of the stop-band at shorter wavelengths, no SEM images of the filters are available at the time of writing, so it is difficult to understand what caused the issues in the transmission. The high losses might be explained by the smaller-than-expected cross-section of the S-shaped filters: high bending losses might be the result of the lower confinement of the waveguides. Moreover, disorder in the pillar size or misplacement due to adhesion problems might be responsible for the distorted stop-band transmission dip and to the overall lower attenuation of the filter.

In conclusion, further experimental tests are required in order to better characterize the Bragg filters described in this section and to proceed to a new iteration of the devices; however, the fact that the width of the stop-band is comparable to the expected one makes this approach promising for realizing high-attenuation Bragg filters based on external structures.

Chapter 5

Collapse speed of a delocalized photon state

According to Quantum Mechanics [252, 253, 289], the evolution of a particle state, represented by a wavefunction $|\psi\rangle$, is determined by two principles.

The first is represented by the *Schrödinger equation.* A closed system will produce a deterministic evolution of the wavefunction $|\psi\rangle$, according to

$$i\hbar\frac{\partial\,|\psi(t)\rangle}{\partial t} = \hat{H}\,|\psi(t)\rangle \quad \longrightarrow \quad |\psi(t)\rangle = e^{-i(\hat{H}/\hbar)t}\,|\psi_0\rangle \quad \text{(Shrödinger equation)} \tag{5.0.1}$$

Moreover, the linearity of the Shrödinger equation implies that a complex linear superposition of solutions will be another solution for the evolution of the system.

The second principle is the *reduction postulate*: when a measurement is performed on the wavefunction, the quantum state will “collapse” at random on one of the eigenstates $|\psi\rangle_n$ of the observable that describes the measurement; the probability of each outcome, p_n, is determined by the expansion of the state on the set of eigenstates before the measurement.

$$|\psi\rangle = \sum_n c_n\,|\psi\rangle_n \;\longrightarrow\; |\psi\rangle_n\,, \quad p_n = |c_n|^2 \quad \text{(reduction postulate)} \tag{5.0.2}$$

According to Quantum Mechanics, the reduction happens *immediately after* the end of the measurement process.

During the 5ft Solvay’s Conference in 1927 [289, 290], Einstein was concerned with the case of a particle experiencing diffraction at a pin hole and subsequently being detected, say, at two points on a screen placed after the pin-hole. While conservation of the energy implies that the particle can be detected at only one of the points, the concerning case for Einstein was when the possible detection events were space-like separated. In fact, there is no possibility of sub-luminal coordination between them, in this case. Quantum theory gives an answer to this dilemma with the statistical interpretation of the detection process, i.e. the reduction postulate. Still, if one assumes that the wavefunction has a physical meaning (realism), some doubt might persist on whether or not some sort of collapse process might be involved in the measurement, and whether or not this process takes a finite time.

As discussed in more detail in Section 1.3, photons have been used in the past to test various properties of Quantum Mechanics [291], such as the speed of the collapse. For instance, entangled pairs of photons have been used extensively to test the nonlocality of Quantum Mechanics through violations of Bell's inequalities [99], from the seminal works of S. Freedman et al. [5] and A. Aspect et al. [163, 164], to more recent results where almost all the loopholes have been closed [226, 292], or where large distances of up to 144 km have been used [293]. A lower bound of $10^4\,c$ has also been put on the speed of nonlocal Bell correlations [294], as well. In all these experiments, however, two separate particles have been used to test the speed of the collapse of internal degrees of freedom, such as the polarization of the photons. Instead, no experiment investigated the collapse of a single delocalized particle. This scenario is different with respect to experiments based on EPR pairs, where the wavefunction associated to the individual particles' position is in a factorized state: the separation of a single particle's wavefunction in space, through quantum superposition, might require coordination between its distant parts, possibly inducing a delay in the collapse upon detection, while localized separated particles might be detected “in place”, with no influence on the collapse.

To this purpose, for instance, a photon can be put in a superposition state at a Beam Splitter (BS) and the two resulting parts of its wavefunction can be sent to separated single-photon detectors. Indeed, this chapter describes an experiment aimed at testing whether or not the collapse time of a spatially separated single-photon state takes a time. The absence of coincident detection events for this scenario (*antibunching*) has been already confirmed [165, 295], also with setups that include space-like separated detectors [296]. In all these and other single-particle experiments, however, the measurement of the time at which the detection events were taking place was not precisely recorded.

Section 5.1 gives the formalism used to describe the spatial separation of light states and the detection process, while Section 5.2 describes the setup, the results of the experiment, and it is concluded with a discussion on the lower bound put on the speed of the collapse for single photon states.

This chapter is based on ref. [297], published with the contribution of the Author.

5.1 Conceptual scheme

As we have seen in Sections 2.2 and 2.4, the kind of light that interacts with a Beam Splitter (BS) has important consequences on the outcomes of the process.

In particular, as we have seen in Paragraph 2.4.3 for the Hanbury Brown and Twiss interferometer, a single-photon Fock state $|1\rangle$ is put into a superposition output state, as in eq. (2.4.13), while a coherent state $|\alpha\rangle$ is left in a factorized state, as in eq. (2.4.17). The results discussed there can be summarized here with the following equations

$$\begin{aligned} |\psi\rangle_{\text{in}} = |1\rangle \quad &\longrightarrow \quad \hat{U}_{\text{BS}}\,|1\rangle = \mathcal{T}\,|1\rangle_{\text{T}} + \mathcal{R}\,|1\rangle_{\text{R}} \\ |\psi\rangle_{\text{in}} = |\alpha\rangle \quad &\longrightarrow \quad \hat{U}_{\text{BS}}\,|\alpha\rangle = |\beta\rangle_{\text{T}}\,|\gamma\rangle_{\text{R}} \end{aligned} \tag{5.1.1}$$

where $|\mathcal{T}|^2$ and $|\mathcal{R}|^2$ indicate the transmittance and reflectance of the BS, $\mathcal{R}$ and $\mathcal{T}$ being complex numbers, where T and R label the transmitted and reflected output beams and where $|\beta\rangle_{\text{T}}$ and $|\gamma\rangle_{\text{R}}$ are coherent states such that

$$\beta = \mathcal{T}\alpha, \quad \gamma = \mathcal{R}\alpha \tag{5.1.2}$$

Thermal light can also be described in terms of a mixture of coherent states [254], as described by the following density matrix

$$\hat{\rho} = \int \frac{1}{\pi\langle n\rangle} e^{-\frac{|\alpha|^2}{\langle n\rangle}}\,|\alpha\rangle\langle\alpha|\,d^2\alpha \tag{5.1.3}$$

where $\langle n\rangle$ is the mean photon number, given by eq. (2.2.43). Consequently, the output of the BS for chaotic light will be given by a mixture of factorized coherent states.

Consider now a Single-Photon Detector (SPD) placed along the transmitted arm past the BS, which is now taken to be balanced ($\mathcal{T} = 1/\sqrt{2}$, $\mathcal{R} = i/\sqrt{2}$). According to the theory of light detection [2, 249], when a single photon impinges on an ideal SPD, it is absorbed (destroyed) and its energy is transferred to the detector which reacts producing a classical electrical pulse. The process may be described by the following evolution

$$|1\rangle_{\mathrm{T}}\,|D_0\rangle \quad \longrightarrow \quad |D_+\rangle \tag{5.1.4}$$

where $|D_0\rangle$ and $|D_+\rangle$ represent the states of the "ready" and "reacted" SPD, and where we assume that the photon wavefunction is annihilated upon detection. When a photon is found on the reflected arm, instead, nothing happens:

$$|1\rangle_{\mathrm{R}}\,|D_0\rangle \quad \longrightarrow \quad |1\rangle_{\mathrm{R}}\,|D_0\rangle \tag{5.1.5}$$

According to the reduction postulate, in the case of the superposition state either of the two outcomes happens with probability given by the coefficients of the expansion, as in

$$\hat{U}_{\mathrm{BS}}\,|1\rangle\,|D_0\rangle = \frac{1}{\sqrt{2}}(|1\rangle_{\mathrm{T}} + i\,|1\rangle_{\mathrm{R}})\,|D_0\rangle \quad \longrightarrow \quad \begin{cases} |D_+\rangle\,, & p_{\mathrm{T}} = 1/2 \\ |1\rangle_{\mathrm{T}}\,|D_0\rangle\,, & p_{\mathrm{R}} = 1/2 \end{cases} \tag{5.1.6}$$

Notice that in this case the process is *non-local*, as the photon is delocalized in the two output arms of the beam splitter, and when the detector reacts the distant part of the wavefunction is annihilated.

When we consider factorized coherent states on the BS output arms, the outcome of the detection is given by the following evolution

$$\begin{aligned} &\hat{U}_{\mathrm{BS}}\,|\alpha\rangle\,|D_0\rangle = |\beta\rangle_{\mathrm{T}}\,|\gamma\rangle_{\mathrm{R}}\,|D_0\rangle \quad \longrightarrow \\ \longrightarrow \quad &\begin{cases} |0\rangle_{\mathrm{T}}\,|\gamma\rangle_{\mathrm{R}}\,|D_0\rangle\,, & p_0 = e^{-|\beta|^2} \\ |1^+\rangle_{\mathrm{T}}\,|\gamma\rangle_{\mathrm{R}}\,|D_0\rangle \quad \longrightarrow \quad |\gamma\rangle_{\mathrm{R}}\,|D_+\rangle\,, & p_{1^+} = 1 - e^{-|\beta|^2} \end{cases} \end{aligned} \tag{5.1.7}$$

where the two outcomes are distinguished because the coherent state is a superposition of Fock states, as described in eq. (2.2.32), and where $|1^+\rangle$ indicate the *at least one photon* state. The important point to notice here is that the process is *local*, since detection affects only the transmitted part of the wavefunction, while it leaves unaffected the reflected part, at variance with the single photon case discussed above.

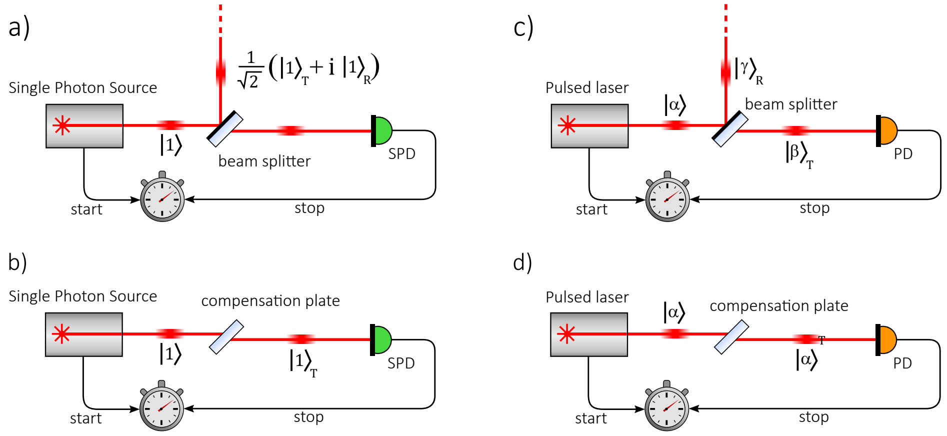

Figure 5.1: Conceptual scheme of the time of flight experiment. The time of flight of a single photon through a beam splitter (a) can be compared to the time of flight of a single photon through a compensation plate (b), or with coherent pulses through the same components (c) and (d). PD: PhotoDiode, SPD: Single-Photon Detector.

If we assume that the collapse time is influenced by the delocalization of the photon state, then *the delay would be observable only if superposition states are used*, while it would not be observed by time-of-flight experiments performed with pulses produced by coherent sources (such as LIDAR systems [298]) or thermal sources (such as LEDs or distant astronomical sources [299]).

The possible delay can then be measured using two approaches. The time of flight of a single photon detected by the SPD after it travelled through a BS (Fig. 5.1-a) can be compared to the one of the same photon travelling through a Compensation Plate (CP) (Fig. 5.1-b): the CP is required when dispersion or misalignments introduced by the BS are not negligible. Alternatively, the time of flight of single photons can be compared with the one of coherent pulses travelling through the BS (Fig. 5.1-c) and the CP (Fig. 5.1-d).

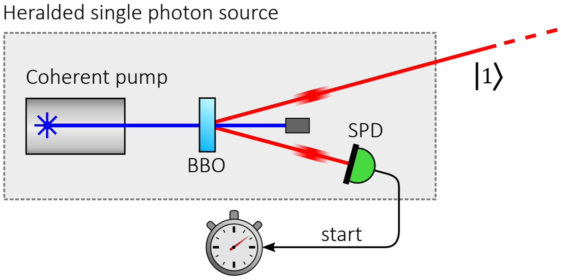

Figure 5.2: Scheme of a source of heralded single photons based on Parametric Down-Conversion in a Beta-Barium Borate (BBO) crystal.

5.2 Experiment

The ideal choice for implementing the measurement described above is to use a source of heralded single photons. In fact, as discussed in Section 2.1, sources based on Spontaneous Parametric Down-Conversion (SPDC) [17] emit coincident pairs of photons, so that the detection of one of the two, the *herald* photon, can be used to keep track of the time of emission of the other, the *heralded* photon. In our case, the electrical pulse produced by the SPD detecting the herald photon will set the start time of the time-of-flight experiment, as pictured in Figure 5.2. According to the assumptions made above, the collapse process associated to the herald photon detection, being local, would not influence the other photon's collapse; moreover, as an additional precaution, the setup can be designed so that the detection of the herald photon occurs before the heralded photon reaches the BS/CP stage.

5.2.1 Setup

The setup used to perform the experiment is illustrated in Figure 5.3. The SPDC source was based on a Beta-Barium Borate (BBO) crystal whose cross-section was 5×5 mm^2. Photon pairs are produced by Type-II SPDC [17], meaning that the polarization of the down-converted photons is orthogonal with respect to the polarization of the pump. The crystal was cut in order to generate downconverted photons at 810 nm on a cone with half-opening angle of 3 degrees when pumped with 405 nm radiation.

The crystal actually comprised two 0.5 mm thick slabs in a sandwich configuration [300]: the fast-axis of the second slab is rotated 90 degrees

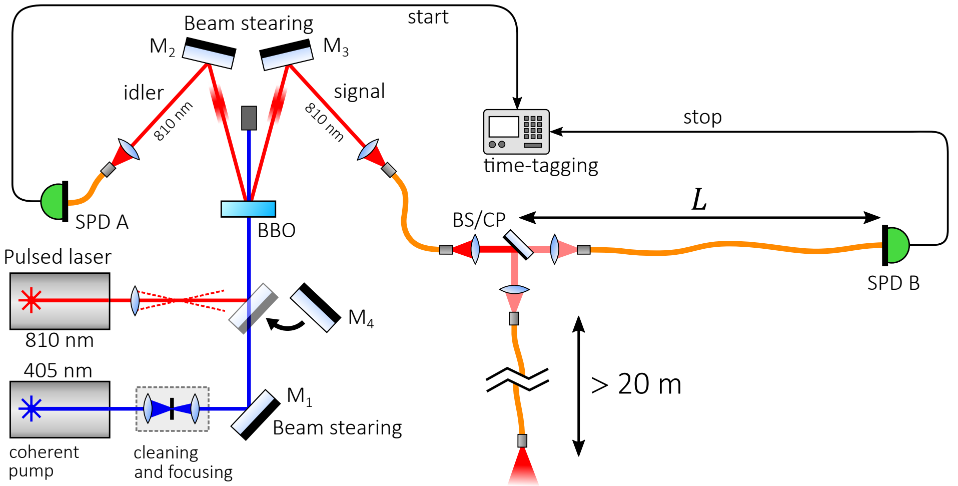

Figure 5.3: Experimental setup of the time of flight experiment. An SPDC source of photon pairs is used to both set the reference time for the experiment by heralding of the idler photon, and to produce a single photon state (signal). L varies between 2 and 20 m. BBO: Beta-Barium Borate, BPF: Band-Pass Filter, BS: Beam Splitter, CP: Compensation Plate, M: Mirror, SPD: Single-Photon Detector.

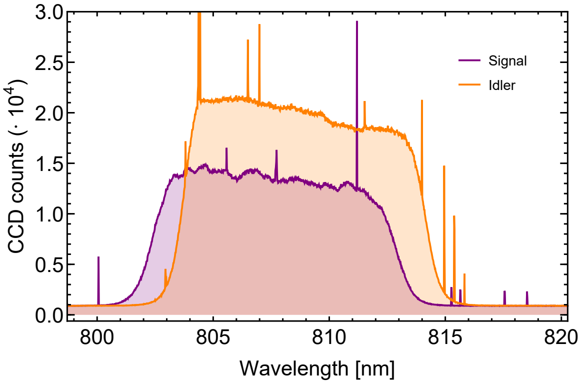

Figure 5.4: Signal and idler spectra collected after filtering by Band-Pass Filters in a 120 s acquisition by a Nitrogen-cooled CCD. The spikes in the plot are a well known artifact caused by cosmic rays exciting the CCD sensor elements.

with respect to the one of the first slab along the propagation axis. This configuration can be used to produce pairs of polarization-entangled photons when the pump polarization is oriented at 45 degrees to both fast axes. Here, however, we were not interested in polarization entanglement, therefore we pumped the crystal with vertical polarization, effectively using only one of the two slabs. The effective thickness of the BBO crystal was then 0.5 mm.

A blue laser diode (Sanyo DL-LS5017) produced 65 mW of pumping radiation at 405 nm; in order to focus the pump and to improve its spacial profile, a system composed of two lenses and a pin-hole was used. A 10 nm wide Band-Pass Filter (BPF) was placed in front of the BBO crystal in order to remove the amplified spontaneous emission emitted by the source. The mirror M_1 was used to steer the pump beam on the center of the nonlinear crystal.

The emitted photons are generated around the doubled pump wavelength. Two opposite sections of the emission cone are directed to two collection stages by mirrors M_2 and M_3; before being focused on multi-mode fibers with core diameter of 60 μm, the photons are spectrally shaped by additional BPFs, as shown in Figure 5.4, to maximize the Coincidence to Accidental Ratio of the coincidences detected.

While the photon labeled idler is sent directly to SPD A for heralding, the signal photon is routed towards the BS/CP stage: the photons are outcoupled from the fibers and collimated so that they can travel through either a Beam Splitter or a Compensation Plate. The Beam Splitter (Thorlabs BSW29R) is made with a 25 by 36 mm UV fused Silica glass plate with a metal coating that provides the 50:50 splitting ratio. The Compensation Plate (Thorlabs BCP44R) is made with the same glass plate, but it is anti-reflection coated around 810 nm. Past the BS/CP, the photons are collimated again into optical fibers at the transmission and reflection ports of the stage.

Fibers with lengths ranging between 2 and 20 m were connected between the transmission port of the BS/CP stage and SPD B. The fiber connected to the reflection port is 20 m long, and it was left open on its far end during the experiment, in order to preserve the photon superposition and avoid its early collapse due to the possible absorption of the reflected part of the wavefunction. The two fibers past the BS/CP stage were laid down at a 90 degree angle.

The electrical pulses emitted by SPD A and B are sent to time-tagging electronics (Picoquant HydraHarp-400) with coaxial cables. The connections were characterized before the experiment to ensure that dispersion or other effects would not introduce unwanted effects on the time-of-flight measurement. The left panel of Figure 5.5 shows that no appreciable difference is noticeable between the oscilloscope traces of the electrical pulses as they travelled through coaxial cables of increasing lengths. Moreover, the right panel of Figure 5.5 shows that the relative delay between signal and idler photons is only slightly affected by the length of the coaxial cables at the picosecond scale; notice, in any case, that the length of the coaxial connections remained unchanged in the final experiment, and that only relative times are of interest.

The Single Photon Detectors (ID Quantique id100-MMF50-STD) A and B had 10% and 5% detection efficiency at 810 nm respectively, and exhibited time jitters of 35 ps, which determined the time resolution of our experiment.

The time-tagging electronics produced a log file containing the reaction times of the detectors throughout the experiment. After completing the acquisition phase, the log was analyzed to determine the time correlation between the detected events.

Comparisons with coherent pulses were performed with the use of an additional laser source: a pulsed supercontinuum laser was spectrally filtered to emit radiation around 810 nm and its beam was directed through the BBO crystal with the flip-flop mirror M_4. The beam was focused on the same spot

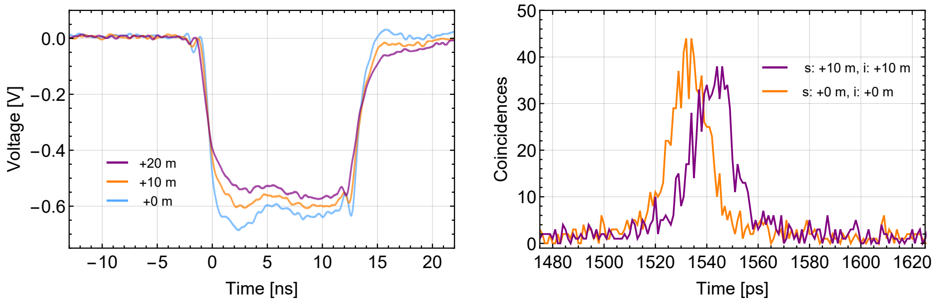

Figure 5.5: Left: Oscilloscope waveforms of the pulses generated by the Single Photon Detectors as they travel through increasingly longer coaxial cables. Right: Coincidence peak with varied length of the coaxial cables.

on the crystal where the SPDC pump was focused, and its divergence was chosen larger than the SPDC cone, so that the pulses travelled along the same path as the down-converted single photons. Thus, SPD A was still used as the time reference for the experiment.

5.2.2 Results and discussion

The coincidence histograms acquired for various configurations of the setup are shown in Figures 5.6 and 5.7. In particular, Figure 5.6 shows the coincidence histograms for all the four scenarios pictured in Figure 5.1, when a 20 m fiber is connected to the transmission port of the BS/CP stage, which corresponds to the maximum distance investigated. Both top and bottom panels show the histograms for both the coherent pulses (background) and single photon states (foreground), while they refer respectively to the BS and CP setup configurations. Figure 5.7 shows similar histograms where coherent pulses and single photons have been compared with the use of the BS only, for fiber lengths varying between 2 and 12 m. All the acquisitions were taken in 200 s.

No appreciable difference in the time of flight between photons and coherent states can be observed in any of the histograms within the resolution of the experiment. By fitting the coincidence peaks, a precise value of the difference in the reaction times between SPD A and B could be obtained. The difference between the mutual delay between the single photon and coherent

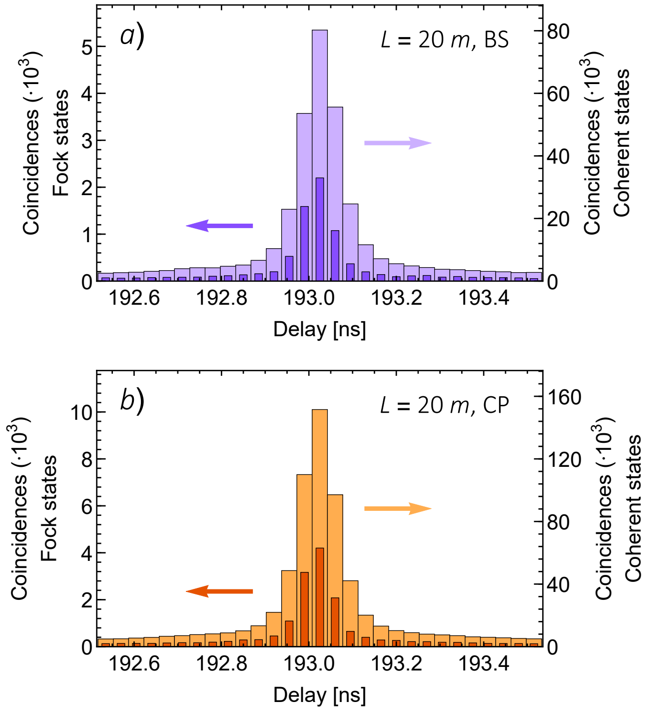

Figure 5.6: Coincidence counts in 200 s as a function of the difference between the reaction times of SPDC A and B when a 20 m fiber was connected to the BS/CP stage. For both panels the histogram for single photon states (left scale) is superimposed on the histogram for coherent pulses (right scale). a) Setup in the Beam Splitter configuration. b) Setup in the Compensation Plate configuration.

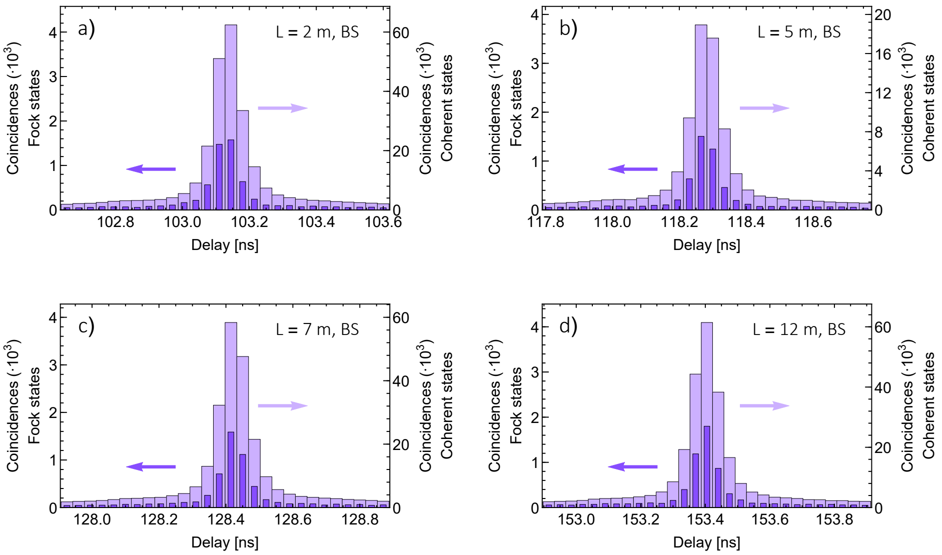

Figure 5.7: Coincidence counts in 200 s for various fiber lengths. The setup was always in the Beam Splitter configuration. For all panels the histogram for single photon states (left scale) is superimposed on the histogram for coherent pulses (right scale). a) 2 m fiber. b) 5 m fiber. c) 7 m fiber. d) 12 m fiber.

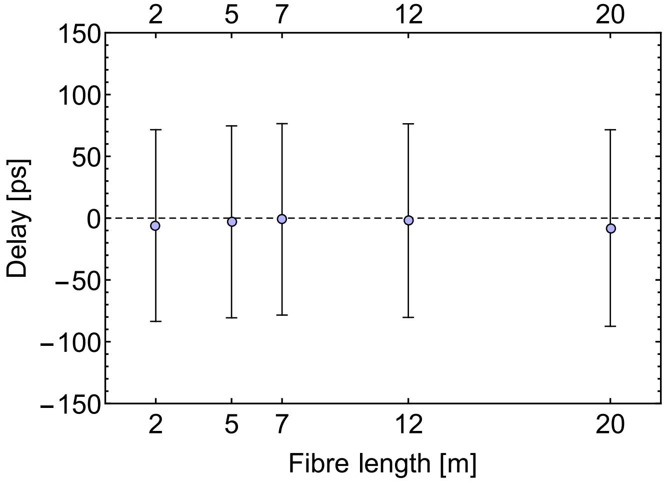

Figure 5.8: Change in the difference between the reaction times of SPD A and B as single photon states are replaced with coherent pulses and when the setup is in the Beam Splitter configuration. Values and error bars are determined from the position and FWHM of the coincidence histograms shown in Figures 5.6 and 5.7.

pulse cases is shown in Figure 5.8, where the error bars were determined from the FWHM of the coincidence peaks.

The experimental data leaves no doubt that the spatial collapse of the single photon state, if present, takes a time much shorter than the resolution of the experimental setup. If a delay is actually present, it cannot take more than $T = 60$ ps. Given the maximum spread reached by the photon wavefunction during the experiment, equal to $S = \sqrt{2}\cdot 20$ m $= 28.4$ m, we can therefore put a lower bound to the speed of the collapse of $c' = S/T \simeq 1550c$, about 6 times lower than the bound found in reference [294] for EPR pairs.

This boundary is about one order of magnitude smaller than the one reported for EPR pairs in ref. [294]; nonetheless, here we tested the collapse of a single delocalized particle, while previous tests were performed with entangled states of particle pairs.

Chapter 6

Conclusions and future perspectives

Silicon photonics is an interesting platform for the realization of quantum optical application because of the decades-long experience in its fabrication: facilities are now readily producing photonic devices comprising a large number of components with a high degree of reliability. However, since Silicon is an indirect bandgap semiconductor, direct radiative transitions have very low efficiency, thus preventing the realization of a sources of light based on this material.

The work described in Chapter 3 represents a way in which this drawback can be overcome, showing that Silicon microresonators can be self-pumped, without the use of an external laser source, to emit pairs of photons by Spontaneous Four-Wave Mixing [213]. In particular, we showed that a racetrack microresonator, with Q-factor equal to roughly 20'000 and operating around the 1550 nm telecom wavelength, can be used to emit pairs of photons by Spontaneous Four-Wave Mixing in two cavity configurations, differing by the presence of a tunable Fabri-Perot filter placed along the loop, with consequently different frequency correlations in the emitted photon pairs.

For the first configuration, labeled *multi-mode cavity*, we showed that the resonator could emit photon pairs with internal generation rates of up to 3.69 MHz and with varying degrees of correlations. We first performed the linear characterization of the resonator transmission, followed by the analysis of the lasing action of the fiber loop cavity containing the resonator and an optical amplifier. The lasing model, based on measured properties of the cavity, highlighted that at ring input powers in excess of 1 mW the measured output power was lower than expected. A measurement of the shift of the resonances due to the thermo-optic effect was compared to the redshift of the lasing radiation: at lower powers the lasing radiation followed the ring resonance automatically, as expected from the self-pumping configuration, while an additional redshift of the laser was found at higher powers; moreover, the spectrum of the lasing radiation, strongly multi-moded, widened at increasing power, becoming comparable to the width of the racetrack resonance. These measurements suggest that gain saturation phenomena occur in the gain medium of the optical amplifier included in the cavity, degrading the overall performance of the device.

The nonlinear characterization of the cavity confirmed the presence of saturation effects at higher powers. In particular, Stimulated Four-Wave Mixing measurements exhibited the expected power scaling behaviours only at lower resonator input pump powers. Time correlation measurements were also performed to characterize the emission of pairs by Spontaneous Four-Wave Mixing: the coincidence peak had roughly 120 ps FWHM and the scaling was quadratic, as expected, until it reached saturation at higher pump powers.

Through the use of Stimulated Emission Tomography [257], we investigated the degree of frequency correlation present between the emitted signal and idler photons, which changed at increasing pump powers. In particular, the measured Joint Spectral Densities were compared to numerical simulations, showing the expected behaviour only at lower powers; from numerical simulations we saw that the Schmidt number K, the figure of merit that quantifies the degree of correlation between the photons, decreased from 4.07 to 1.92 at increasing powers.

The subsequent measurement of the $g^{(2)}(\tau)$ autocorrelation function of the heralded idler field indicates that the state is the one of a single photon at low power (with minimum measured $g^{(2)}(0) = 15 \pm 7.5 \cdot 10^{-3}$), while at higher powers it rises above 0.5, the threshold under which a state can be considered quantum.

Regarding the single-mode cavity configuration, the linear and nonlinear characterization produced similar results compared to the multi-mode cavity configuration. The main difference, however, was the lasing action occurring on a single longitudinal mode of the cavity: compared to the multi-mode cavity, the pump spectrum was much narrower, with an optical bandwidth smaller than 300 kHz, as determined by heterodyne measurements, corresponding to coherence lengths in excess of 300 m. Thus, the photon pairs produced were expected to be strongly time-energy entangled, and a Franson-type experiment [260] was performed to confirm this. The fringe produced by quantum interference exhibited 93.9 ± 0.9% visibility, corresponding to the violation of the Bell inequality by 26 standard deviations.

These works represent proofs of principle that Silicon based devices can emit pairs of photons with a self-pumping configuration. A much more interesting scenario would be the realization of analogous sources in a completely integrated fashion. Time-energy entanglement, in fact, is an interesting resource for the implementation of QKD protocols on optical fiber networks, since it is intrinsically more reliant against environmental fluctuations than, for instance, polarization entanglement [79]. A small integrated device producing time-energy entangled photon pairs without the need for an external laser source would represent an ideal source to implement these protocols, which would also bring various advantages with it. For instance, the much smaller lenght of the lasing cavity would increase the Free Spectral Range between its modes, likely allowing to remove the need to add a selective filter to force single-mode operation, besides the microring itself. Moreover, the total round-trip losses of the cavity will be reduced because of the absence of lossy coupling stages to the outside of the sample, reducing the threshold current of lasing operation and power requirements with it.

On the other hand, additional challenges will have to be overcome. So far, no active medium operating at telecom wavelength has been realized using Silicon alone, therefore complex integration of III-V gain media, for example, has to be employed, making the fabrication process overall more complex. Filtering of deleterious amplified spontaneous emission produced by the active medium and of the photons emitted by the ring will become more cumbersome, since bulk filters would not be available anymore; then, approaches employing add-drop microring resonators or high-attenuation integrated Bragg filters will become likely necessary, although no filter with the required performance has yet been demonstrated.

Chapter 4 was dedicated to the description of the work of the Author performed at the University of Southampton.

Silicon Carbide (SiC), and in particular its 3C-SiC and 4H-SiC polytypes, is a semiconductor material that is recently gaining attention because of its numerous color centers emitting in the near infrared. These color centers, that exhibit excellent coherence properties, can be used as single-photon emitters or as systems on which qubits can be encoded. The fabrication of Silicon Carbide is, however, difficult and some challenges have to be overcome.

Section 4.1 illustrated a proposed scalable photonic platform for Silicon Carbide, based on suspended subwavelength waveguides [135], for operation around 1550 nm. The use of subwavelength structures simplifies the fabrication process, allowing the definition of geometries with a single etch step.

Regarding light propagation, subwavelength structures can be approximated as an effective homogeneous medium, whose index of refraction can be controlled by the specific geometry employed to realize the structures themselves. First, we illustrated the straight waveguide. In order to calculate their supported modes, the effective index of the suspending lateral arms, modeled as a homogeneous medium, has been calculated from a multilayer approach. Under this approximation, the modes profiles and dispersion were then numerically calculated with an eigensolver and compared with the photonic band structure of the waveguide treated as a one-dimensional photonic crystal, where a good agreement was found between the two approaches. Given the high $\chi^{(2)}$ nonlinearity of Silicon Carbide, an estimation of the performance of a simple electro-optical modulator was performed, obtaining a figure of merit $V_\pi L_\pi = 36.9 \text{ V} \cdot \text{cm}$.

Other simple structures were then illustrated, such as bends and directional couplers, followed by the description of the design process that led to the geometries for a uniform subwavelength grating coupler. From FDTD simulations of the coupler we expect -3.8 dB maximum transmission at 1550 nm and a 1-dB bandwidth of 75 nm.

The platform proposed here is well suited for the realization of slow light applications: the periodicity of the structure can be increased to reduce the group velocity of light, obtaining a consequent increase in the theoretical Purcell Factor experienced by color centers embedded in the waveguide by at least a factor of 3.

Two samples were realized in 3C-SiC. While the first sample exhibited fabrication defects and no transmitted radiation could be detected, the improved design of the second sample eliminated the issue. Nonetheless, the transmission measurements of 80 μm microring resonators based on subwavelength structures revealed very high propagation losses, in excess of 100 dB/cm; in fact, the Q-factor of these microrings, found in the under-coupling condition, ranged between 5000 and 7000. The high attenuation losses were attributed to the low quality of the fabrication, since the lower interface of the Silicon Carbide film is likely dense of defects due to the mismatched heteroepitaxial growth on the Silicon substrate; the effect of disorder or surface roughness, however, is not yet excluded.

The main goal to improve the performance of the device is clearly the reduction of attenuation losses. Despite the introduction of additional guided modes, an immediate approach towards this end is the use of waveguides with larger cross-sections: the field will be less localized close to the lossy lower interface of the Silicon Carbide layer; moreover, the interaction with the lateral boundaries of the waveguide will be reduced, both lowering scattering losses due to surface roughness and those due to disorder on the periodicity of the subwavelength structure. Another approach involves the reduction of intrinsic material losses, either by improving the fabrication technique of 3C-SiC, or by realizing the device on a different polytype, such as 4H-SiC, for which fabrication process resulting in lower losses are already demonstrated.

One challenge in realizing a completely integrated source of photon pairs by Spontaneous Four-Wave Mixing in microring resoators is the separation of the strong residual pump beam from the weak stream of signal-idler pairs. Selective attenuations in the order of 100 dB are required and various approaches exist, based on Coupled Ring Optical Waveguides (CROW) [286], cascaded Mach-Zehnder interferometers [285] and waveguide Bragg grating filters [264].

To this end, in Section 4.2 we presented a novel design for a waveguide Bragg grating filter for which the required periodic modulation of the dielectric structure is performed with the use of structures external to the waveguide itself. Two designs have been proposed: one based on isolated pillars placed at the sides of the waveguide, and one based on a similar layout, but where the pillars are all connected together to form a comb-shaped structure. The external structures interact with the tails of the mode propagating in the central waveguide, whose cross-section remains unchanged along the whole device. The advantage of this approach should be lower propagation losses compared to filters based on waveguide-modulation: the uniform central waveguide, in fact, should have a lower amount of roughness and disorder, reducing the coupling to radiative modes.

The proposed designs for Bragg gratings was based on Silicon Nitride and targeted 1600 nm as the stop-band wavelength. First, in order to derive the geometric dimensions of the Bragg filter required to obtain a given stop-band, the system was modeled as a multilayer. The equivalent indexes for the layers were obtained in terms of the effective indexes of the natural waveguide's fundamental TE mode, and of the fundamental mode of the filter cross-section containing the pillars. Thus, the index contrast of the multilayer $\Delta n/n$, the fundamental quantity that determines the width of the stop-band, can be controlled by changing the confinement effect of the pillars, either increasing their size or by bringing them closer to the waveguide.

Then, the full photonic band structure of the filter has been calculated in order to confirm the absence, close to the fundamental stop-band, of additional photonic stop-bands due to the coupling between the fundamental and higher order TE modes supported by the full structure of the filter.

A preliminary test sample has been fabricated, containing both filter designs and traditional filters based on the modulation of the waveguide width, targeting moderate attenuations of 50 dB. The transmission measurements of filters based on both the novel and the traditional design showed that the stop-bands were less deep than expected, with maximum attenuations ranging between 10 and 40 dB, and were found around 1540 nm rather than 1600 nm; the stop-bands, on the other hand, had roughly the expected width, demonstrating the validity of the new design.

Further experimental iterations, performed after a more thorough investigation of the cause of these issues, are expected to produce better performing devices. The analysis of SEM images of the fabricated samples, for instance, may give clues on the cause of the lower attenuation, which, at the moment, is tentatively attributed to disorder in the placement of the lateral pillars. Once this is performed, a more controlled investigation on the properties of filters could be performed.

While integrated optics may possess significant advantages compared to bulk devices in terms of cost and production volumes, the latter approach is still a powerful tool to perform experiments that investigate fundamental aspects of physics.

The experimental work described in Chapter 5 regarded the study of one counterintuitive phenomenon described by Quantum Mechanics, the collapse of the wavefunction upon measurement. In particular, we investigated whether the collapse of a single delocalized photon state, which Quantum Mechanics postulates to be instantaneous, takes a time. Similarly to other experiments performed on entangled pairs of particles [105, 294], no delay in the collapse time was observed within the resolution of the experiment, which allowed us to put a lower bound to the collapse speed of 1550 times the speed of light. This was the first time that a *single* delocalized particle state was investigated.

In the chapter we described the realization and characterization of a heralded source of single photons based on Spontaneous Parametric Down-Conversion. The source is based on a BBO crystal, pumped with a 405 nm laser diode, and emitting pairs of photons at 810 nm. One of the photons is detected by a first Single-Photon Detector, setting the reference for time-of-flight experiments of the second photon: in order to compare the time of collapse of delocalized and localized states, the second photon is sent first to either a Beam Splitter, which creates a spatial superposition state, or to a Compensation Plate, which leaves the spatial distribution unaffected, before being detected by a distant second detector. Moreover, these scenarios were compared to similar ones, where coherent pulses of light were travelling along the same paths of the down-converted photons, the difference being that a coherent state remains in a separable state upon travelling through the Beam Splitter, thus remaining in a localized state.

In the future, the experiment could be improved by increasing the distance over which the collapse is investigated. For instance, inter-city optical fiber links may be employed to scale the experiments to the hundreds of kilometers scale. Alternatively, similarly to works on entangled photon pairs [105], long-distance free-space optical channels could be employed with the aid of telescopes.

Summarizing, there were two main motivations at the heart of the experimental works described in this thesis.

First of all, what has been described in Chapters 3 and 4 aimed at developing and improving integrated photonic devices in the context of generation of quantum states of light. In particular, the ultimate goal of the work of Chapter 3 is the realization of an electrically pumped, fully integrated source of photon pairs based on Spontaneous Four-Wave Mixing in microresonators and operating at telecom wavelengths; some challenges have to be overcome, however, such as the strong on-chip filtering required to suppress the pump below the signal-idler photons, which was the aim of the work on Silicon Nitride Bragg filters. The work on suspended waveguides aims at realizing a complete photonic platform that can exploit the color centers of Silicon Carbide for quantum applications.

The study of one fundamental aspect of Quantum Mechanics was the second motivation of the thesis, behind the work described in Chapter 5, where quantum states of light, pairs produced by Parametric Down-Conversion, have been employed to probe the time of collapse of the wavefunction.

Appendix A

Design parameters of Silicon Nitride Bragg filters

Here we report the design parameters of all the Silicon Nitride bragg filters discussed in Chapter 4. The simulations that led to these parameters assumed that the index of Silicon Nitride and of the Silicon Oxide cladding equal to 2 and 1.44, respectively. The thickness of all the devices is 300 nm. The 3-dB bandwidth equals 35.58% of the expected stop-band.

Devices labeled with the letter A are comb-like pillar Bragg filters and they have 150 nm wide comb rods and 200 nm wide extrusions (total comb width equal to 350 nm). Devices labeled with B are external pillars Bragg filters; the width of the pillars is always equal to 400 nm. Devices labeled with C are traditional waveguide modulation filters.

The symbols found on the following tables have these meaning
w: waveguide width
g: waveguide-pillar gap
m: waveguide corss-section modulation width
a: periodicity
N: number of periods
$\Delta\lambda$: expected bandwidth
exp. att.: expected attenuation.

Table A.1: Comb-like Bragg filters parameters (1/2).

Device	w [nm]	a [nm]	g [nm]	N	$\Delta\lambda$ [pm]	exp. att. [dB]
A1	800	512.47	350	2100	n/a	> 50
A2	800	512.47	400	2100	3140	50
A3	800	512.47	450	2800	2350	50
A4	800	512.47	500	3700	1760	50
A5	800	512.47	550	3700	1320	< 50
A6	850	509.41	325	1900	n/a	> 50
A7	850	509.41	375	1900	3550	50
A8	850	509.41	425	2400	2780	50
A9	850	509.41	475	3000	2200	50
A10	850	509.41	525	3000	n/a	< 50
A11	900	506.25	300	2200	4000	> 50
A12	900	506.25	350	2200	2960	50
A13	900	506.25	400	3000	2190	50
A14	900	506.25	450	4000	1620	50
A15	900	506.25	500	4000	1200	< 50
A16	950	503.60	275	2800	n/a	> 50
A17	950	503.60	325	2800	2380	50
A18	950	503.60	375	4100	1600	50
A19	950	503.60	425	6200	1060	50
A20	950	503.60	475	6200	n/a	< 50

Table A.2: Comb-like Bragg filters parameters (2/2).

Device	w [nm]	a [nm]	g [nm]	N	$\Delta\lambda$ [pm]	exp. att. [dB]
A21	1000	500.96	250	2100	n/a	> 50
A22	1000	500.96	300	2100	3130	50
A23	1000	500.96	350	2700	2410	50
A24	1000	500.96	400	3500	1860	50
A25	1000	500.96	450	3500	1430	< 50
A26	1050	498.62	225	2500	n/a	> 50
A27	1050	498.62	375	2500	2580	50
A28	1050	498.62	325	3700	1760	50
A29	1050	498.62	375	5500	1190	50
A30	1050	498.62	425	5500	n/a	< 50
A31	1100	496.73	250	1900	3530	50
A32	1100	496.73	300	2500	2650	50
A33	1100	496.73	350	3200	2060	50
A34	1200	493.01	200	2000	3250	50
A35	1200	493.01	250	5900	2280	50
A36	1200	493.01	300	4100	1590	50
A37	1300	490.20	150	2000	3220	50
A38	1300	490.20	200	3300	1970	50
A39	1300	490.20	250	5600	1180	50

Table A.3: Pillar Bragg filters parameters (1/2). *) For these devices, the number of periods N was chosen higher than the one required for 50 dB attenuation, by mistake.

Device	w [nm]	a [nm]	g [nm]	N	$\Delta\lambda$ [pm]	exp. att. [dB]
B1	900	506.25	250	2200	n/a	> 50
B2	900	506.25	350	2200	3010	50
B3	900	506.25	400	3000	2190	50
B4	900	506.25	450	4000	1590	50
B5	900	506.25	500	4000	1160	< 50
B6	950	503.60	250	2400	n/a	> 50
B7	950	503.60	300	2400	2800	50
B8	950	503.60	350	3500	1890	50
B9	950	503.60	400	5200	1270	50
B10	950	503.60	450	5200	n/a	< 50
B11	1000	500.96	250	2100	n/a*	> 50*
B12	1000	500.96	300	2100	n/a*	> 50*
B13	1000	500.96	350	2700	n/a*	> 50*
B14	1000	500.96	400	3500	n/a*	> 50*
B15	1000	500.96	450	3500	n/a*	> 50*
B16	1050	498.62	200	2200	n/a	> 50
B17	1050	498.62	250	2200	2940	50
B18	1050	498.62	300	3200	2040	50
B19	1050	498.62	350	4800	1370	50
B20	1050	498.62	400	4800	n/a	< 50

Table A.4: Pillar Bragg filters parameters (2/2).

Device	w [nm]	a [nm]	g [nm]	N	$\Delta\lambda$ [pm]	exp. att. [dB]
B21	1100	496.73	250	1900	n/a	> 50
B22	1100	496.73	300	1900	3450	50
B23	1100	496.73	350	2200	2990	50
B24	1100	496.73	400	3000	2420	50
B25	1100	496.73	450	3000	1960	< 50
B26	1150	494.86	200	2200	n/a	> 50
B27	1150	494.86	250	2200	3030	50
B28	1150	494.86	300	2800	2330	50
B29	1150	494.86	350	3600	1810	50
B30	1150	494.86	400	3600	1470	< 50
B31	1200	493.01	200	2200	3060	50
B32	1200	493.01	250	3100	1790	50
B33	1200	493.01	300	4200	1060	50
B34	1300	490.20	150	2200	2950	50
B35	1300	490.20	200	3700	1790	50
B36	1300	490.20	250	6200	1060	50
B37	1400	487.76	150	2100	3100	50
B38	1400	487.76	200	3000	2170	50
B39	1400	487.76	250	4200	1550	50

Table A.5: Waveguide modulation Bragg filters parameters.

Device	w [nm]	a [nm]	m [nm]	N	$\Delta\lambda$ [pm]	exp. att. [dB]
C1	800	512.50	15	3800	1710	50
C2	800	512.50	30	1900	3400	50
C3	800	512.50	50	1100	6100	50
C4	900	506.20	15	4500	1460	50
C5	900	506.20	30	2000	3300	50
C6	900	506.20	50	1200	5360	50
C7	1000	500.10	15	5200	1270	50
C8	1000	500.10	30	2500	2600	50
C9	1000	500.10	50	1400	4770	50
C10	1100	496.70	15	5600	2850	50
C11	1100	496.70	30	2500	1300	50
C12	1100	496.70	50	1700	900	50
C13	1200	493.00	30	4100	1590	50
C14	1200	493.00	50	2300	2870	50
C15	1200	493.00	100	1100	5810	50
C16	1300	490.20	30	4200	1570	50
C17	1300	490.20	50	2600	2530	50
C18	1300	490.20	100	1200	5080	50
C19	1400	487.80	30	5300	1240	50
C20	1400	487.80	50	2900	2290	50
C21	1400	487.80	100	1600	4180	50

List of Acronyms

ASE	Amplified Spontaneous Emission
BPF	Band-Pass Filter
CAR	Coincidence to Accidental Ratio
CMOS	Complementary Metal-Oxide Semiconductor
CROW	Coupled-Resonator Optical Waveguide
CWDM	Coarse Wavelength Division Multiplexer
DFWM	Degenerate Four-Wave Mixing
EPR	Einstein Podolsky Rosen
FCA	Free-Carrier Absorption
FDTD	Finite-Difference Time-Domain
FP	Fabri-Perot
FSR	Free Spectral Range
FWHD	Full Width at Half Dip
FWHM	Full Width at Half Maximum
FWM	Four-Wave Mixing
HBT	Hanbury Brown and Twiss
HOM	Hong Ou Mandel
JSD	Joint Spectral Density
MPW	Multi-Project Wafer
MZI	Mach-Zehnder Interferometer
NV	Nitrogen Vacancy

PDC	Parametric Down-Conversion
PF	Purcell Factor
PIC	Photonic Integrated Chip
QD	Quantum Dot
QKD	Quantum Key Distribution
QWS	Quarter-Wave Stack
SEM	Scanning Electron Microscope
SiC	Silicon Carbide
SiN	Silicon Nitride
SiV	Silicon Vacancy
SNR	Signal to Noise Ratio
SOI	Silicon on Insulator
SPD	Single-Photon Detector
SPDC	Spontaneous Parametric Down-Conversion
SpFWM	Spontaneous Four-Wave Mixing
SSPD	Superconducting Single-Photon Detector
StFWM	Stimulated Four-Wave Mixing
TE	Transverse-Electric
TIR	Total Internal Reflection
TM	Transverse-Magnetic
TPA	Two-Photon Absorption
WCP	Weak Coherent Pulse

Bibliography

[1] Albert Einstein. "Über einen die Erzeugung und Verwandlung des Lichtes betreffenden heuristischen Gesichtspunkt". In: *Annalen der physik* 322.6 (1905), pp. 132–148.

[2] Rodney Loudon. *The quantum theory of light.* OUP Oxford, 2000.

[3] Vittorio Giovannetti, Seth Lloyd, and Lorenzo Maccone. "Quantum metrology". In: *Physical review letters* 96.1 (2006), p. 010401.

[4] Nicolas Gisin and Rob Thew. "Quantum communication". In: *Nature photonics* 1.3 (2007), p. 165.

[5] Stuart J Freedman and John F Clauser. "Experimental test of local hidden-variable theories". In: *Physical Review Letters* 28.14 (1972), p. 938.

[6] Dik Bouwmeester et al. "Experimental quantum teleportation". In: *Nature* 390.6660 (1997), p. 575.

[7] Michael A Nielsen and Isaac Chuang. *Quantum computation and quantum information.* 2002.

[8] David Elieser Deutsch. "Quantum computational networks". In: *Proceedings of the Royal Society of London. A. Mathematical and Physical Sciences* 425.1868 (1989), pp. 73–90.

[9] Adriano Barenco et al. "Elementary gates for quantum computation". In: *Physical review A* 52.5 (1995), p. 3457.

[10] David Deutsch and Richard Jozsa. "Rapid solution of problems by quantum computation". In: *Proceedings of the Royal Society of London. Series A: Mathematical and Physical Sciences* 439.1907 (1992), pp. 553–558.

[11] Peter W Shor. “Algorithms for quantum computation: Discrete logarithms and factoring”. In: *Proceedings 35th annual symposium on foundations of computer science*. Ieee. 1994, pp. 124–134.

[12] Lov K Grover. “A fast quantum mechanical algorithm for database search”. In: *arXiv preprint quant-ph/9605043* (1996).

[13] Ronald L Rivest, Adi Shamir, and Leonard Adleman. “A method for obtaining digital signatures and public-key cryptosystems”. In: *Communications of the ACM* 21.2 (1978), pp. 120–126.

[14] Jie Chen et al. “Active polarization stabilization in optical fibers suitable for quantum key distribution”. In: *Optics express* 15.26 (2007), pp. 17928–17936.

[15] Christian Reimer et al. “Cross-polarized photon-pair generation and bi-chromatically pumped optical parametric oscillation on a chip”. In: *Nature communications* 6 (2015), p. 8236.

[16] Amnon Yariv and Pocji Yeh. *Photonics: optical electronics in modern communications*. Oxford Univ., 2006.

[17] Paul G Kwiat et al. “New high-intensity source of polarization-entangled photon pairs”. In: *Physical Review Letters* 75.24 (1995), p. 4337.

[18] Han-Sen Zhong et al. “12-photon entanglement and scalable scattershot boson sampling with optimal entangled-photon pairs from parametric down-conversion”. In: *Physical review letters* 121.25 (2018), p. 250505.

[19] Alberto Peruzzo et al. “Quantum walks of correlated photons”. In: *Science* 329.5998 (2010), pp. 1500–1503.

[20] Jianwei Wang et al. “Multidimensional quantum entanglement with large-scale integrated optics”. In: *Science* 360.6386 (2018), pp. 285–291.

[21] HW Li et al. “Reconfigurable controlled two-qubit operation on a quantum photonic chip”. In: *New Journal of Physics* 13.11 (2011), p. 115009.

[22] Jürgen Brendel et al. “Pulsed energy-time entangled twin-photon source for quantum communication”. In: *Physical Review Letters* 82.12 (1999), p. 2594.

[23] Ivan Marcikic et al. "Time-bin entangled qubits for quantum communication created by femtosecond pulses". In: *Physical Review A* 66.6 (2002), p. 062308.

[24] Ivan Marcikic et al. "Distribution of time-bin entangled qubits over 50 km of optical fiber". In: *Physical Review Letters* 93.18 (2004), p. 180502.

[25] Christian Reimer et al. "Generation of multiphoton entangled quantum states by means of integrated frequency combs". In: *Science* 351.6278 (2016), pp. 1176–1180.

[26] Michael Kues et al. "On-chip generation of high-dimensional entangled quantum states and their coherent control". In: *Nature* 546.7660 (2017), p. 622.

[27] Adeline Orieux et al. "Experimental generation of robust entanglement from classical correlations via local dissipation". In: *Physical review letters* 115.16 (2015), p. 160503.

[28] Xi-Lin Wang et al. "18-qubit entanglement with six photons' three degrees of freedom". In: *Physical review letters* 120.26 (2018), p. 260502.

[29] Kevin Hennessy et al. "Quantum nature of a strongly coupled single quantum dot–cavity system". In: *Nature* 445.7130 (2007), p. 896.

[30] David Press et al. "Photon antibunching from a single quantum-dot-microcavity system in the strong coupling regime". In: *Physical Review Letters* 98.11 (2007), p. 117402.

[31] Emanuel Knill, Raymond Laflamme, and Gerald J Milburn. "A scheme for efficient quantum computation with linear optics". In: *nature* 409.6816 (2001), p. 46.

[32] Charles H Bennett et al. "Teleporting an unknown quantum state via dual classical and Einstein-Podolsky-Rosen channels". In: *Physical review letters* 70.13 (1993), p. 1895.

[33] Daniel Gottesman and Isaac L Chuang. "Demonstrating the viability of universal quantum computation using teleportation and single-qubit operations". In: *Nature* 402.6760 (1999), p. 390.

[34] TB Pittman et al. "Experimental controlled-NOT logic gate for single photons in the coincidence basis". In: *Physical Review A* 68.3 (2003), p. 032316.

[35] Jeremy L O'Brien et al. "Demonstration of an all-optical quantum controlled-NOT gate". In: *Nature* 426.6964 (2003), p. 264.

[36] Sara Gasparoni et al. "Realization of a photonic controlled-NOT gate sufficient for quantum computation". In: *Physical review letters* 93.2 (2004), p. 020504.

[37] Jeremy L O'Brien et al. "Quantum process tomography of a controlled-NOT gate". In: *Physical review letters* 93.8 (2004), p. 080502.

[38] Alberto Politi et al. "Silica-on-silicon waveguide quantum circuits". In: *Science* 320.5876 (2008), pp. 646–649.

[39] Jonathan CF Matthews et al. "Manipulation of multiphoton entanglement in waveguide quantum circuits". In: *Nature Photonics* 3.6 (2009), p. 346.

[40] Brian J Smith et al. "Phase-controlled integrated photonic quantum circuits". In: *Optics Express* 17.16 (2009), pp. 13516–13525.

[41] Robert Raussendorf and Hans J Briegel. "A one-way quantum computer". In: *Physical Review Letters* 86.22 (2001), p. 5188.

[42] Robert Raussendorf, Daniel E Browne, and Hans J Briegel. "Measurement-based quantum computation on cluster states". In: *Physical review A* 68.2 (2003), p. 022312.

[43] Michael A Nielsen. "Optical quantum computation using cluster states". In: *Physical review letters* 93.4 (2004), p. 040503.

[44] Tetsufumi Tanamoto et al. "Producing cluster states in charge qubits and flux qubits". In: *Physical review letters* 97.23 (2006), p. 230501.

[45] Massoud Borhani and Daniel Loss. "Cluster states from Heisenberg interactions". In: *Physical Review A* 71.3 (2005), p. 034308.

[46] Nicolas C Menicucci et al. "Universal quantum computation with continuous-variable cluster states". In: *Physical review letters* 97.11 (2006), p. 110501.

[47] Jeremy L O'brien. "Optical quantum computing". In: *Science* 318.5856 (2007), pp. 1567–1570.

[48] Thaddeus D Ladd et al. "Quantum computers". In: *nature* 464.7285 (2010), p. 45.

[49] David J Wineland and Wayne M Itano. "Laser cooling of atoms". In: *Physical Review A* 20.4 (1979), p. 1521.

[50] Rainer Blatt and David Wineland. “Entangled states of trapped atomic ions”. In: *Nature* 453.7198 (2008), p. 1008.

[51] David J Wineland et al. “Experimental issues in coherent quantum-state manipulation of trapped atomic ions”. In: *Journal of Research of the National Institute of Standards and Technology* 103.3 (1998), p. 259.

[52] Christian Ospelkaus et al. “Trapped-ion quantum logic gates based on oscillating magnetic fields”. In: *Physical review letters* 101.9 (2008), p. 090502.

[53] Justin G Bohnet et al. “Quantum spin dynamics and entanglement generation with hundreds of trapped ions”. In: *Science* 352.6291 (2016), pp. 1297–1301.

[54] D Jaksch et al. “Fast quantum gates for neutral atoms”. In: *Physical Review Letters* 85.10 (2000), p. 2208.

[55] Marco Anderlini et al. “Controlled exchange interaction between pairs of neutral atoms in an optical lattice”. In: *Nature* 448.7152 (2007), p. 452.

[56] Jonathan P Home et al. “Complete methods set for scalable ion trap quantum information processing”. In: *Science* 325.5945 (2009), pp. 1227–1230.

[57] Ronald Hanson et al. “Spins in few-electron quantum dots”. In: *Reviews of modern physics* 79.4 (2007), p. 1217.

[58] Mete Atatüre et al. “Quantum-dot spin-state preparation with near-unity fidelity”. In: *Science* 312.5773 (2006), pp. 551–553.

[59] S Olmschenk et al. “Quantum teleportation between distant matter qubits”. In: *Science* 323.5913 (2009), pp. 486–489.

[60] Rutger Vrijen et al. “Electron-spin-resonance transistors for quantum computing in silicon-germanium heterostructures”. In: *Physical Review A* 62.1 (2000), p. 012306.

[61] Hongwu Liu et al. “A gate-defined silicon quantum dot molecule”. In: *Applied Physics Letters* 92.22 (2008), p. 222104.

[62] CB Simmons et al. “Charge sensing and controllable tunnel coupling in a Si/SiGe double quantum dot”. In: *Nano letters* 9.9 (2009), pp. 3234–3238.

[63] Bruce E Kane. “A silicon-based nuclear spin quantum computer”. In: *nature* 393.6681 (1998), p. 133.

[64] A Yang et al. “Simultaneous subsecond hyperpolarization of the nuclear and electron spins of phosphorus in silicon by optical pumping of exciton transitions”. In: *Physical review letters* 102.25 (2009), p. 257401.

[65] Joanne Harrison, MJ Sellars, and NB Manson. “Measurement of the optically induced spin polarisation of NV centres in diamond”. In: *Diamond and related materials* 15.4-8 (2006), pp. 586–588.

[66] MV Gurudev Dutt et al. “Quantum register based on individual electronic and nuclear spin qubits in diamond”. In: *Science* 316.5829 (2007), pp. 1312–1316.

[67] R Hanson et al. “Coherent dynamics of a single spin interacting with an adjustable spin bath”. In: *Science* 320.5874 (2008), pp. 352–355.

[68] Christian Hepp et al. “Electronic structure of the silicon vacancy color center in diamond”. In: *Physical Review Letters* 112.3 (2014), p. 036405.

[69] Lachlan J Rogers et al. “All-optical initialization, readout, and coherent preparation of single silicon-vacancy spins in diamond”. In: *Physical review letters* 113.26 (2014), p. 263602.

[70] Peter Y Yu and Manuel Cardona. *Fundamentals of semiconductors: physics and materials properties*. Springer, 2010.

[71] Susumu Takahashi et al. “Quenching spin decoherence in diamond through spin bath polarization”. In: *Physical review letters* 101.4 (2008), p. 047601.

[72] Yu Nakamura, Yu A Pashkin, and JS Tsai. “Coherent control of macroscopic quantum states in a single-Cooper-pair box”. In: *nature* 398.6730 (1999), p. 786.

[73] Denis Vion et al. “Manipulating the quantum state of an electrical circuit”. In: *Science* 296.5569 (2002), pp. 886–889.

[74] I Chiorescu et al. “Coherent quantum dynamics of a superconducting flux qubit”. In: *Science* 299.5614 (2003), pp. 1869–1871.

[75] AO Niskanen et al. “Quantum coherent tunable coupling of superconducting qubits”. In: *Science* 316.5825 (2007), pp. 723–726.

[76] G Wendin. “Quantum information processing with superconducting circuits: a review”. In: *Reports on Progress in Physics* 80.10 (2017), p. 106001.

[77] Leonardo DiCarlo et al. “Demonstration of two-qubit algorithms with a superconducting quantum processor”. In: *Nature* 460.7252 (2009), p. 240.

[78] Frank Arute et al. “Quantum supremacy using a programmable superconducting processor”. In: *Nature* 574.7779 (2019), pp. 505–510.

[79] H Jeff Kimble. “The quantum internet”. In: *Nature* 453.7198 (2008), p. 1023.

[80] Stephanie Wehner, David Elkouss, and Ronald Hanson. “Quantum internet: A vision for the road ahead”. In: *Science* 362.6412 (2018), eaam9288.

[81] Juan Ignacio Cirac et al. “Quantum state transfer and entanglement distribution among distant nodes in a quantum network”. In: *Physical Review Letters* 78.16 (1997), p. 3221.

[82] A David Boozer et al. “Reversible state transfer between light and a single trapped atom”. In: *Physical Review Letters* 98.19 (2007), p. 193601.

[83] William K Wootters and Wojciech H Zurek. “A single quantum cannot be cloned”. In: *Nature* 299.5886 (1982), p. 802.

[84] DGBJ Dieks. “Communication by EPR devices”. In: *Physics Letters A* 92.6 (1982), pp. 271–272.

[85] L-M Duan et al. “Long-distance quantum communication with atomic ensembles and linear optics”. In: *Nature* 414.6862 (2001), p. 413.

[86] Jian-Wei Pan et al. “Entanglement purification for quantum communication”. In: *Nature* 410.6832 (2001), p. 1067.

[87] Jian-Wei Pan et al. “Experimental entanglement purification of arbitrary unknown states”. In: *Nature* 423.6938 (2003), p. 417.

[88] H-J Briegel et al. “Quantum repeaters: the role of imperfect local operations in quantum communication”. In: *Physical Review Letters* 81.26 (1998), p. 5932.

[89] M Zwerger, W Dür, and HJ Briegel. “Measurement-based quantum repeaters”. In: *Physical Review A* 85.6 (2012), p. 062326.

[90] Jian-Wei Pan et al. “Experimental entanglement swapping: entangling photons that never interacted”. In: *Physical Review Letters* 80.18 (1998), p. 3891.

[91] Zhen-Sheng Yuan et al. “Experimental demonstration of a BDCZ quantum repeater node”. In: *Nature* 454.7208 (2008), p. 1098.

[92] Ji-Gang Ren et al. “Ground-to-satellite quantum teleportation”. In: *Nature* 549.7670 (2017), p. 70.

[93] Sheng-Kai Liao et al. “Satellite-to-ground quantum key distribution”. In: *Nature* 549.7670 (2017), p. 43.

[94] Juan Yin et al. “Satellite-based entanglement distribution over 1200 kilometers”. In: *Science* 356.6343 (2017), pp. 1140–1144.

[95] Sheng-Kai Liao et al. “Satellite-relayed intercontinental quantum network”. In: *Physical review letters* 120.3 (2018), p. 030501.

[96] Charles H Bennett and Gilles Brassard. “Quantum cryptography: public key distribution and coin tossing.” In: *Theor. Comput. Sci.* 560.12 (2014), pp. 7–11.

[97] Hoi-Kwong Lo, Marcos Curty, and Kiyoshi Tamaki. “Secure quantum key distribution”. In: *Nature Photonics* 8.8 (2014), p. 595.

[98] Artur K Ekert. “Quantum cryptography based on Bell’s theorem”. In: *Physical review letters* 67.6 (1991), p. 661.

[99] John S Bell. “On the einstein podolsky rosen paradox”. In: *Physics Physique Fizika* 1.3 (1964), p. 195.

[100] Charles H Bennett et al. “Experimental quantum cryptography”. In: *Journal of cryptology* 5.1 (1992), pp. 3–28.

[101] Bruno Huttner et al. “Quantum cryptography with coherent states”. In: *Physical Review A* 51.3 (1995), p. 1863.

[102] Hoi-Kwong Lo, Xiongfeng Ma, and Kai Chen. “Decoy state quantum key distribution”. In: *Physical review letters* 94.23 (2005), p. 230504.

[103] Tobias Schmitt-Manderbach et al. “Experimental demonstration of free-space decoy-state quantum key distribution over 144 km”. In: *Physical Review Letters* 98.1 (2007), p. 010504.

[104] Alexander Treiber et al. “A fully automated entanglement-based quantum cryptography system for telecom fiber networks”. In: *New Journal of Physics* 11.4 (2009), p. 045013.

[105] Rupert Ursin et al. “Entanglement-based quantum communication over 144 km”. In: *Nature physics* 3.7 (2007), p. 481.

[106] Momtchil Peev et al. “The SECOQC quantum key distribution network in Vienna”. In: *New Journal of Physics* 11.7 (2009), p. 075001.

[107] Damien Stucki et al. “Long-term performance of the SwissQuantum quantum key distribution network in a field environment”. In: *New Journal of Physics* 13.12 (2011), p. 123001.

[108] Teng-Yun Chen et al. “Metropolitan all-pass and inter-city quantum communication network”. In: *Optics express* 18.26 (2010), pp. 27217–27225.

[109] Masahide Sasaki et al. “Field test of quantum key distribution in the Tokyo QKD Network”. In: *Optics express* 19.11 (2011), pp. 10387–10409.

[110] Pieter Kok, Hwang Lee, and Jonathan P Dowling. “Creation of large-photon-number path entanglement conditioned on photodetection”. In: *Physical Review A* 65.5 (2002), p. 052104.

[111] Daniel F Walls. “Squeezed states of light”. In: *nature* 306.5939 (1983), p. 141.

[112] J Abadie et al. “A gravitational wave observatory operating beyond the quantum shot-noise limit”. In: *Nature Physics* 7.12 (2011), p. 962.

[113] LA Lugiato, A Gatti, and E Brambilla. “Quantum imaging”. In: *Journal of Optics B: Quantum and semiclassical optics* 4.3 (2002), S176.

[114] Agedi N Boto et al. “Quantum interferometric optical lithography: exploiting entanglement to beat the diffraction limit”. In: *Physical Review Letters* 85.13 (2000), p. 2733.

[115] Simeon Bogdanov et al. “Material platforms for integrated quantum photonics”. In: *Optical Materials Express* 7.1 (2017), pp. 111–132.

[116] Abdul Rahim et al. “Expanding the silicon photonics portfolio with silicon nitride photonic integrated circuits”. In: *Journal of lightwave technology* 35.4 (2017), pp. 639–649.

[117] David J Moss et al. “New CMOS-compatible platforms based on silicon nitride and Hydex for nonlinear optics”. In: *Nature photonics* 7.8 (2013), p. 597.

[118] Igor Aharonovich, Andrew D Greentree, and Steven Prawer. “Diamond photonics”. In: *Nature Photonics* 5.7 (2011), p. 397.

[119] BJM Hausmann et al. “Diamond nonlinear photonics”. In: *Nature Photonics* 8.5 (2014), p. 369.

[120] Greg Calusine, Alberto Politi, and David D Awschalom. “Silicon carbide photonic crystal cavities with integrated color centers”. In: *Applied Physics Letters* 105.1 (2014), p. 011123.

[121] Go Fujii et al. “Bright narrowband source of photon pairs at optical telecommunication wavelengths using a type-II periodically poled lithium niobate waveguide”. In: *Optics express* 15.20 (2007), pp. 12769–12776.

[122] Cheng Wang et al. “Nanophotonic lithium niobate electro-optic modulators”. In: *Optics express* 26.2 (2018), pp. 1547–1555.

[123] Cale M Gentry et al. “Quantum-correlated photon pairs generated in a commercial 45 nm complementary metal-oxide semiconductor microelectronic chip”. In: *Optica* 2.12 (2015), pp. 1065–1071.

[124] Michael Hochberg and Tom Baehr-Jones. “Towards fabless silicon photonics”. In: *Nature photonics* 4.8 (2010), p. 492.

[125] Matthew Streshinsky et al. “The road to affordable, large-scale silicon photonics”. In: *Optics and Photonics News* 24.9 (2013), pp. 32–39.

[126] Roel Baets et al. “Silicon Photonics: silicon nitride versus silicon-on-insulator”. In: *Optical Fiber Communication Conference*. Optical Society of America. 2016, Th3J–1.

[127] JC Zolper and M Skowronski. “Advances in silicon carbide electronics”. In: *Mrs Bulletin* 30.4 (2005), pp. 273–278.

[128] M Ferrera et al. “Low-power continuous-wave nonlinear optics in doped silica glass integrated waveguide structures”. In: *Nature photonics* 2.12 (2008), p. 737.

[129] Jacob S Levy et al. “Harmonic generation in silicon nitride ring resonators”. In: *Optics express* 19.12 (2011), pp. 11415–11421.

[130] Alessia Pasquazi et al. “Micro-combs: A novel generation of optical sources”. In: *Physics Reports* 729 (2018), pp. 1–81.

[131] Rod C Alferness. “Waveguide electrooptic modulators”. In: *IEEE Transactions on Microwave Theory Techniques* 30 (1982), pp. 1121–1137.

[132] LG Helt et al. “Spontaneous four-wave mixing in microring resonators”. In: *Optics letters* 35.18 (2010), pp. 3006–3008.

[133] M Neviere, R Petit, and M Cadilhac. “About the theory of optical grating coupler-waveguide systems”. In: *Optics Communications* 8.2 (1973), pp. 113–117.

[134] Dirk Taillaert, Peter Bienstman, and Roel Baets. “Compact efficient broadband grating coupler for silicon-on-insulator waveguides”. In: *Optics letters* 29.23 (2004), pp. 2749–2751.

[135] Pavel Cheben et al. “Subwavelength integrated photonics”. In: *Nature* 560.7720 (2018), p. 565.

[136] Robert Halir et al. “Continuously apodized fiber-to-chip surface grating coupler with refractive index engineered subwavelength structure”. In: *Optics letters* 35.19 (2010), pp. 3243–3245.

[137] Vilson R Almeida, Roberto R Panepucci, and Michal Lipson. “Nanotaper for compact mode conversion”. In: *Optics letters* 28.15 (2003), pp. 1302–1304.

[138] Pavel Cheben et al. “Subwavelength waveguide grating for mode conversion and light coupling in integrated optics”. In: *Optics express* 14.11 (2006), pp. 4695–4702.

[139] Pavel Cheben et al. “Refractive index engineering with subwavelength gratings for efficient microphotonic couplers and planar waveguide multiplexers”. In: *Optics letters* 35.15 (2010), pp. 2526–2528.

[140] Pavel Cheben et al. “Broadband polarization independent nanophotonic coupler for silicon waveguides with ultra-high efficiency”. In: *Optics express* 23.17 (2015), pp. 22553–22563.

[141] Eli Yablonovitch. “Inhibited spontaneous emission in solid-state physics and electronics”. In: *Physical review letters* 58.20 (1987), p. 2059.

[142] J.D. Joannopoulos et al. *Photonic Crystals: Molding the Flow of Light - Second Edition*. Princeton University Press, 2011. ISBN: 9781400828241. URL: `https://books.google.it/books?id=owhE36qiTP8C`.

[143] Steven G Johnson et al. “Guided modes in photonic crystal slabs”. In: *Physical Review B* 60.8 (1999), p. 5751.

[144] Sei-ichi Takayama et al. “Experimental demonstration of complete photonic band gap in two-dimensional photonic crystal slabs”. In: *Applied Physics Letters* 87.6 (2005), p. 061107.

[145] Takashi Asano and Susumu Noda. “Photonic Crystal Devices in Silicon Photonics”. In: *Proceedings of the IEEE* 106.12 (2018), pp. 2183–2195.

[146] Susumu Noda, Alongkarn Chutinan, and Masahiro Imada. “Trapping and emission of photons by a single defect in a photonic bandgap structure”. In: *nature* 407.6804 (2000), p. 608.

[147] Takashi Asano et al. “Photonic crystal nanocavity with a Q factor exceeding eleven million”. In: *Optics express* 25.3 (2017), pp. 1769–1777.

[148] Edward M Purcell, H Co Torrey, and Robert V Pound. “Resonance absorption by nuclear magnetic moments in a solid”. In: *Physical review* 69.1-2 (1946), p. 37.

[149] Alongkarn Chutinan and Susumu Noda. “Waveguides and waveguide bends in two-dimensional photonic crystal slabs”. In: *Physical review B* 62.7 (2000), p. 4488.

[150] Thomas F Krauss. “Slow light in photonic crystal waveguides”. In: *Journal of Physics D: Applied Physics* 40.9 (2007), p. 2666.

[151] Toshihiko Baba. “Slow light in photonic crystals”. In: *Nature photonics* 2.8 (2008), p. 465.

[152] Mizuki Shinkawa et al. “Nonlinear enhancement in photonic crystal slow light waveguides fabricated using CMOS-compatible process”. In: *Optics express* 19.22 (2011), pp. 22208–22218.

[153] VSC Manga Rao and Stephen Hughes. “Single quantum-dot Purcell factor and β factor in a photonic crystal waveguide”. In: *Physical Review B* 75.20 (2007), p. 205437.

[154] Hong C Nguyen et al. “10 Gb/s operation of photonic crystal silicon optical modulators”. In: *Optics express* 19.14 (2011), pp. 13000–13007.

[155] Alongkarn Chutinan et al. “Surface-emitting channel drop filters using single defects in two-dimensional photonic crystal slabs”. In: *Applied Physics Letters* 79.17 (2001), pp. 2690–2692.

[156] Marko Lončar, Axel Scherer, and Yueming Qiu. “Photonic crystal laser sources for chemical detection”. In: *Applied Physics Letters* 82.26 (2003), pp. 4648–4650.

[157] Oskar Painter et al. “Two-dimensional photonic band-gap defect mode laser”. In: *Science* 284.5421 (1999), pp. 1819–1821.

[158] Takasumi Tanabe et al. “All-optical switches on a silicon chip realized using photonic crystal nanocavities”. In: *Applied Physics Letters* 87.15 (2005), p. 151112.

[159] DN Nikogosyan. “Beta barium borate (BBO)”. In: *Applied Physics A* 52.6 (1991), pp. 359–368.

[160] John D Bierlein and Herman Vanherzeele. “Potassium titanyl phosphate: properties and new applications”. In: *JOSA B* 6.4 (1989), pp. 622–633.

[161] D Eimerl. “Electro-optic, linear, and nonlinear optical properties of KDP and its isomorphs”. In: *Ferroelectrics* 72.1 (1987), pp. 95–139.

[162] Chong-Ki Hong, Zhe-Yu Ou, and Leonard Mandel. “Measurement of subpicosecond time intervals between two photons by interference”. In: *Physical review letters* 59.18 (1987), p. 2044.

[163] Alain Aspect, Philippe Grangier, and Gérard Roger. “Experimental tests of realistic local theories via Bell’s theorem”. In: *Physical review letters* 47.7 (1981), p. 460.

[164] Alain Aspect, Philippe Grangier, and Gérard Roger. “Experimental realization of Einstein-Podolsky-Rosen-Bohm Gedankenexperiment: a new violation of Bell’s inequalities”. In: *Physical review letters* 49.2 (1982), p. 91.

[165] Philippe Grangier, Gerard Roger, and Alain Aspect. “Experimental evidence for a photon anticorrelation effect on a beam splitter: a new light on single-photon interferences”. In: *EPL (Europhysics Letters)* 1.4 (1986), p. 173.

[166] Xi-Lin Wang et al. “Experimental ten-photon entanglement”. In: *Physical review letters* 117.21 (2016), p. 210502.

[167] Shuntaro Takeda et al. “Deterministic quantum teleportation of photonic quantum bits by a hybrid technique”. In: *Nature* 500.7462 (2013), p. 315.

[168] Jun Chen, Xiaoying Li, and Prem Kumar. “Two-photon-state generation via four-wave mixing in optical fibers”. In: *Physical Review A* 72.3 (2005), p. 033801.

[169] Jun Chen et al. “Fiber-based telecom-band degenerate-frequency source of entangled photon pairs”. In: *Optics letters* 31.18 (2006), pp. 2798–2800.

[170] Alex R McMillan et al. “Narrowband high-fidelity all-fibre source of heralded single photons at 1570 nm”. In: *Optics express* 17.8 (2009), pp. 6156–6165.

[171] Alan D Bristow, Nir Rotenberg, and Henry M Van Driel. “Two-photon absorption and Kerr coefficients of silicon for 850–2200 nm”. In: *Applied Physics Letters* 90.19 (2007), p. 191104.

[172] Amnon Yariv et al. “Coupled-resonator optical waveguide:? a proposal and analysis”. In: *Optics letters* 24.11 (1999), pp. 711–713.

[173] Q Lin and Govind P Agrawal. “Silicon waveguides for creating quantum-correlated photon pairs”. In: *Optics letters* 31.21 (2006), pp. 3140–3142.

[174] Jay E Sharping et al. “Generation of correlated photons in nanoscale silicon waveguides”. In: *Optics express* 14.25 (2006), pp. 12388–12393.

[175] Hiroki Takesue et al. “Entanglement generation using silicon wire waveguide”. In: *Applied Physics Letters* 91.20 (2007), p. 201108.

[176] Ken-ichi Harada et al. “Generation of high-purity entangled photon pairs using silicon wire waveguide”. In: *Optics express* 16.25 (2008), pp. 20368–20373.

[177] Hiroki Takesue et al. “Generation of polarization entangled photon pairs using silicon wire waveguide”. In: *Optics express* 16.8 (2008), pp. 5721–5727.

[178] Hanna Le Jeannic et al. “Monolithically-integrated polarization-entangled photon pair source on a silicon-on-insulator photonic circuit”. In: *2012 Conference on Lasers and Electro-Optics (CLEO)*. IEEE. 2012, pp. 1–2.

[179] Laurent Olislager et al. “Silicon-on-insulator integrated source of polarization-entangled photons”. In: *Optics letters* 38.11 (2013), pp. 1960–1962.

[180] Stéphane Clemmen et al. “Continuous wave photon pair generation in silicon-on-insulator waveguides and ring resonators”. In: *Optics express* 17.19 (2009), pp. 16558–16570.

[181] Ken-ichi Harada et al. “Frequency and polarization characteristics of correlated photon-pair generation using a silicon wire waveguide”. In: *IEEE Journal of Selected Topics in Quantum Electronics* 16.1 (2009), pp. 325–331.

[182] Joshua W Silverstone et al. “On-chip quantum interference between silicon photon-pair sources”. In: *Nature Photonics* 8.2 (2014), p. 104.

[183] Amy C Turner et al. “Ultra-low power parametric frequency conversion in a silicon microring resonator”. In: *Optics express* 16.7 (2008), pp. 4881–4887.

[184] Stefano Azzini et al. “From classical four-wave mixing to parametric fluorescence in silicon microring resonators”. In: *Optics letters* 37.18 (2012), pp. 3807–3809.

[185] Marc Savanier, Ranjeet Kumar, and Shayan Mookherjea. “Photon pair generation from compact silicon microring resonators using microwatt-level pump powers”. In: *Optics express* 24.4 (2016), pp. 3313–3328.

[186] Davide Grassani et al. “Micrometer-scale integrated silicon source of time-energy entangled photons”. In: *Optica* 2.2 (2015), pp. 88–94.

[187] Ryota Wakabayashi et al. “Time-bin entangled photon pair generation from Si micro-ring resonator”. In: *Optics express* 23.2 (2015), pp. 1103–1113.

[188] Davide Grassani et al. “Energy correlations of photon pairs generated by a silicon microring resonator probed by Stimulated Four Wave Mixing”. In: *Scientific reports* 6 (2016), p. 23564.

[189] Erman Engin et al. “Photon pair generation in a silicon micro-ring resonator with reverse bias enhancement”. In: *Optics express* 21.23 (2013), pp. 27826–27834.

[190] Vilson R Almeida and Michal Lipson. “Optical bistability on a silicon chip”. In: *Optics letters* 29.20 (2004), pp. 2387–2389.

[191] Wei C Jiang et al. “Silicon-chip source of bright photon pairs”. In: *Optics express* 23.16 (2015), pp. 20884–20904.

[192] Marcelo Davanco et al. “Telecommunications-band heralded single photons from a silicon nanophotonic chip”. In: *Applied Physics Letters* 100.26 (2012), p. 261104.

[193] Nobuyuki Matsuda et al. “Slow light enhanced correlated photon pair generation in photonic-crystal coupled-resonator optical waveguides”. In: *Optics express* 21.7 (2013), pp. 8596–8604.

[194] Kazuhiro Ikeda et al. “Thermal and Kerr nonlinear properties of plasma-deposited silicon nitride/silicon dioxide waveguides”. In: *Optics express* 16.17 (2008), pp. 12987–12994.

[195] DTH Tan et al. “Group velocity dispersion and self phase modulation in silicon nitride waveguides”. In: *Applied Physics Letters* 96.6 (2010), p. 061101.

[196] Yoshitomo Okawachi et al. “Octave-spanning frequency comb generation in a silicon nitride chip”. In: *Optics letters* 36.17 (2011), pp. 3398–3400.

[197] Martin HP Pfeiffer et al. “Photonic Damascene process for integrated high-Q microresonator based nonlinear photonics”. In: *Optica* 3.1 (2016), pp. 20–25.

[198] Martin HP Pfeiffer et al. “Ultra-smooth silicon nitride waveguides based on the Damascene reflow process: fabrication and loss origins”. In: *Optica* 5.7 (2018), pp. 884–892.

[199] L Razzari et al. “CMOS-compatible integrated optical hyper-parametric oscillator”. In: *Nature Photonics* 4.1 (2010), p. 41.

[200] Jacob S Levy et al. “CMOS-compatible multiple-wavelength oscillator for on-chip optical interconnects”. In: *Nature photonics* 4.1 (2010), p. 37.

[201] Tobias J Kippenberg, Ronald Holzwarth, and Scott A Diddams. “Microresonator-based optical frequency combs”. In: *science* 332.6029 (2011), pp. 555–559.

[202] Adrea R Johnson et al. “Chip-based frequency combs with sub-100 GHz repetition rates”. In: *Optics letters* 37.5 (2012), pp. 875–877.

[203] Adrea R Johnson et al. “Octave-spanning coherent supercontinuum generation in a silicon nitride waveguide”. In: *Optics letters* 40.21 (2015), pp. 5117–5120.

[204] Martin HP Pfeiffer et al. “Octave-spanning dissipative Kerr soliton frequency combs in Si 3 N 4 microresonators”. In: *Optica* 4.7 (2017), pp. 684–691.

[205] Xingyuan Xu et al. “Reconfigurable broadband microwave photonic intensity differentiator based on an integrated optical frequency comb source”. In: *Apl Photonics* 2.9 (2017), p. 096104.

[206] Xingyuan Xu et al. “Advanced RF and microwave functions based on an integrated optical frequency comb source”. In: *Optics express* 26.3 (2018), pp. 2569–2583.

[207] Brian Stern et al. “Battery-operated integrated frequency comb generator”. In: *Nature* 562.7727 (2018), p. 401.

[208] Michael Kues et al. “Quantum optical microcombs”. In: *Nature Photonics* 13.3 (2019), p. 170.

[209] Christian Reimer et al. “Integrated frequency comb source of heralded single photons”. In: *Optics express* 22.6 (2014), pp. 6535–6546.

[210] Jose A Jaramillo-Villegas et al. “Persistent energy–time entanglement covering multiple resonances of an on-chip biphoton frequency comb”. In: *Optica* 4.6 (2017), pp. 655–658.

[211] Poolad Imany et al. “50-GHz-spaced comb of high-dimensional frequency-bin entangled photons from an on-chip silicon nitride microresonator”. In: *Optics express* 26.2 (2018), pp. 1825–1840.

[212] Xiyuan Lu et al. “Chip-integrated visible–telecom entangled photon pair source for quantum communication”. In: *Nature Physics* 15.4 (2019), p. 373.

[213] M Peccianti et al. “Demonstration of a stable ultrafast laser based on a nonlinear microcavity”. In: *Nature communications* 3 (2012), p. 765.

[214] Alessia Pasquazi et al. “Stable, dual mode, high repetition rate mode-locked laser based on a microring resonator”. In: *Optics express* 20.24 (2012), pp. 27355–27363.

[215] Alessia Pasquazi et al. “Self-locked optical parametric oscillation in a CMOS compatible microring resonator: a route to robust optical frequency comb generation on a chip”. In: *Optics express* 21.11 (2013), pp. 13333–13341.

[216] Adrea R Johnson et al. “Microresonator-based comb generation without an external laser source”. In: *Optics express* 22.2 (2014), pp. 1394–1401.

[217] Marcus W Doherty et al. “The nitrogen-vacancy colour centre in diamond”. In: *Physics Reports* 528.1 (2013), pp. 1–45.

[218] Andrei Faraon et al. “Resonant enhancement of the zero-phonon emission from a colour centre in a diamond cavity”. In: *Nature Photonics* 5.5 (2011), p. 301.

[219] Michael J Burek et al. “Free-standing mechanical and photonic nanostructures in single-crystal diamond”. In: *Nano letters* 12.12 (2012), pp. 6084–6089.

[220] Janine Riedrich-Möller et al. “One-and two-dimensional photonic crystal microcavities in single crystal diamond”. In: *Nature nanotechnology* 7.1 (2012), p. 69.

[221] Loïc Rondin et al. “Magnetometry with nitrogen-vacancy defects in diamond”. In: *Reports on progress in physics* 77.5 (2014), p. 056503.

[222] Florian Dolde et al. “Room-temperature entanglement between single defect spins in diamond”. In: *Nature Physics* 9.3 (2013), p. 139.

[223] Emre Togan et al. “Quantum entanglement between an optical photon and a solid-state spin qubit”. In: *Nature* 466.7307 (2010), p. 730.

[224] Hannes Bernien et al. “Two-photon quantum interference from separate nitrogen vacancy centers in diamond”. In: *Physical Review Letters* 108.4 (2012), p. 043604.

[225] Alp Sipahigil et al. “Quantum interference of single photons from remote nitrogen-vacancy centers in diamond”. In: *Physical review letters* 108.14 (2012), p. 143601.

[226] Bas Hensen et al. “Loophole-free Bell inequality violation using electron spins separated by 1.3 kilometres”. In: *Nature* 526.7575 (2015), p. 682.

[227] Norbert Kalb et al. “Entanglement distillation between solid-state quantum network nodes”. In: *Science* 356.6341 (2017), pp. 928–932.

[228] Peter C Humphreys et al. “Deterministic delivery of remote entanglement on a quantum network”. In: *Nature* 558.7709 (2018), p. 268.

[229] IJ Wu and GY Guo. “Second-harmonic generation and linear electro-optical coefficients of SiC polytypes and nanotubes”. In: *Physical Review B* 78.3 (2008), p. 035447.

[230] A Lohrmann et al. “A review on single photon sources in silicon carbide”. In: *Reports on Progress in Physics* 80.3 (2017), p. 034502.

[231] H Matsunami. “Current SiC technology for power electronic devices beyond Si”. In: *Microelectronic Engineering* 83.1 (2006), pp. 2–4.

[232] F Fuchs et al. “Engineering near-infrared single-photon emitters with optically active spins in ultrapure silicon carbide”. In: *Nature communications* 6 (2015), p. 7578.

[233] William F Koehl et al. “Room temperature coherent control of defect spin qubits in silicon carbide”. In: *Nature* 479.7371 (2011), p. 84.

[234] David J Christle et al. “Isolated electron spins in silicon carbide with millisecond coherence times”. In: *Nature materials* 14.2 (2015), p. 160.

[235] S Castelletto et al. “A silicon carbide room-temperature single-photon source”. In: *Nature materials* 13.2 (2014), p. 151.

[236] Matthias Widmann et al. “Coherent control of single spins in silicon carbide at room temperature”. In: *Nature materials* 14.2 (2015), p. 164.

[237] A Lohrmann et al. “Single-photon emitting diode in silicon carbide”. In: *Nature communications* 6 (2015), p. 7783.

[238] Bong-Shik Song et al. “Demonstration of two-dimensional photonic crystals based on silicon carbide”. In: *Optics express* 19.12 (2011), pp. 11084–11089.

[239] Greg Calusine, Alberto Politi, and David D Awschalom. “Cavity-enhanced measurements of defect spins in silicon carbide”. In: *Physical Review Applied* 6.1 (2016), p. 014019.

[240] Jaime Cardenas et al. “High q sic microresonators”. In: *Optics express* 21.14 (2013), pp. 16882–16887.

[241] Xiyuan Lu et al. “High Q silicon carbide microdisk resonator”. In: *Applied Physics Letters* 104.18 (2014), p. 181103.

[242] Sébastien Tanzilli et al. “Highly efficient photon-pair source using periodically poled lithium niobate waveguide”. In: *Electronics Letters* 37.1 (2001), pp. 26–28.

[243] Igor Aharonovich, Dirk Englund, and Milos Toth. “Solid-state single-photon emitters”. In: *Nature Photonics* 10.10 (2016), p. 631.

[244] Niccolo Somaschi et al. “Near-optimal single-photon sources in the solid state”. In: *Nature Photonics* 10.5 (2016), p. 340.

[245] Xing Ding et al. “On-demand single photons with high extraction efficiency and near-unity indistinguishability from a resonantly driven quantum dot in a micropillar”. In: *Physical review letters* 116.2 (2016), p. 020401.

[246] Mathieu Munsch et al. “Dielectric GaAs antenna ensuring an efficient broadband coupling between an InAs quantum dot and a Gaussian optical beam”. In: *Physical review letters* 110.17 (2013), p. 177402.

[247] Manuel Gschrey et al. “Highly indistinguishable photons from deterministic quantum-dot microlenses utilizing three-dimensional in situ electron-beam lithography”. In: *Nature communications* 6 (2015), p. 7662.

[248] CL Salter et al. “An entangled-light-emitting diode”. In: *Nature* 465.7298 (2010), p. 594.

[249] Leonard Mandel and Emil Wolf. *Optical coherence and quantum optics*. Cambridge university press, 1995.

[250] Robert W Boyd. *Nonlinear optics*. Elsevier, 2003.

[251] Geoffrey New. *Introduction to nonlinear optics*. Cambridge University Press, 2011.

[252] David J Griffiths and Darrell F Schroeter. *Introduction to quantum mechanics*. Cambridge University Press, 2018.

[253] Jun John Sakurai, Jim Napolitano, et al. *Modern quantum mechanics*. Vol. 185. Pearson Harlow, 2014.

[254] Agata M Brańczyk, Aurélia Chenu, and JE Sipe. “Thermal light as a mixture of sets of pulses: the quasi-1D example”. In: *JOSA B* 34.7 (2017), pp. 1536–1541.

[255] R Hanbury Brown and RQ Twiss. “A test of a new type of stellar interferometer on Sirius”. In: *Nature* 178.4541 (1956), pp. 1046–1048.

[256] Albert Einstein, Boris Podolsky, and Nathan Rosen. “Can quantum-mechanical description of physical reality be considered complete?” In: *Physical review* 47.10 (1935), p. 777.

[257] Marco Liscidini and JE Sipe. “Stimulated emission tomography”. In: *Physical review letters* 111.19 (2013), p. 193602.

[258] Artur Ekert and Peter L Knight. “Entangled quantum systems and the Schmidt decomposition”. In: *American Journal of Physics* 63.5 (1995), pp. 415–423.

[259] CK Law, Ian A Walmsley, and JH Eberly. “Continuous frequency entanglement: effective finite Hilbert space and entropy control”. In: *Physical Review Letters* 84.23 (2000), p. 5304.

[260] James D Franson. “Bell inequality for position and time”. In: *Physical review letters* 62.19 (1989), p. 2205.

[261] Q Lin, Oskar J Painter, and Govind P Agrawal. “Nonlinear optical phenomena in silicon waveguides: modeling and applications”. In: *Optics express* 15.25 (2007), pp. 16604–16644.

[262] William W Rigrod. “Saturation effects in high-gain lasers”. In: *Journal of Applied Physics* 36.8 (1965), pp. 2487–2490.

[263] Micol Previde Massara et al. “Four-wave mixing in a silicon microring resonator using a self-pumping geometry”. In: *Applied Physics Letters* 113.12 (2018), p. 121111.

[264] Nicholas C Harris et al. “Integrated source of spectrally filtered correlated photons for large-scale quantum photonic systems”. In: *Physical Review X* 4.4 (2014), p. 041047.

[265] Yuan Guo et al. “The impact of nonlinear losses in the silicon microring cavities on cw pumping correlated photon pair generation”. In: *Optics express* 22.3 (2014), pp. 2620–2631.

[266] Jing Suo et al. “Generation of hyper-entanglement on polarization and energy-time based on a silicon micro-ring cavity”. In: *Optics express* 23.4 (2015), pp. 3985–3995.

[267] Florent Mazeas et al. “High-quality photonic entanglement for wavelength-multiplexed quantum communication based on a silicon chip”. In: *Optics express* 24.25 (2016), pp. 28731–28738.

[268] Hyundai Park et al. “A hybrid AlGaInAs–silicon evanescent amplifier”. In: *IEEE Photonics Technology Letters* 19.4 (2007), pp. 230–232.

[269] Yannick De Koninck, Gunther Roelkens, and Roel Baets. “Electrically pumped 1550 nm single mode III-V-on-silicon laser with resonant grating cavity mirrors”. In: *Laser & Photonics Reviews* 9.2 (2015), pp. L6–L10.

[270] Tianren Fan et al. “High-Q integrated photonic microresonators on 3C-SiC-on-insulator (SiCOI) platform”. In: *Optics express* 26.20 (2018), pp. 25814–25826.

[271] L Di Cioccio et al. “Silicon carbide on insulator formation using the Smart Cut process”. In: *Electronics Letters* 32.12 (1996), pp. 1144–1145.

[272] Francesco Martini and Alberto Politi. “Linear integrated optics in 3C silicon carbide”. In: *Optics express* 25.10 (2017), pp. 10735–10742.

[273] J Soler Penades et al. “Suspended silicon mid-infrared waveguide devices with subwavelength grating metamaterial cladding”. In: *Optics express* 24.20 (2016), pp. 22908–22916.

[274] J Soler Penadés et al. “Suspended silicon waveguides for long-wave infrared wavelengths”. In: *Optics letters* 43.4 (2018), pp. 795–798.

[275] Ahmed Osman et al. “Suspended low-loss germanium waveguides for the longwave infrared”. In: *Optics letters* 43.24 (2018), pp. 5997–6000.

[276] Steven G Johnson and John D Joannopoulos. “Block-iterative frequency-domain methods for Maxwell’s equations in a planewave basis”. In: *Optics express* 8.3 (2001), pp. 173–190.

[277] FP Payne and JPR Lacey. “A theoretical analysis of scattering loss from planar optical waveguides”. In: *Optical and Quantum Electronics* 26.10 (1994), pp. 977–986.

[278] F Grillot et al. “Size influence on the propagation loss induced by sidewall roughness in ultrasmall SOI waveguides”. In: *IEEE Photonics Technology Letters* 16.7 (2004), pp. 1661–1663.

[279] Alejandro Ortega-Moñux et al. "Disorder effects in subwavelength grating metamaterial waveguides". In: *Optics express* 25.11 (2017), pp. 12222–12236.

[280] Davide Janner et al. "Micro-structured integrated electro-optic LiNbO3 modulators". In: *Laser & Photonics Reviews* 3.3 (2009), pp. 301–313.

[281] Qianfan Xu et al. "Micrometre-scale silicon electro-optic modulator". In: *nature* 435.7040 (2005), p. 325.

[282] Robert Halir et al. "Waveguide grating coupler with subwavelength microstructures". In: *Optics letters* 34.9 (2009), pp. 1408–1410.

[283] Zhenzhou Cheng et al. "Broadband focusing grating couplers for suspended-membrane waveguides". In: *Optics letters* 37.24 (2012), pp. 5181–5183.

[284] Francesco Martini and Alberto Politi. "Four wave mixing in 3C SiC ring resonators". In: *Applied Physics Letters* 112.25 (2018), p. 251110.

[285] Mateusz Piekarek et al. "High-extinction ratio integrated photonic filters for silicon quantum photonics". In: *Optics letters* 42.4 (2017), pp. 815–818.

[286] Jun Rong Ong, Ranjeet Kumar, and Shayan Mookherjea. "Silicon microring-based wavelength converter with integrated pump and signal suppression". In: *Optics letters* 39.15 (2014), pp. 4439–4441.

[287] Luigi Scaccabarozzi et al. "Dichroic mirror embedded in a submicrometer waveguide for enhanced resonant nonlinear optical devices". In: *Optics letters* 31.22 (2006), pp. 3285–3287.

[288] Robert Cernansky, Francesco Martini, and Alberto Politi. "Complementary metal-oxide semiconductor compatible source of single photons at near-visible wavelengths". In: *Optics letters* 43.4 (2018), pp. 855–858.

[289] John Archibald Wheeler and Wojciech Hubert Zurek. *Quantum theory and measurement*. Vol. 49. Princeton University Press, 2014.

[290] M Jammer. *1974The philosophy of quantum mechanics.*

[291] Peter Shadbolt et al. "Testing foundations of quantum mechanics with photons". In: *Nature Physics* 10.4 (2014), p. 278.

[292] Lynden K Shalm et al. "Strong loophole-free test of local realism". In: *Physical review letters* 115.25 (2015), p. 250402.

[293] Thomas Scheidl et al. “Violation of local realism with freedom of choice”. In: *Proceedings of the National Academy of Sciences* 107.46 (2010), pp. 19708–19713.

[294] Daniel Salart et al. “Testing the speed of ‘spooky action at a distance’”. In: *Nature* 454.7206 (2008), p. 861.

[295] John F Clauser. “Experimental distinction between the quantum and classical field-theoretic predictions for the photoelectric effect”. In: *Physical Review D* 9.4 (1974), p. 853.

[296] Thiago Guerreiro et al. “Single-photon space-like antibunching”. In: *Physics Letters A* 376.32 (2012), pp. 2174–2177.

[297] Francesco Garrisi et al. “Experimental test of the collapse time of a delocalized photon state”. In: *Scientific reports* 9.1 (2019), pp. 1–7.

[298] Gerald S Buller et al. “Multiple wavelength time-of-flight sensor based on time-correlated single-photon counting”. In: *Review of Scientific Instruments* 76.8 (2005), p. 083112.

[299] Benjamin P Abbott et al. “GW170817: observation of gravitational waves from a binary neutron star inspiral”. In: *Physical Review Letters* 119.16 (2017), p. 161101.

[300] Paul G Kwiat et al. “Ultrabright source of polarization-entangled photons”. In: *Physical Review A* 60.2 (1999), R773.

Index